Université
de Toulouse

THÈSE

En vue de l'obtention du

DOCTORAT DE L'UNIVERSITÉ DE TOULOUSE

Délivré par :

Institut Supérieur de l'Aéronautique et de l'Espace (ISAE)

Présentée et soutenue par :
Zhongxun LIU
le lundi 27 mai 2013

Titre :

Modélisation des signatures radar des tourbillons de sillage par temps de pluie

---

École doctorale et discipline ou spécialité :

ED AA : Dynamique des fluides & Signal, image, acoustique et optimisation

Unité de recherche :

Équipe d'accueil ISAE-ONERA SCANR

Directeur(s) de Thèse :

M. François VINCENT (directeur de thèse)
M. Nicolas JEANNIN (co-directeur de thèse)

Jury :

François VINCENT, Enseignant-Chercheur ISAE - Directeur de thèse
Nicolas JEANNIN, Ingénieur ONERA - Co-directeur de thèse
Danielle VANHOENACKER-JANVIER, Professeur UC Louvain - Rapporteur
François LE CHEVALIER, Professeur TU Delft - Rapporteur
Frédéric BARBARESCO, Ingénieur Thalès Air Systems - Examinateur
Vincent BRION, Ingénieur ONERA - Examinateur

Abstract

In recent years, wake vortex monitoring in real time has emerged as one of the key challenges in air traffic control at landing or taking-off. In clear air, several experimental tests have demonstrated that Lidar is an effective sensor for wake vortex monitoring. In rainy weather, Lidar becomes blind and Radar is a candidate sensor to detect the motion of raindrops in wake vortices. Thus, investigation on radar monitoring of wake vortices in rainy weather is of both scientific and practical interests. This topic has been tackled through three successive steps during this thesis.

Firstly, the motion of raindrops in wake vortices has been modeled and simulated. The equation of the motion has been derived and the methodology to compute the raindrops' trajectory and distribution in the flow induced by the wake vortices has been proposed.

Secondly, two simulators have been developed for evaluating the radar signatures of raindrops in wake vortices. One simulator is based on the simulation of radar signal time series, by superimposing the radar backscattered signal from each raindrop in the wake vortex region. The other one is based on the raindrops' number concentration and velocity distribution in wake vortices, enabling the computation of radar signatures much more efficiently. Those simulators have been used to reproduce experimental configurations and the comparison between measured and simulated signature has shown an interesting agreement at X and W band.

Lastly, the interpretation of radar signatures of raindrops in wake vortices has been presented. Based on the computation of three spectral moments, the dependence of radar signatures on rain rate, vortex circulation and radar parameters has been studied for vortices generated by different aircraft types. A wake vortex detection method based on the analysis of Doppler spectrum width of raindrops has been proposed. Considering radar scanning under flight path, a methodology to estimate the wake vortex characteristics has been proposed. Preliminary simulation results have shown its effectiveness.

The radar signatures of wake vortices in rainy weather have been modeled and analyzed in this thesis. The simulation results have demonstrated the capability of radar to detect wake vortex in rainy weather. The methodologies developed in this thesis can be further exploited for designing new wake vortex radar systems.

Key words: Wake vortex, radar, rain, Doppler spectrum, detection

Résumé

Ces dernières années, la détection des turbulences de sillage est apparue comme étant un des enjeux les plus importants pour l'amélioration des procédures de contrôle aérien, et plus particulièrement au décollage et à l'atterrissage. Par beau temps, plusieurs expérimentations ont montré que le LIDAR était un capteur efficace pour ce type d'application. En présence de pluie ou de nuages, le LIDAR ne peut plus opérer du fait de la perte de visibilité et le radar devient un capteur intéressant pour détecter le mouvement des gouttes d'eau dans les turbulences de sillage. Dès lors, la surveillance des turbulences de sillage par radar en temps de pluie présente un intérêt à la fois pratique et scientifique. Cette thématique a été traitée à travers trois étapes successives.

Tout d'abord, le mouvement et la distribution des gouttes d'eau dans les vortex ont été modélisés et simulés. A partir de l'équation de la dynamique appliquée sur une goutte d'eau, une méthode de calcul de la trajectoire des gouttes d'eau et de leur concentration dans les turbulences de sillage a été proposée.

Ensuite, deux simulateurs de réponse radar des gouttes d'eau dans et autour des vortex ont été proposés. Le premier simulateur vise à générer des séries temporelles de signal radar, simulant la réponse individuelle de chaque goutte, pour le développement des chaines de traitement radar. Le second simulateur vise à générer directement la réponse radar idéalisée à partir de la concentration et de la vitesse des gouttes dans l'écoulement provoqué par les vortex, ce qui est algorithmiquement plus efficace. Ces deux simulateurs ont été utilisés pour reproduire des configurations expérimentales, et une comparaison préliminaire avec les mesures a montré une concordance intéressante entre mesures et simulations en bande X et W.

Enfin, l'interprétation de la signature radar des gouttes de pluie dans les vortex a été présentée. Considérant le calcul de trois moments spectraux, la dépendance de la signature envers différents paramètres, à savoir l'intensité de précipitation, la circulation des vortex et les paramètres radar, a été étudiée pour des turbulences de sillage générées par différents types d'avions. Une méthode de détection des turbulences de sillage basée sur la largeur du spectre Doppler des gouttes de pluie a été proposée. Considérant un radar balayant sous les trajectoires d'approche, un algorithme permettant d'estimer les caractéristiques des turbulences de sillage est proposé. Des simulations préliminaires ont montré son efficacité.

La signature radar des turbulences de sillage par temps de pluie a été modélisée et analysée dans cette thèse. Les résultats de simulations ont démontré les capacités du radar pour la détection de ces turbulences. Les méthodes développées dans cette thèse pourront être utilisées pour le dimensionnement de systèmes radar dédiés à la surveillance des turbulences de sillage par temps de pluie.

Mots clés:

Tourbillons de sillage, wake vortex, radar, pluie, spectre Doppler, détection

Acknowledgement

I was very excited and moved when I finished the draft version of this manuscript. During this fulfilling and meaningful period of PhD study, I have experienced a lot and a large number of people in France and China are sincerely appreciated.

I would like to express my deepest gratitude to Professor Francois Vincent from ISAE and Dr. Nicolas Jeannin from ONERA, for their helpful joint supervision of this PhD work and unconditional support all along the way. The investigation into a multi-disciplinary subject was not very easy, but their generosity and encouragement helped me to overcome all the obstacles. This manuscript would not have been possible without their constructive corrections and comments. I wish to specially thank Mr. Florent Christophe, the director of DEMR in ONERA Toulouse center, for his helpful supervision of my PhD progress. He accepted my PhD application in France, proposed this interesting PhD subject and also supported my PhD study all along the way. The discussions with him on the PhD progress meetings inspired me a lot. I would like to express my great gratitude to Mr. Frédéric Barbaresco from THALES Air System for his helpful supervision of my six months' training in TRT (Thales Research & Technology). It was his publications on wake vortex that mostly attracted my motivation to choose France as the destination of my PhD study. Professor Michel Bousquet from ISAE is also specially thanked for his sending me the invitation letter and support of my stay at Toulouse. Appreciation must also go to my colleagues in ISAE-DEOS and ONERA-DEMR for their kind hearted help during my stay there.

I wish to specially thank Professor Xuesong Wang from NUDT in China, who has supervised my study since I was an undergraduate student and guided me to carry out research work on wake vortex as a PhD student in NUDT since 2008. His everlasting support, encouragement and supervision was a great source of my interest and progress on wake vortex study. Sincere thanks must also go to Dr. Tao Wang from NUDT in China for his valuable suggestions on my PhD work. He

has always been willing to help me whenever I needed it. Prof. Shunping Xiao, Prof. Wei Wang, Dr. Dahai Dai, Dr. Jianbing Li, Dr. Jun Li, Dr. Longhai Qu, Dr. Junkai Liu and some other colleagues from NUDT are also thanked for their unconditional help and sharing their knowledge on radar and wake vortex.

Very special thanks to my friends who I met with in France. I have benefitted a lot from this life enriching and unforgettable three years and half with them in France. Very special thanks to my friends in China. Their greetings and encouragement have always been appreciated. My deepest gratitude goes to my parents and parents in law. My study and life in France would not have been so easy without their understanding and support. I wish to express my deepest love to my dear wife, Jing Xu. Her immeasurable support and endless love encourages me to meet with various challenges.

Last but not least, I wish to express my appreciation of this multi-disciplinary PhD subject, which has brought me a broad view of the scientific research activities, including wake vortex aerodynamics, radar, precipitation, information geometry, spiral geometry of wake vortex, the interaction between particle and turbulent flow, etc. The valuable expertise and competence I have been rewarded will be of great significance to my future career road.

Contents

Résumé des travaux en Francais

0.1 Introduction

La télédétection des turbulences de sillage générées par les avions en phase d'atterrissage et de décollage constitue un enjeu majeur en vue d'augmenter la capacité des aéroports tout en garantissant la sécurité des aéronefs. En effet, afin de prévenir les incidents liés à la rencontre de turbulences générées par un avion, une distance minimale imposée par des normes de l'organisation internationale de l'aviation civile (ICAO) doit être respectée. Cette distance dépend des catégories de poids de l'avion de tête et de l'avion suiveur comme illustré à la Figure 1.

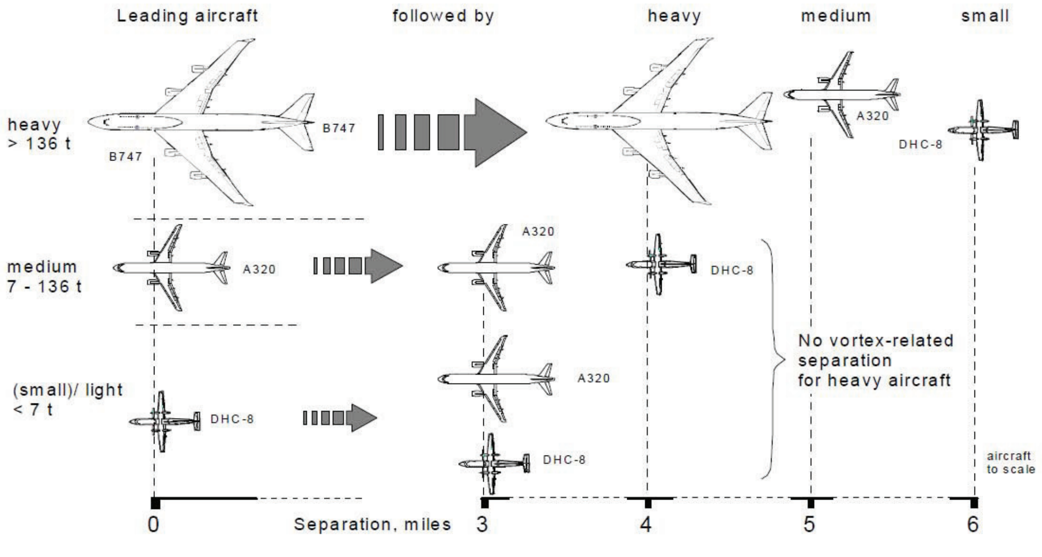

FIGURE 1 – Règle ICAO de séparation entre les différentes catégories d'avions [1]

Ces contraintes de distances basées sur des hypothèses pires cas imposent des contraintes fortes sur la capacité des aéroports. De plus, pour la majorité des conditions atmosphériques rencontrées, des distances restreintes permettraient, sans remettre en cause la sécurité, d'augmenter les flux d'avion entrant et sortant d'un aéroport. Dans cette optique, deux applications directes peuvent être envisagées à la télédétection des turbulences de sillage. La première, liée à l'amélioration de la connaissance des caractéristiques des sillages générés par chaque type d'avion peut permettre d'affiner les normes de séparation datant des années 60 avec une catégorisation frustre des différents types d'avion. La seconde, liée à l'observation temps réel des turbulences, pourrait permettre une meilleure évaluation du risque dans les procédures de contrôle aérien et l'utilisation de distances entre avion dépendant des conditions atmosphériques. Ces applications sont néanmoins assujetties à la possibilité d'observer et de caractériser ces turbulences quelque soit les conditions climatiques pour d'évidentes raisons opérationnelles. Ces turbulences sont de plus invisibles à l'œil nu la plupart de temps. Des exemples de turbulences de sillage rendues visibles par la présence de gouttes d'eau en suspension dans l'air ou de particules de fumées colorées sont illustrées à la Figure 2.

(a) Turbulences de sillage derrière un Learjet 60 dans un nuage [2]

(b) Matérialisation des turbulences de sillage sous forme de traînées de condensation [3]

(c) Turbulences de sillage ensemencées de fumées colorées lors de tests effectués par la NASA [4]

Figure 2 – Photographies de turbulences de sillage visibles

Ces turbulences, caractérisées par un écoulement hautement rotationel occasionnent un danger pour les aéronefs qui peut être quantifié en partie par la circulation du champ de vitesse. Différents capteurs dédiés à la télédétection de ces turbulences pour l'évaluation de cette circulation ont été expérimentés depuis les années 70, à savoir principalement des radar et lidar et plus marginalement des sodar [5–13]. En l'absence de précipitation et dans des conditions de visibilité favorables (absence de brouillard par exemple), les lidar semblent les capteurs les plus adaptés. Ils permettent d'obtenir avec une résolution spatiale très fine du fait de la forte directivité des laser, une cartographie du champ de vitesse des aérosols atmosphériques entraînés par les vortex. De ce fait ils permettent une évaluation aisée de la circulation du champ de vitesse des vortex. Les différents essais menés par radar font apparaître qu'en l'absence de précipitations, et ce quelque soit les bandes de fréquences, les niveaux de rétro-diffusion des vortex sont extrêmement faibles. La rétro-diffusion en air clair induite par les turbulences de sillage est causée par les fluctuations d'indice de réfraction liées aux variations des paramètres thermodynamiques de l'écoulement. Même dans des conditions d'humidité extrême, vraisemblablement les plus favorables, des niveaux de réflectivités extrêmement faibles ont été rapportés et ne peuvent être détectés qu'avec des radars excessivement puissants. En présence de pluie, la problématique s'avère être différente. En effet, les gouttes de pluies rétrodiffusent une énergie importante aux longueurs d'ondes centimétriques et décimétriques, ce qui a permis le développement des radars météorologiques. Ces capteurs sont capables d'estimer la concentration de gouttes d'eau dans des volumes d'atmosphère ainsi que leur vitesse projetée sur la ligne de visée du radar. Une modification locale de la concentration en gouttes d'eau et de leur vitesse, induite par la présence de turbulences de sillage est dès lors potentiellement détectable à l'aide de capteurs radar dédiés. La modélisation de cette signature et son interprétation est l'objet de cette thèse.

Ce travail est hautement pluri-disciplinaire et fait appel à des notions issues de divers domaines scientifiques. Une étape préalable à la modélisation de la signature radar en elle même a été la compréhension des divers phénomènes physiques. Les principales caractéristiques des gouttes d'eau, des sillages et le principe de la mesure radar sont présentés dans la première section de ce document. La seconde section de ce document est dédiée à l'étude de la trajectoire des gouttes de pluies dans l'écoulement généré par le passage de l'avion. L'étude de la cinématique des gouttes dans les turbulences de sillage est ensuite utilisée pour le développement de deux simulateurs de signatures radar. L'algorithmie et quelques résultats issues de ces simulateurs est décrite à la troisième section. Enfin une validation préliminaire du travail est présentée dans la dernière partie, en comparant les résultats obtenus à partir de simulations à des résultats obtenus pendant différentes campagnes de mesures. Une analyse paramétrique de la sensibilité de la signature à divers paramètres liés à la mesure radar, aux conditions météorologiques ou aux caractéristiques des turbulences de sillage est ensuite présentée.

Chaque section de cette partie en français constitue un récapitulatif des travaux réalisés et correspond à un chapitre du manuscrit en anglais auquel le lecteur est invité à se référer pour de plus amples détails. Les références bibliographiques correspondent également aux références de la partie en anglais.

0.2 Turbulences de sillage, gouttes de pluie et radar

Cette section vise à rappeler les principaux éléments de modélisation employés dans la suite du travail. Ainsi, diverses caractéristiques des champs de vitesses des turbulences de sillage, des propriétés mécaniques, statistiques et électromagnétiques de gouttes de pluie ainsi que des radars météorologiques sont présentées.

0.2.1 Turbulences de sillage

Les turbulences de sillage suivant le passage d'un avion sont intrinsèquement liées à la force de portance maintenant l'avion en sustentation. Ces vortex de bouts d'ailes se créent par écoulement de l'air situé à l'intrados de l'aile en surpression par rapport au fluide à l'extrados en dépression, comme schématisé à la Figure 3. La dimension de ces vortex est liée à l'envergure de l'avion et leur force, caractérisée par la circulation du champ de vitesse dépend de la portance (donc du poids de l'avion) et de la vitesse de vol de l'aéronef. Ces structures tourbillonnaires peuvent subsister plusieurs minutes en représentant un danger potentiel pour le trafic aérien. Elles sont caractérisées par plusieurs stades de développement comme illustré à la Figure 4 [14].

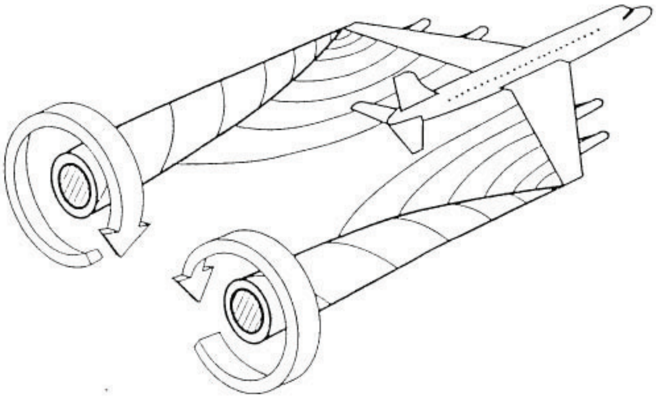

Figure 3 – Illustration de deux vortex contra-rotatifs [5, 15]

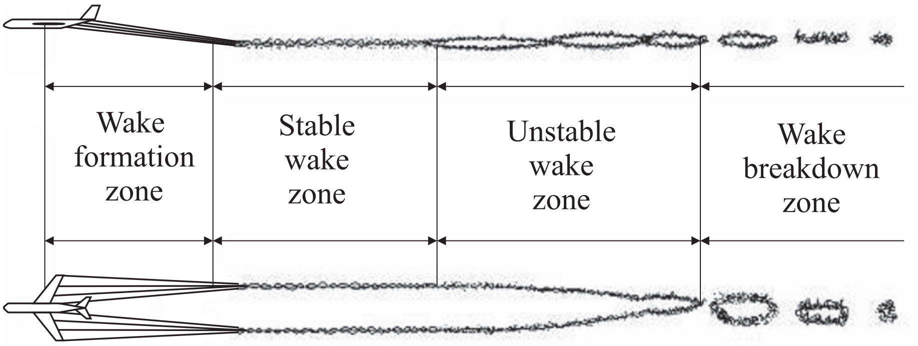

FIGURE 4 – Différentes phases d'évolution des turbulences de sillage [14]

A une phase de formation correspondant à l'enroulement du fluide autour du vortex succède une phase stationnaire qui est considérée dans ce travail car la plus longue et la plus dangereuse pour le transport aérien. Après cette phase stationnaire, l'écoulement se déstabilise et disparait.

Afin de modéliser le champ de vitesse créé par les turbulences de sillage dans ce travail, le modèle de vortex de Hallock Burnham est utilisé. Ce modèle approche la vitesse radiale $V_\theta(r)$ de l'écoulement à une distance r du centre de chaque vortex par l'expression suivante [16, 17] :

$$V_\theta(r) = \frac{\Gamma}{2\pi r} \cdot \frac{r^2}{r^2 + r_\mathrm{c}^2} \tag{1}$$

où Γ représente la circulation du vortex, r_c le rayon du cœur du vortex et r la distance au centre du vortex. Il est supposé que la vitesse radiale de l'écoulement est nulle et que le champ de vitesse est invariant suivant l'axe porté par le vecteur vitesse de l'avion, ce qui permettra dans la suite de ne considérer que la problématique bidimensionnelle. L'expression de la circulation initiale du vortex en fonction de la masse de l'avion de sa vitesse et de son envergure peut être approchée de manière générique par [18] :

$$\Gamma_0 = \frac{Mg}{\rho U b_0}, b_0 = \frac{\pi}{4} b \tag{2}$$

Un exemple de profil de vitesse vertical pour des vortex générés par différents type d'avion est illustré à la Figure 5.

Après leur création les deux vortex descendent du fait de l'induction mutuelle entre les deux tourbillons. Au premier ordre, la vitesse de descente peut être approchée en négligeant les effets de la stratification atmosphérique par :

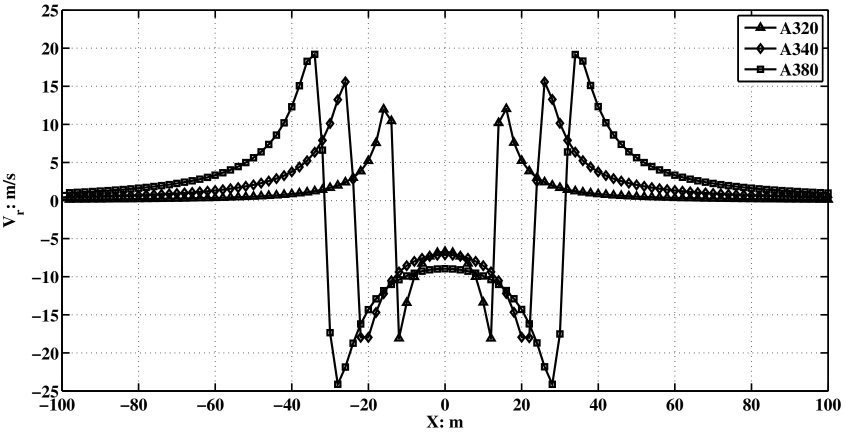

FIGURE 5 – Profil de vitesse vertical sur une ligne joignant les centres des deux vortex induits par les turbulences de sillage d'un A320, d'un A340 et d'un A380.

$$V_d = \frac{\Gamma}{2\pi b_0} \tag{3}$$

En descendant l'énergie des tourbillons se dissipe, et la circulation diminue. Cette diminution de circulation peut être reliée au temps caractéristique de descente des vortex, correspondant au temps pris par les vortex pour descendre d'une envergure :

$$t^{'} = \frac{b_0}{V_d} = 0.38\frac{B^3 U}{M} \tag{4}$$

où B,U et M représentent l'envergure, la vitesse de vol et le poids de l'aéronef respectivement. Si l'air ambiant a un taux de dissipation turbulente ε supérieure à une valeur seuil, $\varepsilon_0 = 10^{-4}\mathrm{m}^2/\mathrm{s}^2$, il a été observé empiriquement que la décroissance de la circulation est due à l'instabilité de Crow et mène à un taux de dissipation linéaire [19]. L'évolution de la circulation peut dès lors être approchée par la relation suivante :

$$\Gamma = \Gamma_0 \left(1 - \frac{t^*}{8}\right) \quad \text{avec} \quad t^* = \frac{t}{t'} \tag{5}$$

Près du sol les vortex peuvent rebondir et des vortex secondaires peuvent apparaître. Il est à noter que les turbulences de sillage peuvent également être advectées par le champ de vent à large échelle. Dans ce cas le champ de vitesse du vent macroscopique est à ajouter au champ de vitesse engendré par les vortex.

0.2.2 Gouttes de pluie

L'étude de la la distribution de taille des gouttes de pluie a commencé historiquement avec les observations de Marshall-Palmer qui mirent en évidence une distribution de type exponentielle [20] du nombre de gouttes de pluie en fonction de leur diamètre. Des études ultérieures plus poussées mirent en évidence que ce modèle surestimait assez largement le nombre de gouttes de petite taille. Il a été montré ([21–23]) que des distributions de taille de gouttes de type Gamma modifiées permettent de décrire de manière plus appropriée la granulométrie pour différents types de pluie et différentes zones géographiques. Cette distribution utilisée dans la suite des travaux, représente la densité de gouttes de diamètre D par unité de volume et s'exprime sous la forme :

$$N(D) = N_0 D^{\mu} e^{-\wedge D}, m^{-3} mm{-}1 \tag{6}$$

où N_0, μ et $\wedge$ représentent la concentration, le coefficient de forme de la distribution et le paramètre de taille de la distribution respectivement. La plus grande difficulté tenant à l'usage de ces distributions est leur paramétrage. A cet effet, un paramétrage générique représentatif des climats tempérés Européens a été choisi [23]. Sauf mention contraire des valeurs $\mu = 2$ et $N_0 = 64500 R^{-0.5}$ (en $\mathrm{m}^{-3}\mathrm{mm}^{-1-\mu}$), $\wedge = 7.09 R^{-0.27}$ (en mm^{-1}) sont adoptées. Outre la distribution granulométrique, la connaissance de la vitesse de chute des gouttes d'un diamètre D dans une atmosphère libre est également une donnée utilisée par la suite car représentative du coefficient de traînée des gouttes de pluies. Différentes études ont montré que la vitesse terminale de chute (à savoir la vitesse pour laquelle le poids de la goutte d'eau et la force de frottement fluide sont égales) pouvait prendre le forme approchée [21, 24, 25] :

$$V_{\mathrm{T}}(D) = [\alpha_1 - \alpha_2 exp(-\alpha_3 D)](\frac{\rho_0}{\rho})^{0.4}, \mathrm{m/s} \tag{7}$$

avec $\alpha_1 = 9.65$ m/s, $\alpha_2 = 10.3$ m/s et $\alpha_3 = 0.6\ \mathrm{m}^{-1}$. Le terme $(\frac{\rho_0}{\rho})^{0.4}$ représente un facteur de correction sur la densité de l'air variant avec l'altitude. La Figure 7 présente la vitesse terminal de chute de gouttes d'eau à différentes altitudes. il peut être remarqué que la vitesse de chute croit avec l'altitude et que les grosses gouttes (dont le diamètre est de l'ordre de 5 mm) ne dépassent généralement pas 10m/s.

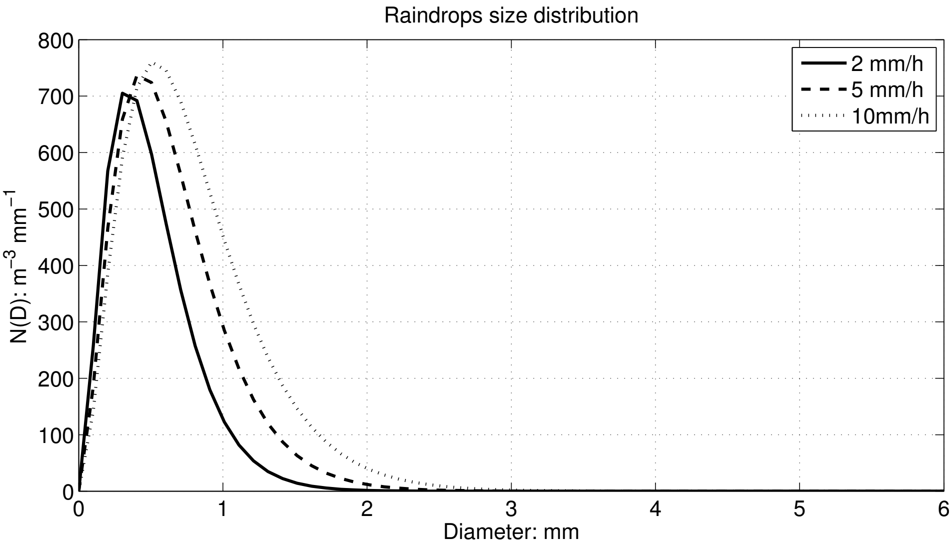

FIGURE 6 – Distribution de taille de goutte pour différentes intensités de précipitation : R =2 mm/h, 5 mm/h et 10 mm/h.

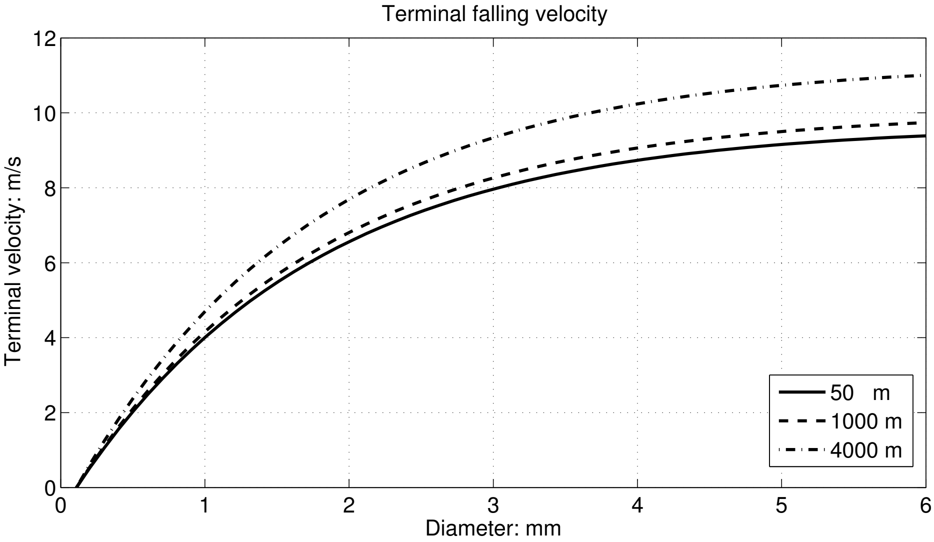

FIGURE 7 – Vitesse terminale des gouttes de pluie à 50 m, 1000 m et 4000 m au dessus du niveau de la mer.

0.2.3 Radar météorologique

Le radar météorologique est un outil largement répandu pour la télédétection des champs de précipitation. Il permet d'établir avec une répétitivité temporelle importante des cartographies des champs de précipitation. Le signal renvoyé par ce type de radar est sensible à la distribution de taille de gouttes dans chaque cellule de résolution et à leur vitesse radiale dans le cas de traitements Doppler. Le volume sondé est défini par la résolution radiale du radar dépendant de la bande de fréquence utilisée et par les ouvertures angulaires de l'antenne dépendant principalement de la taille de l'antenne. Le signal rétrodiffusé par chaque goutte peut être calculé par une diffusion de Rayleigh si le diamètre des gouttes d'eau est très inférieur à la longueur d'onde utilisée ou par une diffusion de Mie si la longueur d'onde et le diamètre des gouttes sont du même ordre de grandeur. La surface équivalente radar fonction du diamètre des gouttes est illustré à la Figure 8 en diffusion de Mie et à la Figure 9 pour la diffusion de Rayleigh.

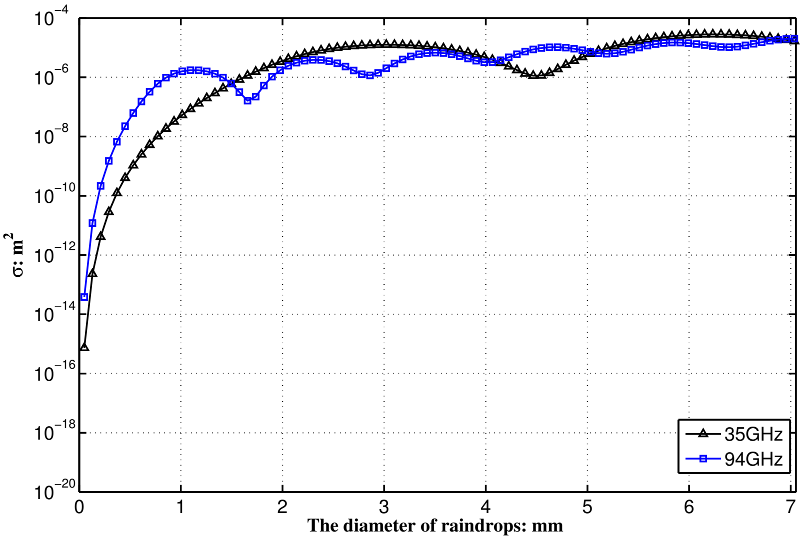

Figure 8 – Section radar efficace d'une goutte d'eau en fonction de son diamètre : approximation de Mie.

La réflectivité mesurée par le radar dans le cas de cibles distribuées est définie comme la section radar efficace par unité de volume. Cette réflectivité dans le cas du radar météorologique peut être liée à l'intensité de précipitation, connaissant ou supposant un modèle de distribution de taille de goutte.

Des radars similaires à ces radars météorologiques apparaissent comme les senseurs les plus adaptés pour la télédétection des turbulences de sillage par temps de pluie.

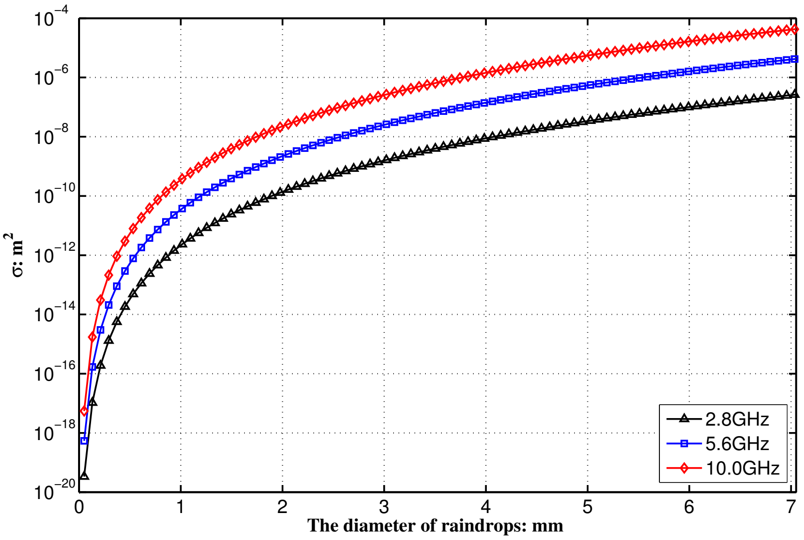

FIGURE 9 – Section radar efficace d'une goutte d'eau en fonction de son diamètre : approximation de Rayleigh.

0.3 Trajectoire des gouttes d'eau dans les tourbillons de sillage

L'écoulement généré par le passage de l'avion, provoque en présence de gouttes de pluie, une modification de la force de frottement aérodynamique s'exerçant sur les gouttes d'eau. En effet cette force de frottement fluide est proportionnelle au carré de la vitesse relative entre la goutte et l'air ambiant en supposant un écoulement à nombre de Reynolds très supérieur à un. La modification de la trajectoire des gouttes d'eau va modifier les caractéristiques de la réponse radar de la pluie autour des vortex par rapport à la réponse radar de la pluie tombant en atmosphère libre. Afin de caractériser au mieux la réponse radar dans la pluie, une étude paramétrique de la trajectoire des gouttes de pluie autour des vortex est donc nécessaire.

0.3.1 Analyse qualitative

Le problème de gouttes d'eau entraînées dans l'écoulement créé par le passage de l'avion peut en toute généralité s'inscrire dans la classe générique des problèmes étudiant le mouvement de particules dans un écoulement. Une métrique particulièrement intéressante pour classifier ce type de problème est le nombre de Stokes. Cette grandeur adimensionnée permet de quantifier l'impact de l'écoulement sur la

TABLE 1 – Nombre de Stokes correspondant à des gouttes d'eau entraînées par les turbulences de sillage générées par un A340.

Diameter	t_s	t_{flow}	S_t
0.5 mm	0.2061	0.7198	0.2863
1.0 mm	0.4079	0.7198	0.5667
2.0 mm	0.6681	0.7198	0.9282
4.0 mm	0.8893	0.7198	1.2355

trajectoire des particules. Il est défini comme le rapport de temps caractéristiques du problème, à savoir le temps de relaxation de la particule t_s (représentatif du temps que met une goutte d'eau pour atteindre une fraction de sa vitesse limite) et le temps caractéristique de l'écoulement engendré par le vortex t_{flow} :

$$S_t = \frac{t_s}{t_{flow}} \tag{8}$$

Un nombre de Stokes très supérieur à un indique que la trajectoire des particules n'est que peu perturbée par l'écoulement, alors qu'un nombre de Stokes très inférieur à un indique que les particules vont être complètement emportée par l'écoulement.

Dans le cas d'un vortex, le temps caractéristique de l'écoulement est donné par :

$$t_{flow} = \frac{2\pi r_{max}}{V_{max}} \tag{9}$$

où V_{max} est la vitesse maximale dans l'écoulement et r_{max} la distance entre le centre du vortex et l'endroit ou se produit cette vitesse. Le temps de relaxation des gouttes d'eau est lui donné par :

$$t_s = \frac{V_T}{g} \tag{10}$$

Le nombre de Stokes peut être calculé pour différents diamètres de goutte considérant les turbulences en phase stationnaire générées par un A340, comme illustré à la table 3.1.

Vu la gamme de nombre de Stokes considérée pour le problème des gouttes de pluie prise dans les turbulences de sillage, aucune conclusion générique n'est satisfaisante. les gouttes de pluie ne sont ni complètement entraînées ni insensibles à l'écoulement car S_t n'est pas très éloigné de 1). Par conséquent une analyse de la trajectoire des gouttes de pluie par l'intermédiaire de l'équation de la dynamique est requise afin de mieux quantifier la trajectoire des gouttes. Il est à noter que dans le cas d'aérosols atmosphériques ou de gouttelettes d'eau nuageuse $S_t << 1$ et il est dès lors possible d'assimiler le champ de vitesse de ces particules au champ de vitesse induit par les vortex.

0.3.2 Équation du mouvement

Afin de caractériser la trajectoire d'une goutte d'eau de diamètre D dans l'écoulement, en utilisant un nombre limité de paramètres, le problème peut être simplifié en un problème de dynamique du point dans un écoulement supposé stationnaire. De ce fait différents phénomènes physiques sont négligés comme : la déformation et les mouvements éventuels de rotation propre (surtout important pour les grosses gouttes), l'impact de l'échange d'énergie entre l'écoulement et la pluie, l'évolution du champ de vitesse du vortex... Ces hypothèses induisent certainement des imprécisions sur les trajectoires calculées, mais permettent de s'affranchir de certaines variables au paramétrage inconnu. Sous ces hypothèses l'équation du mouvement d'une goutte d'eau de masse m soumise à son poids et la force de traînée exercée par l'air ambiant $\mathbf{F}_{\mathrm{d}}(t)$ peut se mettre sous la forme :

$$\mathbf{a}(t) = \frac{\mathbf{F}_{\mathrm{d}}(t)}{m_{\mathrm{p}}} + \mathbf{g} \tag{11}$$

L'expression de la force de frottement fluide s'exprime en fonction de la vitesse relative de la goutte d'eau par rapport à l'air ambiant et du coefficient de traînée C_{d} de la goutte d'eau comme :

$$\mathbf{F}_{\mathrm{d}}(t) = \frac{1}{2} C_{\mathrm{d}} \rho_a \delta \mathbf{v}^2 \left(\frac{\pi D}{2} \right)^2, \delta \mathbf{v} = \mathbf{u}[\mathbf{z}_{\mathrm{p}}(t)] - \mathbf{v}_{\mathrm{p}}(t) \tag{12}$$

Où $\mathbf{u}[\mathbf{z}_{\mathrm{p}}(t)]$ représente la vitesse de l'écoulement au point $\mathbf{z}_{\mathrm{p}}(t)$ et $\mathbf{v}_{\mathrm{p}}(t)$ est la vitesse de la goutte. Cela permet d'obtenir une estimation du coefficient de traînée des gouttes d'eau en fonction du diamètre des gouttes d'eau et de la vitesse terminale par :

$$C_{\mathrm{d}} = \frac{4 \rho_w g D}{3 \rho_a V_{\mathrm{T}}^2} \tag{13}$$

Du fait de la dépendance de la force de frottement au carré de la vitesse relative, l'équation du mouvement (3.4) est un système d'équation différentielle non linéaire du second ordre. Comme il n'existe pas de méthode analytique pour résoudre ce problème, une résolution numérique utilisant un algorithme de type Runge-Kutta d'ordre 4 a été entreprise. Des exemples de solutions correspondant à des trajectoires de gouttes d'eau relâchées au dessus de turbulences de sillage générées par un A340, sont illustrées à la Figure 10.

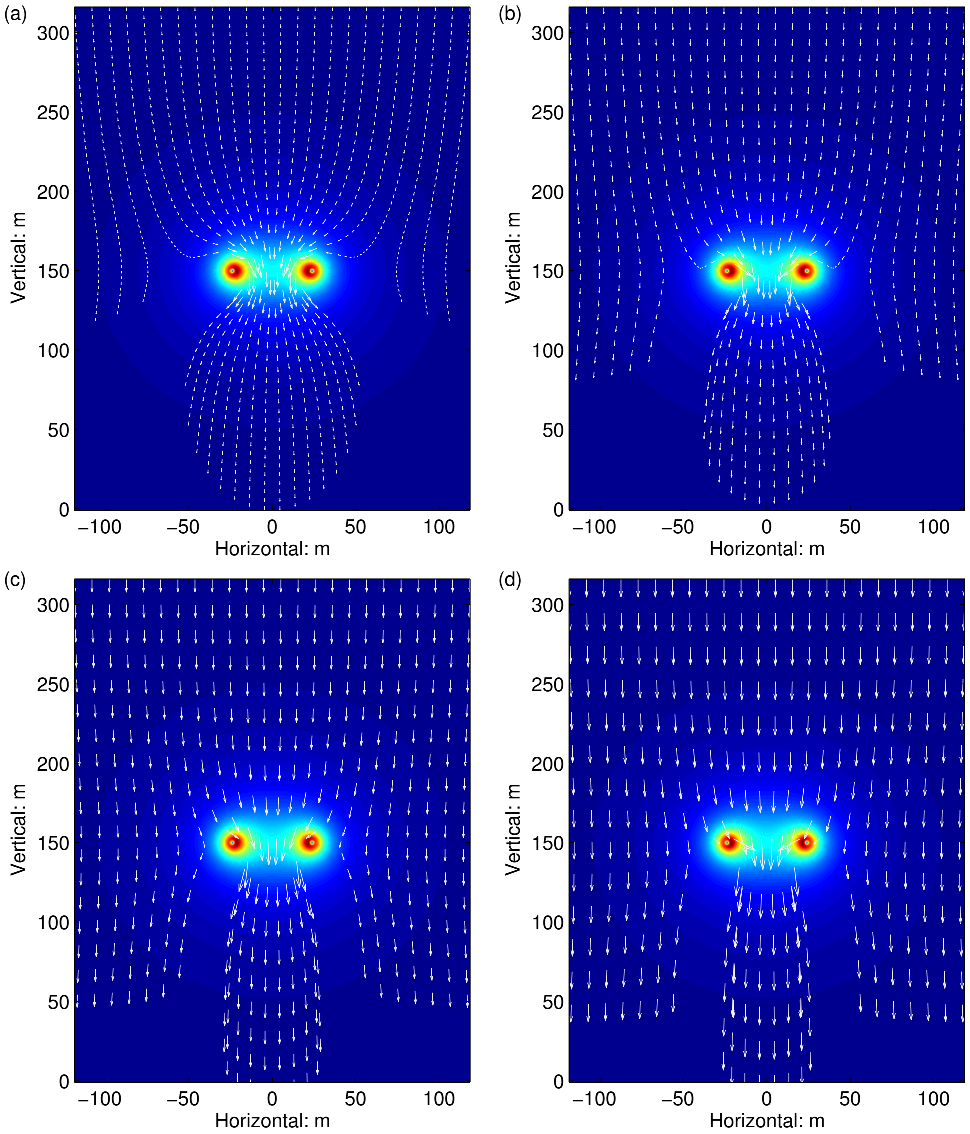

Figure 10 – Trajectoire des gouttes d'eau dans les turbulences de sillage : (a) D = 0.5 mm, Durée de la trajectoire : 106.6s, (b) D = 1.0 mm, Durée de la trajectoire : 62.2 s, (c) D = 2.0mm, Durée de la trajectoire : 41.0s, (d) D= 4.0 mm, Durée de la trajectoire : 31.8s. L'image de fond correspond au champ de vitesse engendré par les turbulences de sillage d'un A340.

Il peut être remarqué à la Figure 3.2 que la trajectoire des gouttes dépend fortement de la position initiale et du diamètre des gouttes, sachant que les gouttes ont initialement leur vitesse terminale de chute. Il est également à noter que comme évoqué lors de l'analyse du nombre de Stokes, les gouttes d'eau les plus petites tendent à suivre les lignes de courant de l'écoulement tandis que la trajectoire des grosses gouttes est moins affectée par le champ de vitesse des vortex.

La trajectoire des gouttes d'eau considérant la vitesse de descente des vortex et l'évolution concomitante de la circulation a également été étudiée et calculée sur le même principe et intégrée dans les simulateurs de signatures radar présentés à la section suivante.

0.4 Simulateur de signature radar de vortex par temps de pluie

Deux méthodes de simulations de la signatures radar des gouttes d'eau dans la pluie ont été développées au cours de la thèse. La première méthodologie repose sur une individualisation du signal renvoyé par chaque goutte contenue dans le volume balayé par le faisceau du radar. Cette méthode extrêmement coûteuse en temps de calcul du fait du grand nombre de gouttes de pluie à considérer permet d'obtenir des séries temporelles de signal reçu par le radar. La seconde méthodologie beaucoup plus efficace d'un point de vue calculatoire repose sur l'intégration des distributions granulométriques calculées en différents points de l'écoulement. La connaissance de cette distribution de gouttes en tout point de l'écoulement, combinée à la connaissance de la vitesse des gouttes de chaque diamètre et de la section radar efficace permet de calculer, le spectre Doppler de la réponse radar.

Ces deux méthodes de simulation de signature radar des gouttes de pluie entraînées par l'écoulement sont brièvement décrites dans la suite de cette section.

0.4.1 Simulation d'un sous ensemble des gouttes de pluie

La première méthode de simulation de la signature radar des gouttes de pluies entraînées dans les turbulences de sillage consiste à agréger les échos générés par chacune des gouttes d'eau présente dans un volume de résolution radar. La première étape de simulation est la définition du volume d'intérêt qui dépend principalement des caractéristiques du radar considéré (ouverture, résolution radiale, position) et de son balayage éventuel. Connaissant, ce volume d'intérêt et le champ de vitesse induit par le vortex à l'intérieur de ce volume, il est nécessaire de le peupler avec des gouttes d'eau.

Connaissant une intensité de précipitation R et la distribution granulométrique correspondante, un tirage aléatoire des gouttes d'eau suivant cette distribution est effectué dans un volume situé au dessus du volume d'intérêt (la hauteur de ce volume dépend du pas de temps utilisé pour les calculs). Les gouttes tirées aléatoirement sont supposées être à leur vitesse terminale $V_T(D)$ car supposées suffisamment éloignées du vortex pour ne pas être impactées significativement par son champ de vitesse. Le calcul de la trajectoire de ces gouttes est ensuite entrepris comme décrit à la section précédente. A chaque pas de temps du calcul de trajectoire, un nouveau tirage aléatoire de gouttes d'eau dans le volume duquel sont sorties les gouttes d'eau précédemment considérer est effectué. Cette procédure est itérée jusqu'à ce que les gouttes d'eau appartenant à la classe des gouttes d'eau les plus lentes (à savoir les plus petites) sortent du volume radar considéré. Cette procédure d'initialisation est illustrée à la 11.

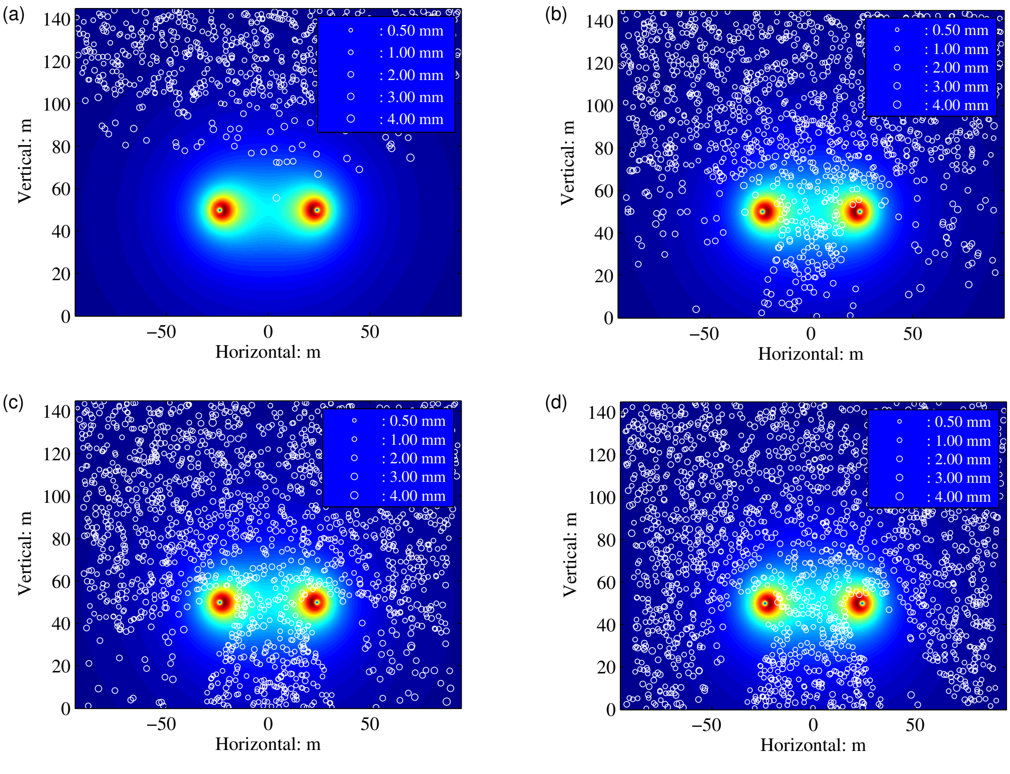

FIGURE 11 – Initialisation de la position des gouttes de pluie autour des turbulences de sillage avant le calcul du signal radar : (a) t=12.5 s, (b) t=25 s, (c) t=37.5 s, (d) t=50 s

Une fois cette initialisation terminée, le signal radar retourné par chaque goutte dans le volume de résolution est calculé en tenant compte de l'équation radar. La somme de ces contributions permet d'obtenir les séries temporelles de signal radar simulées à partir desquelles les spectres Doppler peuvent être calculés. Des exemples de spectres Doppler simulés pour un radar en bande X et une intensité de précipitation de 5 mm/h sont présentés à la Figure 13, et correspondent à la configuration de mesure de la Figure 12.

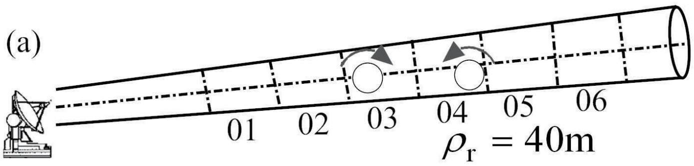

FIGURE 12 – Configuration de simulation correspondant aux spectres Doppler de la figure 4.12.

Il peut être observé sur la Figure 13, que les cellules de résolution dans lesquelles se trouvent les turbulences de sillage ont un spectre Doppler plus large que celles loin des turbulences pour laquelle le spectre Doppler présente un pic assez étroit principalement du à la projection des vitesses terminales des gouttes sur la direction de visée de radar. Cette largeur du spectre Doppler est utilisé à la section 0.5, comme indicateur de la circulation des vortex. Cette méthode de simulations n'a néanmoins pas été utilisée intensivement car le grand nombre de gouttes à générer pour obtenir des résultats représentatifs est prohibitif en terme de temps de calcul. Par conséquent une méthode moins couteuse en terme de mémoire et de temps de calcul a été développée dans un second temps.

0.4.2 Intégration des distributions granulométriques dans l'écoulement

La deuxième méthode de simulation proposée se base sur un pré-calcul des distributions granulométriques à l'intérieur de vortex reposant sur des simulations intensives de trajectoires de gouttes dans les champs de vitesses entourant le vortex. Ainsi considérant un champ de vitesse correspondant à des vortex de bouts d'aile donnés (circulation, profil de vitesse, écartement, position), la concentration des gouttes d'eau d'un certain diamètre D en tout point de l'écoulement est calculée par analyse statistique des trajectoires des gouttes de cette classe de diamètre. Cette analyse est faite en subdivisant en domaines élémentaires, la zone autour du vortex. Les subdivisions sont prises suffisamment petites pour que les variations de vitesses le long de la trajectoire à l'intérieur de ces subdivisions soient faibles. Considérant des gouttes d'eau uniformément réparties au dessus du vortex, le temps passé dans

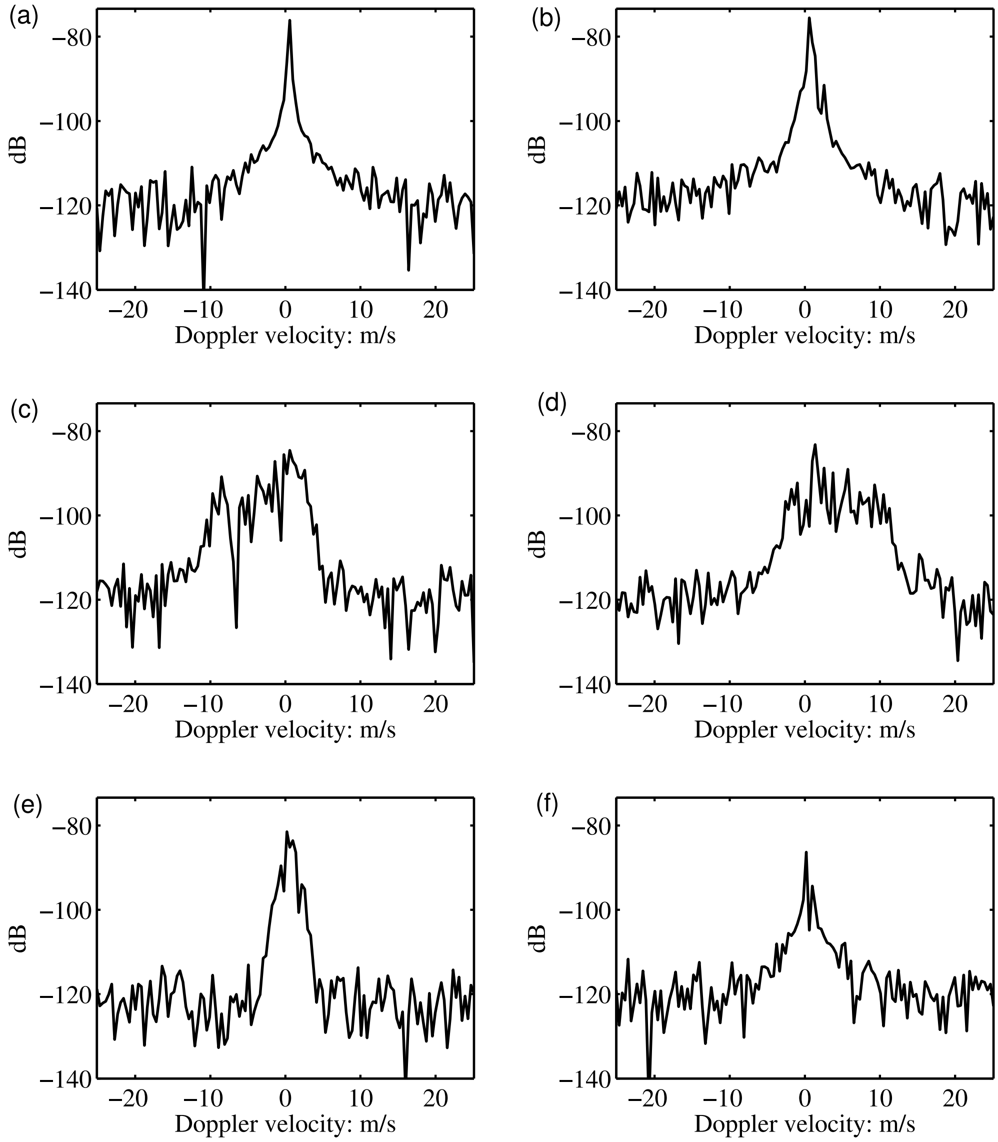

Figure 13 – Spectres de Doppler dans chacune des cellules de résolution illustrées à la Figure 4.11 : (a) cellule 01, (b) cellule 02, (c) cellule 03, (d) cellule 04, (e) cellule 05, (f) cellule 06.

chaque subdivision par chaque goutte d'eau est calculé comme illustré à la Figure 14. Il est ensuite comparé au temps passé dans chaque subdivision par des gouttes chutant en atmosphère libre. Le rapport de ces deux temps pour chacune des sub-

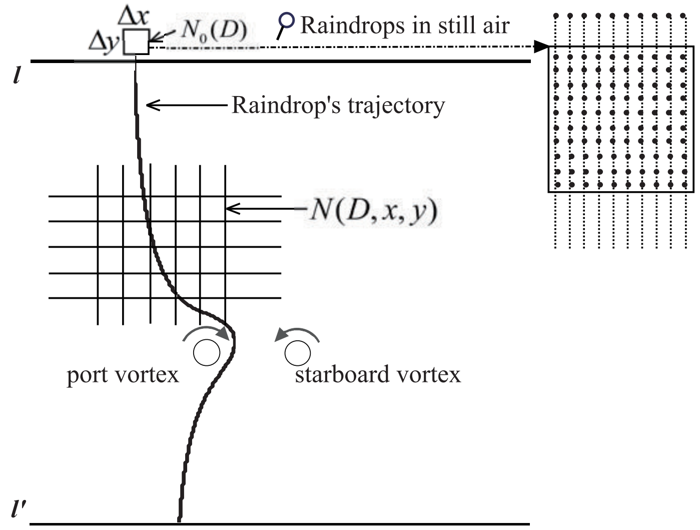

FIGURE 14 – Illustration de la méthode de calcul de la distribution granulométrique dans l'écoulement

divisions permet de déduire la variation de la concentration de gouttes pour chaque classe de diamètre. Un exemple pour des turbulences de sillage générées par un A340 est présenté à la Figure 15.

A ce stade, connaissant la distribution de taille de goutte en atmosphère libre correspondant à une certaine intensité de précipitation, il est possible d'en déduire la concentration de goutte dans l'écoulement pour chaque classe de diamètre. L'intégration de cette concentration de goutte associée à la connaissance de la vitesse moyenne des gouttes dans chaque subdivision du domaine permet d'en déduire réflectivité et spectre Doppler pour différentes configurations radar. En effet, il suffit de faire la somme de la distribution granulométrique sur chaque classe de diamètre pondérée par la section équivalente radar afférente a cette classe diamètre. Le spectre Doppler peut être obtenu sur le même principe, en triant les contributions par classe de vitesse.

0.4.3 Comparaison à des mesures expérimentales

Les simulateurs développés ont été utilisés afin de reproduire des configurations expérimentales pour lesquelles des mesures radar sur des turbulences de sillage par temps de pluie ont été réalisées. Plus particulièrement des mesures en bande X et en bande W ont été reproduites. La configuration des mesures expérimentales réalisées par Thales en bande X sous la trajectoire d'approche de l'aéroport Roissy-Charles

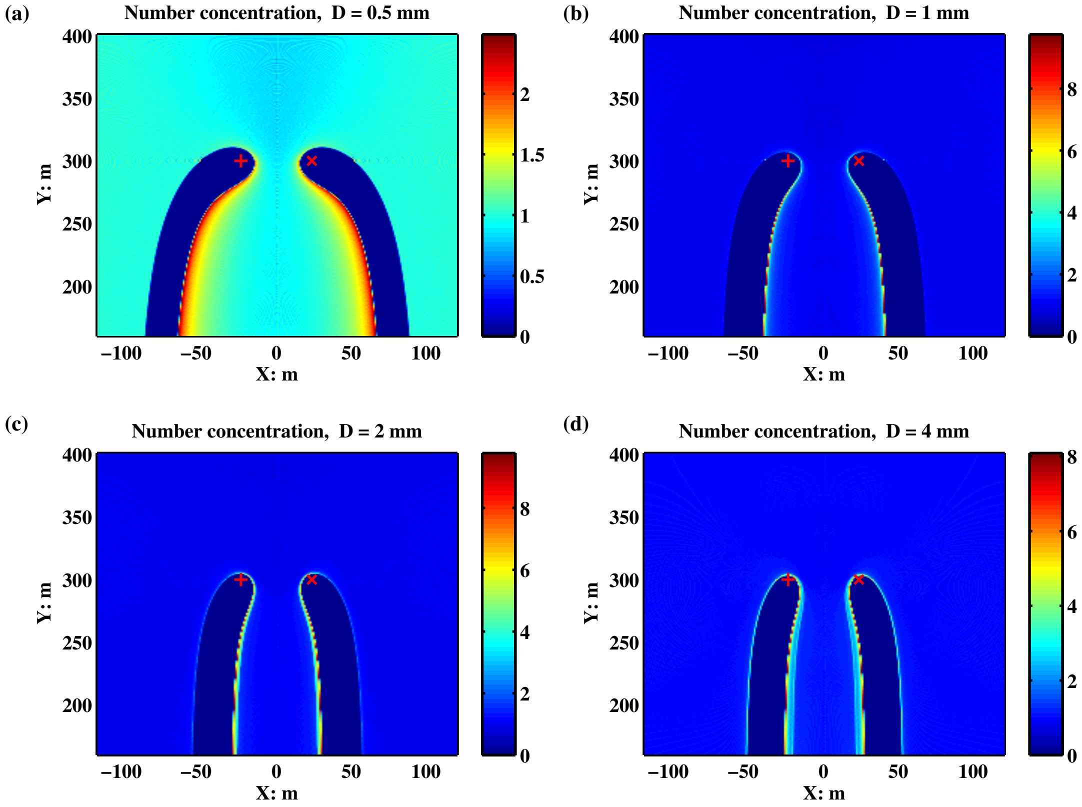

FIGURE 15 – Fluctuation relative de la concentration des gouttes d'eau d'un certain diamètre autour des turbulences de bouts d'aile

de Gaulle est illustrée à la Figure 16. Les principaux paramètres utilisés pour les mesures et les simulations sont donnés dans la table 2. Le radar balayait un secteur angulair de 20^o autour de la verticale avec une vitesse de balayage de $8^o s^{-1}$.

TABLE 2 – Paramètres du radar en bande X utilisé pour les mesures [19].

Paramètres	Valeur
Fréquence	10 GHz
Puissance crête émise	70 W
Facteur de bruit	2 dB
Pertes système	3 dB
Gain d'antenne	30 dB
Ouverture	$2.8° \times 4°$
Distance aux turbulences de sillage	500 m
Fréquence de répétition des impulsions	3348 Hz
Nombre d'impulsions par paquet	256

Les simulations ont été effectuée en supposant un vent latéral de -4 $m.s^{-1}$ et une

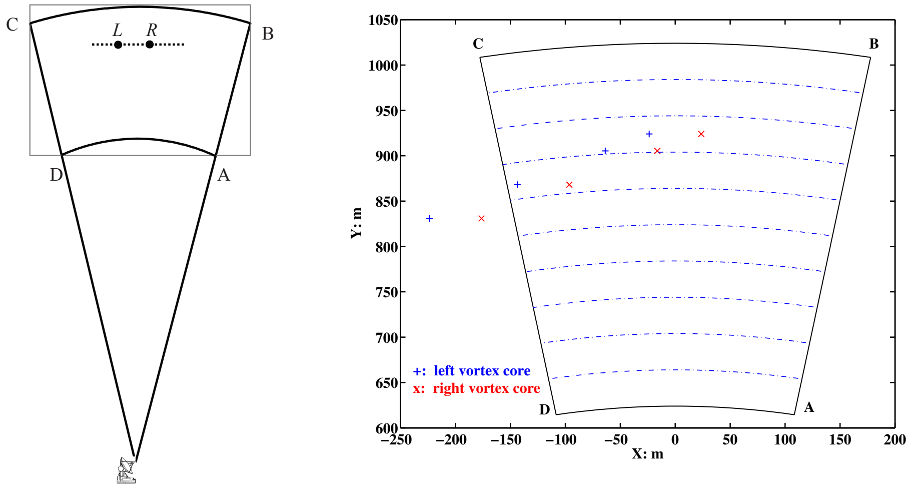

FIGURE 16 – Configuration géométrique des mesures en bande X sous la trajectoire d'approche des avions. Les marqueurs '+' et 'x' représentent la position des vortex de haut en bas aux instants t = 0 s, 10 s, 30 s et 50 s.

vitesse de descente constante de 1.86 $m.s^{-1}$. Le champ de vitesse des turbulences utilisé correspond à celui d'un A340 volant à 300km/h. La comparaison entre les simulations et les mesures est présentée à la Figure 17.

Différentes observations sur les mesures et les simulations peuvent être faites :

- les élargissements périodiques du clutter de pluie correspondent au passage de la direction de visée du radar vers les vortex. Le champ de vitesse des vortex est responsable du ralentissement ou de l'accélération des gouttes d'eau et donc de l'élargissement du spectre Doppler,
- la vitesse de chute des vortex et l'entraînement par le vent ambiant les font changer de cellule de résolution.

Les allures des motifs des spectres Doppler simulés et mesurés sont assez similaires.

Une autre configuration expérimentale en bande W, rapportée dans [27] a été reproduite par simulation. Le radar positionné en bord de piste balayait dans le plan vertical, orthogonalement à la piste. Les principales caractéristiques du radar sont données dans la Table 3.

Il est intéressant de noter que dans la cas du radar en bande W, les ouvertures beaucoup plus réduites permettent presque de réaliser une imagerie du vortex. Résultats expérimentaux et simulations exhibent des similitudes intéressantes. Plus particulièrement les fluctuations de réflectivités autour des cœurs de vortex

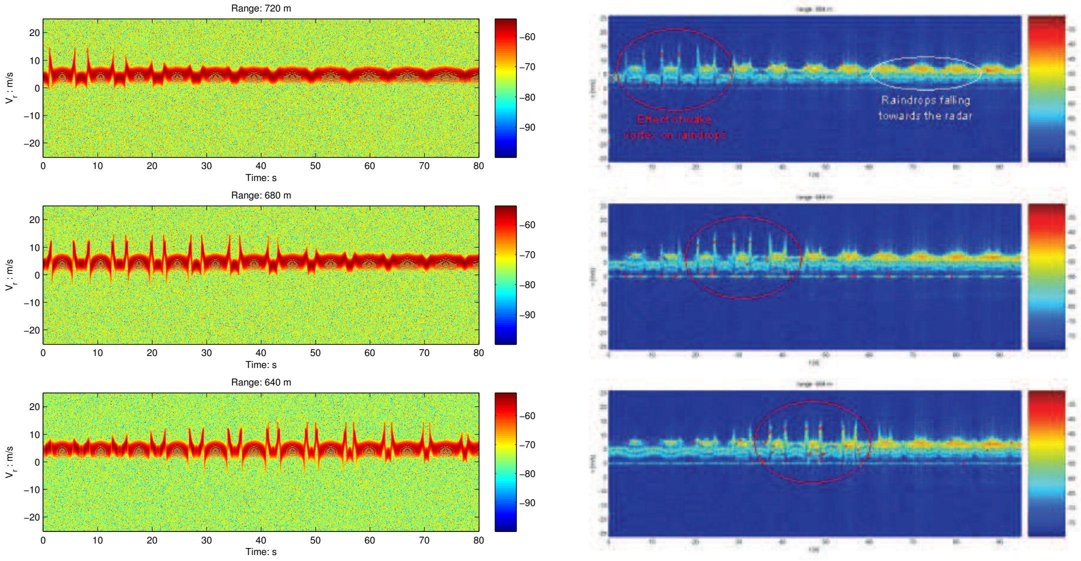

(a) Spectre Doppler simulé

(b) Spectre Doppler mesuré lors des essais Thales en 2011 [26]

FIGURE 17 – Comparaison des résultats d'essai de Thales en bande X aux simulations

TABLE 3 – Paramètres de simulation radar en bande W

Paramètres	Valeurs
Fréquence	94GHz
Puissance crête émise	100 mW
Facteur de bruit	12dB
Gain d'antenne	58dB
Vitesse de balayage de l'antenne	$5°/s$
Fréquence de répétition des impulsions	20 kHz

sont retrouvées et correspondent bien aux tendances déjà observées lors du calcul des distributions de tailles des gouttes. A savoir que les gouttes se concentrent de manière préférentielle entre les cœurs de vortex et qu'il existe une zone sous les cœurs de vortex ou la concentration de goutte est plus faible. L'information Doppler renvoyée semble elle, intéressante pour la quantification de la circulation car donnant un champ de vitesse radial assez semblable à celui généré par le vortex.

La concordance observée entre les résultats de simulation et les résultats expérimentaux permet d'accorder un certain crédit aux résultats obtenus par simulations, même si des comparaisons plus quantitatives et exhaustives seraient d'intérêt. Le bon

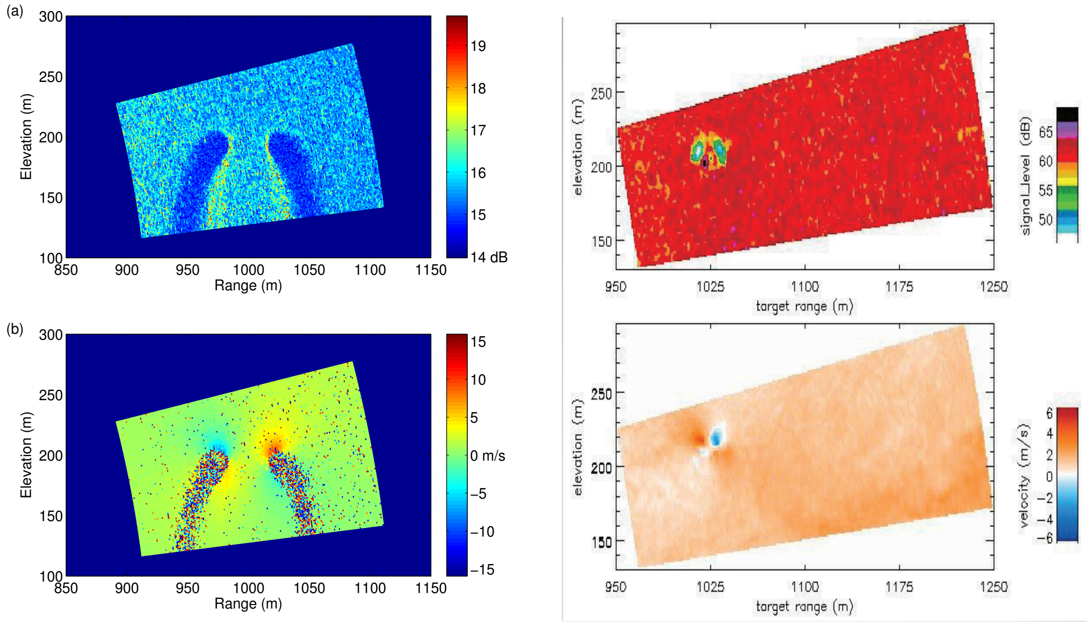

(a) Signature radar obtenue par simulation, les niveaux de puissance sont relatifs. Le bruit sur le Doppler moyen est du a un nombre trop faible d'échantillons.

(b) Signature radar en bande W obtenue par les expérimentations de T. A. Seliga in 2009 [27]

FIGURE 18 – Comparaison des simulations aux mesures réalisées en bande W

agrément trouvé permet de justifier l'étude de sensibilité et le développement d'algorithme de détection présentés dans la partie suivante du manuscrit.

0.5 Interprétation des signatures et algorithmes de détection

Les simulateurs présentés à la section précédente ont été pendant la dernière partie de la thèse exploités en vue du développement d'algorithme de détection, localisation et d'estimation de paramètres. A cet effet de nombreuses études paramétriques ont été menées afin de mieux comprendre l'impact des différents paramètres entrant en jeu dans la création de la signature. Un exemple est donné à la Figure 19 où les caractéristiques du spectre Doppler pour des turbulences de sillage générées par différents avions pour différentes intensités de précipitation sont présentées. Les vortex sont supposés être contenus dans un seule cellule de résolution d'un radar au bord de la piste avec une élévation de 2^o. La Figure 20 présente les mêmes résultats pour un radar sous la trajectoire d'approche des avions pour une cellule de résolution englobant les deux vortex.

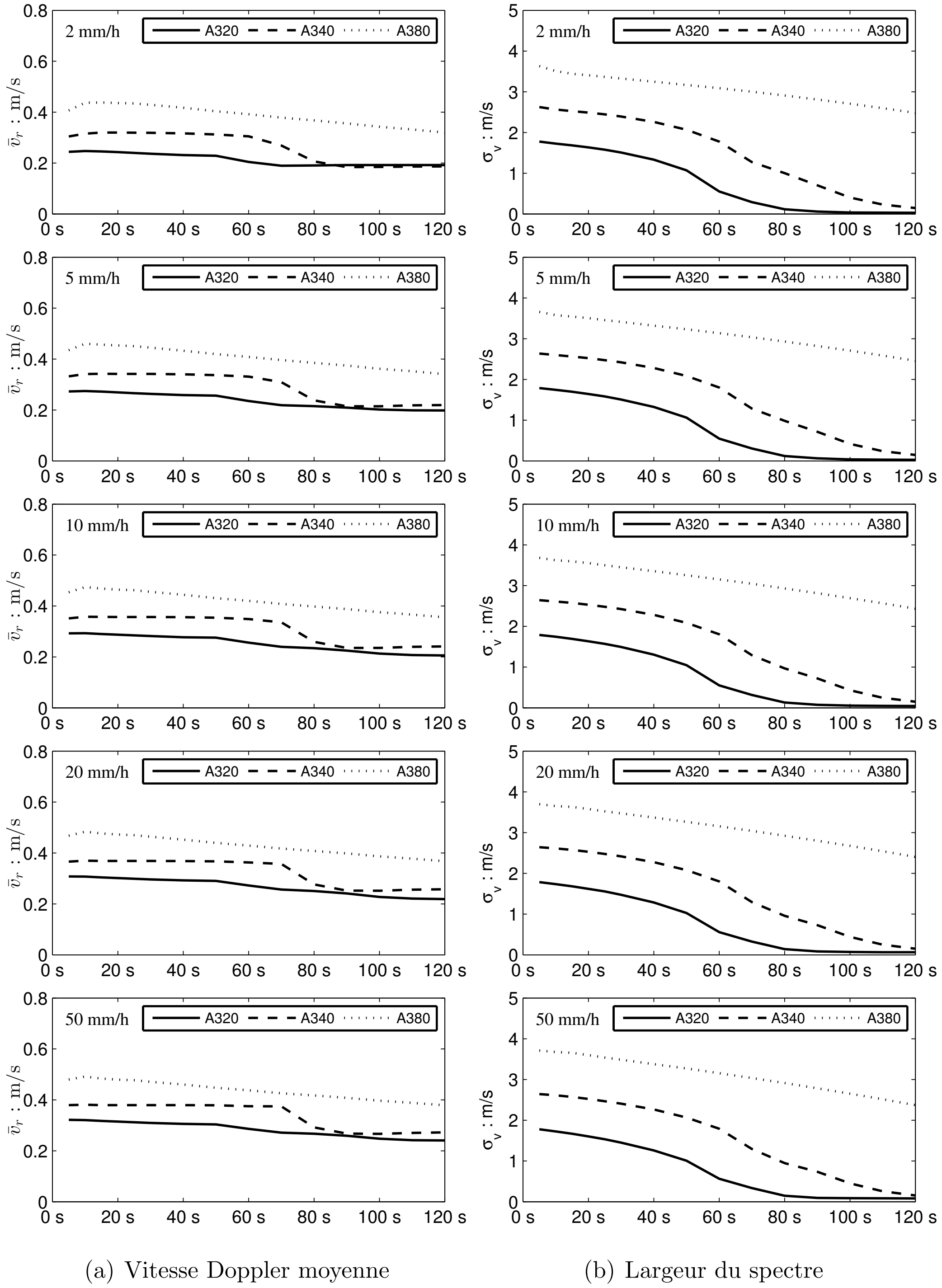

(a) Vitesse Doppler moyenne

(b) Largeur du spectre

Figure 19 – Vitesse Doppler moyenne et largeur du spectre en fonction du temps pour différentes intensité de précipitation (Angle d'élévation : 2°)

Il est intéressant de noter dans ces exemples que la dépendance des moments

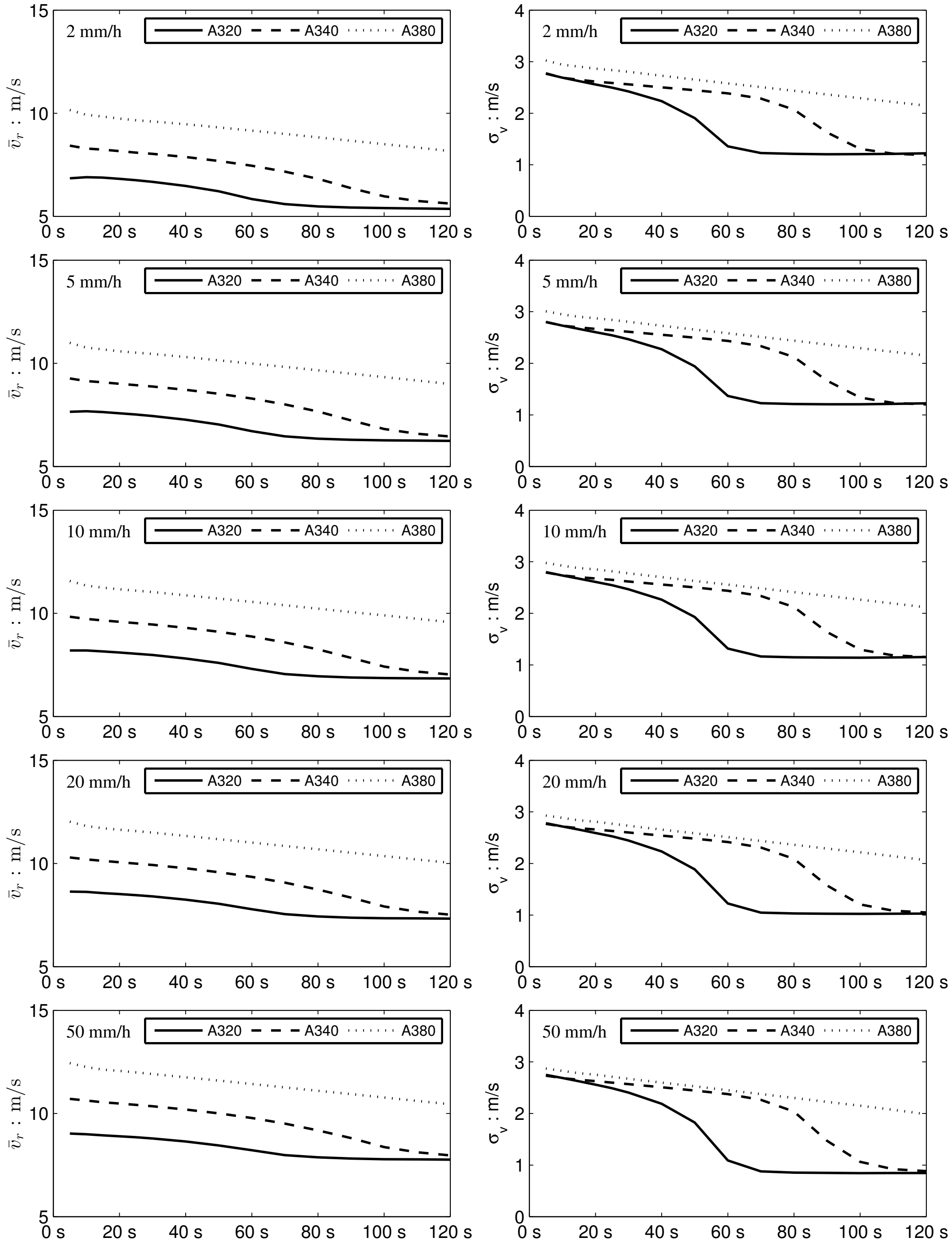

(a) Vitesse Doppler moyenne (b) Largeur du spectre

FIGURE 20 – Vitesse Doppler moyenne et largeur du spectre en fonction du temps pour différentes intensité de précipitation (Angle d'élévation : 90°)

Doppler à l'intensité de précipitation est faible, le seul changement notable porte sur la vitesse moyenne en visée verticale qui augmente évidemment avec l'intensité de précipitation car les grosses gouttes ont une vitesse de chute plus importante vers le radar. Il semble également y avoir un lien intéressant entre largeur Doppler et circulation puisque la largeur du spectre Doppler est plus élevée pour les aéronefs les plus lourds. Ce type de lien entre largeur du spectre Doppler et circulation est intéressant, une régression semblant possible dans le cas du radar à visée latéral. Dans le cas de la visée verticale, il semble plus délicat de se baser sur la largeur Doppler du spectre pour évaluer la circulation. En effet, jusqu'à une certaine valeur de décroissance de la circulation, les largeurs de spectres causées par les turbulences de porteurs sensiblement différents et de gamme de circulation différentes sont comparables. Une utilisation de la vitesse Doppler moyenne pourrait alors être considérée car très liée à la circulation comme illustré sur les résultats de la Figure 20. Néanmoins cette vitesse est très sensible à la distribution granulométrique que l'on suppose connue dans les simulations. De ce fait, il semble peu opportun d'utiliser cette grandeur comme un traceur de circulation. Des algorithmes basées sur la mesure de la vitesse de descente des vortex, elle même liée à la circulation pourraient être plus appropriés dans cette configuration de mesure.

Les résultats obtenus au cours de cette thèse sont très préliminaires mais ouvrent des perspectives intéressantes sur le sujet de la détection. En effet, une analyse de sensibilité plus approfondie pourrait permettre le développement d'algorithme de détection et de quantification plus aboutis ainsi qu'une évaluation de leur performance. L'utilisation des méthodes de simulation décrites dans ce manuscrit pouvant permettre de tenir compte à la fois des paramètres environnementaux et des paramètres radar.

0.6 Conclusion et perspectives

Le travail conduit au cours de cette thèse a permis d'accroître la connaissance phénoménologique de la réponse radar des turbulences de sillage par temps de pluie. A partir de calculs de trajectoires de gouttes d'eau tombant dans les turbulences de sillage en phase stationnaire, la concentration des gouttes d'eau autour des vortex a été étudiée. La connaissance de cette distribution de gouttes a ensuite été utilisée pour calculer la réponse radar des vortex par temps de pluie. Deux algorithmies ont été développés pour calculer cette réponse. Le premier algorithme permet d'obtenir la série temporelle du signal radar par superposition des échos générés par chacune des gouttes de pluie. Le second algorithme moins complexe d'un point de vue calculatoire se base sur un pré-calcul des distributions de taille de gouttes autour des vortex à partir desquelles, connaissant le champ de vitesse des gouttes d'eau, un spectre Doppler idéalisé peut être calculé. Il a été montré, en paramétrant ces simulateurs avec la configuration expérimentale de deux cas de mesures de turbulences de sillage dans la pluie en bande X et en bande W, une concordance entre mesures et simulations. Le principal intérêt de ces méthodes de simulations réside dans leur potentialité pour le développement d'algorithmes d'estimation des caractéristiques des turbulences de sillage à savoir principalement leur trajectoire et l'évolution de leur circulation. En effet, ces simulations permettent de réaliser des études sur les paramètres environnementaux (turbulences de sillage et intensité de précipitation) et les paramètres de la mesure radar. Il a en particulier été montré dans la dernière partie de ce travail que l'étude des trois premiers moments Doppler pouvait permettre de dériver de manière approchée la plupart des paramètres caractéristiques des vortex pour un radar balayant sous la trajectoire d'approche des avions, ou latéralement en bord de piste.

Ce travail s'est attaché à proposer une modélisation de la signature radar des turbulences de sillage en présence de pluie au travers de la modélisation simplifiée des différents phénomènes. Des premiers résultats sur le sujet ont pu être obtenus. Néanmoins de nombreux points pourrait être améliorés ou mériteraient des recherches plus poussées. Les pistes suivantes semblent parmi les plus prometteuses :

- L'utilisation pour les simulations de conditions atmosphériques standard ne permet pas de prendre en compte les variabilités sur les vitesses de descente des vortex liées aux fluctuations de stratification atmosphérique ainsi que le taux de dissipation de la circulation liée à la turbulence atmosphérique ambiante. Une prise en compte de ces phénomènes permettrait de reproduire de manière plus fidèle les différentes configurations expérimentales. De même une étude de l'impact des gouttes de pluie sur la circulation du vortex semble intéressante
- L'utilisation du simulateur pour l'évaluation de la signature radar de différents types d'hydrométéores ou de particules peut également être d'intérêt. En effet, en cas de faible visibilité liée à du brouillard, de la poussière ou de la neige, l'utilisation du Lidar pour surveiller les turbulences de sillage n'est pas forcément pertinente. La question ouverte est dès lors de savoir si la taille et les propriétés électromagnétiques de ces particules sont compatibles avec une détection par des radars à faible encombrement et puissance d'émission.
- L'approfondissement de l'étude des algorithmes de détection des turbulences

devra également être entrepris. En effet, le présent travail n'a permis que d'ébaucher quelques pistes de métriques pour l'identification, la localisation et l'estimation des caractéristiques des turbulences de sillage. Des études à partir de simulations permettant de quantifier les probabilités de détection et de fausses alarmes permettraient de mieux évaluer l'adéquation des algorithmes proposés aux procédures de contrôle aériens.

Chapter 1

Introduction

1.1 Background and requirements

Wake vortex forms behind a flying aircraft when a wing is generating lift. The pressure on the wing intrados is higher than the pressure on the wing extrados. Therefore, the high-pressure air moves around the wingtip from the intrados to the extrados, generating the so-called "wingtip vortex", which trails from the tip of each wing [28]. The two wingtip vortices behind an aircraft make up the major component of wake turbulence and do not merge because they are circulating in opposite directions [4, 29], as shown in Figure 1.1.

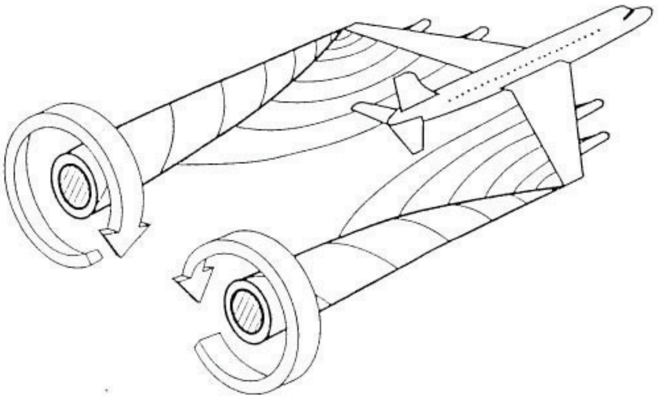

Figure 1.1: Illustration of two counter-rotating vortices [5, 15]

Depending on the ambient atmospheric humidity and temperature, the wake vortex may be visible by eyes at some conditions. For instance, in presence of cloud or fog, the wake vortex behind a Learjet 60 can be visible on the photography of P. Bowen [2], as shown in Figure 1.2 (a). At high altitude, the formation of contrail is usually triggered by the water vapour in the exhaust of aircraft engines and the changes in air pressure in wingtip vortices [3, 30], as shown in Figure 1.2 (b). The contrail may persist for several hours and thus is thought to possibly affect the global climate, by impacting the radiative transfer budget [31–33]. In Figure 1.2 (c), the wake vortex is made visible in a NASA (National Aeronautics and Space Administration) test by using colored smoke rising from the ground [4]. Generally speaking, the strength of wake vortex depends on the aircraft's weight and flying speed. The heavier the aircraft is or the slower it flies, the stronger the wake vortex is. The wake vortices of large airplanes have a lifespan of several minutes and can be stretched up to 30 km behind the aircraft, depending on atmospheric conditions. In their core region, the cross flow velocities are up to 100 km/h. Due to their invisibility and large associated aerodynamic forces, those wake vortices may be hazardous if encountered by other flying aircraft, especially during take-off and landing phases [14, 28].

(a) Wake vortices of Learjet 60 in cloud [2]

(b) Wake vortices at high altitude as contrail [3]

(c) Wake vortices made visible in a NASA test by using colored smoke rising from the ground [4]

Figure 1.2: Visible wake vortices

As shown in Figure 1.3, there are three main categories of vortex encounters, when an aircraft approaches or flies into the wake vortex of the leading aircraft with various consequence: an increased structural dynamic load, a loss of lift (or loss of altitude/reduced climb rate) and the induced roll, depending upon how the aircraft penetrates the wake vortex [28, 34–36].

The increased structural dynamic loads occurs when the encountering aircraft trajectory is perpendicular to the trailing wake vortex of another aircraft. The

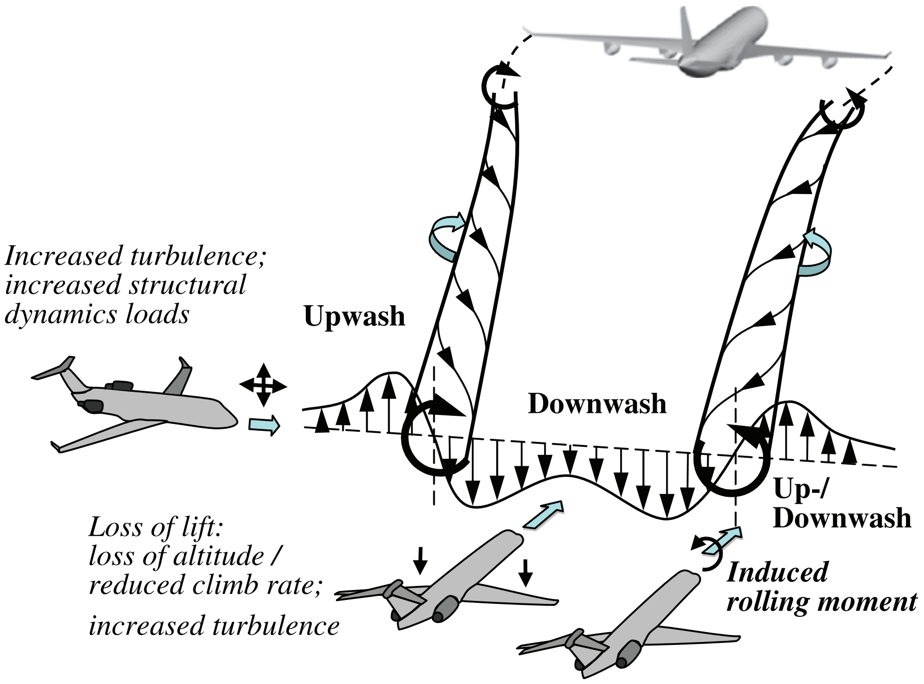

Figure 1.3: Wake vortex hazard [28, 34]

loss of lift occurs when the encountering aircraft flies into the region between the trailing vortices (i.e. in the downwash region) of the leading aircraft, experiencing a reduction in its rate of climb during take-off or an increased rate of descent during landing. The induced roll occurs when the encountering aircraft penetrates along the vortex axis, experiencing an upwind field and a downwind field simultaneously. If the induced rolling moment exceeds the roll control of the encountering aircraft, the hazard induced is serious and believed to be the most dangerous at a low altitude [34]. The capability of an aircraft to counteract the induced roll imposed by the vortex primarily depends on its wingspan and its command responsiveness. If the wingspan of an encountering aircraft is shorter than the one of the leading aircraft, the counter control is much more difficult [37].

In recent years, erroneous instructions from flight controllers have caused several accidents with aircrafts entering into the wake vortex of the previous aircraft [17,38]. Between 1983 and 2000, 130 aircraft accidents and 60 aircraft incidents in the United States resulting from probable wake vortex encounters have been reported, leading to 35 occupants killed, 25 occupants seriously injured and 112 aircrafts substantially damaged or destroyed. It has also been shown that the wake turbulence accidents, incidents and events were more frequent at low altitude during approach and landing than during any other phase of flight [39].

In order to assure aviation safety, the wake vortex encounters are expected to be avoided at a maximum extent and the minimum separation distances between two aircrafts flying in the same direction (longitudinal separation) should be defined for air traffic control applications [14]. The strength of wake vortices is characterized by their circulation and thus relative to the lift which equals to the aircraft weight. Therefore the current ICAO (International Civil Aviation Organization) safety separation standard is based on the maximum take-off weight (MTOW) of the aircrafts, as shown in Figure 1.4, without considering the dynamic evolution of wake vortex [1, 28]. It can be easily noticed that the minimum separation between two aircrafts is 3 nautical miles (5.56 km) and that a small aircraft must follow at least 6 nautical miles (11.12 km) behind a heavy jet such as a Boeing 747. This standard separation is very conservative most of the times but may still enable vortex encounter in some particular weather conditions. Under the effects of large cross wind or atmospheric turbulence, the wake vortex of the leading aircraft may move away from the runway shortly after roll-up or decay at a more rapid dissipation rate, posing less hazards to another aircraft [1, 14]. In this case, the separation distance between two aircrafts can be reduced accordingly. Under stable atmospheric conditions or ground effect, the wake vortex may remain over the runway or around glide path for longer time than what anticipated by the ICAO separation rules.

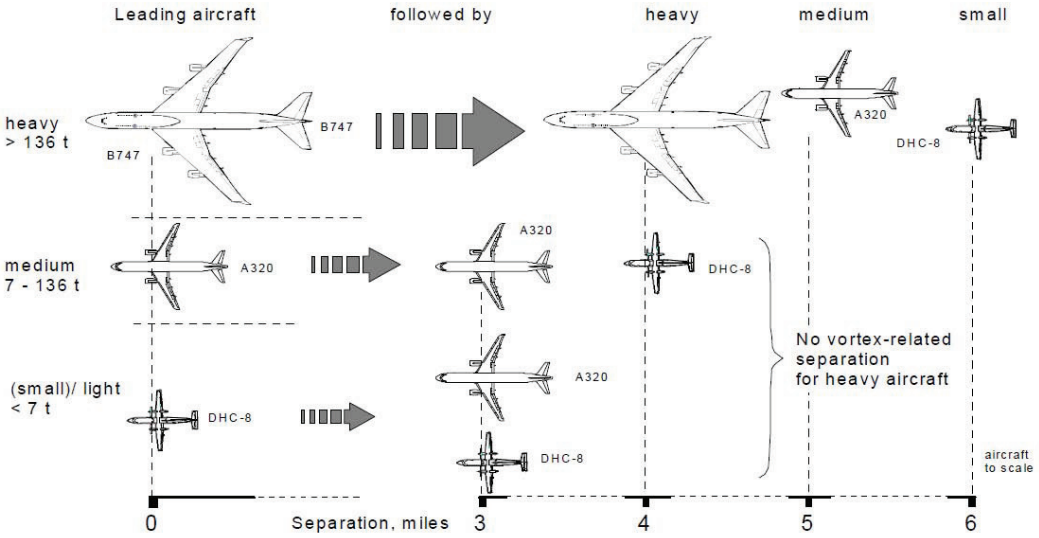

Figure 1.4: ICAO separation scheme for single runway approaches [1]

The current ICAO separation rules, which were implemented over 40 years ago, have set a upper bound on the runway capacity. It limits thus the capacity of the entire airport and constitute one of the major obstacle to the growth of air traffic [28, 40]. Thus, if an optimal separation scheme based on the monitoring of wake vortex behavior in real time is used, the handling capacity of the airport which is a major commercial issues can greatly be increased without being detrimental to aviation safety [19, 41]. Meanwhile, in 2004, an European collaborative project "SESAR (Single European Sky ATM Research: 2004-2020)" was initiated, aiming at developing the new generation air traffic management system capable of ensuring the safety and fluidity of air transport worldwide over the next 30 years [42]. One of the key technologies in SESAR is "Runway Wake Vortex detection, prediction and decision support tools (SESAR Project 12.2.2)", thus, the new aircraft separation modes allowing increased safety, capacity and efficiency will be redefined with the development of wake vortex monitoring sensors.

The candidate sensors for wake vortex monitoring include RADAR (RAdio Detection And Ranging) [5–7], LIDAR (LIght Detection And Ranging) [8–10] and SODAR (SOnic Detection And Ranging) [11–13]. Among them, Sodar is sensitive to the the temperature fluctuations in wake vortices but has a too short detection range to be effective, Lidar is sensitive to the motion of aerosols in wake vortices and currently appears as the most mature wake vortex sensor, capable of locating wake vortices with good accuracy and of estimating the vortex circulation, but in foggy, cloudy or rainy weather, it cannot work effectively. Compared to Sodar and Lidar, Radar has several operational advantages including the good weather adaptability, long detection range, low cost and wide spatial coverage. In rainy weather, the Radar electromagnetic waves are not severely attenuated by raindrops or fog at short range. Contrarily, the droplets rolled up by the wake vortices are strong scatterers enhancing the intensity of the scattered signals [26,27,43–46]. Radar could be seen as an efficient instrumentation for monitoring wake vortex to complement other sensors such as Lidar that are effective only in clear sky [26]. However, few studies on the radar backscattering of wake vortices in rainy weather have been reported. Thus, the present work mainly concentrates on the modeling of radar signatures of wake vortices, which is of significant scientific and practical interest. The research results presented in the following of the manuscript can provide technical guidance for the development of new radar sensor dedicated to the monitoring of wake vortex.

1.2 Previous research activities on wake vortices

Since the first description of wingtip vortices by British aerodynamicist F.W. Lanchester in 1907, the wake vortex research activities have gradually evolved. Ever since 1960s, a large number of wake vortex research programs driven by the requirements of aviation safety and airport capacity have been conducted. Four historical research phases, during which the wake vortex topic were considered under different aspect, can be distinguished [47]. The research activities in the first phase from 1900s to 1950s were mainly motivated by the knowledge requirements needed for aircraft design. The research activities in the second phase from 1960s to 1980s were focused on the security issues raised by several accidents due to wake vortex encounters. The research activities during the third Phase from 1990s to 2005 were more dedicated to the mitigation of the effect of the impact of wake vortex to increase capacity limitations of airport to support the ever-increasing air traffic. During the fourth phase ranging from 2005 to now, the research activities were mainly driven by two large projects SESAR and NGATS(Next Generation Air Transportation System) which are dedicated to the construction of new generation of air transportation systems.

The current wake vortex researches cover a wide range of topics from wake vortex physics, wake vortex alleviation, wake vortex encounters and safety assessment to the development of wake vortex monitoring sensors and avoidance systems. Theoretical modeling, computational simulations and experimental tests prove to be valuable tools to highlight a dependence of this phenomenon on various parameters. Those parameters encompass aircraft characteristics such as weight, wingspan, speed, flap and spoiler settings, proximity to the ground, engine thrust, lift distribution, as well as atmospheric conditions such as stratification, turbulence, crosswind, wind shear and precipitations [48].

1.2.1 Physical understanding of the wake vortex phenomenon

The significant contributions to the better understanding of the wake vortex physical phenomenon during the four research phases are briefly summarized in this section.

The first Phase(1900s-1950s)

Wingtip vortices were first described by British aerodynamicist F.W. Lanchester in 1907, even before the advent of jet aircraft and the discovery of CAT(clear air turbulence) [49–52]. In the early research activities before 1950, wake vortices were mainly used to explain the dissipation of lift and drag energy as well as actual sources of lift and control, in order to improve the design of aircraft shape and flight quality. At that time the hazards associated to wake vortices were not considered [47,50,51]. Some basic theories describing wake vortex were formed in this phase, including the dependence of vortex strength on the size, weight, and speed of the aircraft, the descent of the pair of wake vortices after generation and the effect of ambient wind on vortex motion [48].

The second phase(1960s-1980s)

Research on wake vortex has gradually evolved with the advent of more types of aircrafts in the airport. From 1960s to 1980s, the incentive for wake vortex research started to come from the consideration of aviation safety, because at that time, the size difference between large and small aircraft was becoming larger. Wake vortex was thought to be an invisible killer in several landing and take-off accidents [34,53]. Thus, a series of scientific and practical research topics about wake vortex, including how to describe the wake vortex behavior [54–56], how to alleviate or avoid wake vortex [57,58], and how to effectively detect wake vortex [59–63], gradually attracted concerns from some aviation organizations in USA and Russia. In September 1970, a Symposium on aircraft wake turbulence, jointly sponsored by the Air Force Office of Scientific Research and the Boeing Company, was held in Seattle [64]. The most important practical problem of the symposium was to determine the interaction between wake vortex and aircraft, some pioneering works on wake vortex formation, characteristics, stabilities and decay, wake vortex experimental methods were presented [64].

In this phase, intensive ground based and flight-research programs were conducted or sponsored by NASA to better understand the wake vortex phenomenon and decay mechanisms. The concepts about wake vortex detection and the first on-board and ground-based wake vortex detection systems also began to appear [48, 65, 66]. Aircraft wake vortex transport models were studied in 1974 by M. R. Brashears and J. N. Hallock [67]. In 1976, the effects of fog droplets on wake vortex decay rate was studied by T. H. Moulden and W. Frost [68]. The wake vortex ground effect was studied in 1977 by Steven J. Barker and Steven C. Crow from University of California [69]. From the end of 1970s to the beginning of 1980s, a Monostatic Acoustic Vortex Sensing System (MAVSS) was installed at Chicago's O'Hare International Airport, the understanding of the decay of wake vortex strength was put forward from these experimental results [70–73]. The wake vortex alleviation studies with a variable twist wing were done in 1985 by Holbrook, G. T., Dunham, D. M. and Greene, G. C. from NASA Langley Research Center [74]. From 1980s, some theoretical studies on wake vortex were also conducted by a Russian pioneer, S.M. Belotserkovsky, concentrating on the development of discrete vortex method [14].

The third Phase(1990s-2005)

During the 90s, with the advent of a new FAA (Federal Aviation Administration) wake vortex program, the wake vortex research in USA entered into a new period. In [48], the state of knowledge about aircraft wake vortices in the summer 1990 was summarized and some recommendations for further wake vortex research programs were sketched, including the development of wake vortex sensors, wake vortex modeling, wake vortex hazard definition, reclassification and so on. In the following years, a series of studies on wake vortex were conducted by the researchers from NASA [75–80], Johns Hopkins University Applied Physics Laboratory [81,82], MIT Lincoln Laboratory [5,83] , Boeing Company [84], WLR Research Inc. [85,86], USDOT Volpe National Transportation Systems [87, 88], and some other research organizations [89–91].

Since the middle of 1990s, a lot of wake vortex projects were also initiated in Europe, including MFLAME (project on multi-function future laser atmospheric measurement equipment, 1996-2000), S-Wake (project on assessment of wake-vortex safety, 2000-2002), WAVENC (project on wake-vortex evolution and encounter, 1998-1999), EUROWAKE (project on wake-vortex formation of transport aircraft, 1996-1999), WakeNet & WakeNet II (thematic network on aircraft wake vortices, 1998-2002 & 2002-2005), C-Wake (project on wake-vortex characterisation and control, 2000-2002), I-Wake (project on instrumentation systems for onboard wake-vortex and other hazards detection warning and avoidance, 2002-2005), ATC-Wake (project on integrated air traffic control wake-vortex safety and capacity system, 2002-2005) [17]. In Russia, some investigations on wake vortex evolution, flight safety problems and airport operation capacity were initiated in the central aerohydrodynamic institute of Russia [92].

During this phase, a wide range of techniques were attempted to monitor aircraft wake vortices near the ground or on board, including Radar [5, 15, 77–79, 81, 82, 84, 90, 91, 93–96], Lidar [9, 10, 97–107], Sodar [12, 86, 88, 108–110] and RASS [85, 111–114]. Lidar was demonstrated to be a relative mature sensor for monitoring wake vortex in real time. The obtained Lidar data from field trials were also used to estimate wake vortex parameters and analyze the atmospheric effects on wake vortex evolution or decay. Another important progress on the understanding of wake vortex phenomenon at this phase was the research towards a wake-vortex advisory system for optimal aircraft spacing in USA and Europe [16, 115–118]. In USA, the concept to develop and implement a prototype of Aircraft VOrtex Spacing System (AVOSS) was firstly presented in 1996 [16, 115, 119], aiming at providing dynamical weather dependent separation criteria to ATC facilities. Lately in 2003, the concept of Wake Vortex Advisory System (WakeVAS) was presented in a joint Wake Turbulence Research Program (WTRP) sponsored by FAA and NASA, relying on a number of enabling technologies demonstrated during AVOSS [117, 118]. In Europe, the wake vortex warning system (WVWS) was developed for the independent use of the two parallel runways under favourable (low) cross-wind conditions at Frankfurt Airport [116, 117]. A series of new questions and research topics were raised to meet the requirements of the systems, thus stimulating continuous progresses on wake vortex and weather sensors, wake vortex transport and decay, wake vortex prediction, wake vortex ground effect and the effects of atmospheric conditions on wake vortex behavior.

The fourth phase(2005-now)

During this last phase, with the initiation of two large projects SESAR [120] and NGATS [121], the incentive for wake vortex research has become much stronger than in any other phases before. The operational concepts in SESAR and NGATS have demanded much higher aviation efficiency in terms of flight safety and airport capacity. Meanwhile, the advent of unmanned aircraft systems, very light jets and very large aircraft like the twin-deck A380 have prompted extensive wake vortex investigations [52, 122]. Continuous endeavors from interdisciplinary research communities in Europe, USA, Russia, China, Japan have been contributing more and more to the understanding of wake vortex phenomenonology. In the framework of WakeNet3-Europe(2008-2012), the wake vortex research activities mainly covered three aspects of technologies, safety and concepts. Since 2009, a series of WakeNet3-Europe workshops have been organized in France, Belgium, Germany and UK and some fruitful progresses on wake vortex operational models, wake vortex & wind monitoring sensors, wake vortex & short-term weather forecasting, wake vortex concepts & capacity, wake vortex encounter, wake vortex recategorisation have been presented.

For wake vortex operational models, the current real-time wake vortex modeling methods were well summarized and evaluated in [123]. A wide range of different theoretical methods have been proposed until now, including the Direct Numerical Simulation (DNS) of turbulent flow based on the Navier-Stokes equations, Large Eddy Simulation (LES) using the Navier-Stokes equations and subgrid-scale modeling, Reynolds-Averaged Navier-Stokes simulations (RANS) and Discrete Vortex Method (DVM) [14, 123]. For wake vortex and wind monitoring sensors, some of the Lidar sensors have gradually been installed in the airport for real time monitoring wake vortex and wind shear, such as WindTracer manufactured by Coherent Technologies, Inc. (CTI). Meanwhile, radar and lidar have been demonstrated to be complementary sensors for monitoring wake vortices in all weather conditions [26].

1.2.2 Radar monitoring of wake Vortex

For wake vortex detection and monitoring, everlasting efforts have been dedicated to the Lidar and Sodar since the 60s. The feasibility of using a microwave or millimeter wave radar to monitor wake vortex was ever reported as early as in 1970 [65]. Up to now, a significant part of the research on wake vortex radar sensors has been concentrated on field tests, in order to measure the radar reflectivity of wake vortex. On the other hand, theoretical studies on radar scattering mechanism of wake vortices also have been conducted to provide technological guidance for the development of new wake vortex radar sensors since the 90s.

Wake vortex radar scattering mechanism in clear air

Compared to other regular radar target, radar scattering characteristics of wake vortex are much more complicated due to its temporal-spatial evolution. In recent years, progresses have been gradually achieved in the understanding of wake vortex radar scattering mechanism in clear air. In [47], a division in two distinct period of the research activities on this topic is proposed.

During the fist period, the wake vortex scattering mechanism in clear air was assumed to be Bragg scatter from refractive index fluctuations produced by turbulence within the wake vortex [91]. Under this assumption, the radar reflectivity of wake vortex was mainly thought to be caused by reflected energy from the turbulent eddies of sizes centered on half the radar wavelength. According to Tatarskii's wave propagation and scattering theory in turbulent medium [124], the mono-static radar reflectivity of wake vortex is given by

$$\eta = 0.38 C_n^2 \lambda^{-\frac{1}{3}} \tag{1.1}$$

where C_n^2 is the refractive index structure constant and λ is the radar wavelength. C_n^2 is dependent upon the eddy dissipation rate and the flow concentration gradients [15]. Based on Bragg scattering mechanism, R. E. Marshall and A. Mudukutore computed the radar reflectivity of wake vortices of C-130 aircraft in clear air, by using the outputs of eddy dissipation rate and mean flow concentration gradients from the Terminal Area Simulation System (TASS) [125]. In [82], the radar reflectivity of wake vortex was also approximated by the clear air turbulence reflectivity given by Equation (1.1), and the analytical expression of refractive index structure constant C_n^2 was derived in function of dry air and humidity density and of the velocity of the flow.

Actually, the radar reflectivity computed from the turbulent Bragg scattering was always distinguished from the experiment results because the turbulent assumption of wake vortex didn't stand up for all the wake vortex evolution phases [47]. The laminar structure of wake vortex was demonstrated by theoretical analysis, numerical simulation and comparison with experimental tests in [126] and [127]. The air density, temperatures and velocity distribution in wake vortex is relatively stable during several evolution phases and wake vortex becomes turbulent only in the decay phase. In [15], the laminar scattering mechanism of wake vortex was proposed and a new period for the analysis of wake vortex radar reflectivity was initiated. The main contributions in this period have been reported in the publications by T. J. Myers from Virginia Polytechnic Institute and State University in USA [15, 128], K. Shariff and A. Wray from NASA Ames Research Center in USA [80], J. Li from NUDT in China [129–131] and D. Vanhoenacker-Janvier and K. Djafri from UCL in Belgium [7, 132].

T. J. Myers developed a Wake Vortex-Passive Conservative Simulation (WV-PCS) scheme to determine the refractive index field that causes RCS of wake vortex and the simulation results were shown to be quantitatively consistent with experimental data. But the contribution of the air density variations to the RCS of wake vortex was neglected. K. Sharrif computed the RCS of wake vortex based on two mechanisms producing refractive index variation: radial density gradient in the vortex cores and transport of atmospheric fluid in the oval surrounding the vortices, the RCS-frequency characteristics of wake vortex were obtained. J. Li systematically studied the scattering characteristics of wake vortex by solving three key problems: to determine the wake vortex's dielectric constant distribution, to obtain the total electric field in the wake vortex, to calculate the highly oscillatory integral rapidly and accurately. A series of radar scattering characteristics of wake vortex were obtained, including the RCS-Frequency, RCS-Time, HRR profile of wake vortex. D. Vanhoenacker-Janvier and K. Djafri developed a software for the simulation of the RCS of wake vortex for a wide frequency range, various airplanes and various tropospheric parameters and in [7], a new model to calculate the radar cross section and the power backscattered by wake vortices of take-off and landing airplanes was developed.

Wake vortex radar detection trials

In recent years, a lot of experiments have been conducted to detect and monitor wake vortices, by using a radar system which was designed for applications other than wake vortex monitoring. In [133], highly distinct radar echoes of wing tip vortices at a commercial jet airport have been observed at a range of 100-300 m, by using a 3 GHz FM-CW radar. In [63], the wake vortex of a DC-8 aircraft was detected by an S band FM-CW bi-static radar at the range of 600 meters, 15 seconds after the aircraft was passing by. In [5], the wake vortex of C-5A aircraft was successfully detected by pulsed Doppler radar operating at VHF, UHF, L,S and C bands and its radar reflectivity was shown to be flat decreasing with wavelength down to 5 cm. In [134], the vortices of a small fighter aircraft were detected at a range of 2.7 km by using a 1MW C band pulse Doppler radar. In [95], GEC-Marconi research center executed wake vortex detection trials by using multi-functional coherent pulse Doppler radar in both S and X band. In [77], the evidence of wake vortices was found for up to 2 min after the passage of the Lockheed C-130 airplane by analysis of the C band radar data. In [81] and [82], the wake of C-130 aircraft was detected by an X band bi-static continuous-wave radar. In [6] and [135], the aircraft wake vortices at a range of 7 km was effectively detected by an X band Radar in scanning mode, and the Radar Doppler signatures were observed in rainy weather as well as in clear air. In [27], a W-Band Radar was used to detect wake vortices in rainy conditions and the reflectivity RHI plots showed clear evidence of enhanced droplet concentration between the vortices and reduced droplet concentration in columns directly below and towards the outside of each vortex.

Wake vortex radar sensors development

The current research on wake vortex scattering mechanism and detection trials have shown the need for specific and more reliable radar sensors for wake vortex monitoring.

In [136], the first generation of transmit and receive antennas for an on-board wake vortex detection front end module at 76.5 GHz was presented. In [137], a W band radar system will be updated for wake vortex monitoring in precipitation, providing dual polarization capabilities, mobility and higher transmit power. In [138], a low power X-band radar was being developed to provide all-weather wake vortex detection and high-resolution weather monitoring in the TMA (Traffic Management Advisor).

Wake vortex monitoring has also attracted concerns from the meteorological societies. The main idea in [139] is that the early warning information of the potential wake vortex area in danger could be provided by the display and track of the image of precipitation cloud, which is a kind of meteorological products. In [43], the aircraft wake vortex was found to affect the backscattering properties of rain, because the perturbations of wake vortices may generate new periodic clustering in rain capable of increasing radar coherent backscatter. Besides, there are also some discussion on the application of Multi-function phased array weather radar to wake vortex monitoring [140].

1.2.3 Problems and Challenges

In recent years, the research on wake vortex radar monitoring has made some very important progress, however, radar is still far away from airport application for wake vortex monitoring due to some unresolved problems and challenges.

Radar signatures of wake vortex in clear air

In clear air, the radar scattering characteristics of wake vortex has been studied and some fruitful results have been obtained by numerical simulations. However, the radar monitoring of wake vortices in clear air for operational application is far from being effective. Firstly, the radar reflectivity of wake vortices in clear air is extremely low and extremely high transmitted powers should be envisaged, leading thus to high infrastructural costs. Secondly, the validation of these models by experimental data is still not well executed. Thirdly, theoretical studies on Doppler radar signatures of wake vortex, which are very critical to distinguish wake vortex from the background atmosphere, also need to be completed. Lastly, the characterization of vortex circulation from the radar measurements in clear air has not been made until now.

Radar signatures of wake vortex in rain, fog and cloud

Compared to Lidar and Sodar, Radar is a potential sensor for monitoring wake vortex in rain, fog and cloud. In foggy or cloudy weather, the radar reflectivity of wake vortex is dominated by Rayleigh scattering from small spherical fog or cloud droplets. In [78] and [91], the radar reflectivity of wake vortex in fog was also computed according to the distribution of liquid water content in the foggy wake vortex obtained from TASS outputs. In rainy weather, the radar backscattering echoes are mainly reflected from the rain droplets in the wake vortices. In [27], a W band radar was shown to have the capability of monitoring wake vortices in light precipitation. However, very few research has been reported until now to model and evaluate the radar signatures of wake vortex in rainy weather. Thus, some critical problems need to be studied: the interaction between raindrops and wake vortex, the modeling and simulation of radar signatures of wake vortex in rainy weather and the interpretation of wake vortex radar signatures.

1.3 Contents of the Thesis

The main objective of the work presented in this dissertation is to model and simulate the radar signature of wake vortices in rainy weather. This work can be decomposed into three parts:

- The study of the motion and of the distribution of raindrops in wake vortices;

- The modeling and simulation of the radar signatures,
- The radar signature interpretation.

Those different steps are described in separate chapters of the manuscript.

Chapter 2 briefly recalls the basics for modeling and simulating the radar signatures of wake vortices in rainy weather, including the wake vortex velocity field, the wake vortex transportation and the vortex circulation decay model. Raindrops' parametrization by terminal falling velocity and drop size distribution is also presented. The microwave properties of raindrops, the radar equation for distributed target and the basics of Doppler radar for rain observation are recalled.

Chapter 3 presents a study of the motion and distribution of raindrops in wake vortices. The motion equation of raindrops in wake vortices is derived and some simulations of raindrops' trajectory are presented. The methodology to compute the raindrops' distribution in wake vortices is proposed. The relative number concentration and velocity distribution of raindrops in wake vortices are illustrated by simulations. Based on the analysis of the impact of descent velocity, uniform crosswind and initial release position on raindrops' motion, the time evolution of raindrop distribution is also presented.

Chapter 4 deals with the radar signatures modeling and simulation. Two simulation methodologies to compute the radar echo are presented. The first simulation methodology allows computing the raw radar signal backscattered by all the raindrops within a given volume at a given position. The second simulation methodology is based on raindrop's distribution, enabling the computation of radar signatures much more efficiently. Typical X band and W band radar parameters are used to compute the radar signatures of raindrops in wake vortices under different radar scanning modes.

Chapter 5 aims at interpreting the radar signatures of raindrops in wake vortices. The dependence of radar signatures on rain rate, wake vortex circulation, radar antenna elevation angle and range resolution is analyzed. The wake vortex detection is achieved by the analysis of Doppler spectrum width. The retrieval of wake vortex parameters from the Doppler velocity spectrum in scanning mode for radar deployed under flight path is also studied and preliminary results show effectiveness of the proposed methodology.

Chapter 6 presents the conclusions and perspectives. The main contributions of this dissertation are summarized. Considering the practical requirements of wake vortex monitoring in air traffic control, future research perspectives are also given in this Chapter.

Chapter 2

Basics of wake vortex, rain and radar

The present research work requires knowledge and concepts coming from various scientific and technical fields, including fluid mechanic, electromagnetism, signal processing and meteorology. Those prerequisite are presented in this chapter. The basic concepts used further in the work, concerning wake vortices, scattering by raindrops and weather radar are briefly presented.

2.1 Wake vortex

In the atmosphere, the flow induced by the aircraft wake vortices introduces fluctuations of temperature, pressure, humidity and velocity field inside and outside the vortex core. As shown in Figure 2.1, the aircraft wake vortex may be described

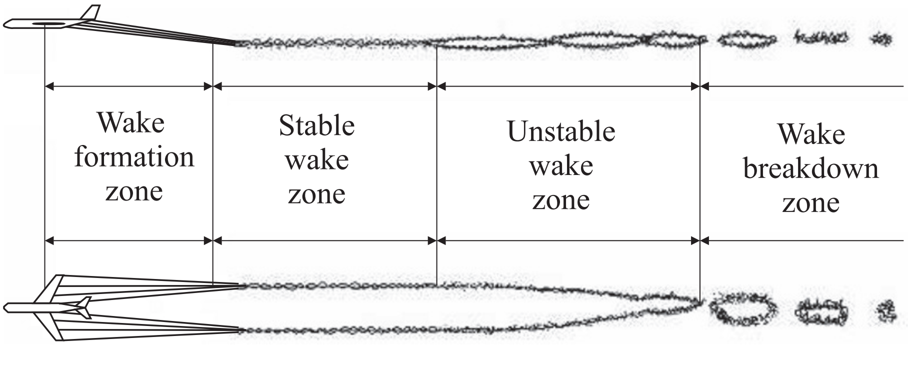

Figure 2.1: Breakdown of the aircraft vortex wake in accordance with its evolution phases [14]

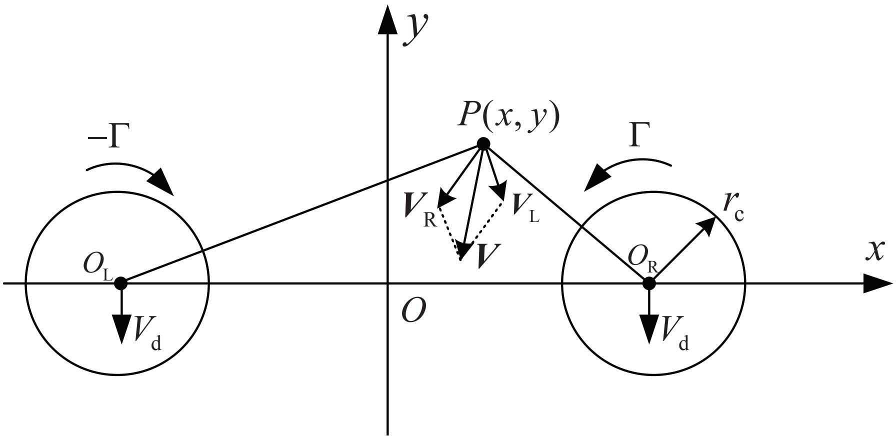

Figure 2.2: Velocity field of two counter-rotating vortices [141]

.

by four specified zones and the vortex velocity profile in each zone is changing with time and space [14]. In the wake formation zone, small vortices emerge from the vortex sheet at the wing tips and at the edges of the landing flaps. After rolling up, the wake enters into the stable phase, maintaining a relatively stable velocity profile which may last for several minutes. In the analysis made in this thesis the emphasis has been put on fully rolled-up wake vortex in stable phase where the flow can almost be approximated by a stationary flow.

2.1.1 Wake vortex velocity field

In stable phase, the aircraft wake vortex is constituted of two counter-rotating vortices with equal intensity and yielding to an axis-symmetric velocity field, as shown in Figure 2.2. According to the Biot-Savart Law, the local flow velocity at the point P can be expressed as

$$\mathbf{u}(x,y) = V_\mathrm{L} + V_\mathrm{R} \tag{2.1}$$

where $V_\mathrm{L}, V_\mathrm{R}$ are the velocity components induced by the left and right vortex separately.

For each single vortex, a large number of models including Rankine vortex, Lamb-Oseen vortex, Hallock-Burnham vortex, adapted vortex, smooth blending vortex profile and multiple scale vortex have been developed in the past [17,142]. They refer to the geometry, the evolution and the characteristics of the velocity field. In [17], a wide range of models for vortex velocity profiles are summarized and reviewed. In the present work, the widely-used Hallock-Burnham model is considered to depict the tangential velocity distribution of wake vortex. The tangential velocity fields from this model is expressed as [16, 17]:

$$V_\theta(r) = \frac{\Gamma_0}{2\pi r} \cdot \frac{r^2}{r^2 + r_{\mathrm{c}}^2} \tag{2.2}$$

where $V_\theta(r)$ (m/s) is the tangential velocity at the distance r (m) from the vortex core, r_{c} (m) is the vortex core radius and Γ_0 (m^2/s) is the initial circulation which describes the vortex strength and is determined mainly by the aircraft lift that is comparable to its weight [8].

Different kinds of parametrization for the vortex core in Hallock-Burnham vortex model have been summarized in [142]. In the present work, the vortex radius core is chosen to be $r_c = 0.052b_0$ [16, 142].

Considering an elliptical distribution of the lift, the initial circulation of wake vortex is expressed as [18]

$$\Gamma_0 = \frac{Mg}{\rho U b_0}, b_0 = \frac{\pi}{4}b \tag{2.3}$$

where M(kg) is the weight of the airplane, U (m/s) is the flying speed, g ($\mathrm{m/s}^2$) is the gravitational acceleration, ρ $\mathrm{kg/m}^3$ is the air density, b (m) is the the aircraft's wingspan, and b_0 is the separation between two vortices. During the taking off and landing phases near the airport runway, U is relatively small, thus the circulation of wake vortices is larger than that in the cruise phase.

In Table 2.1, the parameters of three typical aircrafts namely a medium-range airliner like A320, a long-range wide body airliner A340 and a long-range wide body airliner high capacity A380 are presented, including the maximum taking off weight (MTOW), wingspan, FAA category (based on Aircraft length) and ICAO category (based on Aircraft overall length and maximum fuselage width).

Table 2.1: Parameters of three typical aircrafts

Type	MTOW (tons)	Wingspan (m)	FAA category	ICAO category
Airbus A380-800	569	79.75	Heavy	Super
Airbus A340-300	259	60.30	Heavy	Heavy
Airbus A320-200	78	34.10	Medium	Large

In Figure 2.3, the vertical velocity profiles on a line passing through the wake vortex centroids of A320, A340 and A380 are illustrated, considering the Hallock-Burnham model in Equation (2.2). The flying speed of these three aircrafts is assumed to be 300 km/h. The maximum tangential velocity of A380 reaches to around 20 m/s.

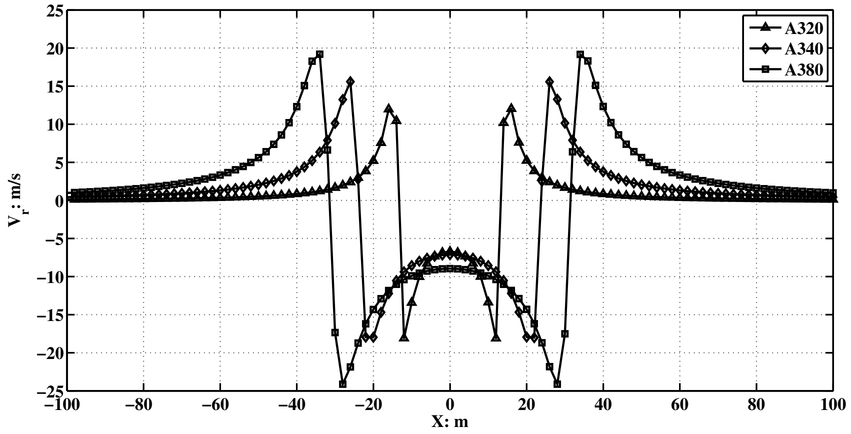

Figure 2.3: Vertical velocity profile on a line passing through the wake vortex centroids of three types of aircrafts: an A320, an A340 and an A380

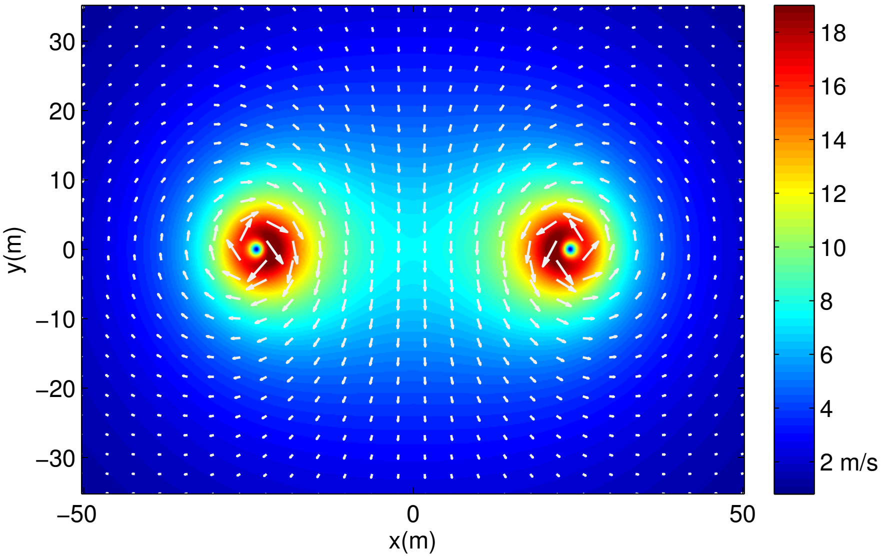

Figure 2.4: Two dimensional velocity distribution of the wake vortices generated by an A340

Still considering the Hallock-Burnham model, Figure 2.4 illustrates the two dimensional velocity distribution of the wake vortices generated by an A340, each white arrow represents the velocity of the local vortex flow. It can be noticed that around the two vortex cores, the velocity is changing rapidly, the tangential velocity is decreasing with the distance to the vortex center inside the vortex core and increasing with the distance to the vortex center outside the vortex core.

In Figure 2.5, the vertical velocity profiles in the vortex core for an A380 at three flying speeds: 300 km/h, 400 km/h and 500 km/h are presented. It is easy to find that the vortex velocity is inversely proportional to the flying speed. If the aircraft flies at a lower speed, the induced vortex velocity is larger.

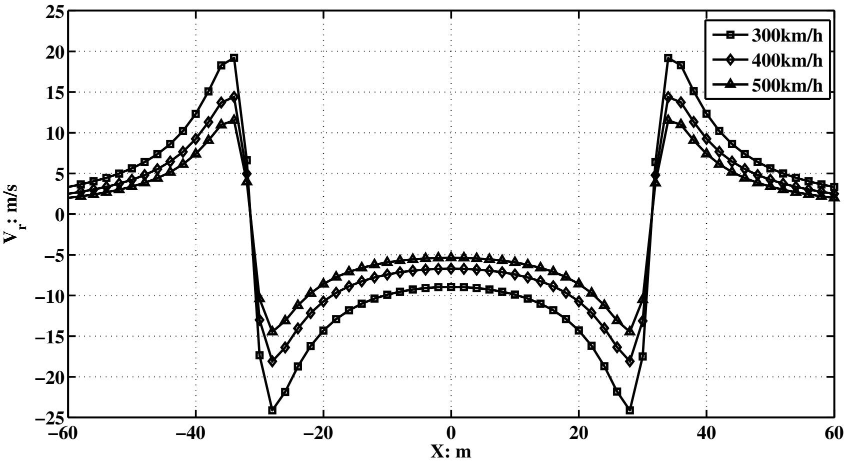

Figure 2.5: Vertical velocity distributions in the vortex core for A380 at three flying speeds: 300 km/h, 400 km/h and 500 km/h.

2.1.2 Wake vortex transportation and circulation decay

Wake vortex transportation strongly depends on the atmospheric background such as crosswind, wind shear, ground effect, ambient turbulence and thermal stratification, as shown in Figure 2.6 [19, 143]. In recent years, field studies, laboratory experiments, and numerical simulations have been conducted to understand the wake vortex behaviors under crosswind shear or atmospheric turbulence [144–149]. Regardless of the ground effect [150], the wake vortex pair descends due to its mutual induction while being transported horizontally with the ambient wind [149]. Possible parameterizations for the descent velocity of the vortex pair, the vortex circulation decay model and the vortex motion under uniform crosswind are presented in this section. In order to support the further analysis of raindrop's motion in wake vortices, here only the descent velocity of the vortex pair, the vortex circulation

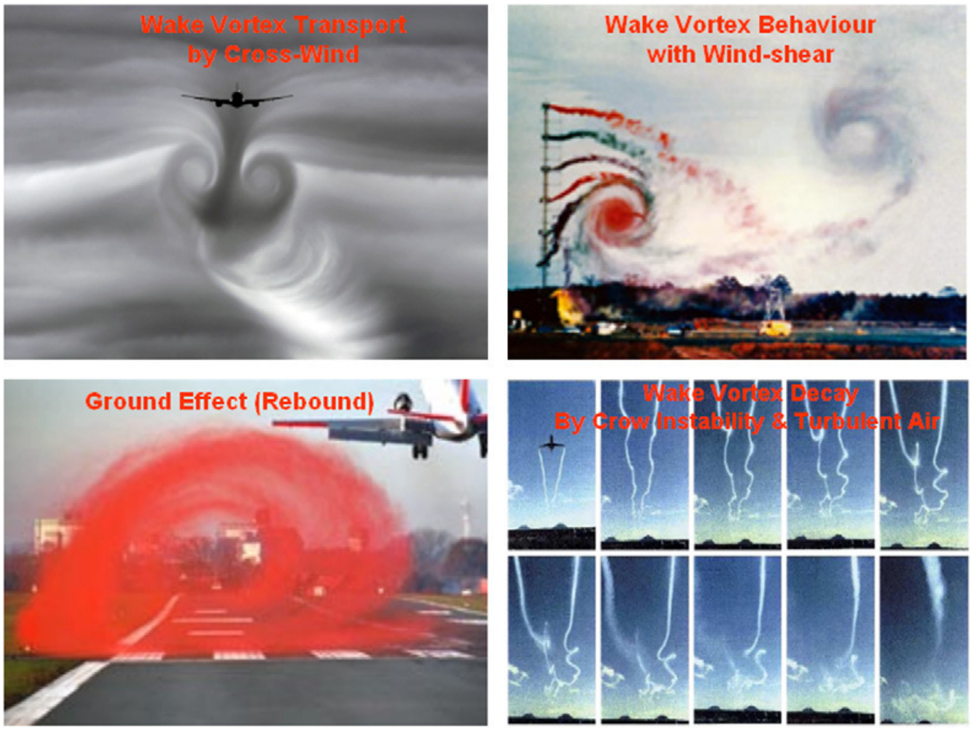

Figure 2.6: Wake vortex dynamics and behavior [19]

decay model and the vortex motion under uniform crosswind will be reviewed.

Descent velocity of the vortex pair

After roll-up, the two counter-rotating trailing vortices of nearly equal strength form the aircraft wake [28], a downwash velocity that pulls the wake vortex pair down after leaving the aircraft is generated. According to the Biot-Savart Law, the mutually induced descent velocity of the vortex pair is given by

$$V_d = \frac{\Gamma_0}{2\pi b_0} \tag{2.4}$$

where Γ_0 is the initial vortex circulation (m^2/s) and b_0 is the vortex core separation. For simplification, the atmosphere stratification is not considered in the following analysis. As the vortex circulation decays with time, the descent speed of the vortex pair will also decrease with time after wake vortex formation. Considering the circulation decay model that will be described in next section, Figure 2.7 illustrates the descent of the wake vortex pairs behind an A320, A340 and A380. From the slopes of the three curves representing the position of wake vortex, the descent velocities are shown to be decreasing with time.

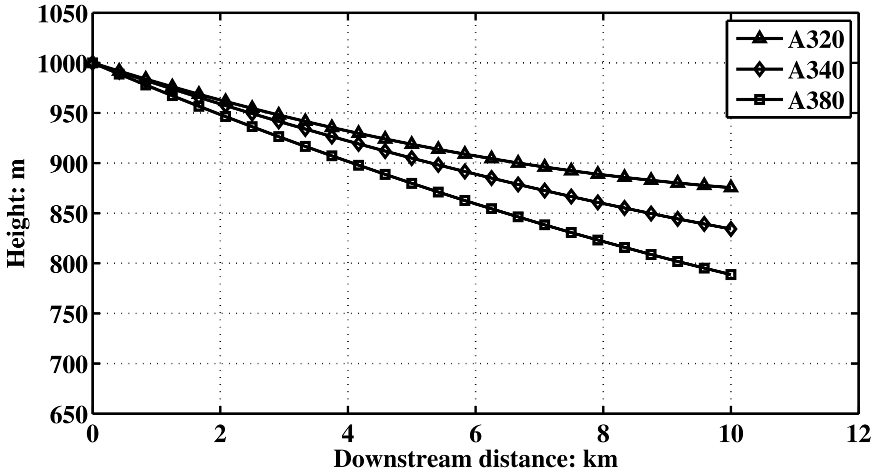

Figure 2.7: Illustration of the descent of wake vortex pairs behind three types of aircrafts: A320, A340 and A380

Wake vortex motion under uniform cross wind

As mentioned earlier, the transport of wake vortex in the wind flow has been widely studied. In the present work, the motion of wake votex advected by an uniform cross wind is briefly introduced to support the radar simulations of the following chapters.

To this aim, it is assumed that the counter-rotating vortices of strength Γ_0 are in a uniform cross wind with a horizontal speed denoted U_w. The resulting flow field is the superimposition of the two flows, thus the instantaneous velocity at position (x, y) can be given by [148]

$$\begin{cases} u_x^{'} = U_w + u_x(x, y) \\ u_y^{'} = u_y(x, y) \end{cases} \tag{2.5}$$

where $u_x(x, y)$ and $u_y(x, y)$ are the horizontal and vertical velocities of the wake vortex flow field in absence of cross wind. Supposing that the two vortices are located at (x_+, y_+) and (x_-, y_-) respectively, the time dependent locations of the vortices are given by:

$$\begin{cases} \frac{\mathrm{d}}{\mathrm{d}t}\overline{x}_+ = \frac{\mathrm{d}}{\mathrm{d}t}\overline{x}_- = U_w \\ \frac{\mathrm{d}}{\mathrm{d}t}\overline{y}_+ = \frac{\mathrm{d}}{\mathrm{d}t}\overline{y}_- = -V_d = -\frac{\Gamma_0}{2\pi b_0} \end{cases} \tag{2.6}$$

which indicate that each vortex is advected horizontally by the cross wind and vertically by the velocity induced by the other vortex.

In Figure 2.8, the motion of the wake vortex pair under a 3 m/s crosswind is illustrated for t = 0 s and 20 s. The aircraft is assumed to be an A340, flying at 300 km/h. The motion of the vortex is a combination of the descent velocity and of the cross wind. The resulting velocity field is the superimposition of the vortex flow and of the transport flow.

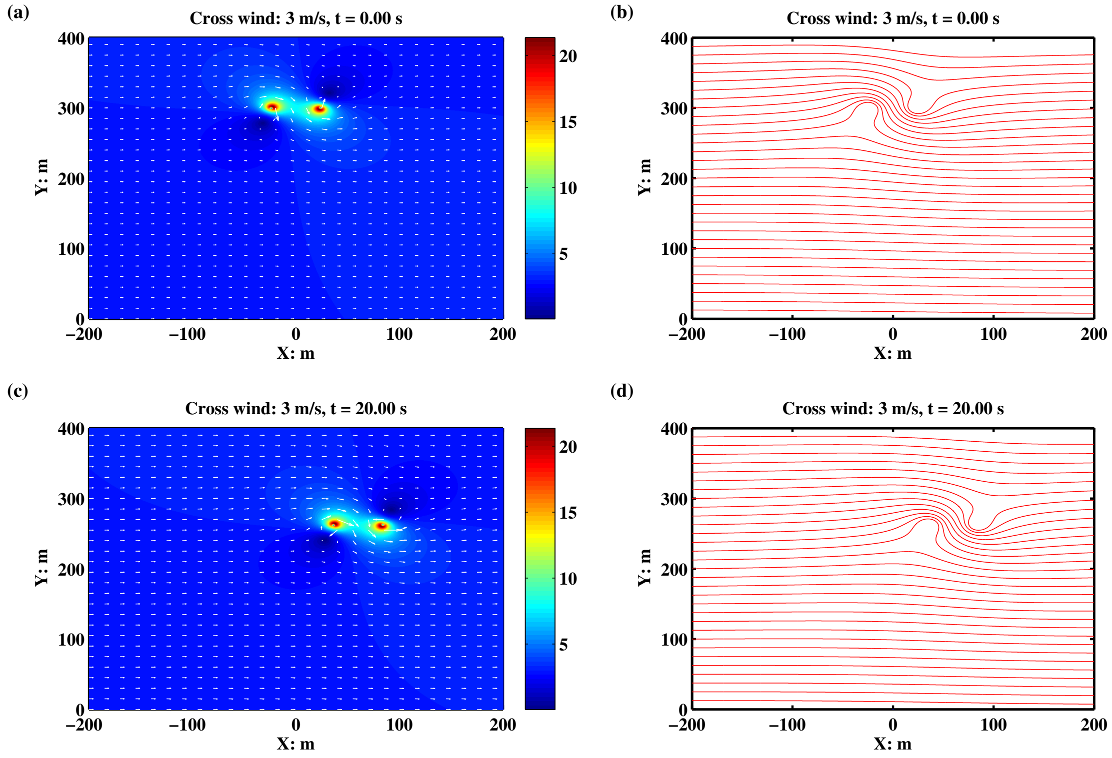

Figure 2.8: The motion of wake vortex pair under the crosswind of 3 m/s: (a) The 2D velocity field at t = 0 s, (b) The streamlines of the velocity field at t = 0 s, (c) The 2D velocity field at t = 20 s, (d) The streamlines of the velocity field at t = 20 s

Wake vortex circulation decay

Circulation describes vortex strength in a form that is correlated with the potential hazards caused by wake encounters, thus it is very important to characterize the circulation of wake vortex [8]. The energy of the vortex is progressively dissipated in the ambient atmosphere after its creation. The rate of decay of the vortex and of its circulation is highly dependent on the atmospheric conditions. Various studies have been focused on the wake vortex decay mechanisms and the wake vortex transportation models [151–154]. In the present work, an empirically observed equation is adopted to describe the decay of wake vortex circulation.

The characteristic time scale for the wake vortex to decay is usually defined as the time it takes for the vortex pair to descend one wing span, which is given by

$$t^{'} = \frac{b_0}{V_d} = 0.38\frac{B^3U}{M} \tag{2.7}$$

where B,U and M are the aircraft wingspan, flying speed and weight respectively. If the ambient background turbulence eddy dissipation rate ε is above a threshold value, $\varepsilon \geq 10^{-4}$ m^2/s^2, the crow instability is empirically observed to lead to a linear circulation decay rate [19]. The empirical observed circulation evolution is given by

$$\Gamma = \Gamma_0 \left(1 - \frac{t^*}{8}\right) \quad \text{with} \quad t^* = \frac{t}{t'} \tag{2.8}$$

In Figure 2.9, the wake vortex circulation decay is illustrated for three types of aircrafts: A320, A340 and A380. The time scale is the absolute time. The flying speeds of these three aircrafts are set to be 300km/h and other parameters refer to the values in Table 2.1. It is easy to find that the initial circulation of A380 wake vortex is larger than that of A340 and A320, and the decaying time for A380 is longer.

2.2 Raindrops

Various properties of raindrops that will act partially as passive tracer in the considered problems have been studied in the past mainly by meteorologist. Different properties of raindrops that strive to be useful for the present work are briefly recalled in this section.

2.2.1 Terminal falling velocity

In still air, a falling raindrop reaches its terminal fall velocity V_{T} with the equilibrium between the inertial force and the drag force acting on it [155]. A widely used exponential expression between V_{T} (m/s) and the diameter D (mm) is given by [21, 24, 25]

$$V_{\mathrm{T}}(D) = [\alpha_1 - \alpha_2 exp(-\alpha_3 D)](\frac{\rho_0}{\rho})^{0.4} \tag{2.9}$$

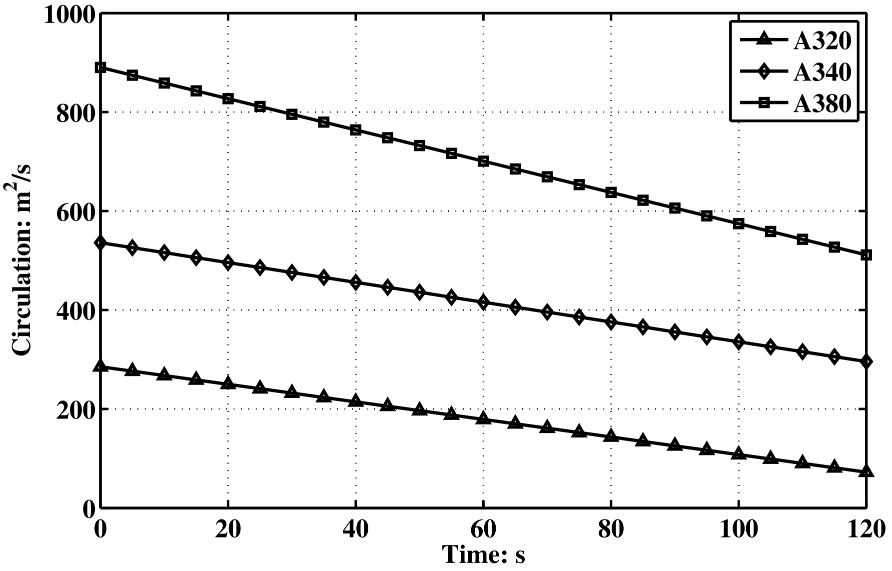

Figure 2.9: Illustration of the wake vortex circulation decay for three types of aircrafts: A320, A340 and A380

where $\alpha_1 = 9.65$ m/s, $\alpha_2 = 10.3$ m/s, $\alpha_3 = 0.6$ m/s and $(\rho_0/\rho)^{0.4}$ is a density ratio correction factor adjusting deviation of the terminal fall velocity due to the air density change with the fall altitude. Figure 2.10 presents the terminal falling velocity of raindrops for different altitude levels. It can be noticed that: (1) the larger the diameter of the raindrops, the faster the terminal falling velocity; (2) at a relatively high altitude, the raindrop's speed is a little higher due to the lower local air density. For the largest raindrops of more than 6 millimeters of diameter, the terminal falling velocity approaches 10 meters per second.

2.2.2 Shape of a raindrop

A large number of investigations on the shape of raindrops falling at their terminal velocity are reported in the literature [157]. There are five key factors commonly agreed to affect the raindrop shape, namely, the surface tension, the hydrostatic pressure, the aerodynamic pressure, the internal circulation and the electric stress. In Figure 2.11, the shape of raindrops falling at terminal velocity are illustrated for different diameters, the raindrops are with origin at center of volume, the dashed circles of diameter D are shown for comparison [156]. Raindrops with diameters comprised between 0.5 mm and 4 mm, are almost spherical and constitute the large

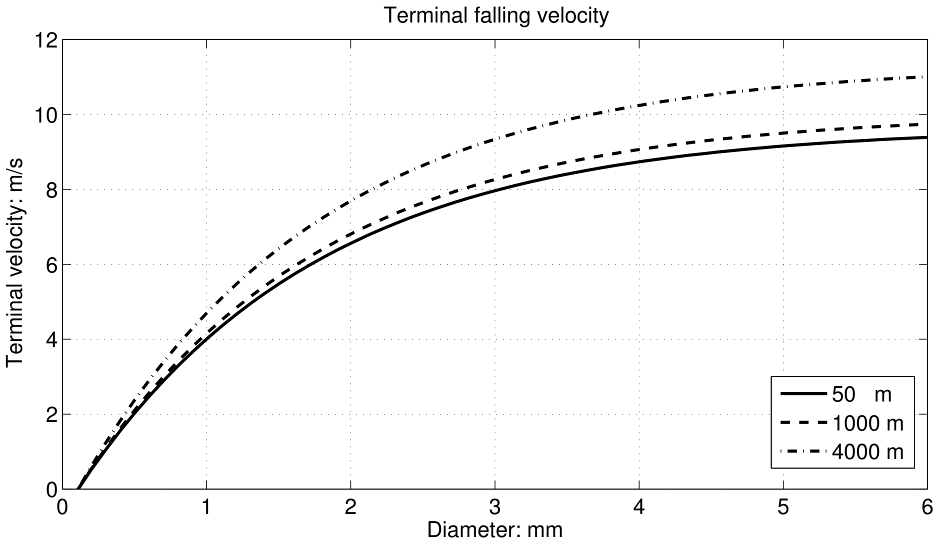

Figure 2.10: Raindrops' terminal falling velocity at altitudes of 50 m, 1000 m and 4000 m

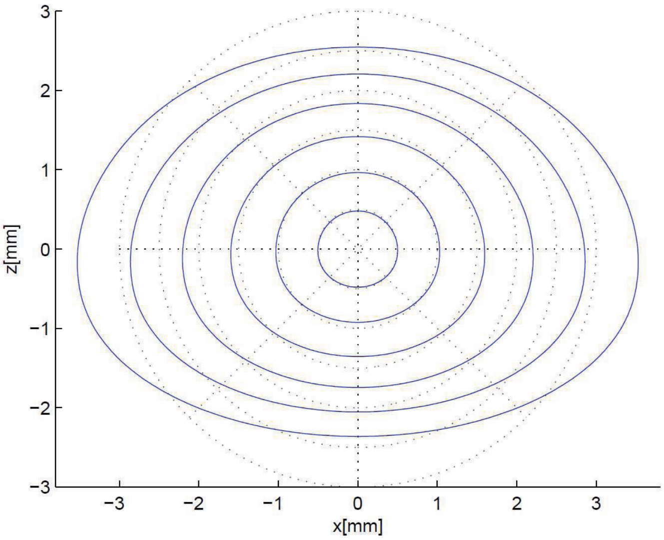

Figure 2.11: Shape of raindrops falling at terminal falling velocity: the raindrops are of diameters D = 1, 2, 3, 4, 5 and 6 mm and with origin at center of volume, the dashed circles of diameter D are shown for comparison [156]

majority of raindrops for rain in temperate areas. In the following analysis, the raindrops are assumed to be spherical. This assumption is of minor significance unless the polarimetric signature of raindrops is of interest.

2.2.3 Raindrop size distribution

Drop size distributions (DSD) have been widely used by radar-meteorologists as they can directly be related to the radar reflectivity [20]. A series of models to describe this kind of distribution in different climatic regions and seasons is summarized in [23].

In 1904, the rain phenomenology was first quantitatively documented by Bentley and von Lenard [158,159], whose experiments were lately confirmed by the measurements of Marshall and Palmer [20], showing that the raindrop size distribution is a monotonically decreasing function of the size, the number density of drops $N(D)$ ($\mathrm{m}^{-3}\mathrm{mm}^{-1}$) with a diameter between D and $D + \mathrm{d}D$ per unit volume of space is given by [159]

$$N(D) = N_0 e^{-\wedge D} \tag{2.10}$$

where N_0 (in $\mathrm{m}^{-3}\mathrm{mm}^{-1}$) is a constant reflecting the average spatial density of the drops and equal to 8×10^3 at the ground level, D is the raindrop diameter in millimeter, and $\wedge$ (mm^{-1}) is related to the rain rate R by

$$\wedge = 4.1R^{-0.21} \tag{2.11}$$

where R is in millimeters per hour. Due to its exponential increase when D tends toward zero, this model overestimates the number of small raindrops of diameter smaller than 1.5 mm [23]. It was shown latter by [21] [22] that the modified gamma distribution is more accurate to estimate the number of small raindrops. In this case, the raindrops size distribution is given by

$$N(D) = N_0 D^{\mu} e^{-\wedge D} \tag{2.12}$$

where N_0, μ and $\wedge$ are the concentration, distribution shape, and size parameters, respectively. The greatest difficulty in the use of this distribution model lies in obtaining experimentally the above parameters [23].

In the following analysis, a suitable model to describe the size distribution of the rainfall in Europe is adopted. For a given rain rate R (mm/h), the raindrops size distribution is given by [23, 160, 161]

$$N(D) = N_0 D^2 e^{-\wedge D}, \tag{2.13}$$

where $N_0 = 64500R^{-0.5}$ ($\mathrm{m}^{-3}\mathrm{mm}^{-3}$), $\wedge = 7.09R^{-0.27}$ (mm^{-1}), $N(D)$ ($\mathrm{m}^{-3}\mathrm{mm}^{-1}$) represents the number of raindrops of the diameter D per unit volume per unit

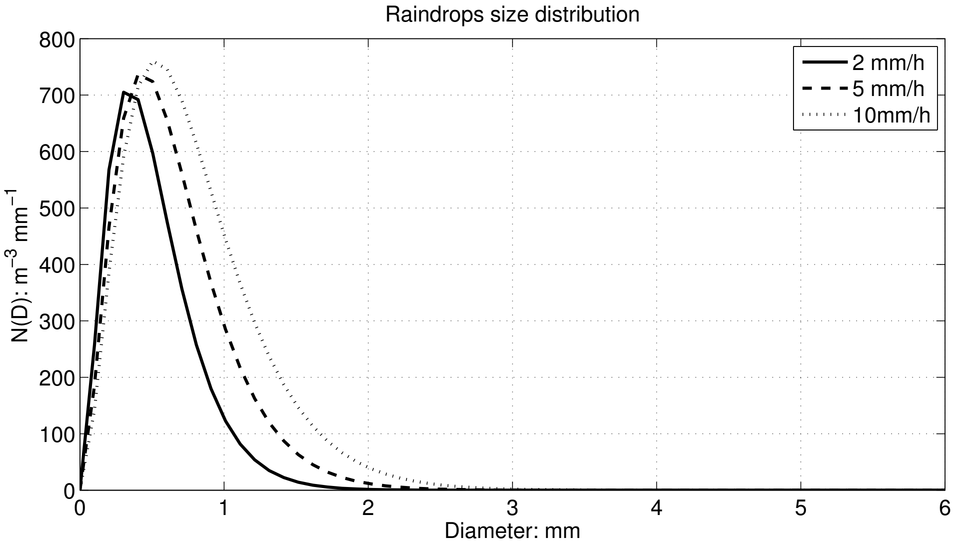

Figure 2.12: Raindrops size distribution for different rain rates: R =2 mm/h, 5 mm/h and 10 mm/h

diameter class interval. If the raindrops are divided into several diameter classes, the number of raindrops with the diameters between $D - \Delta D/2$ and $D + \Delta D/2$ in a unit volume can be approximately computed by $\Delta D N(D)$. Figure 2.12 presents raindrops size distribution for rain rates of 2 mm/h, 5 mm/h and 10 mm/h. As it can be noticed on Figure 2.12, the average raindrop size is becoming larger for higher rain rates.

2.2.4 Microwave properties of raindrops

The theory of the scattering of electromagnetic waves by particles is based on the application of Maxwell's equation to the scattering of a planar wave by a homogeneous water sphere in a nonabsorbing medium [155].

Rayleigh approximation

Considering a homogeneous spherical raindrop of diameter D (m) and an incident electromagnetic wave of wavelength λ (m), the radar cross section (RCS) of the raindrop is closely related to its radio-electric size $\alpha = \pi D/\lambda$. α is generally smaller than 1 for a wide range of radar bands (S, C, X bands), because the sizes of raindrop scatterers are smaller than the wavelengths. In this case, the radar cross section of a raindrop is well described by the Rayleigh approximation [162]

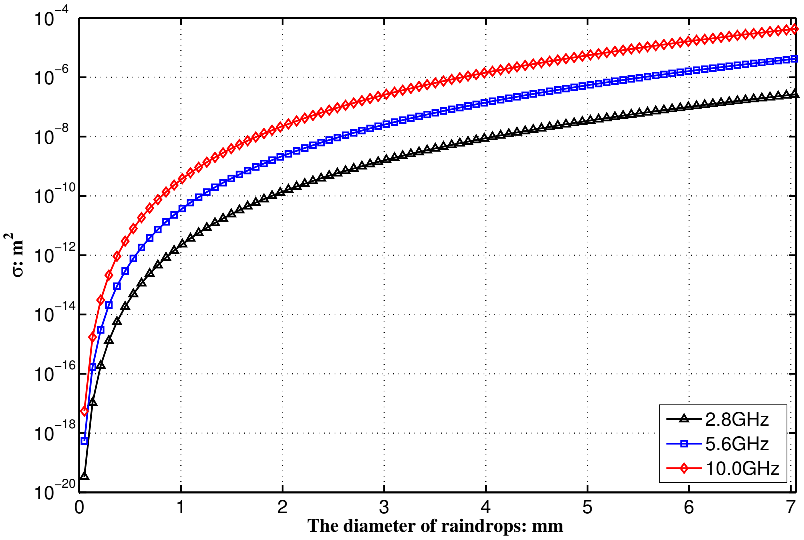

Figure 2.13: Backscattering cross section of a raindrop as a function of its diameter: Rayleigh approximation

$$\sigma = \frac{\pi^5}{\lambda^4}|K|^2 D^6, K = \frac{m^2-1}{m^2+2} \tag{2.14}$$

where $|K|^2$ is a coefficient related to the dielectric constant of water, m is the complex refractive index of the raindrops relative to the air background and can be expressed as $m = n - ik$. $n = \sqrt{\varepsilon_r}$ is the ordinary refractive index with ε_r being the relative permittivity, and k the absorption coefficient of the raindrops. Practically, $|K|^2$ could be considered as constant at temperatures found in the atmosphere and centimetric wavelengths [155]. In the following simulations, the standard value $|K|^2 = 0.93$ is adopted. In Figure 2.13, the backscattering cross section function of raindrop's diameter, is computed by Rayleigh approximation for 2.8 GHz (S band), 5.6 GHz (C band) and 10 GHz (X band) incident waves respectively.

Mie formulas

For higher frequency bands, if α is comparable to 1, the backscattering cross section of a raindrop is better approximated by Mie formulas

$$\sigma = \frac{\lambda^2}{4\pi}\left|\sum_{n=1}^{\infty}(-1)^n(2n+1)(a_n-b_n)\right|^2 \tag{2.15}$$

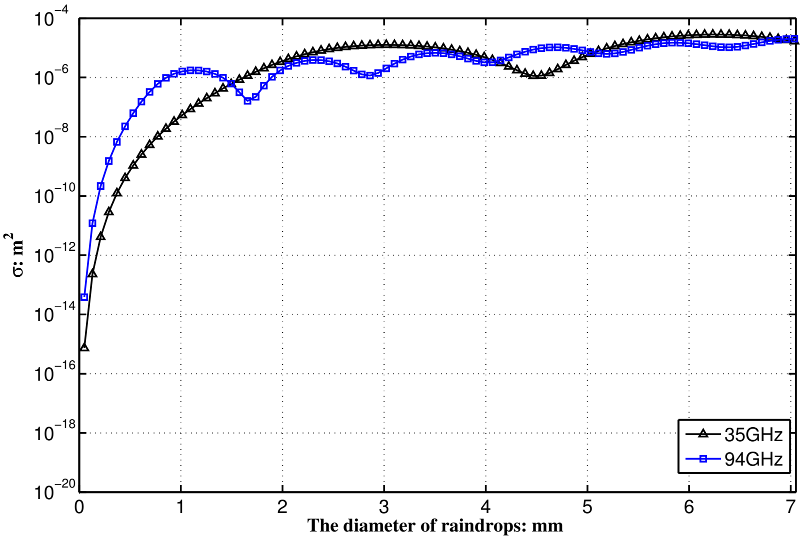

Figure 2.14: Backscattering cross section of a raindrop as a function of its diameter: Mie formulas

where a_n and b_n are the "Mie Coefficients" obtained from Bessel and Hankel functions with arguments α and m. Detailed expressions for computation can be found in [155]. In Figure 2.14, the backscattering cross section function of raindrop's diameter, is computed by Mie formulas for 35 GHz (Ka band) and 94 GHz (W band) incident waves respectively.

Attenuation of raindrops

The attenuation by rain can be a critical effect for some radar applications where the losses caused by the crossing of rain clutter may severly limit the detection of a radar, especially for a radar operating above 10 GHz. For a given wavelength λ, and for a rather broad interval of variation of rain rates R, the specific attenuation rate a_{r} (dBkm^{-1}) can be estimated with a good precision by:

$$a_{\mathrm{r}} = kR^{\gamma} \tag{2.16}$$

where the constants k and γ depend on the frequency and the temperature. In the following analysis for wake vortex monitoring, the radar is usually deployed close to the airport runway, at a range less than 2 km, so the radar signal is not severely attenuated due to the short path through rain and the attenuation due to raindrops is not considered.

2.3 Radar

During the last few decades, radar has proved to be a valuable sensor for the detection and quantification of precipitation, for the measurement of velocity fields, and for the polarimetric observation of the microstructure of hydrometeors [155]. Radar directly derived from those weather radar appears therefore as the best candidates to detect the wake vortices in rainy weather. The basic principles of operation of those weather radar are recalled in this section.

2.3.1 Doppler frequency and ambiguities

Doppler frequency

Considering a radar with carrier frequency f_0 (wavelength λ), the phase of the received signal from the scattered target at range r can be given by

$$\varphi(t) = \varphi_0 - \frac{4\pi r(t)}{\lambda} \tag{2.17}$$

where φ_0 is the initial phase of the transmitted signal. If the radial velocity of the target with respect to the radar is v_r ($v_r > 0$ if moving towards the radar), the rate of change of phase to the time can be derived as

$$\frac{\mathrm{d}\varphi}{\mathrm{d}t} = -\frac{4\pi}{\lambda} \cdot \frac{\mathrm{d}r}{\mathrm{d}t} = \frac{4\pi}{\lambda} \cdot v_r \tag{2.18}$$

On the other hand, $\frac{\mathrm{d}\varphi}{\mathrm{d}t}$ equals to the angular frequency ω_d, that is

$$\frac{\mathrm{d}\varphi}{\mathrm{d}t} = \omega_d = 2\pi f_d \tag{2.19}$$

where f_d is the Doppler frequency. Thus, the relationship between the Doppler frequency and radial velocity is given by

$$f_d = \frac{2v_r}{\lambda} \tag{2.20}$$

In order to preserve the information on the sign of the Doppler frequency, a phase demodulator is usually used in the radar system. The outputs of the demodulator are two signals in phase and in quadrature, that can be expressed as:

$$I(t) = A_0 \mathrm{cos}(\omega_d t); Q(t) = A_0 \mathrm{sin}(\omega_d t) \tag{2.21}$$

Ambiguities

For a meteorological Doppler radar, in order to measure ω_d, the phase change between two successive pulses is usually taken into account [155]. If the radial velocity of the target is so large that the phase difference between two successive pulses is greater than π rads, there is ambiguity concerning the measurement of the radial speed. For a radar of wavelength λ and pulse repetition frequency f_r, the maximum radial velocity that can be measured is:

$$V_{\max} = f_r \frac{\lambda}{4} \tag{2.22}$$

which means that between two successive pulses, the target must not move a distance greater than one-quarter radar wavelength. Thus, a Doppler radar having long wavelength or operating at high PRF is capable of measuring a large range of velocities. However, for a large unambiguous range, a Doppler radar must operate at a low PRF. The pulse repetition frequency f_r determines the maximum unambiguous range:

$$R_{\max} = \frac{c}{2f_r} \tag{2.23}$$

where c is the light speed. Combining Equations (2.22) and (2.23), we have

$$R_{\max} V_{\max} = \frac{c\lambda}{8} \tag{2.24}$$

which indicates that the product of the maximum measurable values of the range and velocity is proportional to the radar wavelength.

2.3.2 Radar equation

The radar equation expresses the fundamental relations between the characteristics of the radar, the target, and the received signal. Assuming that the transmitter and the receiver are at the same location, for a point target situated at range r in the (θ, ϕ) direction, the received power is given by the equation [155]:

$$P_r = \frac{P_t G_0^2 |f_n(\theta, \phi)|^2 \lambda^2 L_r}{(4\pi)^3} L^2 \frac{\sigma}{r^4} \tag{2.25}$$

where P_t is the transmitted power, G_0 the antenna gain, $f_n(\theta, \phi)$ the antenna directivity function, λ the radar wavelength, L_r the attenuation due to the finite band width of the receiver, L the attenuation on the radar-target path and σ the effective radar backscattering cross section of the target. It can be noticed that for a point target, the radar received power is inversely proportional to the fourth power of the distance [155].

For a "distributed target" such as raindrops filling the resolution volume V, the radar backscattering cross section is equal to the summation of each raindrop over the entire resolution volume, which can be expressed as:

$$\sum_V \sigma_i = V(\sum_V \sigma_i/V) = V\eta \tag{2.26}$$

where η is the average cross section of the target per unit volume and called the radar reflectivity. Thus, Equation (2.25) can be written as:

$$\overline{P}_r = \frac{P_t G_0^2 \lambda^2 L_r L^2 \eta}{(4\pi)^3} \int_V \frac{|f_n(\theta,\phi)|^4}{r^4} \mathrm{d}V \tag{2.27}$$

where P_r is replaced by the average power $\overline{P}_r$, $dV = r^2 \mathrm{d}r\mathrm{d}\Omega$ and $\mathrm{d}\Omega$ is the element of solid angle [155]. If r is large that the depth of the resolution volume $\mathrm{d}r \approx c\tau/2$, then Equation (2.27) can be rewritten as:

$$\overline{P}_r = \frac{P_t G_0^2 \lambda^2 L_r L^2}{(4\pi)^3} \frac{c\tau}{2} \frac{\eta}{r^4} \int_\Omega |f_n(\theta,\phi)|^4 \mathrm{d}\Omega \tag{2.28}$$

In most cases, the antenna directivity is represented by a Gaussian function given as [155]:

$$|f_n(\theta,\phi)|^2 = exp\left[-\left(\frac{\theta^2}{2\sigma_\theta^2} + \frac{\phi^2}{2\sigma_\phi^2}\right)\right] \tag{2.29}$$

where σ_θ and σ_ϕ are related to the beam width. Assuming that the 3 dB beam widths of the antenna are θ_0 and ϕ_0 and neglecting the effects of side lobes, it can be derived that :

$$\int_\Omega |f_n(\theta,\phi)|^4 \mathrm{d}\Omega = \frac{\pi\theta_0\phi_0}{8\ln 2} \tag{2.30}$$

where ln 2 is the natural logarithm of 2. Finally, the radar equation of distributed target can be given by

$$\overline{P}_r = \frac{P_t G_0^2 \lambda^2 \theta_0 \phi_0 L_r L^2}{1024\pi^2 \ln 2} \frac{\eta}{r^2} \tag{2.31}$$

It is interesting to notice from Equations (2.25) and (2.31) that, for point target, the received power is proportional to r^{-4}, and for distributed targets, the received power is proportional to r^{-2}.

2.3.3 Radar Doppler velocity spectrum

The Doppler velocity spectrum is a power weighted distribution of radial velocities of raindrops in the radar resolution cell. The knowledge of the radar Doppler spectrum is useful in a wide range of applications, such as those concerning the microphysics of cloud and precipitation [24, 155, 163–166], and those concerning the detection of atmospheric turbulence [167–171], wind shear [172] or tornado [173,174], which enables better warnings of severe weather and hazards to aviation safety [175]. Typically, these required information can be interpreted by the first three moments of radar Doppler spectrum, namely, the radar average received power (zeroth moment), mean Doppler velocity (first moment) and spectrum width (second moment, or standard deviation of the Doppler velocities), thus appreciably reducing the volume of radar data [155, 165, 166].

Given the sampled radar time series, the Doppler velocity spectrum can be computed by Fast Fourier Transform. Under the condition of short radar time series, a number of high resolution spectral estimation methods, including the maximum entropy method and parametric methods, can be utilized to estimate the Doppler spectrum of the $S_r(n)$ as well [19]. Assuming that the Doppler spectrum of raindrops in the radar cell located at a range r_k is expressed as $S(r_k, v_n)$, the radar average power of the signal can be estimated by computing the sum of average power in each Doppler spectrum bin as given by:

$$\overline{P_r} = \sum_{n=1}^{N_\mathrm{p}} S(r_k, v_n) \cdot \Delta v \tag{2.32}$$

where $\overline{P_r}$ is the average power, Δv is the Doppler velocity resolution, N_p is the number of coherently integrated pulses or the number of Doppler velocity bins.

In order to calculate the mean Doppler velocity and the spectrum width, the normalized expression of the Doppler velocity spectrum is adopted as [176]:

$$\overline{S}(r_k, v_n) = \frac{S(r_k, v_n)}{\sum\limits_{n=1}^{N_\mathrm{p}} S(r_k, v_n) \cdot \Delta v} = \frac{S(r_k, v_n)}{\overline{P_r}} \tag{2.33}$$

Thus, the mean Doppler velocity is given by:

$$\overline{v_r} = \sum_{n=1}^{N_\mathrm{p}} v_n \overline{S}(r_k, v_n) \cdot \Delta v \tag{2.34}$$

and the radar Doppler spectrum variance is given by:

$$\sigma_v^2 = \sum_{n=1}^{N_\mathrm{p}} (v_n - \overline{v_r})^2 \overline{S}(r_k, v_n) \cdot \Delta v \tag{2.35}$$

where σ_v is the Doppler spectrum widths, i.e., standard deviation of Doppler velocities. Obviously, the mean Doppler velocity is related to the power weighted mean radial motion of the particles and the spectrum width is related to the relative particle motions.

2.4 Conclusions

In this Chapter, the basic concepts about wake vortex, raindrops and radar have been reviewed and summarized. The parametrization for those elements that are used in the following of the thesis have been presented. In particular, the wake vortex velocity field, induced by three different kinds of aircrafts: A320, A340 and A380, has been studied. A method to account for their transportation under cross wind, their decay rate and their descent has also been presented. The properties of raindrops namely, the fall velocity, the DSD , the shape and their backscattering cross section under various assumptions have been presented. The basics of Doppler radar for rain observation, radar equation for distributed target and the parametrization of Doppler velocity spectrum by three spectral moments have also been presented.

Importantly it has to be kept in mind that the parametrization of the different element and the choice of the most appropriate model may appear to be arbitrary and that different choices could have been made. Aware of those possible limitations, large flexibility on the parametrization of those various element has been preserved in the following of the work.

Chapter 3

Raindrops' motion and distribution in wake vortices

In still air, the raindrops fall vertically towards the ground and reach a constant terminal falling velocity. When an aircraft takes off or lands in rainy weather, the raindrops will inevitably enter into the aircraft wake vortices. Raindrops' motion in wake vortex is modified by the vortex flow. This modification of the trajectories of the raindrops may induce changes in raindrops' number concentration and velocity distribution in wake vortices, therefore yielding to a change in the recorded radar signal. This chapter is thus devoted to the modeling of raindrops' motion within wake vortex induced air flow.

3.1 Raindrops' trajectories in wake vortices

In this section, the equation of motion of raindrops in wake vortices is established considering several assumptions.

3.1.1 Stokes number

Before deriving the equation of motion, the Stokes number of raindrops in wake vortex flow is preliminarily analyzed. Stokes number is a dimensionless parameter that describes the particle's response to the surrounded fluid. One of the possible definition is:

$$S_t = \frac{t_s}{t_{flow}} \tag{3.1}$$

Table 3.1: The Stokes number of raindrops in wake vortex flow

Diameter	t_s	t_{flow}	S_t
0.5 mm	0.2061	0.7198	0.2863
1.0 mm	0.4079	0.7198	0.5667
2.0 mm	0.6681	0.7198	0.9282
4.0 mm	0.8893	0.7198	1.2355

where t_s is the particle relaxation time and t_{flow} is the characteristic time of the flow [177]. S_t characterizes to which extent the particle follows the streamlines of the flow. If $S_t > 1$, the particle's motion is weakly affected by the flow; if $S_t \sim 1$, the particle's motion is substantially modified by the flow; if $S_t < 1$, the particle's motion approximately follows the flow. Thus, the Stokes number is able to qualitatively describe the particle trajectories [177].

For the raindrops falling in still air, the relaxation time t_s is defined as:

$$t_s = \frac{V_T}{g} \tag{3.2}$$

where V_T is the terminal falling velocity of raindrops. The characteristic time of the wake vortex flow is given by:

$$t_{flow} = \frac{2\pi r_{max}}{V_{max}} \tag{3.3}$$

where V_{max} is the maximum tangential velocity due to each vortex and r_{max} is the radius where the maximum occurs. For instance, for a stable stage wake vortex generated by an A340, the maximum tangential velocity is $V_{max} = 21.50$ m/s, the radius where the maximum occurs is r_{max}= 2.46 m, the initial circulation is $\Gamma_0 = 332.65$ m^2/s, the separation between two vortices is $b_0 = 47.36$ m. Then we obtain $t_{flow} = 0.7198$ s. In Table 3.1, the Stokes number of raindrops in wake vortex flow is computed. It can be found that the Stokes number increases with the raindrops' diameter. As for the raindrops usually encountered during rainfall (0.5 mm - 4 mm), $S_t \sim 1$, the trajectories will significantly differ from the streamlines and also from the free fall in still air. To obtain those trajectories, the computation of the equation of motion applied to the raindrops is thus required.

3.1.2 The equation of motion

For simplification, one-way coupling assumptions is considered for the motion of raindrops in wake vortices, which allows significant reduction in complexity [177].

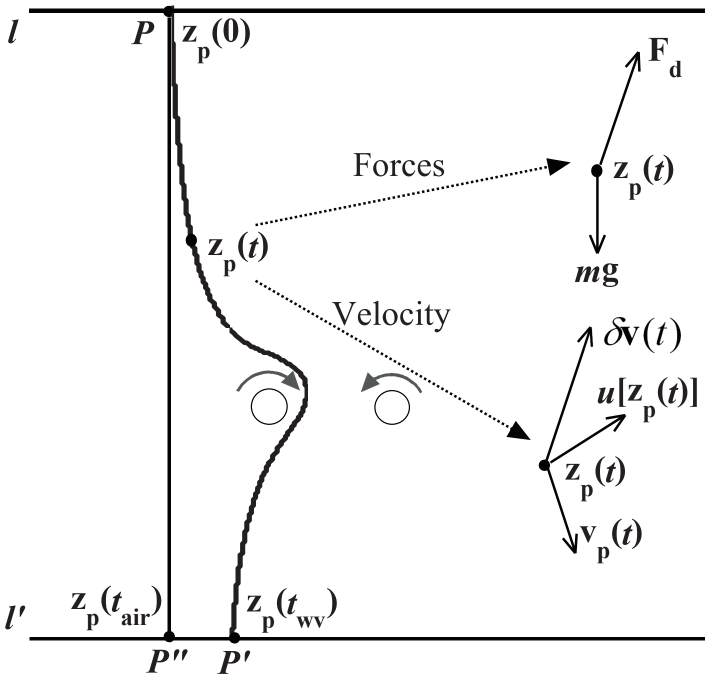

Figure 3.1: Interaction between raindrops and wake vortices

Firstly, it is assumed that the raindrops are spherical and not deformable [178]. Secondly, the interaction between raindrops such as collision or coalescence, as well as the effects of wind and atmospheric turbulence on the raindrops, are not considered. Thirdly, the raindrops could possibly decrease the vorticity and therefore speed up the decay process of the vortex, however, considering that the mass loading of raindrops for non exceptional rain rates is far below one, it can be assumed that this effect is very small and negligible [179]. Fourthly, no significant evaporation or condensation of the raindrops occurs in the vortex flow. For the wake turbulence, the background atmosphere is assumed to be still air and the wake vortex velocity field is stationary. Hence, the problem is simplified as a point particle dynamic problem.

In Figure 3.1, the motion of a raindrop in the wake vortex is illustrated. The vorticity axis of the wake vortex is assumed to be perpendicular to the wake vortex flow between the two boundaries l and l'. The vortex flow is thus assumed to be invariant along the z direction. When a raindrop enters into the wake vortex flow at P, its movement is governed by:

$$\mathbf{a}(t) = \frac{\mathbf{F}_{\mathrm{d}}(t)}{m_{\mathrm{p}}} + \mathbf{g} \tag{3.4}$$

where t is the time, $\mathbf{a}$ is the acceleration of the raindrop, $\mathbf{F}_{\mathrm{d}}$ is the fluid drag force acting on the raindrop, m_{p} is its mass, $\mathbf{g}$ is the downward gravitational acceleration which is taken as negative. For a raindrop moving with velocity $\mathbf{v}_{\mathrm{p}}$ in the fluid whose velocity field is $\mathbf{u}[\mathbf{z}_{\mathrm{p}}(t)]$, if its diameter D is ranging from 0.5 mm to 4 mm, the drag force $\mathbf{F}_{\mathrm{d}}$ can be approximately considered in the Newton regime [180] and given by:

$$\mathbf{F}_{\mathrm{d}}(t) = \frac{1}{2} C_{\mathrm{d}} \rho_a \delta\mathbf{v}^2 \left(\frac{\pi D}{2}\right)^2, \delta\mathbf{v} = \mathbf{u}[\mathbf{z}_{\mathrm{p}}(t)] - \mathbf{v}_{\mathrm{p}}(t) \tag{3.5}$$

where $\mathbf{z}_{\mathrm{p}}(t)$ denotes raindrops' position, $\delta\mathbf{v}$ is the relative velocity between the vortex flow and the raindrop, and C_{d} is the fluid drag coefficient. The impact of air density variations in the vortex flow on C_{d} can be neglected because the raindrops are much denser than air [179]. Thus, C_{d} for a raindrop of diameter D is derived by the equilibrium equation of its weight and the drag force when falling at terminal falling velocity in still air:

$$C_{\mathrm{d}} = \frac{4\rho_w g D}{3\rho_a V_{\mathrm{T}}^2} \tag{3.6}$$

where ρ_{w} is the density of raindrops. Substituting equation (3.5) and (3.6) into equation (3.4), the motion equation of raindrops within wake vortices can be further expressed as:

$$\left\{\begin{array}{rcl} \mathbf{a}(t) & = & \mathbf{g} + \frac{g}{V_{\mathrm{T}}^2}|\delta\mathbf{v}|\delta\mathbf{v} \\ \frac{\mathrm{d}\mathbf{v}_{\mathrm{p}}(t)}{\mathrm{d}t} & = & \mathbf{a}(t) \\ \frac{\mathrm{d}\mathbf{z}_{\mathrm{p}}(t)}{\mathrm{d}t} & = & \mathbf{v}_{\mathrm{p}}(t) \end{array}\right. \tag{3.7}$$

The instantaneous position and velocity of raindrops can be obtained from the above equations. However, its nonlinearity does not enable its analytical computation. Therefore, a 4th order four variables Runge-Kutta algorithm is used to compute the equation of motion.

3.1.3 Numerical solution

In Eq. (3.7), four variables related to the motion of raindrops need to be determined, namely, the position and velocity of the raindrops in a 2D plane orthogonal to the vorticity axis of the flow: $x_{\mathrm{p}}, y_{\mathrm{p}}, v_x$, and v_y. The Runge-Kutta algorithm is widely used for numerically solving non-linear differential equations, with high accuracy and good computational performance. A 4th order four variables Runge-Kutta algorithm has been developped to compute the above motion equation. The corresponding differential equations for these four variables can be written as:

$$\begin{cases} \frac{\mathrm{d}x_\mathrm{p}}{\mathrm{d}t} = f_1(x_\mathrm{p}, y_\mathrm{p}, v_x, v_y) = v_x \\ \frac{\mathrm{d}y_\mathrm{p}}{\mathrm{d}t} = f_2(x_\mathrm{p}, y_\mathrm{p}, v_x, v_y) = v_y \\ \frac{\mathrm{d}v_x}{\mathrm{d}t} = f_3(x_\mathrm{p}, y_\mathrm{p}, v_x, v_y) = \frac{g}{V_\mathrm{T}^2}|\delta\mathbf{v}|[u_x(x_\mathrm{p}, y_\mathrm{p}) - v_x] \\ \frac{\mathrm{d}v_y}{\mathrm{d}t} = f_4(x_\mathrm{p}, y_\mathrm{p}, v_x, v_y) = -g + \frac{g}{V_\mathrm{T}^2}|\delta\mathbf{v}|[u_y(x_\mathrm{p}, y_\mathrm{p}) - v_y] \end{cases} \tag{3.8}$$

where the initial position of the raindrop is thought to be located far away from the vortex core and the initial velocity of the raindrop is set to be its terminal velocity in still air. In the above equations, there are no derivatives on the right hand side, and there are only first derivatives on the left hand side. Therefore, these equations can be summarized in vector form as:

$$\mathbf{X}^{'} = \mathbf{f}(\mathbf{X}) \tag{3.9}$$

where $\mathbf{X} = (x_\mathrm{p}, y_\mathrm{p}, v_x, v_y)$ is the vector of the raindrop parameters and $\mathbf{f} = (f_1, f_2, f_3, f_4)$ is the vector of functions. Considering the time interval of length Δt, the raindrop vector $\mathbf{X}$ could be labeled as $\mathbf{X}_n$ and $\mathbf{X}_{n+1}$ at two continuous time steps t_n and t_{n+1} where $t_{n+1} = t_n + \Delta t$. The 4th order Runge-Kutta algorithm enables to get an estimate of the raindrops' position and velocity $\mathbf{X}_{n+1}$ at t_{n+1} from the raindrops' position and velocity $\mathbf{X}_n$ at t_n, considering the following procedure:

$$\begin{cases} \mathbf{a}_n = \mathbf{f}(\mathbf{X}_n) \\ \mathbf{b}_n = \mathbf{f}(\mathbf{X}_n + \frac{1}{2}\Delta t\mathbf{a}_n) \\ \mathbf{c}_n = \mathbf{f}(\mathbf{X}_n + \frac{1}{2}\Delta t\mathbf{b}_n) \\ \mathbf{d}_n = \mathbf{f}(\mathbf{X}_n + \Delta t\mathbf{c}_n) \end{cases} \tag{3.10}$$

where $\mathbf{a}_n$ is the value at beginning of time interval, $\mathbf{b}_n$ and $\mathbf{c}_n$ are two estimates of values at the mid-point, and $\mathbf{d}_n$ is the estimate of value at the end of time interval. Therefore, $\mathbf{X}_{n+1}$ can be finally computed as the weighted sum of the above estimates of derivatives:

$$\mathbf{X}_{n+1} = \mathbf{X}_n + \frac{1}{6}(\mathbf{a}_n + 2\mathbf{b}_n + 2\mathbf{c}_n + \mathbf{d}_n)\Delta t \tag{3.11}$$

where $\mathbf{X}_0$ is equal to $\mathbf{X} = (x_0, y_0, 0, V_\mathrm{T})$.

3.2 Examples of trajectories of raindrops in wake vortices

3.2.1 Trajectory of raindrops

As illustrated on Figure 3.1, a raindrop falling from point P will have different trajectories in wake vortex and in still air, namely, $PP^{'}$ and PP" respectively. In

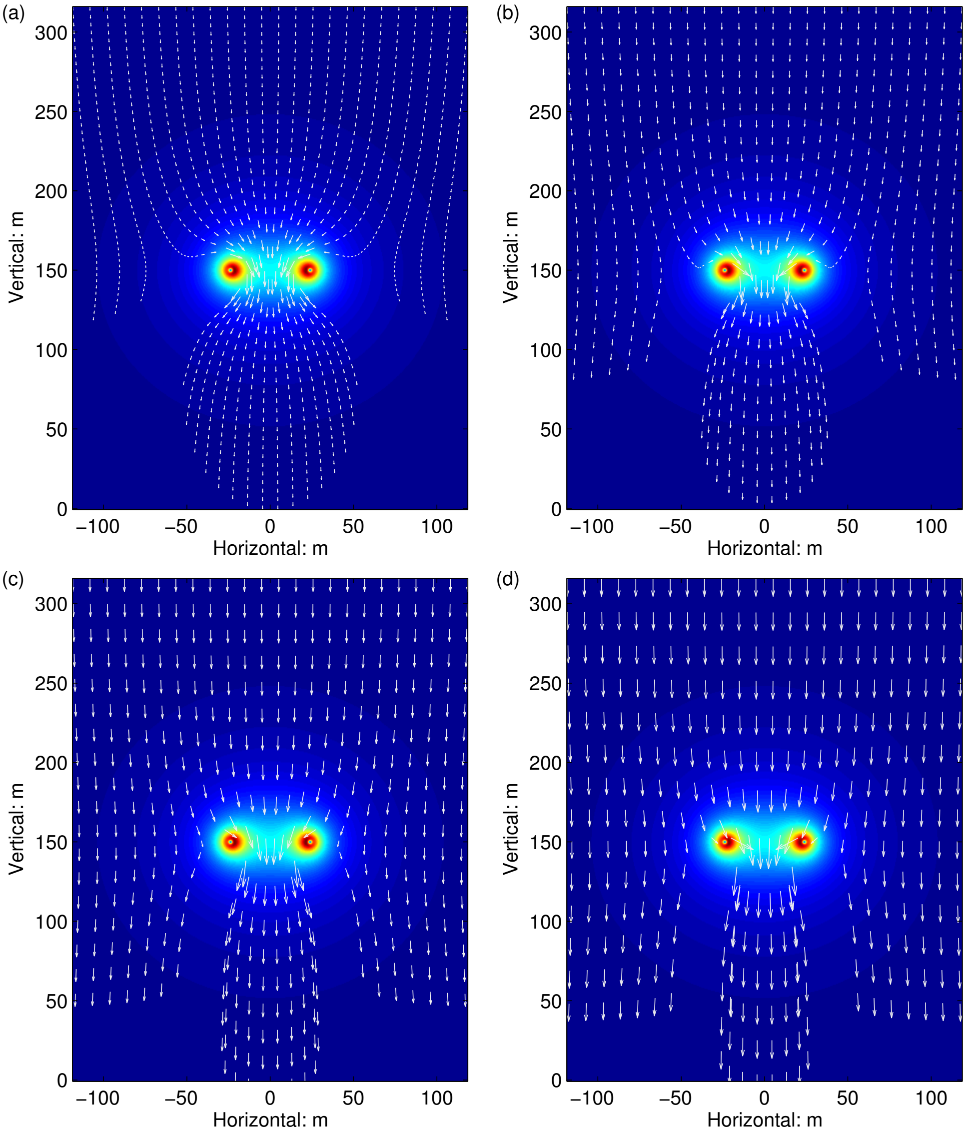

Figure 3.2: The trajectory of raindrops in wake vortices: (a) D = 0.5 mm, Duration: 106.6 s, (b) D = 1.0 mm, Duration: 62.2 s, (c) D = 2.0 mm, Duration: 41.0 s, (d) D = 4.0 mm, Duration: 31.8 s. The color map indicates the wake vortex velocity field of A340.

still air, the raindrop falls along a vertical trajectory to the ground. In presence of wake vortices, the trajectory of a raindrop is depending on its diameter and the location where it enters into the wake vortex flow. In Figure 3.2, the trajectories of four groups of raindrops with different diameters, namely: 0.5 mm, 1 mm, 2 mm, 4 mm are illustrated. The wake vortex pair is 150 meters above the ground. At the initialization of the algorithm, the raindrops are released on a horizontal plane 315.7

meters above the ground with the terminal falling velocity. The background color indicates the velocity of the two dimensional wake vortex flow. The white arrows denote both the position and velocity of the raindrops at each time step. The trajectories of raindrops with smaller diameters seem to be more largely changed by the vortex flow. The fall duration is arbitrarily defined as the total time the fastest moving raindrop takes from the initial position to the ground. The fall duration of the 0.5 mm group of raindrops is longer than the fall duration of other groups of raindrops, as their terminal falling velocity is much lower than the ones of larger drops. In some part of the region under the vortex flow, there are no raindrops falling down. In the region between the two vortex cores, some of raindrops are preferentially concentrated due to the influence of the vortex velocity field, the velocities of the raindrops here are also considerably increased. This trend has been observed whatever the parametrization taken for the wake vortex.

3.2.2 Velocity evolution of raindrops in wake vortices

In still air, the raindrops have an almost constant falling velocity, usually referred as terminal velocity. When a raindrop enters into the wake vortex region, its trajectory is changed, and accordingly, its velocity is also evolving along its trajectory. Here the velocity evolution of a raindrop after entering into the wake vortex region is analyzed.

The vertical section of the wake vortex region is defined as a rectangular region whose size is 400 m × 400 m. As shown in Figure 3.3, the two vortices are located symmetrically in the wake vortex region and at the height of 200 m. In order to facilitate the analysis, four classes of diameters are considered, namely, D = 0.5 mm, 1.0 mm, 2.0 mm and 4.0 mm. For each diameter class, four raindrops are released at the same height of 400 m but different horizontal locations, namely, $x_\mathrm{p}(0)$ =-90 m, -60 m, -30 m and 0 m.

In Figure 3.4 and Figure 3.5, $v_x(t), v_y(t)$, the horizontal and vertical velocities of the raindrops in the vortex flow, are respectively shown as a function of time. The results show that the velocity of the raindrop is disturbed in the vicinity of the vortex flow. In Figure 3.4(a), the raindrop with $x_\mathrm{p}(0)$ = -90 m of initial position takes the longest time to reach the bottom of the wake vortex region.

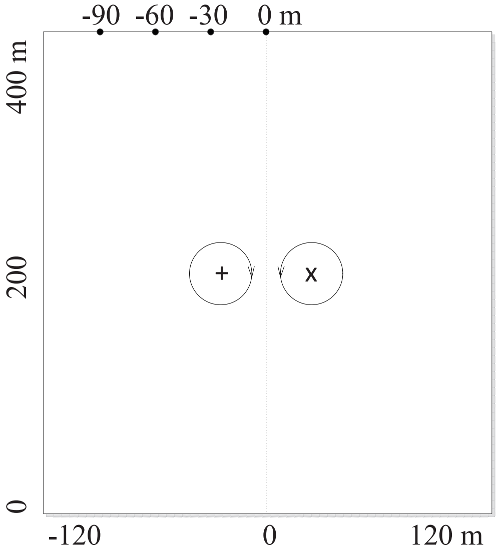

Figure 3.3: Illustration of the wake vortex region and the initial position of the two vortices

3.2.3 Residence time of raindrops within wake vortices

As what has been analyzed in the previous section, the raindrops' velocity is going to be changed when it arrives close to the wake vortices. In order to better understand the behavior of raindrops in wake vortices and distinguish the impact of wake vortex flow on the motion of falling raindrops, we analyze the residence time of raindrops in wake vortices. For each raindrop, three kinds of residence time are computed here with the relationship as in the following expression:

$$T_{\mathrm{a}}(D) = T_{\mathrm{t}}(D) - T_{\mathrm{f}}(D) \tag{3.12}$$

where T_{t} denotes the time the raindrop takes to pass through the wake vortex region, T_{f} denotes the time the raindrop would take to fall in still air without wake vortex, T_{a} denotes the additional residence time of the raindrops in the wake vortex flow. The value of T_{a} directly reflects the impact of the vortex flow on the motion of the raindrops, if T_{a} is positive, the falling velocity of the raindrops is slowed down by the vortex flow, and otherwise, it is speeded up. As illustrated in Figure 3.6, T_{t} and T_{a} are respectively computed as a function of the initial horizontal position for 4 types of diameters: 0.5 mm, 1.0 mm, 2.0 mm, 4.0 mm. The considered region around the wake vortex is defined as $6.3B \times 4B$ rectangle in a two-dimensional plane, where B denotes the wingspan of the aircraft. The wake vortices are located symmetrically

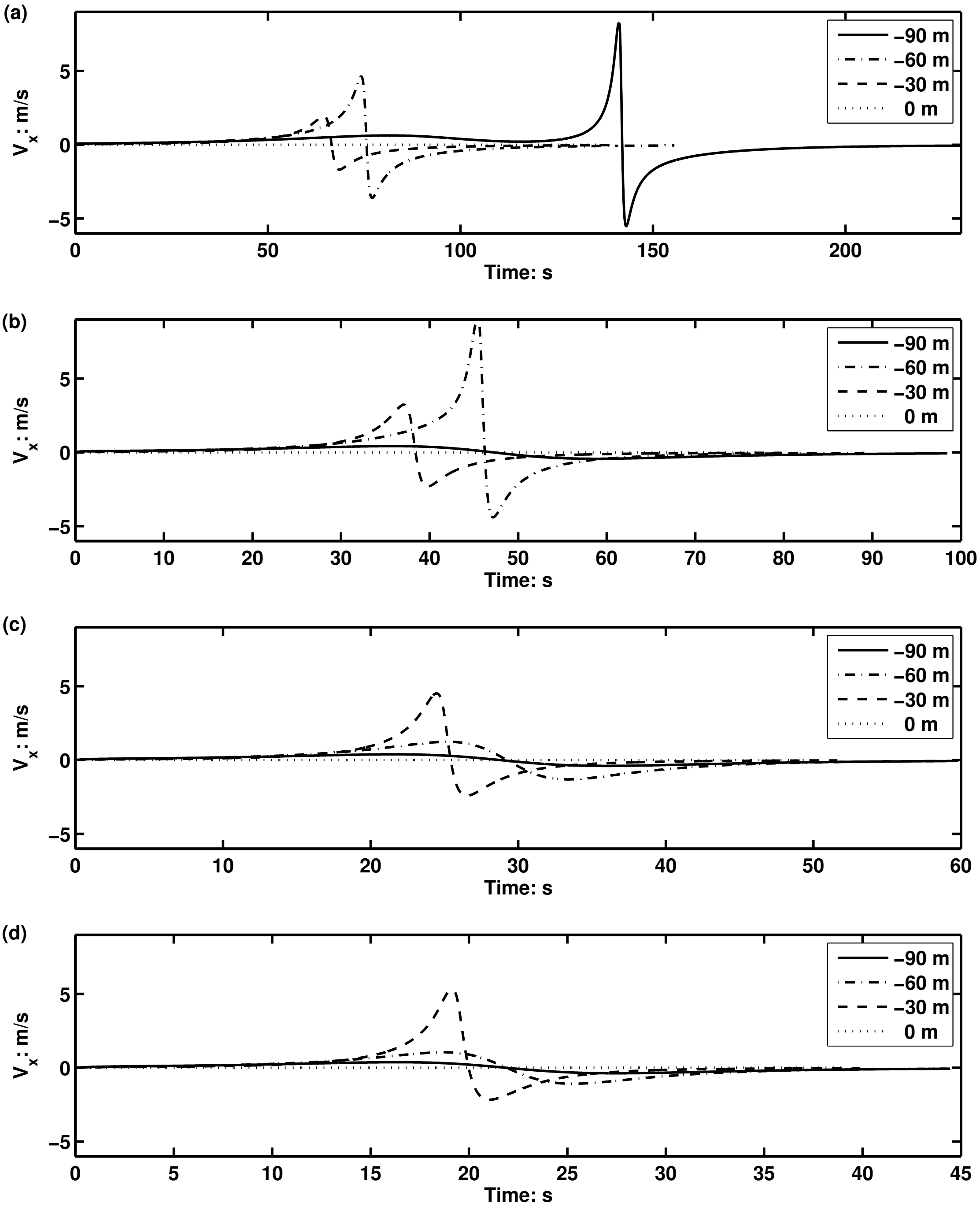

Figure 3.4: Horizontal velocity evolution of raindrops in wake vortices: (a) D = 0.5 mm, (b) D = 1.0 mm, (c) D = 2.0 mm, (d) D = 4.0 mm

in this rectangular region at the height of 200 m. The raindrops are released with the terminal falling velocity at the height of $6.3B = 380.9$ m. The residence time of

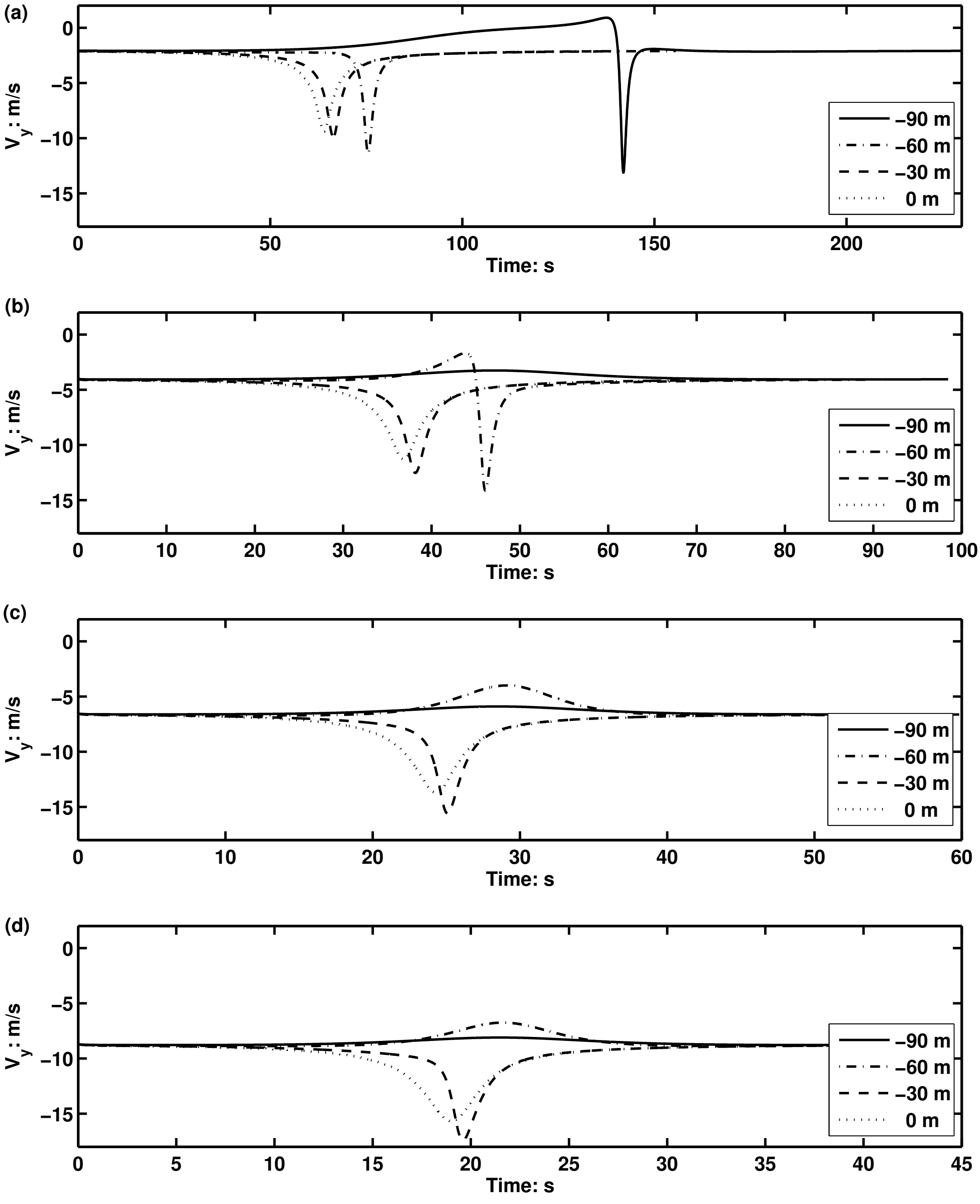

Figure 3.5: Vertical velocity evolution of raindrops in wake vortices: (a) D = 0.5 mm, (b) D = 1.0 mm, (c) D = 2.0 mm, (d) D = 4.0 mm

raindrops within the wake vortex is also computed by solving the equation of motion with the 4th order multiple variable Runge-Kutta algorithm. It is very interesting

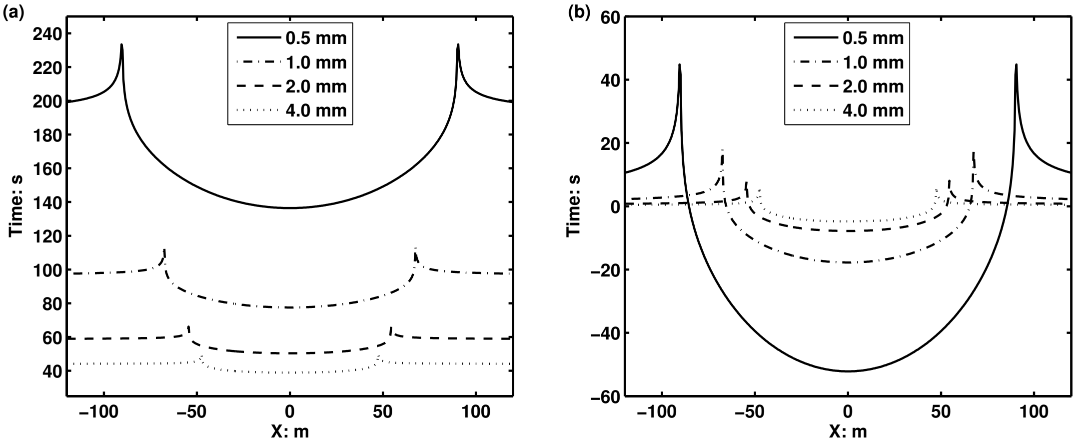

Figure 3.6: Residence time of raindrops within wake vortices: (a) The total time for the raindrops to pass through the wake vortex region, (b)The additional residence time due to the existence of wake vortices

to find that the motion of raindrops with diameter 0.5 mm is more largely impacted by the vortex flow. The additional residence time of raindrops due to the wake vortex flow largely depends on the initial horizontal position and on the diameter. In the region between the two vortex cores, T_a is always negative and the raindrops are speeded up by the vortex flow. If we define this kind of region as the speed up region, then it is easy to conclude that the width of the speed up region decreases with the diameter of the raindrop.

3.2.4 Dependence on wake vortex circulation

Circulation is a very important parameter to characterize wake vortex since it describes the strength of wake vortex in a form that is correlated with effects of potential wake encounters [8, 16]. For raindrops moving in the vortex flow, their motion characteristics, i.e. trajectory and velocity also largely depend on the vortex circulation. It is very difficult to establish a analytical relationship between the vortex circulation and raindrops' motion. Here we analyze the trajectory of raindrops under different circulations.

The wake vortex region is defined as shown in Figure 3.3. For simplicity, only the impacted part of the wake vortex region is shown in Figure 3.7, where four sets of trajectories are illustrated for raindrops of diameters 0.5 mm, 1.0 mm, 2.0 mm and 4.0 mm. Each set of trajectories corresponds to a given circulation value of the wake vortices. For a given circulation, the corresponding trajectory and velocity of raindrops in the wake vortices are unique. Comparing the different trajectories, the following conclusions can be obtained: (1) the smallest raindrops are much more sensitive to the vortex circulation; (2) the motion characteristic of raindrops in wake vortices is representative of the vortex strength.

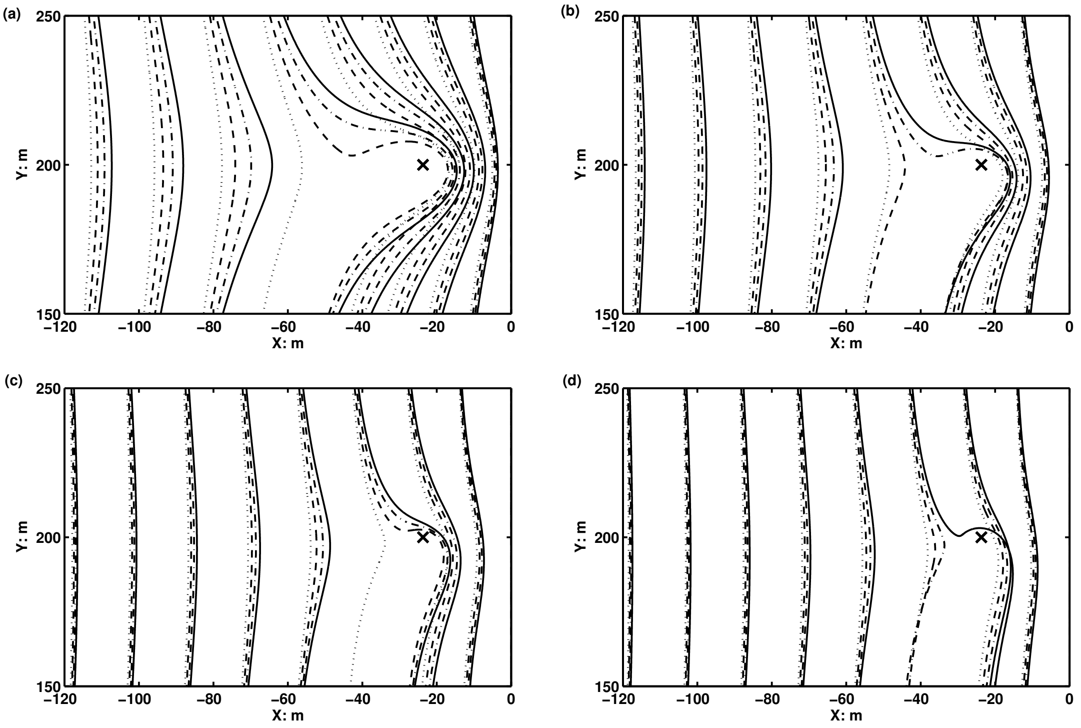

Figure 3.7: Raindrops' trajectories in wake vortices with different circulation: (a) D = 0.5 mm, (b) D = 1.0 mm, (c) D = 2.0 mm, (d) D = 4.0 mm. The solid line '-', the dash-dotted line '-·', the dashed line '–' and the dotted line '...' , correspond to the values of vortex circulation: 490 m^2/s, 430 m^2/s, 360 m^2/s and 300 m^2/s, respectively.

3.3 Raindrops' distribution in wake vortices

The main characteristics of the signal received by a Doppler weather radar will be dependent on the raindrops' distribution in wake vortices. Based on the equation of motion and several assumptions as mentioned in the above section, the motion characteristics of raindrops in wake vortices can be obtained easily. A Doppler radar will be very sensitive to raindrops' motion and possibly enable the detection of wake vortices in rain. To better understand the impact of wake vortices on the raindrops' motion, it is necessary to develop the methodology to quantitatively analyze the raindrops' distribution in wake vortices, including the raindrops' number concentration and velocity distribution.

3.3.1 Raindrops' number concentration

In order to analyze the particle concentration and velocity fields in the fluid flows, there are several widely-used methods reviewed in [181]. The box counting method is adopted here to quantitatively compute raindrops' distribution in wake vortices. For simplification, we still consider the situation where the raindrops are falling into the two dimensional rectangular region of wake vortex in stable phase.

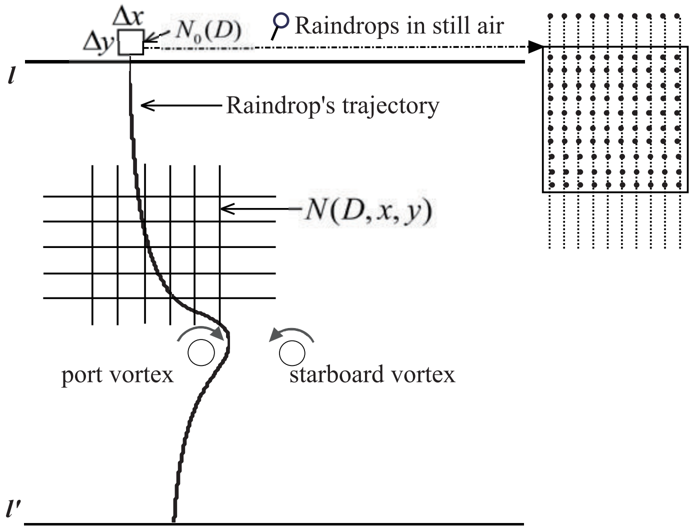

Figure 3.8: Illustration of the box counting method

As shown in Figure 3.8, let the Cartesian coordinates in the 2D plane be x, y and the wake vortex region is located between the two lines l and l'. Before entering into the wake vortex region, the raindrops are falling in still air with the constant terminal falling velocity, and they are named as "initial raindrops". The number density of initial raindrops is assumed to be $N_0(D)$ ($\mathrm{m}^{-3}\mathrm{mm}^{-1}$) where D (mm) is the raindrops' diameter. In the wake vortex region, the raindrops' trajectory and velocity are changed and they are denoted as "disturbed raindrops". The number density of disturbed raindrops is assumed to be $N(D, x, y)$ ($\mathrm{m}^{-3}\mathrm{mm}^{-1}$) where (x, y) are the coordinates in the wake vortex region. Obviously, for a given wake vortex pair, $N(D, x, y)$ is not only depending on the raindrops' diameter, but also depending on the exact location in the wake vortex flow. In order to better illustrate the influence of wake vortices on the raindrops' distribution, the raindrops' relative number concentration at (x, y) is defined as

$$\eta_N(D, x, y) = \frac{N(D, x, y)}{N_0(D)} \tag{3.13}$$

where $\eta_N(D, x, y)$ depicts the change in raindrops' concentration induced by the wake vortex. If $\eta_N > 1$, the concentration of raindrops is enhanced, and otherwise if $\eta_N < 1$, the concentration is reduced.

In order to obtain the quantitative estimation of η_N, the wake vortex region is divided into $n_x \times n_y$ grid boxes with equal size. The size of each grid box in xy plane are Δx and Δy respectively and the size of the grid box along the direction normal to xy plane is set to be 1 meter by default. Above the wake vortex region, there are $n_x \times 1$ grid boxes where the initial raindrops of diameter D are homogeneously distributed, the number of initial raindrops in each grid box is recorded as $Num_0(D)$. At each time step, their positions and velocities are updated by computing the equation of motion. If some of the initial raindrops enter into the wake vortex region, the same number of new initial raindrops is added to the $n_x \times 1$ grid boxes above the wake vortex region. When all the raindrops released at initial time arrive at the bottom of wake vortex region, the number of disturbed raindrops $Num(D, x, y)$ in each grid box in wake vortex region is counted. Thus, $\eta_N(D, x, y)$ can be approximated by the ratio of the number of disturbed raindrops in a grid box centered at (x, y) to the number of initial raindrops in a grid box above the wake vortex region, that is:

$$\eta_N(D, x, y) = \frac{N(D, x, y)}{N_0(D)} \approx \frac{Num(D, x, y)}{Num_0(D)} \tag{3.14}$$

Obviously, the estimation accuracy of $\eta_N(D, x, y)$ depends on the choice of the grid box size: Δx and Δy, and the number of initial raindrops in each grid box above the wake vortex region: $Num_0(D)$.

To conclude, the methodology to approximately obtain raindrops' number concentration in wake vortices by box counting method can be summarized by the following steps:

(1) Input of the wake vortex parameters, compute the wake vortex velocity field model and define the wake vortex region;

(2) Division of the wake vortex region into $n_x \times n_y$ grid boxes with equal size and initialization of the grid size;

(3) Generation of the initial raindrops of each diameter class in the grid boxes above the wake vortex region and initialization of their positions and velocities;

(4) At each time step, computation of the equation of motion of raindrops and making the following judgements: if some of the initial raindrops enter into the wake vortex region, the same number of new raindrops will be generated and initialized, then repeat step (4); for each diameter class, if all the initial raindrops at $t = 0$ have reached the bottom of wake vortex region, then come to step (5);

(5) Counting the number of disturbed raindrops in each grid box;

(6) Estimation of the number concentration of raindrops in wake vortices.

Table 3.2: Parameters for the computation of raindrops' number concentration

Parameters	Values
Aircraft wingspan	60.30 m
Aircraft maximum landing weight	259000 kg
Aircraft landing speed	290 km/h
Grid box size	1m×1 m
$Num_0(D)$	100
Raindrops' diameter	0.5 mm, 1.0 mm, 2.0 mm and 4.0 mm

In Figure 3.9, the raindrops' number concentration in wake vortices is illustrated. The simulation parameters are listed in Table 3.2. It can be noticed that in the wake vortex region, there are two columns where the raindrops' concentration is zero. These two columns appear symmetrically below the two vortex cores and the distance between them in (a) is much wider than the others. Between these two columns, there are two narrow regions where the number concentration of raindrops is enhanced. For the raindrops of 1 mm and 2 mm of diameter, the number concentration value exceeds 8 in some grid boxes.

3.3.2 Raindrops' velocity distribution

Besides the number concentration, the raindrops' velocity distribution in each grid box is of great interest. If the grid box size used for the box counting method is small enough and the number of raindrops in each grid box is large enough, the velocity components of the raindrops in one grid box can be thought to obey Gaussian distributions. The mean value and variance of the velocity of the raindrops

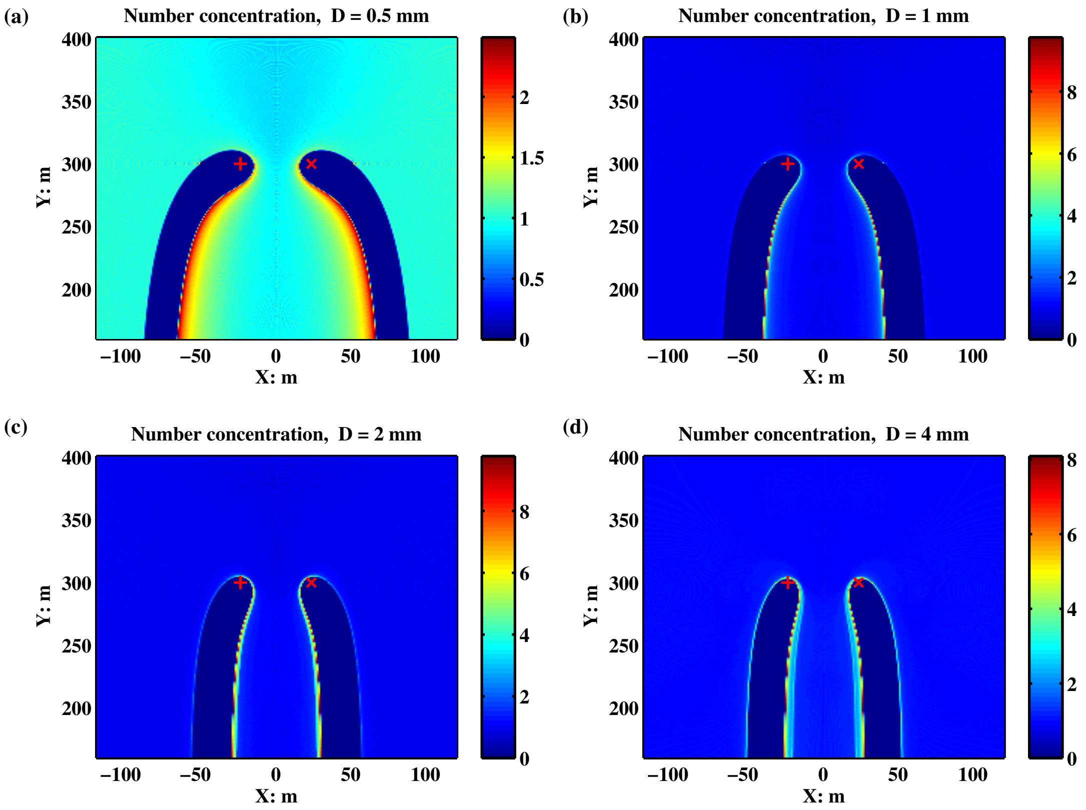

Figure 3.9: Raindrops' number concentration in wake vortices: (a) D = 0.5 mm, (b) D = 1.0 mm, (c) D = 2.0 mm, (d) D = 4.0 mm. The color bar indicates the value of raindrops' number concentration in each grid box.

in each grid box are computed. If the number concentration of the grid box is zero, the raindrops' velocity in this grid box is set to 0.

On Figure 3.10 and 3.11, the raindrops' horizontal and vertical velocity distribution in wake vortices are illustrated respectively. From Figure 3.10, it is interesting to find that the raindrops' horizontal velocity field is similar to the wake vortex velocity field. From Figure 3.11, it is interesting to find that between the two vortex cores, the raindrops' vertical velocity is speeded up. At the same time, the standard deviation of the raindrops' velocity distribution in the grid boxes sufficiently low to consider it as constant within each grid box. In fact, in wake vortex, the raindrops' motion is affected by the vortex flow, the raindrops' velocity field is not the same as the superimposition of the vortex flow velocity and raindrops' terminal velocity, but it is representative of the wake vortex velocity characteristics.

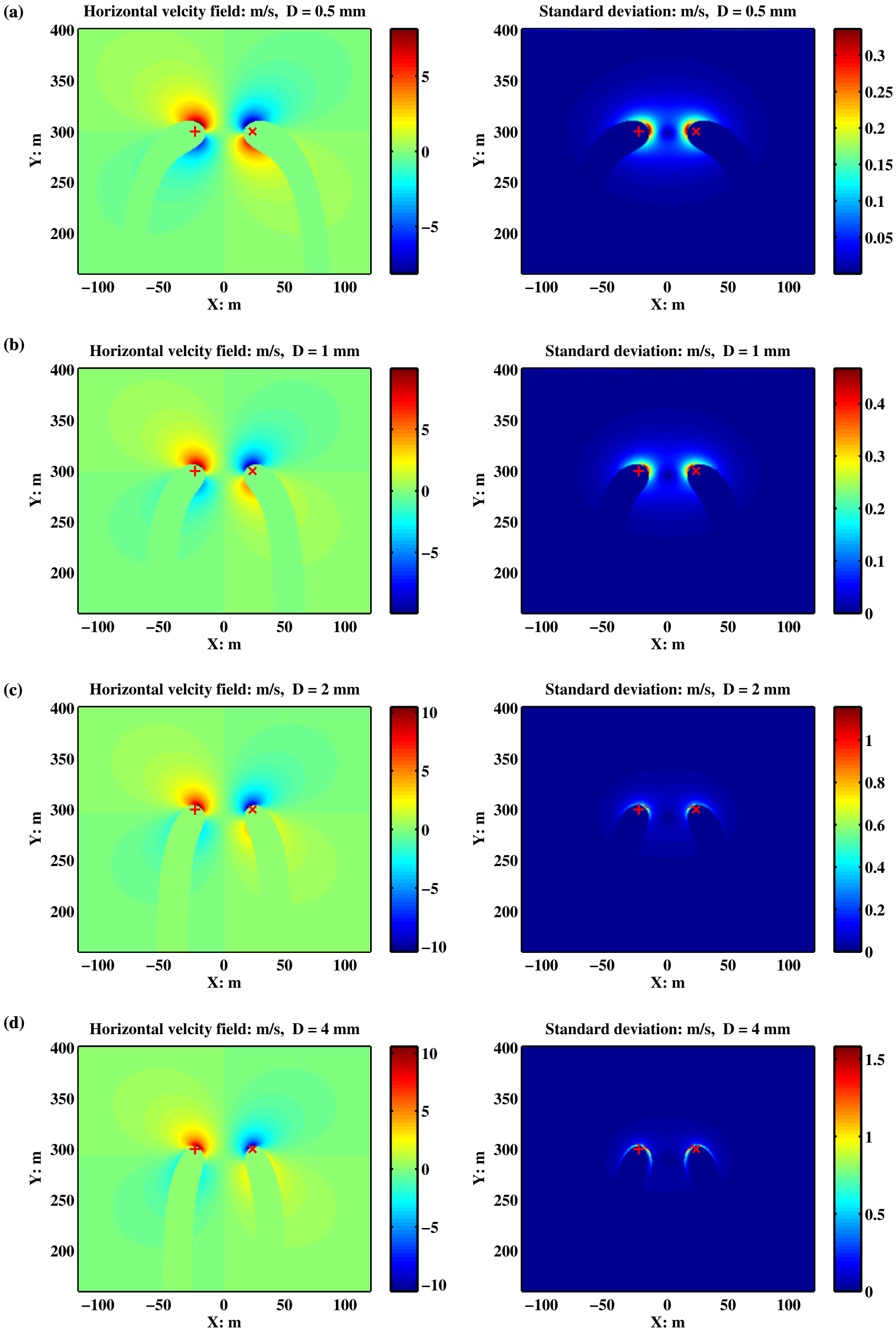

Figure 3.10: Raindrops' horizontal velocity distribution in wake vortices: (a) D = 0.5 mm, (b) D = 1.0 mm, (c) D = 2.0 mm, (d) D = 4.0 mm.

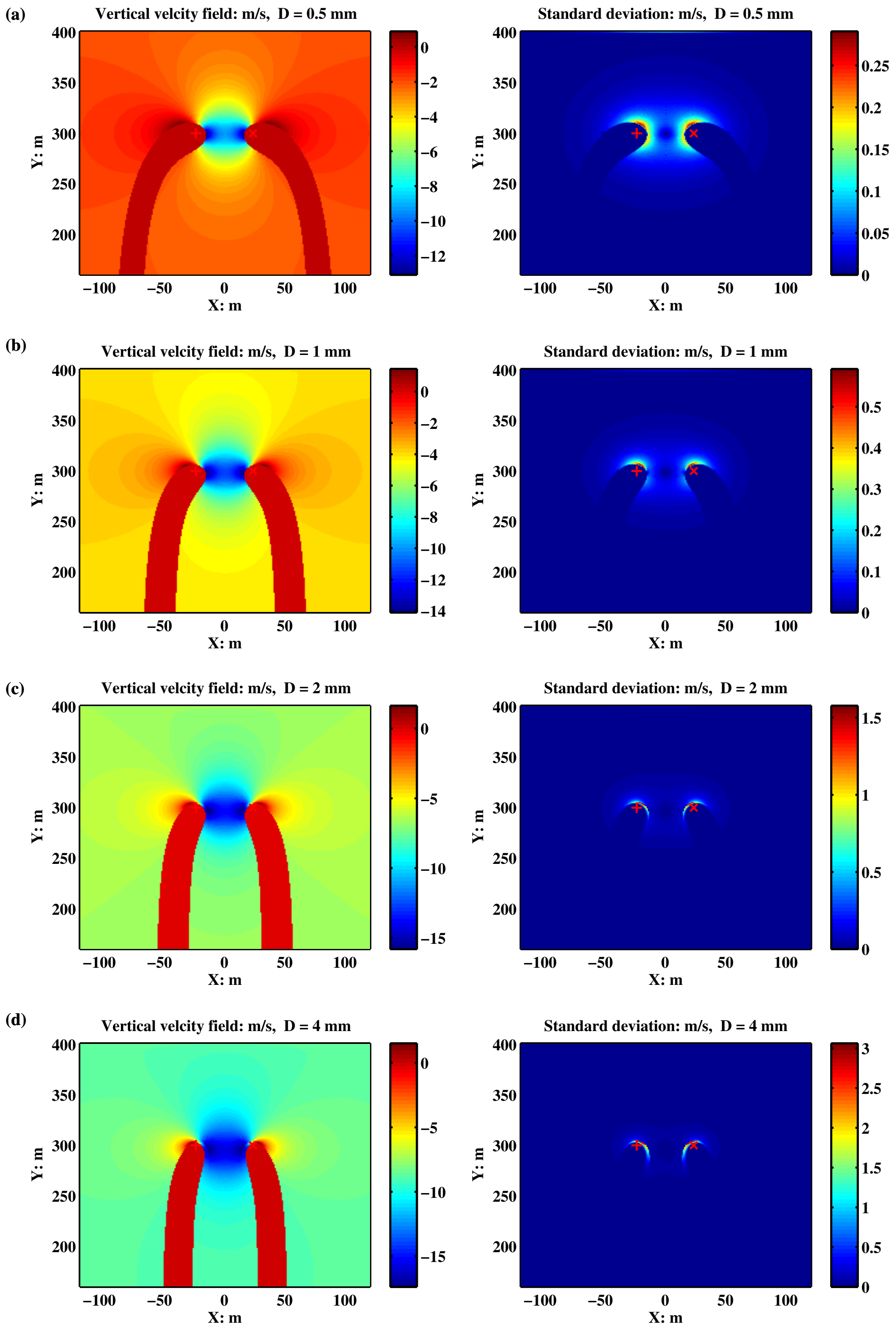

Figure 3.11: Raindrops' vertical velocity distribution in wake vortices: (a) D = 0.5 mm, (b) D = 1.0 mm, (c) D = 2.0 mm, (d) D = 4.0 mm.

3.3.3 Time evolving distribution of raindrops

In the above sections, we concentrated on the motion and distribution of raindrops in steady wake vortices and the descent velocity of the vortex pair has been neglected for the sake of simplicity. With this assumption, the raindrops are released above the wake vortex region and it is very helpful to analyze the influence of wake vortex flow on the raindrops' motion and distribution. However, the descent velocity of wake vortex pair is inevitable. Under the crosswind, the wake vortex pair will be advected by the wind. Here we analyze the time evolving distribution of raindrops in wake vortices by introducing the descent velocity and uniform crosswind.

Impact of descent velocity on raindrops' motion

Due to the mutual induction between the two vortices, the wake vortex pair will descend with a downwash velocity V_d after the generation of two counter-rotating vortices. V_d depends on the initial circulation and vortex pair separation, and it decreases with time as the circulation decays or as the two vortices become further apart [149]. In our analysis, we assume that the vortex pair is descending with a constant downwash velocity.

Considering the parameters of an A340 aircraft, the initial descent velocity of vortex pair is 1.86 m/s. In Figure 3.12, the initial position of the vortex pair is initially at 300 m above ground level, the trajectories of raindrops of 1.0 mm and 2.0 mm of the diameters are illustrated as the vortex pair is descending. The concentration of raindrops is also enhanced between the two vortices and reduced in the two columns below the vortices.

Raindrops' motion under uniform crosswind

Considering a uniform crosswind, the raindrops' velocity is the superimposition of its terminal falling velocity in still air and the crosswind speed. At the same time, the two counter-rotating vortices will move along the direction of the crosswind. When the raindrops enter into the wake vortex region under uniform crosswind, the raindrops' motion is affected by the flow emerged from the wake vortex and crosswind.

In Figure 3.13, the raindrops are released at a height of 400 m and the wake vortex pair is initially located at a height of 300 m. The wake vortex pair is descending at 1.86 m/s. The initial and last positions of the wake vortex pair are indicated

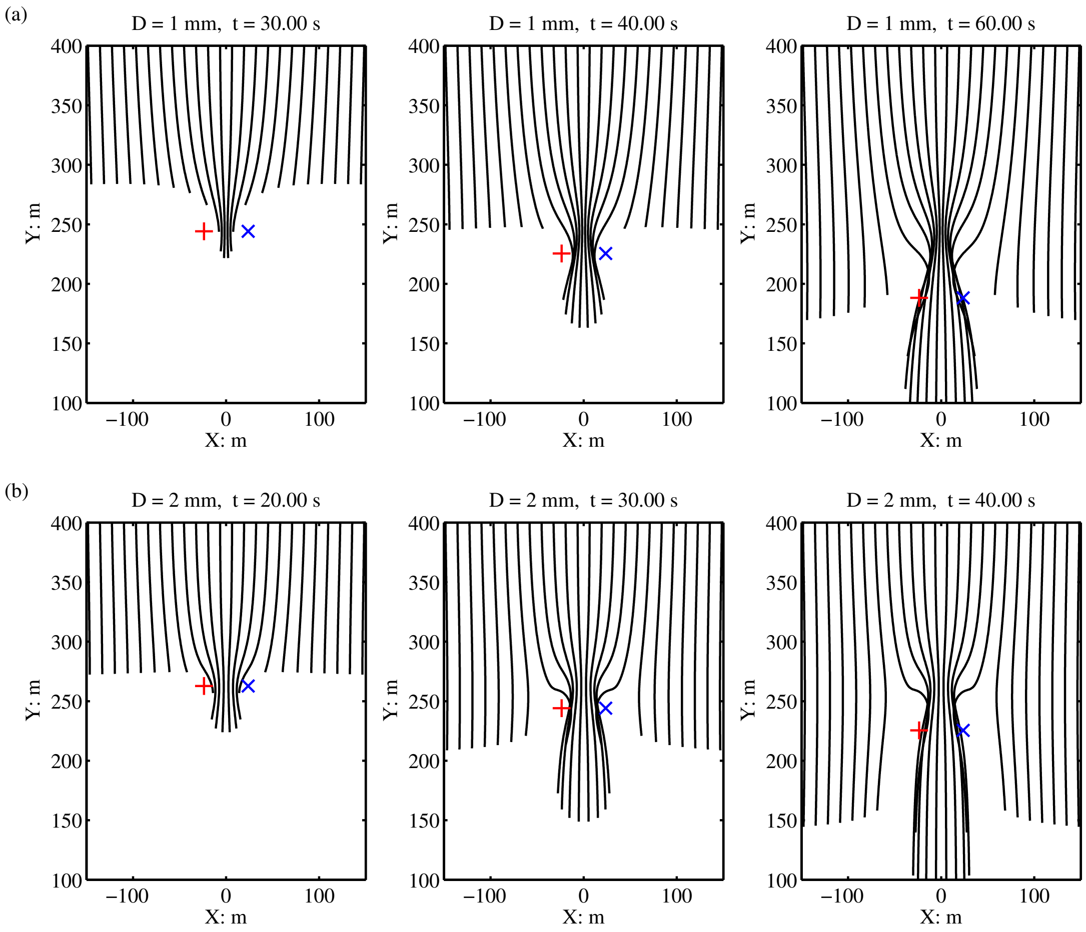

Figure 3.12: Illustration of the trajectory of raindrops in wake vortices taking into account the descent velocity of vortex pair: (a) D = 1.0 mm, (b)D = 2.0 mm

as two pairs of '+' and '×' in each sub figure. For raindrops of 0.5 mm and 1 mm of diameter, the uniform crosswind speed is set to be 1 m/s. For raindrops of 2 mm and 4 mm of diameter, the uniform crosswind speed is set to be 3 m/s. Based on the computation of the equation of motion, the raindrops' trajectory is illustrated. When the raindrops are far away from the vortices, their trajectory is only affected by the crosswind. When they are approaching the vortices, their trajectory is affected by the vortex flow until they are escaping from the wake vortex pair again.

Impact of release position on raindrops' motion

In the previous analysis, the raindrops were released above the wake vortex region at the initialization of the algorithm, that is to say, the raindrops were falling down

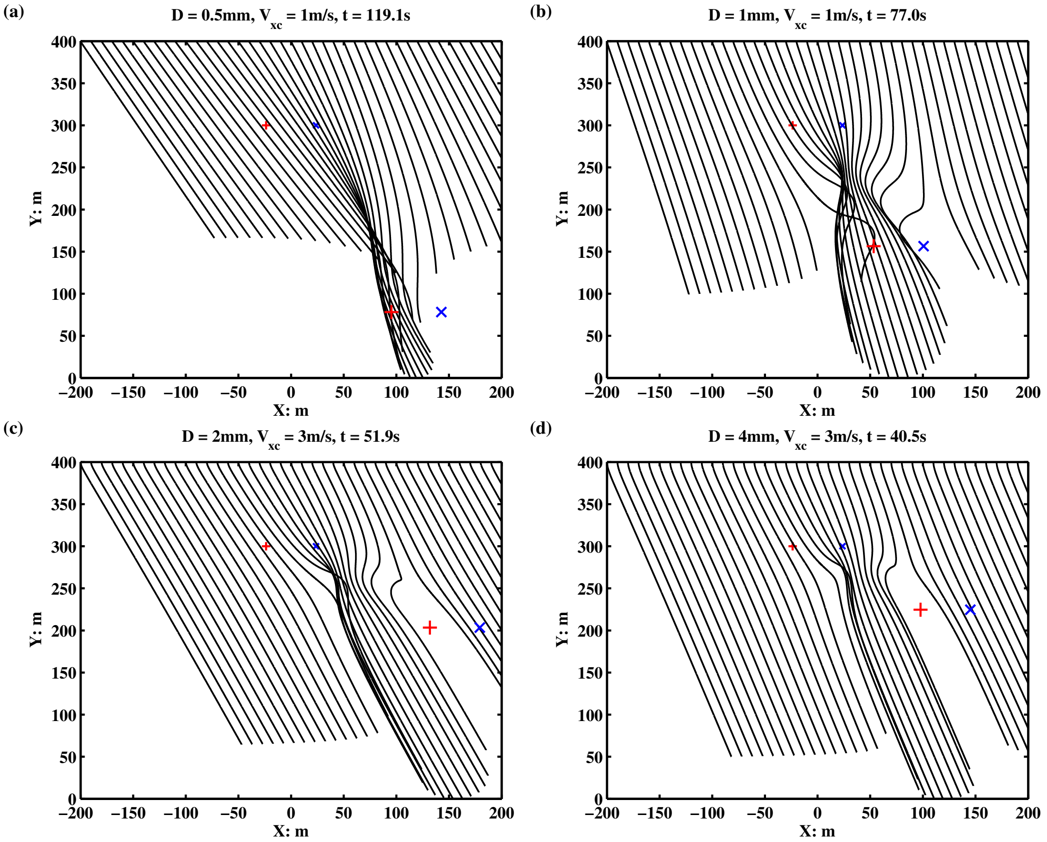

Figure 3.13: Raindrops' trajectory in wake vortices under uniform crosswind: (a) D = 0.5 mm, (b) D = 1.0 mm, (c) D = 2.0 mm, (d) D = 4.0 mm.

into the aircraft wake vortices. However, when wake vortices are generated, there are already some raindrops in the wake vortex region, the initial position of the raindrops need to be reconsidered. The impact of release position on the raindrops' trajectory is thus analyzed.

As shown in Figure 3.14, the wake vortices are initially located at 300 m above the ground and their descent velocity is 1.86 m/s, the raindrops are initially positioned at 350 m, 310 m and 290 m respectively. It is very interesting to find that the trajectories of the 0.5 mm raindrops become much more irregular, if released very close to the vortex core, some of the raindrops will be rolled up for some minutes, but finally they will escape the vortex region.

Simulation and analysis

In order to illustrate the raindrops' time evolving distribution in wake vortices, two groups of raindrops of 0.5 mm and 2 mm of diameter moving in the wake vortex

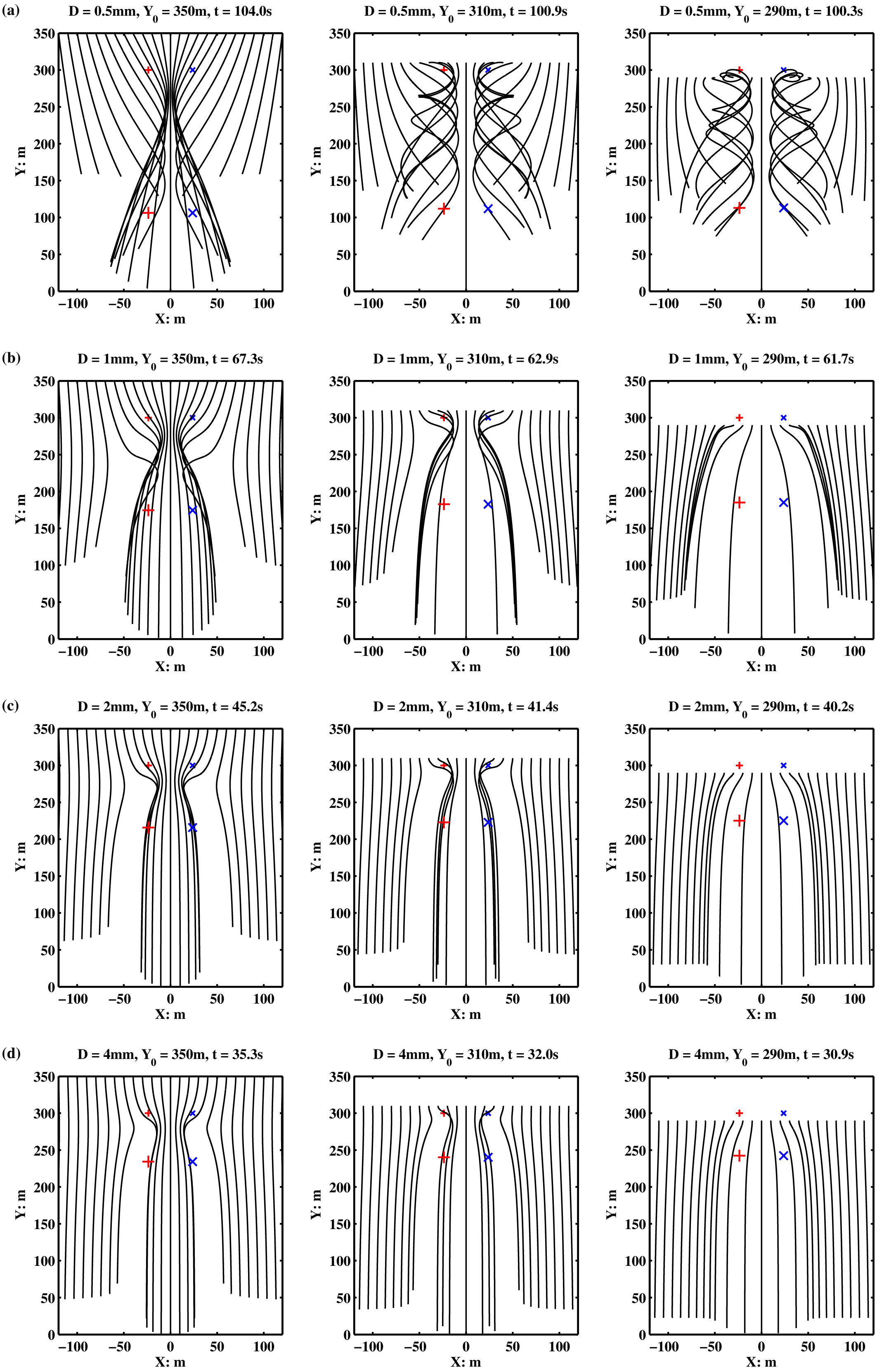

Figure 3.14: Illustration of the trajectory of raindrops in wake vortices released at different initial positions: (a) D = 0.5 mm, (b) D = 1.0 mm, (c) D = 2.0 mm, (d) D = 4.0 mm.

flow are considered. The descent velocity of the vortex pair is also 1.86 m/s and there is no crosswind. At the initialization, the raindrops are uniformly distributed in the wake vortex region as well as above the wake vortex region, falling down at their terminal falling velocity. At each time step, the raindrops' position and velocity are updated by computing the equation of motion. Thus, the number concentration and averaged velocity of raindrops in each grid box can be obtained easily based on the box counting method at each time step.

In Figure 3.15 and Figure 3.16, the relative fluctuations of the number concentrations of raindrops in wake vortices are illustrated for the diameters of 0.5 mm and 2 mm, respectively, at time $t = 1$ s, 5 s, 20 s and 60 s.

For raindrops of 0.5 mm of diameter, there are two holes where the raindrops' number concentration is equal to zero. The size of these two symmetrical holes is increasing with time and they are descending with the vortex pair. In the grid boxes around these two holes, the raindrops' number concentration is enhanced. At time $t = 60$ s, the raindrops' number concentration in some grid boxes even reaches to more than 15 times the still air value. Actually, in these grid boxes where the raindrops' number concentration is extremely high, the interaction between raindrops, such as collisions or coalescence, may not be neglected, but this part of work is beyond our main concern in the current stage. For raindrops of 2.0 mm of diameter, there are also two holes where the raindrops' number concentration is equal to zero. At $t = 20$ s, the shape of these two areas with low raindrops concentration becomes narrower and longer.

In Figure 3.17 and Figure 3.18, the raindrops' horizontal velocity distributions in wake vortices are illustrated for drops of 0.5 mm and 2 mm of diameter, at times $t = 1$ s, 5 s, 20 s and 60 s.

In Figure 3.19 and Figure 3.20, the raindrops' vertical velocity distributions in wake vortices are illustrated for drops of 0.5 mm and 2 mm of diameter at times $t = 1$ s, 5 s, 20 s and 60 s.

3.4 Conclusions

In this chapter, the motion and distribution of raindrops in wake vortices have been analyzed by modeling and simulation.

Firstly, the equation of the motion of raindrops in wake vortices is derived. By using the 4th order four variables Runge-Kutta algorithm, the trajectory of

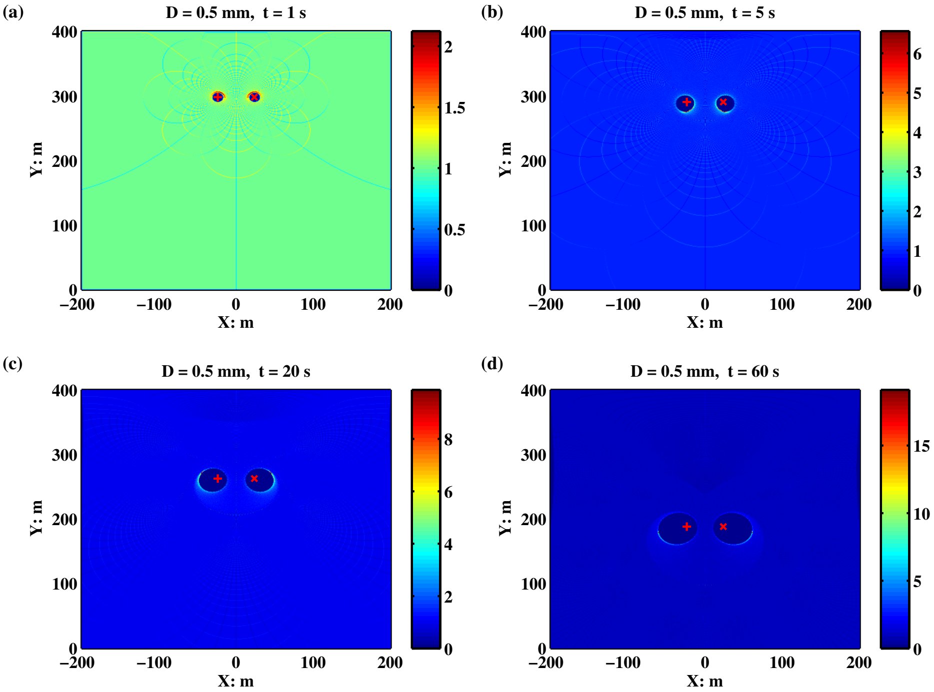

Figure 3.15: Number concentration distribution of raindrops (D = 0.5 mm) at different time steps

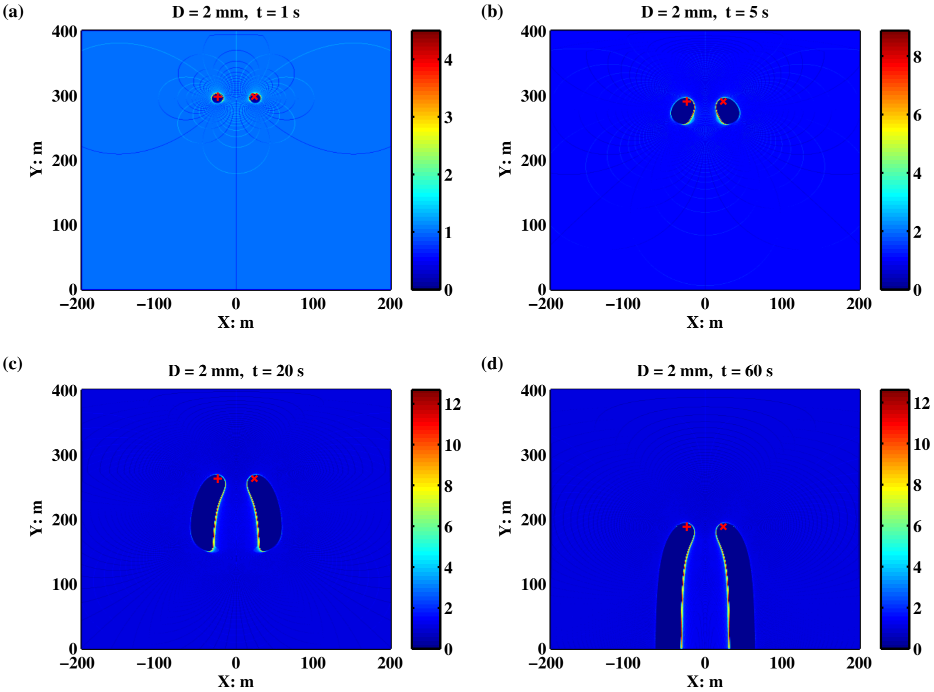

Figure 3.16: Number concentration distribution of raindrops (D = 2.0 mm) at different time steps

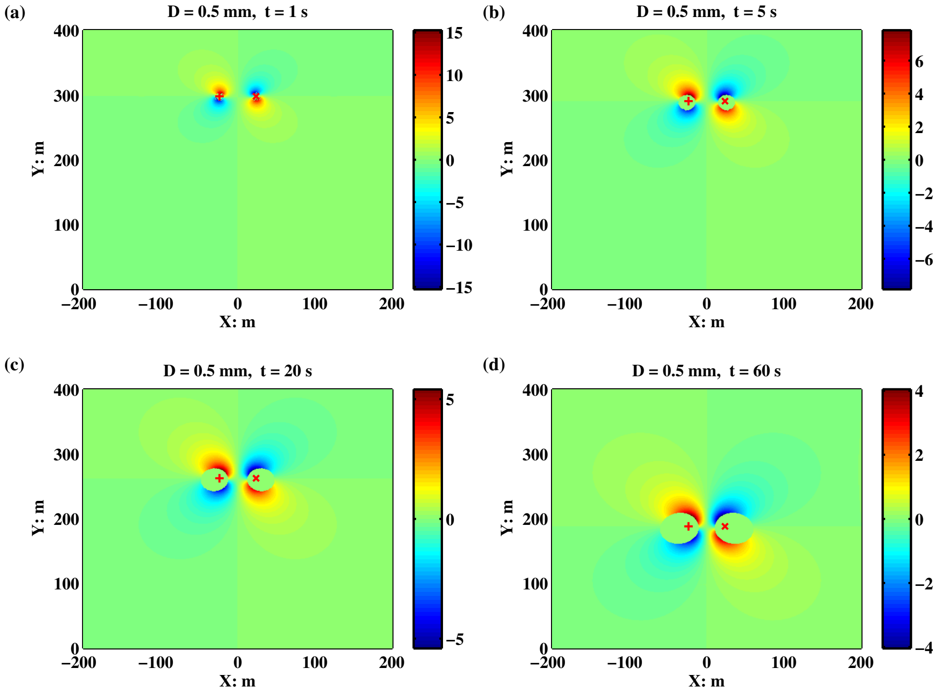

Figure 3.17: Horizontal velocity distribution of raindrops (D = 0.5 mm) at various time steps

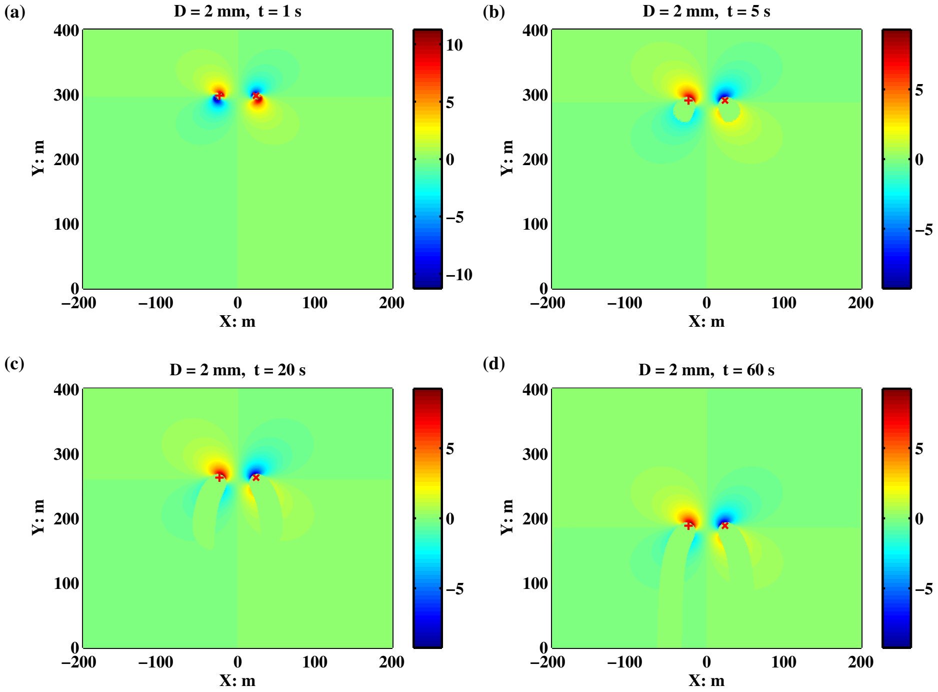

Figure 3.18: Horizontal velocity distribution of raindrops (D = 2.0 mm) at various time steps

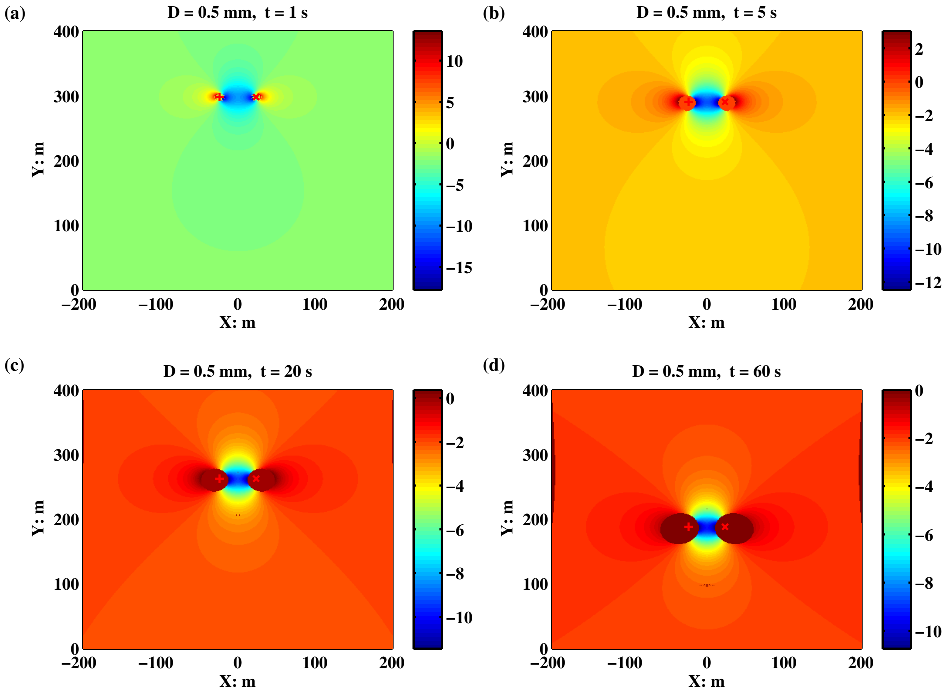

Figure 3.19: Vertical velocity distribution of raindrops (D = 0.5 mm) at various time steps

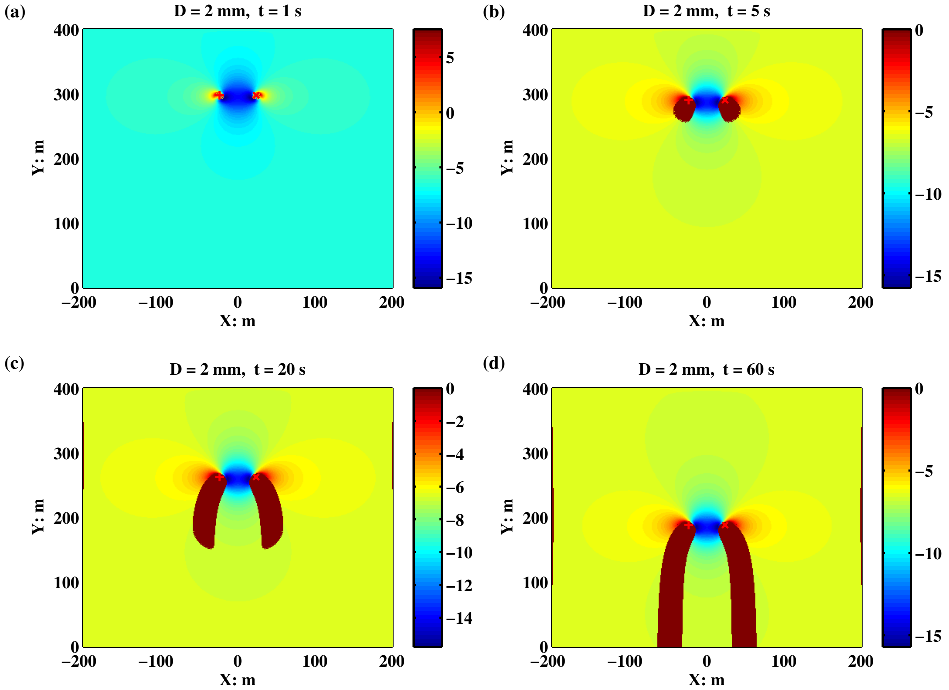

Figure 3.20: Vertical velocity distribution of raindrops (D = 2.0 mm) at various time steps

raindrops can be obtained from the computation of the equation of motion. The Stokes number of raindrops in wake vortex flow can be used to qualitatively explain the different trajectories of raindrops of different sizes in diameter.

Secondly, some simulations of raindrops trajectory have been presented. In the vicinity of the wake vortex flow, the trajectory of the raindrops is changed. For raindrops of a given diameter, the residence time in wake vortices depends on the location where it enters into the wake vortex region. The motion characteristics of raindrops in wake vortices are representative of the wake vortex strength. For the wake vortex of a given circulation, the raindrops' trajectory and velocity depend on its diameter and the location where it enters into the wake vortex flow.

Thirdly, the methodology to compute the raindrops' distribution in wake vortices has been presented. The relative number concentration and velocity distribution of raindrops have been illustrated by simulations. It has been shown that in the wake vortex region, there are two columns where the raindrops' concentration is zero and between these two columns, there are two narrow regions where the number concentration of raindrops is enhanced. The raindrops' velocity field is also shown to be representative of the wake vortex velocity characteristics. Based on the analysis of the impacts of descent velocity, uniform crosswind and initial release position on raindrops' motion, the time evolving distribution of raindrops in wake vortices has also been analyzed.

Chapter 4

Radar signatures of raindrops in wake vortices

Radar has been widely used in meteorology to monitor rain and retrieve parameters such as rainfall intensity or raindrop size distribution. The signal arriving from the scattering volume that contains raindrops can be used to retrieve parametrical information on the raindrops through the interpretation of the Doppler information as already widely used for weather monitoring purposes. In the present case, the heterogenous concentration and velocities of the raindrops perturbed by the vortex flow should induce a distinct signature from the one obtained from volumes with raindrops in still air. This chapter presents two simulation methodologies to compute the radar echo of raindrops in the vicinity of wake vortices. The first simulation methodology allows computing the raw radar signal backscattered by all the raindrops within a given volume at a given position. One of the main drawback of this methodology is that even reducing the simulated number of raindrops with regards to the actual one, the computation time necessary to get the radar signatures is very large. Therefore, a second simulation methodology based on raindrop's distribution in wake vortices is proposed, enabling the computation of idealized radar signatures much more efficiently. Those simulators are then used to produce the simulation examples presented in the second part of this chapter.

4.1 General description of the wake vortex radar simulator

In order to support the radar trials and develop new radar sensors for monitoring wake vortices in rainy weather, a flexible and extensible simulator capable of simulating a wide range of radar systems or design concepts is a great necessity [182,183]. The main objectives of the radar simulator are:

(1) To generate the synthetic environment for radar monitoring wake vortex in rainy weather;

(2) To simulate and evaluate the radar signatures of raindrops in wake vortices under different rain rates;

(3) To research the optimal radar geometry configurations for monitoring wake vortex in rainy weather;

(4) To provide the optimal radar parameters for monitoring wake vortex in rainy weather.

Actually, when raindrops fall into the wake vortex flow, their trajectories and velocities are modified. Therefore the number concentration and velocity distribution of raindrops within wake vortices may be different from the ones in still air. As a consequence it may also have an impact on the radar signatures from different range cells.

The development of a wake vortex radar simulator in rainy weather require the parametrization of three key elements, namely the raindrops, the wake vortex and the radar. The parameters involved for those various elements are listed below:

Raindrops: the parameters include rain rate, drop size distribution, temperature, pressure, terminal falling velocity, radar cross section,

Wake vortex: the parameters include aircraft weight, speed, wing span and vortex velocity model,

Radar: the parameters include carrier frequency, transmitted peak power, antenna gain, beam width, noise figure, system loss, signal waveform and geometry configurations.

Based on the parametrization of the raindrops, wake vortex and radar, the simulator computes the interaction of wake vortices with the raindrops, as well as the interaction of the radar transmitted signal with the raindrops. The radar reflectivity and Doppler velocity spectrum characteristics are of great importance in the radar observation of raindrops in wake vortices. Generally, the radar reflectivity is a measure of the efficiency of a radar target in intercepting and returning electromagnetic energy [184]. In rainy weather, the contribution of radar received power is mainly from the raindrops in the radar resolution volume and the the radar reflectivity of wake

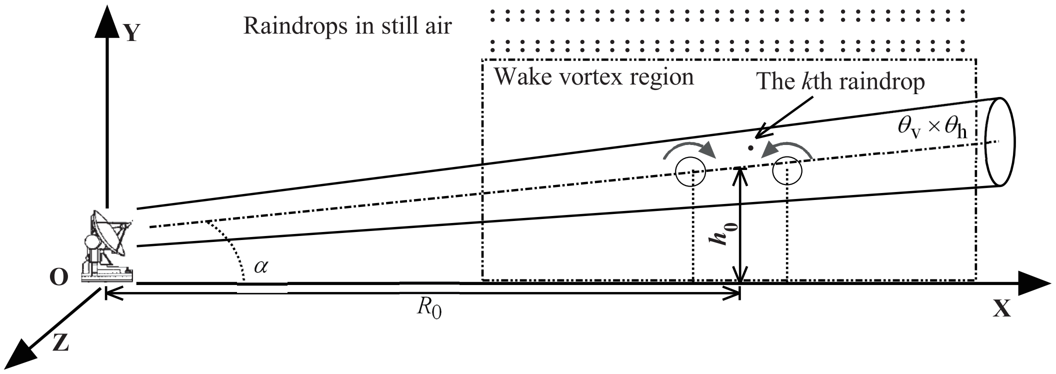

Figure 4.1: Geometry of radar configuration

vortices induced by the refractive index fluctuation is extremely small, referring to the simulations in [141] and radar trials described in [79]. It is easy to conclude that in rainy weather, the radar reflectivity of wake vortices is contributed by the raindrops in wake vortices. The Doppler velocity spectrum is a power-weighted distribution of raindrops radial velocities within the radar resolution volume [173]. In the wake vortex region, the raindrops move towards various directions which are determined by the combination of drag forces and gravity, the Doppler spectrum will be shifted or broadened correspondingly. The Doppler velocity spectrum is thus representative of the wake vortex flow characteristics and very significant to identify the possible wake vortex warnings.

4.2 A time series wake vortex radar simulator: Simulator A

4.2.1 Radar Signal time series

For air traffic management, the detection of wake vortex is of great significance in landing and take off phases [182]. Thus the effort were concentrated on radar monitoring of wake vortices near the airport runways. As shown in Figure 4.1, the XOZ plane denotes the ground and the airport runway is assumed to be perpendicular to the XOY plane, the radar is pointing perpendicularly to the rotation axis of wake vortices, with an elevation angle α_0. The distance between the Radar and the airport runway is $R_\mathbf{0}$, the height of the wake vortex core is h_0. For simplification, the radar reflectivity and velocity of raindrops are assumed to be independent of the location along the Z axis in Figure 4.1, only two dimensional vertical fields of raindrops and wake vortices on the plane XOY are considered. Above the wake vortex region, the raindrops are assumed to be homogeneously distributed. In the area impacted by the vortex flow in stable stage, the position of the raindrops is obtained by numerical computation of the motion equation (3.7). The aim of the simulator is to compute the radar echo backscattered by all the drops in a resolution cell defined by the radar range cell and the beam width of the radar antenna.

A Doppler radar transmits a series of N_p pulses with unitary normalized amplitudes

$$s_0(t) = \exp(j2\pi f_\mathrm{c}t) \sum_{n=0}^{N_\mathrm{p}-1} \mathrm{rect}\left(\frac{t-nT}{\tau}\right) \mu(t-nT) \tag{4.1}$$

where f_c is the carrier frequency of the signal, T is the pulse repetition interval, and τ is the pulse width. rect$(*)$ is a rectangular function equal to 1 for $0 \leq * \leq 1$ and to 0 otherwise, $\mu(t)$ is a pulse modulation function which can be set as linear frequency modulation, or phase coded modulation. Here the simplest situation with $\mu(t) = 1$ is considered. In Figure 4.1, the radar antenna beam points to the direction of (α_0, ϕ_0) where ϕ_0 is equal to 0. The kth raindrop in the considered resolution volume, at time $t = 0$, is assumed to be positioned at P of spherical coordinates (r_k, α_k, ϕ_k) where r_k is the radial distance from the raindrop to the radar, α_k is the elevation angle between OP and the XOZ plane, ϕ_k is the azimuthal angle between OX and the projection of OP on the XOZ plane. The backscattered baseband signal of the kth raindrop from the nth pulse can be expressed as follows:

$$s_k(n) = A_k \exp\left[-j2\pi f_\mathrm{c} \frac{2(r_k + nTv_k)}{c}\right] \tag{4.2}$$

where c is the speed of light, v_k is the radial velocity of the raindrop taken as positive moving towards the radar, A_k is the amplitude of the signal which is derived from the radar equation with the following analytical form:

$$A_k = H\frac{\sqrt{\sigma_k}}{r_k^2} w_\mathrm{a}(\alpha_k, \phi_k) w_\mathrm{r}(r_k), H = \sqrt{\frac{P_\mathrm{t} G^2 \lambda^2}{(4\pi)^3 L}} \tag{4.3}$$

where P_t is the transmitted power, G the antenna gain, λ the wavelength, L the total loss of the radar system, σ_k the radar cross section of the raindrop, and w_a and w_r the angular and radial weighting functions respectively, depending on the location of the raindrop in the radar scattering volume [185–187]. Thus, the composite signal time series reflected from the transmitted pulses can be approximated by the superimposition of the baseband signals backscattered from all the raindrops in the radar scattering volume

$$S_r(n) = \sum_{k=1}^{N_{\mathrm{r}}} s_k(n) + n_s \tag{4.4}$$

where n_s is a centered complex Gaussian white noise of power N_0, N_{r} represents the number of raindrops in the considered resolution volume illuminated by the nth radar pulse. The noise power N_0 at the output of the receiver is given by:

$$N_0 = F_n k_b T_0 B_w G \tag{4.5}$$

where k_b is the Boltzmann's constant and equals to $1.38 \times 10^{-23}\mathrm{J}/^{\circ}\mathrm{K}$, T_0 the receiver temperature(in degrees Kelvin $^{\circ}K$), B_w the receiver bandwidth and F_n the receiver noise figure.

In our analysis, the multiple scattering of raindrops is ignored and the ground clutter competing with the raindrops' signatures is not taken into account as it can be easily removed [188]. Based on the above equation, the radar echo of the considered resolution volume can be computed for each transmitted pulse. It is worth pointing out that the coordinates of each raindrop is changing for different pulses due to their motion in wake vortex flow, the mathematical relationship between its coordinates and its position in two dimensional wake vortex region can be obtained through the computation of the motion equation. At each instant when the radar transmits a pulse, the positions and velocities of the raindrops are updated according to the motion equation.

4.2.2 Simulation procedures

The simulation procedure to obtain the raw radar time series can be summarized through the different steps described below. It has to be noticed that this procedure could be applied considering raindrops in an arbitrary stationary flow encompassing still air, cross wind (cases that correspond to usual weather radar usage), or wake vortices in stable phase. The procedure is the following:

(1) Input of the raindrop's parameters, the minimum and maximum diameters $D_{\min}, D_{\max}$, and diameter interval ΔD, and computation of the drop size distribution model;

(2) Definition of the aircraft type: A320, A340 or A380, and generate the two dimensional wake vortex velocity field;

(3) Input of the radar parameters: X band or W band, definition of the radar-wake vortex geometry configuration and the location of radar cells;

(4) Computation of the equation of motion of raindrops in wake vortices, including replenishment of the volume above the vortex from which the raindrops are assumed to fall from;

(5) Computation of the radar equation for each raindrops in each radar cell and obtention of the radar signal time series;

(6) Analysis of the radar reflectivity and of Doppler velocity spectrum of the raindrops in each radar cell.

Actually, among the above procedures, the step (1)-(3) relate to the definition of simulation environments, step (4)-(6) relate to the computation of radar signatures. In Figure 4.2, a general description of the procedure to compute the radar signal time series of raindrops in wake vortices is summarized. The radar is transmitting successive pulses and receiving the radar signal echo backscattered from the raindrops in the different radar cells. At each radar pulse, the raindrop's position and velocity are updated by computing the equation of motion, and the backscattered radar echo from the raindrops in each radar cell is recorded by superimposing the radar signal reflected from each independent raindrop. This simulation is capable of generating the in-phase and in-quadrature component of the radar echo associated with the raindrops falling in still air and moving within the wake vortex flow, but it requires large computation capacity due to the extremely large number of drops to be simulated. In order to illustrate the functionalities of Simulator $\mathbb{A}$, two typical radar systems already used for experimental measurement of wake vortices will be simulated and analyzed: X band radar in Section 4.4 and W band radar in Section 4.5.

4.3 Raindrop's distribution based radar simulator: Simulator $\mathbb{B}$

In this section, another simulation scheme based on the raindrops' statistical distribution is proposed for evaluating the radar signatures of wake vortices in rainy weather.

As show in Figure 4.3, critical area for wake vortex encounter near the airport is always very large due to the large extension of wake vortices and their long lifetime [189].

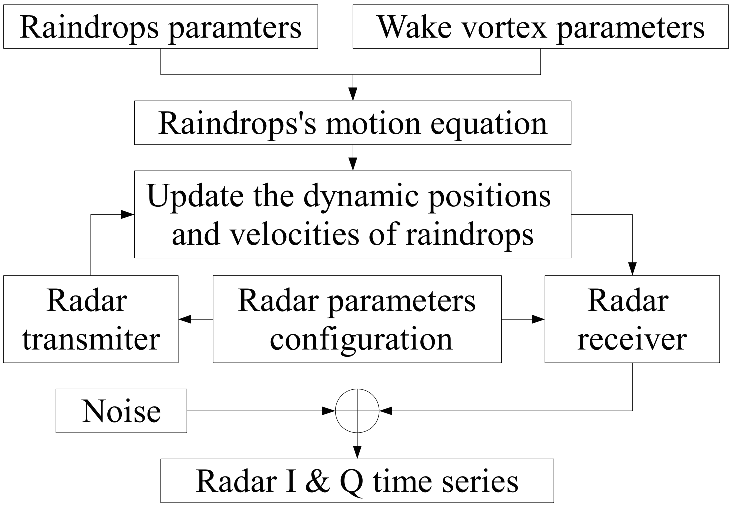

Figure 4.2: Procedures to generate radar signal time series

The time series radar simulator enables the simulation of radar signatures in limited volumes, however, for practical application and exploitation it could be required to get a simulation of the signature in larger domains. With the time series radar simulator, it demands too large computation memory and long computation time as the population of raindrops in the radar scattering volume increases. In order to better evaluate the radar signatures in large domain, it is necessary to develop a more efficient simulation scheme, which will enable a faster computation of radar signatures of raindrops, keeping the same level of flexibility on the parametrization.

4.3.1 Methodology to compute the radar signatures

As shown in Figure 4.4, considering the radar cell in a two dimensional vertical plane, the radar signature of raindrops can be obtained by integrating the contributions from the raindrops of each diameter class in each grid covered by the k^{th} radar cell.

In still air, the raindrop's distribution is homogeneous, so the radar reflectivity of raindrops in the radar cell can be derived as:

$$\eta_k = \sum_{D=D_{\min}}^{D_{\max}} \sigma(D) N(D) \Delta D \tag{4.6}$$

where $\sigma(D)$ is the RCS of raindrops of diameter D, $N(D)$ is the raindrop's number distribution given by Equation 2.13; ΔD is the diameter interval, $D_{\min}$ and $D_{\max}$ are the minimum and maximum values of raindrop's diameter.

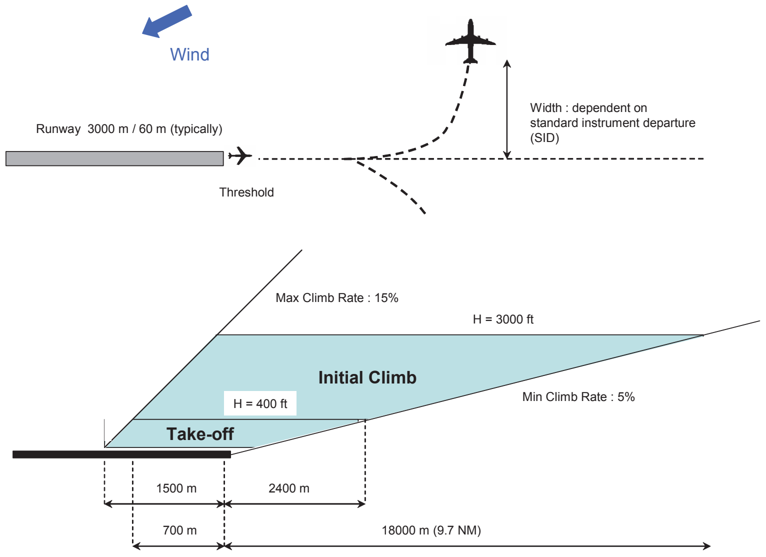

(a) Critical Areas for Take-Off and Initial Climb

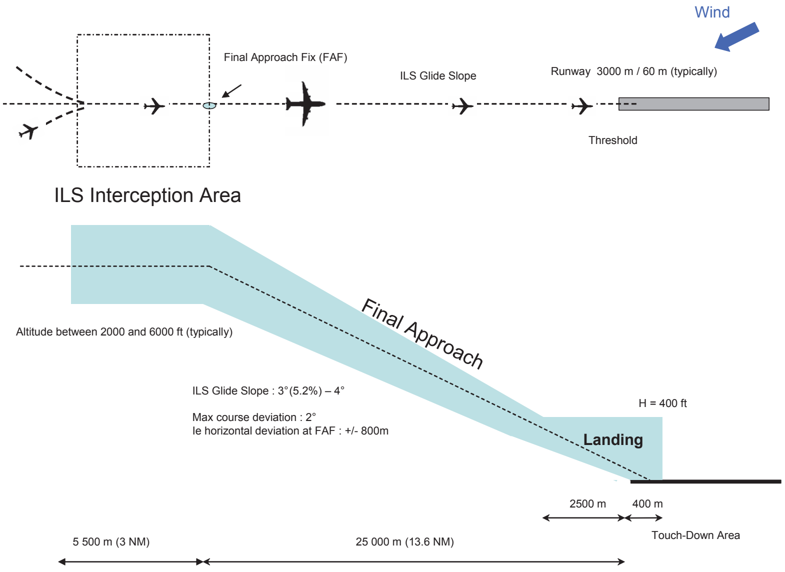

(b) Critical Areas for ILS Interception, Final Approach and Landing

Figure 4.3: Illustration of flight critical areas near the airport [189]

In wake vortices, the raindrop's distribution is inhomogeneous and quite different from the one in the still air. The raindrop's concentration in wake vortices depends on several other critical parameters characterizing the wake vortex, such as vortex circulation, vortex core separation and vortex evolution time after generation. For raindrops of a given diameter, the methodology to compute its relative number concentration and velocity distribution at each grid cell in wake vortex region

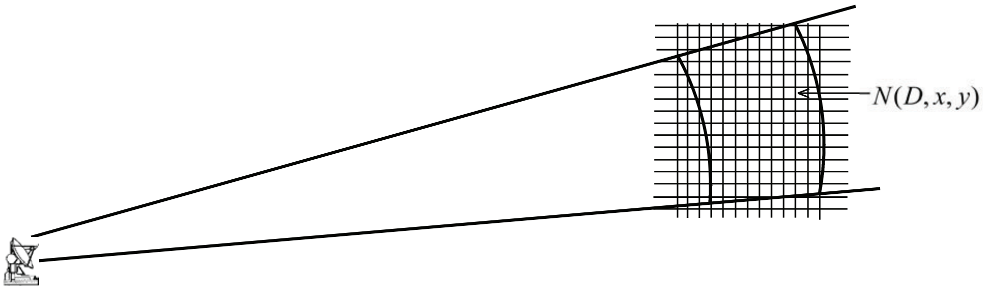

Figure 4.4: The radar geometry for the radar simulator $\mathbb{B}$

can be obtained by numerical simulation as described in Section 3.3. The simulated data can be stored as a database for off-line look-up, considering some typical parametrization of wake vortices. Thus, the radar reflectivity of raindrops in the kth radar cell is given by

$$\eta_k = \frac{1}{V_k} \sum_{D=D_{\min}}^{D_{\max}} \sigma(D) N(D) \Delta D \int_{i,j} \eta_N(D,i,j) \tag{4.7}$$

where i, j are indices of the grid boxes which are located in the kth radar cell Ω_k, V_k is the volume of the kth radar cell, $\eta_N(D,i,j)$ is the relative number concentration of raindrops of diameter between $D - \Delta D/2$ and $D + \Delta D/2$ in the (i,j) grid box, the radar range weighting function and the antenna pattern function are assumed to be unit.

The radar Doppler velocity spectrum is representative of the radial velocity distribution of raindrops in the radar cell. For a given elevation angle α of the radar antenna, the radial velocity of the raindrops in each grid box is derived by:

$$V_d(D,i,j) = V_x(D,i,j)\sin\alpha + V_y(D,i,j)\cos(\pi - \alpha) \tag{4.8}$$

where $V_x(D,i,j)$ and $V_y(D,i,j)$ are the horizontal and vertical velocity distribution of raindrops of diameter between $D - \Delta D/2$ and $D + \Delta D/2$ in the (i,j) grid box. Considering the radar wavelength λ and pulse repetition time T, the maximum positive unambiguous velocity is given by

$$v_a = \lambda / 4T \tag{4.9}$$

The Doppler velocity resolution is given by

$$\Delta v = 2v_a / N_{\mathrm{p}} \tag{4.10}$$

where N_p is the number of Doppler velocity bins. Thus, the discrete Doppler velocity bins are noted as

$$v_n = -v_a + n\Delta v, \tag{4.11}$$

where $n = 1,\ 2,\ \ldots\ ,\ N_\mathrm{p}$. At the nth velocity bin v_n, the magnitude of Doppler velocity spectrum $S(r_k, v_n)$ is the sum of returned power from all the raindrops in the kth radar cell with the same radial velocity. Based on the computation of radar equation for the raindrops of each diameter class at each grid, it can be derived as

$$S(r_k, v_n) = \frac{P_\mathrm{t} G^2 \lambda^2 N_\mathrm{p}^2}{(4\pi)^3 r_k^4 L} \sum_{D=D_\mathrm{min}}^{D_\mathrm{max}} \sigma(D) N(D) \Delta D \int_{i,j} \eta_N(D, i, j) \tag{4.12}$$

where i, j are the indices of the grid boxes where the raindrop's radial velocity $V_d(D, i, j)$ is strictly varied from $v_n - \Delta v/2$ to $v_n + \Delta v/2$, P_t is the radar transmitted peak power, G is the antenna gain, λ is the wavelength, r_k is the range of the kth radar cell, L is the total loss of the radar system.

4.3.2 Simulation procedure

The simulator is based on the raindrop's statistical distribution in wake vortices. Figure 4.5 shows an overview of the operation of this simulator. Generally speaking, there are three key function blocks in the simulator related to the computation of the raindrop's relative number concentration and velocity distribution in wake vortices, the computation of raindrops' RCS and the DSD (rain rate) model in still air and the integration of the contribution of radar average received power and Doppler signatures from the raindrops of each diameter class in each grid box of the radar cell. The methodologies of the first and second function blocks have been presented in Section 3.3 and Section 2.2 respectively. The methodology of the third function block has been presented in the previous subsection. The simulation procedure can be summarized through the following steps:

(1) Input of the raindrop's parameters, the minimum and maximum diameters $D_\mathrm{min}, D_\mathrm{max}$, and diameter interval ΔD;

(2) Definition of the aircraft type: A320, A340 or A380, and generation the two dimensional wake vortex velocity field;

(3) Input of the radar parameters: X band or W band, definition of the radar-wake vortex geometry configuration and the location of radar cells;

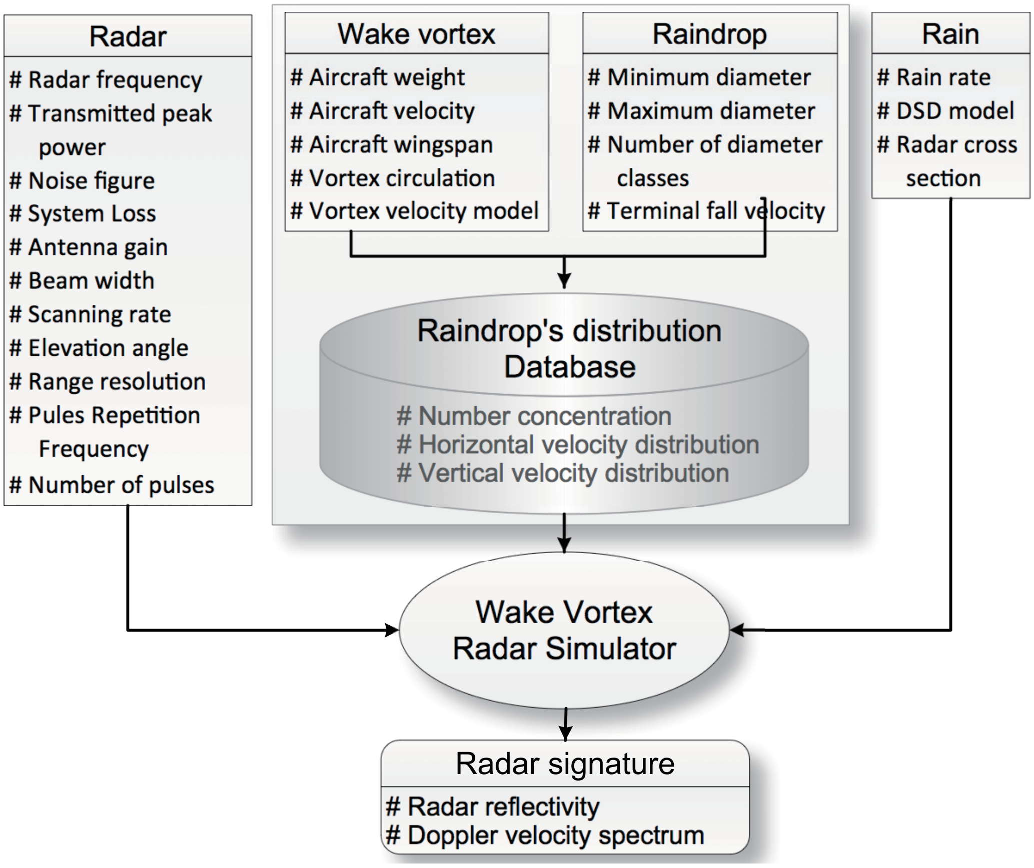

Figure 4.5: Overview of operation of the radar simulator based on raindrop's distribution in wake vortices

(4) Division of the wake vortex region into $n_x \times n_y$ grid boxes with equal size and computation of the raindrop's number concentration $\eta_N(D,i,j)$ and velocity distribution for each diameter class in each grid box $V_x(D,i,j)$ and $V_y(D,i,j)$; the computation results can be stored in the database and be used for different DSD models or rain rates;

(5) For the raindrops of diameter between $D-\Delta D/2$ and $D+\Delta D/2$, computation of the raindrop's radar cross section (RCS) $\sigma(D)$ and of the number of raindrops of diameters per unit volume in still air $\Delta DN(D)$ at a given rain rate R;

(6) For a given radar cell of the volume V_c, calculation of the radar reflectivity and Doppler spectrum by integrating the contribution of radar average received power and Doppler signatures from each diameter class of raindrops. The noise powers at each Doppler velocity bin are added according to the input radar parameters.

Compared with the radar time series simulator, the simulator based on raindrop's distribution in wake vortices has several advantages. Firstly, the database of the raindrop's distribution is independent of the rain rate and DSD model, the radar signatures of raindrops in wake vortices under different rain rates or DSD models can be simulated very easily and efficiently. Secondly, the computation load is much lower compared to the simulation based on the generation a large population of raindrops in the radar resolution volume. Thirdly, the in-phase(I) and quadrature(Q) components of the radar signal time series can also be obtained by taking an inverse discrete Fourier transform of the spectrum and noise model as described in [190] and [173].

4.4 X band radar signatures

X-band radar is an interesting sensor for monitoring wake vortices. Radar waves at X band are not severely attenuated in rainy weather due to the short detection range of wake vortices. In this section, a typical X band radar is assumed to be used for monitoring aircraft wake vortices in rainy weather. Some of the parameters can be found in Table 4.1, referring to the X band radar parameters used for the experiment monitoring wake vortices described in [19].

Table 4.1: Input parameters for the X band radar simulation

Parameters	Values
Radar frequency	10 GHz
Transmitted peak power	20 W
Noise figure	2 dB
System Loss	3 dB
Antenna gain	30 dB
Beam width	2.8° × 4°
Distance to the wake vortex	500 m
Pules Repetition Frequency	3348 Hz
Number of pulses	256

From the model of interactions between raindrops and wake vortices, considering a given radar configuration, the radar signatures of raindrops within wake vortices are here illustrated by numerical simulation. The main objectives of the simulation are to estimate the Doppler velocity spectrum of raindrops within wake vortex and to evaluate the radar detectability of wake vortex in rainy weather. The simulation results are expected to develop knowledge on wake vortex radar sensors.

4.4.1 Raindrops in still air

Before analyzing the radar signature of raindrops in wake vortices, the radar signal time series and Doppler spectrum of raindrops in still air are simulated by using the simulator $\mathbb{A}$. It corresponds to the configuration of an usual weather radar. At first, the initial raindrops in one radar cell are generated according to the DSD model in Equation (2.13). The radar cell is located 1000 m away from the radar with a range resolution of 40 m. The other radar parameters are the ones presented in Table 4.1. The relative position and distribution of raindrops of 0.5 mm, 1.0 mm, 2.0 mm and 4.0 mm diameter under different rain rates are illustrated in Figure 4.6, where in (a), the radar is pointing to the raindrops with a small elevation angle $\alpha = 5°$ and in (b) the radar is almost vertically pointed with an elevation angle of $\alpha = 80°$.

The real and imaginary parts of the complex radar echo (I and Q, respectively) caused by the raindrops in one radar cell are illustrated in Figure 4.7. By using the Doppler spectrum estimation method based on FFT, the radar Doppler signature of raindrops is presented in Figure 4.8. It is easy to find that in (b), the Doppler spectrum width is much wider than the one in (a). The Doppler spectrum width of raindrops in still air is largely depending on the elevation angle of the radar antenna.

4.4.2 Simulations in staring mode

During the taking off or landing phases of the aircraft, the wake vortex above the runway is the most dangerous for the following aircraft. In staring mode, the radar is deployed on one side of the runway and the radar antenna is pointing to the aircraft flight path with a low elevation angle.

The first step in the simulation is to initialize the position of the raindrops in wake vortices. The rain rate is assumed to be 5 mm/h and the wake vortex is assumed to be a stable stage wake vortex generated by an A340.

As shown in Figure 4.1, a region centered around the vortex pair is considered as the region of interest. Its size along the X, Y, Z axes is of $250\text{m}\times150\text{m}\times1\text{m}$. In the region above the wake vortex, the raindrops size distribution is assumed to be given by Equation (2.13). The raindrops with diameters between 0.5 mm and 4 mm are considered in the simulation. The diameter class interval is of 0.1 mm. For each diameter class, the raindrops are initially released in a box above the wake vortex region whose size along the X, Y, Z axes is of $250\text{m} \times 5\text{m} \times 1\text{m}$. At each time

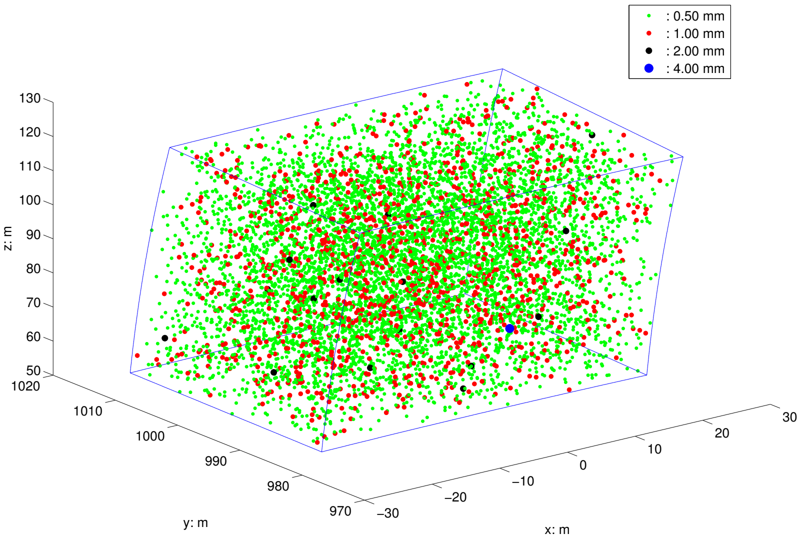

(a) $R = 2$ mm/h, $\alpha = 5°$

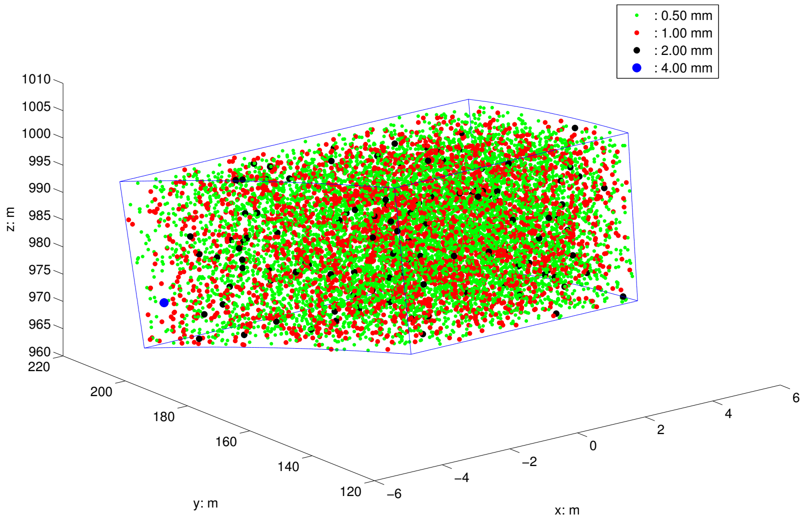

(b) $R = 5$ mm/h, $\alpha = 80°$

Figure 4.6: Illustration of simulated raindrops in one radar cell

step, some of the raindrops will enter into the wake vortex region, their positions and velocities are updated from the numerical computation of the motion equation (3.7). The procedure is continued until the smallest raindrops reach the ground or pass through the wake vortex region. Figure 4.9 illustrates the simulated position of the drops in the wake vortices at the initial time of the radar simulations, the

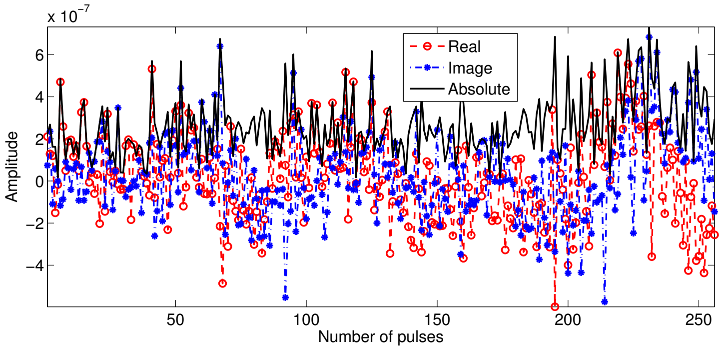

(a) rain rate = 2 mm/h, $\alpha = 5°$

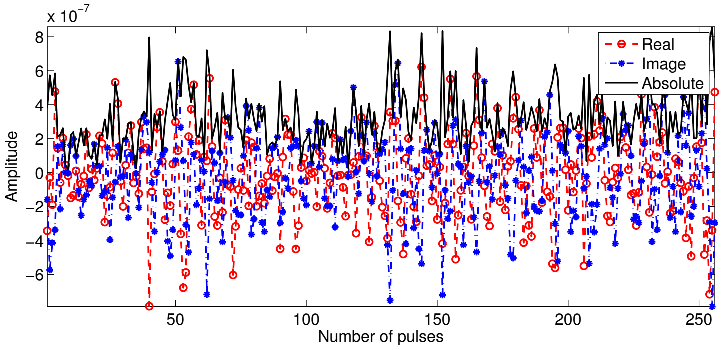

(b) $R = 5$ mm/h, $\alpha = 80°$

Figure 4.7: Simulated radar echo of raindrops in still air

raindrops with diameters of 0.5 mm, 1 mm, 2 mm, 3 mm and 4 mm are displayed in a two-dimensional plane.

In order to better illustrate the initial position of raindrops, the 2D wake vortex region is divided into $M \times N$ independent grids whose size is 2m×2m and in each grid, the number of raindrops for each diameter class is counted. Figure 4.10 illustrates the number of raindrops in 2D wake vortices for the diameter classes of 0.5 mm, 1 mm, 2 mm and 4 mm, the color bar indicates the number of raindrops in each grid. It is interesting to note the enhanced concentration of raindrops between the two vortices and the reduced concentration of raindrops in the columns below the two vortices. Indeed this heterogeneous concentration of raindrops is one of the element that may enable a detection of the vortices.

In order to exploit more about the Doppler signature of raindrops within wake vortices, different radar geometry configurations are considered as shown in Figure 4.11. The input radar parameters are listed in Table 4.1.

In Figure 4.11 (a), the radar volume is divided into 6 continuous range cells where

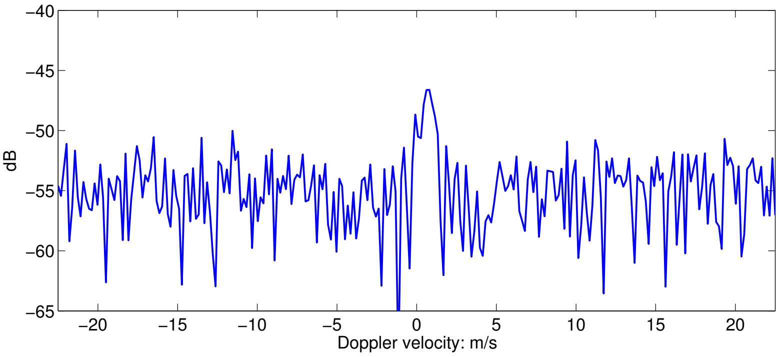

(a) rain rate = 2 mm/h, $\alpha = 5°$

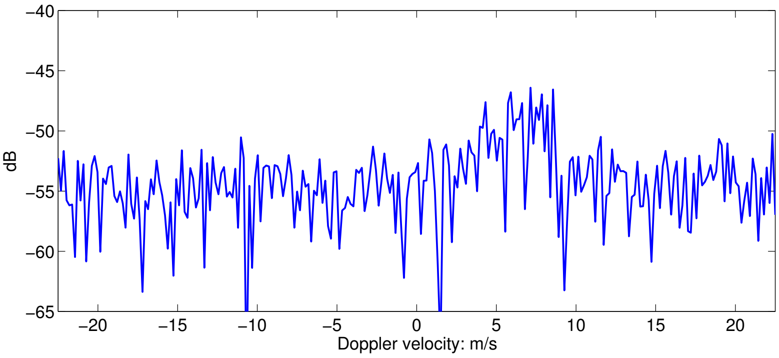

(b) $R = 5$ mm/h, $\alpha = 80°$

Figure 4.8: Radar Doppler spectrum of raindrops in still air

the two vortex cores are located in two adjacent cells, and the range resolution is 40 meters. The elevation angle of the radar beam is 5°. Figure 4.12 shows the obtained Doppler spectrum of radar echo in the 6 considered radar cells. It can be noticed that the width of the Doppler spectrum is wider for radar cell 02-05, and especially for cell 03 and 04 with regards to cell 01 and 06 that are further from the vortex cores. Actually this phenomenon is caused by the richness of radial velocities of the scattered raindrops in the given radar cell, as well as the inhomogeneous concentration of raindrops in the wake vortex region. In [26], the Doppler spectrum of wake vortex in rain was also reported to be extended periodically while the X band radar worked in scanning mode. This extended Doppler spectrum indication is a possible signature that denotes the existence of wake vortex.

In Figure 4.11 (b), the two vortex cores are located in two radar cells separated by one radar cell and the radar echoes from five successive radar cells are simulated. In Figure 4.13, the Doppler velocity spectrum from the raindrops in the three radar

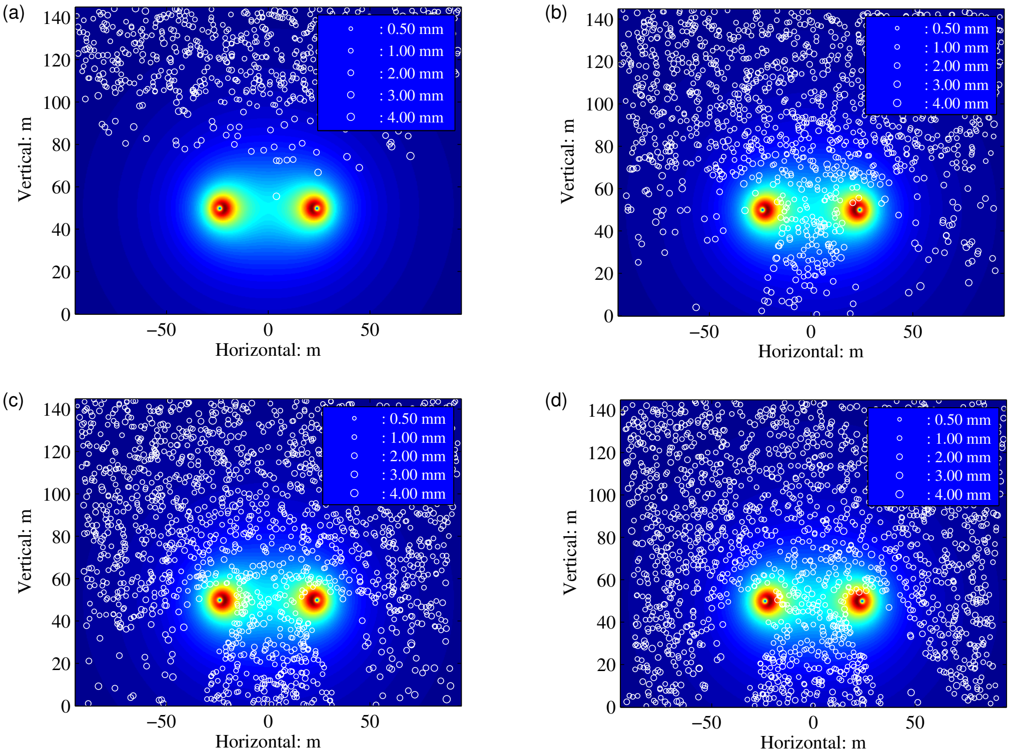

Figure 4.9: Initialization of raindrops within wake vortices before computation of the radar signal: (a) Time: 12.5 s, (b) Time: 25 s, (c) Time: 37.5 s, (d) Time: 50 s

cells around the vortices are illustrated. The elevation angle of the antenna is configurable to be 3°, 5° and 7° as shown in Figure 4.11 (c). It is easily found that the width of Doppler velocity spectrum is depending on the elevation angle. At 3° of elevation, the radar antenna points to the raindrops below the wake vortex cores where the raindrops are tending to fall vertically to the ground as shown in Figure 3.2, thus the richness of radial velocities of raindrops is lower than the one at 5° and 7° of elevation.

In Figure 4.11 (d), two vortex cores are located in the same radar resolution volume while the range resolution is set to 100 m. The corresponding Doppler velocity spectrum is illustrated in Figure 4.14. In radar cell 02, the Doppler velocity spectrum is almost symmetrically distributed and the width is also depending on the elevation angle. In radar cell 01 and 03, the Doppler velocity spectrum of raindrops is not extended and similar to the Doppler spectrum of raindrops falling in still air, because in these two radar cells, the raindrops' trajectory and velocity have not been changed significantly and at the elevation angles of 3°, 5° and 7°, the radar

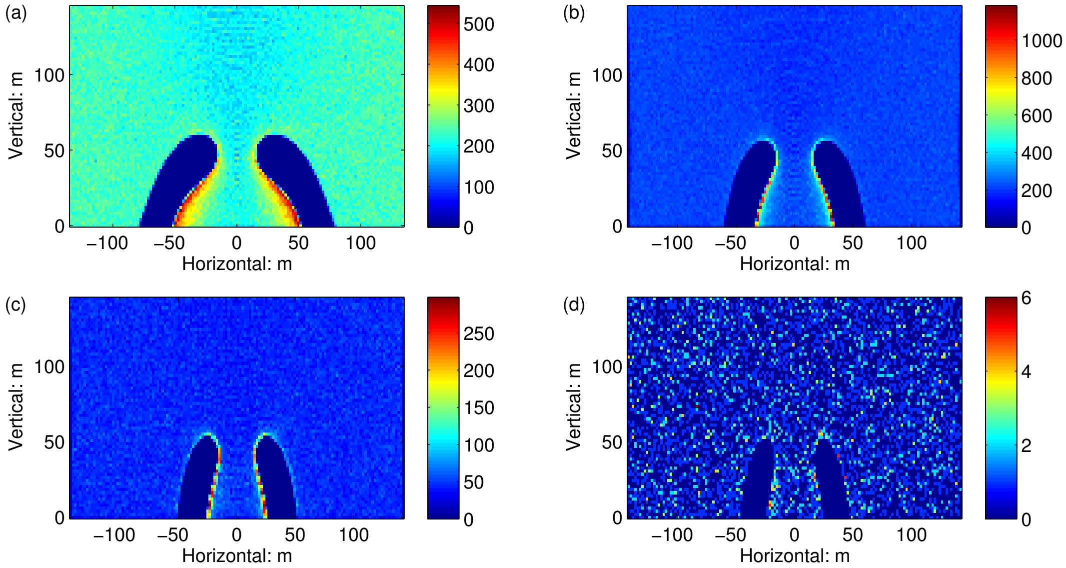

Figure 4.10: Illustration of the number of raindrops in a slice of 1m wake vortices: (a) Diameter: 0.5 mm, (b) Diameter: 1.0 mm, (c) Diameter: 2.0 mm, (d) Diameter: 4.0 mm.

radial velocity of the raindrops falling in still air is very low. Actually, the raindrops size distribution in each pulse resolution volume is depending on the division of the radar cells which are defined by the pulse width and the radar antenna beam width.

4.4.3 Simulations in scanning mode

In scanning mode, there are two relevant radar geometry configurations: close to runways and under the flight path, as shown in Figure 4.15. Those two kinds of radar geometry configurations are tackled in the following subsections separately.

Simulation case: radar under flight path

As shown in Figure 4.16, the X band radar is deployed under the aircraft flight path and the radar antenna is vertically scanning over the wake vortex region with an elevation angle varying from 80° to 100° and from 100° to 80° repeatedly, covering the fan-shaped region ABCD. Considering the size of the area and the corresponding computation load, the Simulator B has been used for this example. The X band radar parameters are given in Table 4.1, the radar antenna scanning rate is $8°/s$. The radar range resolution is 40 m and 10 range cells from 624 m to 1024 m are illuminated at each elevation angle. The time interval for computing the radar

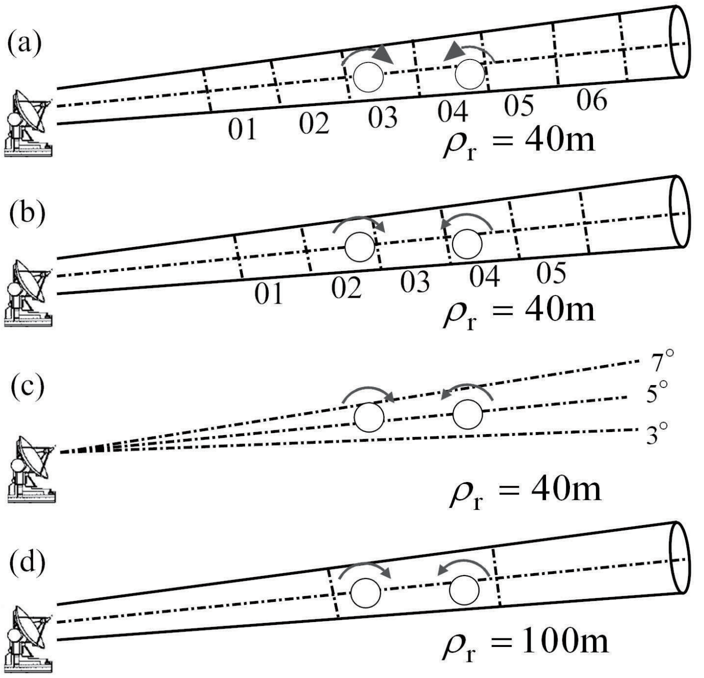

Figure 4.11: Different radar geometry configurations for X band simulation: (a) Two vortex cores in two adjacent cells, (b) Two vortex cores in two interval cells, (c) Elevation angles: 3°, 5°, 7°, (d) Range resolution: 100 m

signatures is set to be every 256 pulses, equal to 0.0765 s while the PRF is 3348 Hz.

The simulated wake vortex corresponds to a stable stage wake vortex generated by an A340 flying at 300 km/h. Other parameters corresponding to this aircraft are given in Table 2.1. The vortex circulation is assumed to be constant during the simulation. The wake vortex pair is descending from an altitude of 924 m at a constant descent velocity of -1.86 m/s, which is computed by Equation (2.4), and horizontally advected by a uniform cross wind of -4 m/s. In our analysis, the simulation region is defined as the rectangular box covering ABCD. Due to the effects of descent velocity and cross wind, the wake vortex pair may move out of this region after some time.

At each time step, the raindrops passing through the simulation region are considered. The raindrop's minimum and maximum diameters are 0.5 mm and 4.0 mm respectively. There are 56 diameter classes spaced of 0.0625 mm. At $t = 0$, the raindrops are falling at their terminal falling velocity and their distributions in the simulation region are assumed to be the same as in still air. At each time step, for raindrops of each diameter class, their number concentration and velocity distribu-

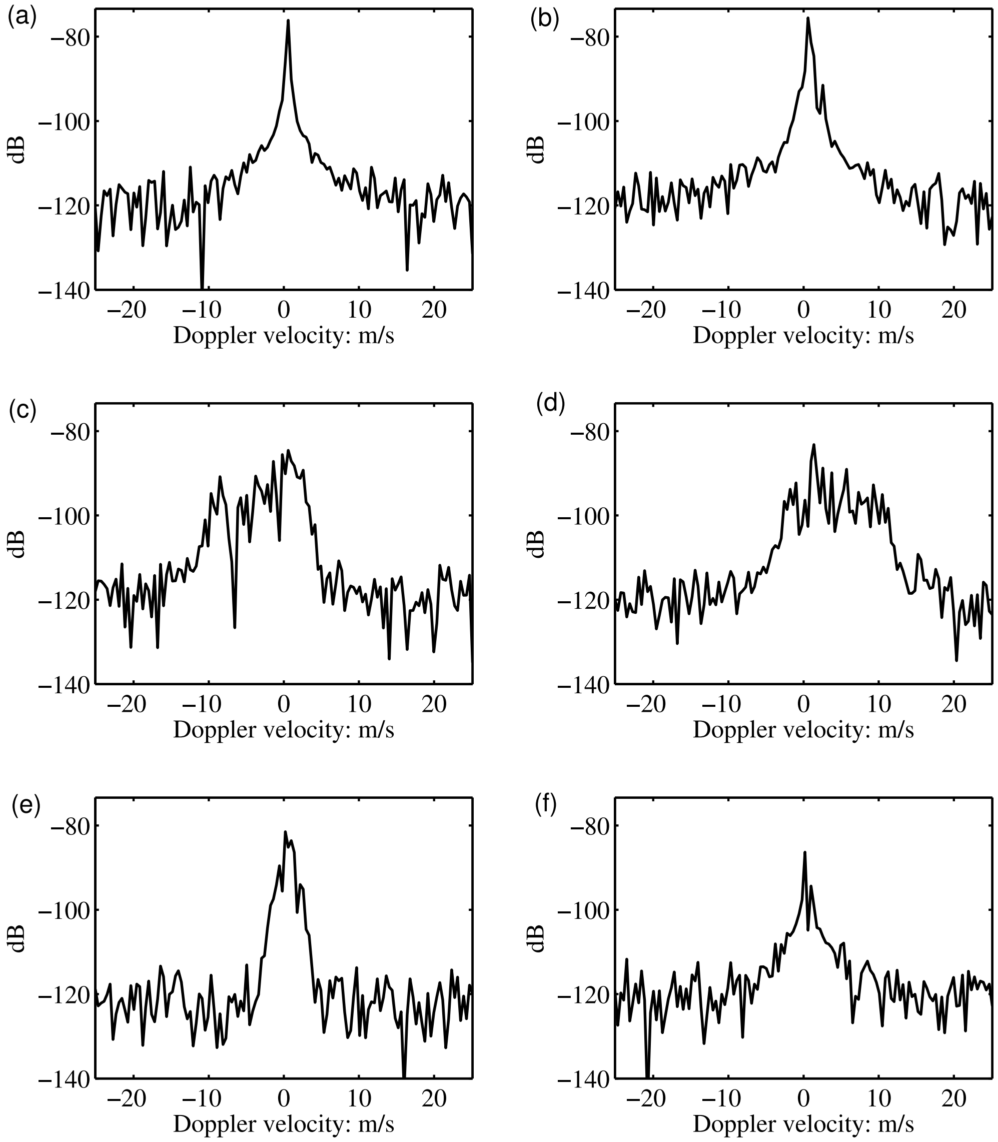

Figure 4.12: X band Radar Doppler velocity spectrum of raindrops while vortex cores in two adjacent cells: (a) cell 01, (b) cell 02, (c) cell 03, (d) cell 04, (e) cell 05, (f) cell 06

tion are updated by the methodology described in Section 3.3.3. As shown in Figure 4.17, for the raindrops of 2 mm of diameter, their number concentration and velocity in the simulation region under horizontal cross wind of -4 m/s are illustrated for t

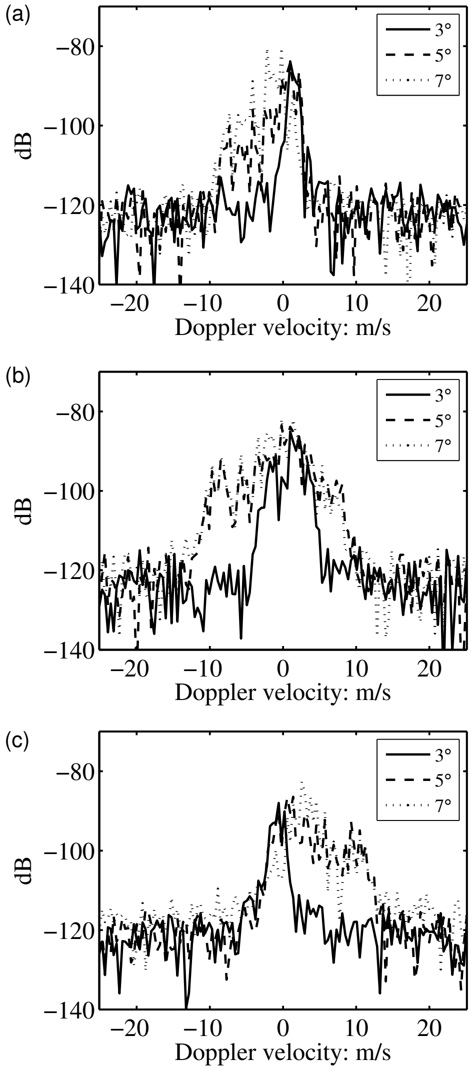

Figure 4.13: X band Radar Doppler velocity spectrum of raindrops while vortex cores in two interval radar cells with 40 m range resolution: (a) cell 02, (b) cell 03, (c) cell 04

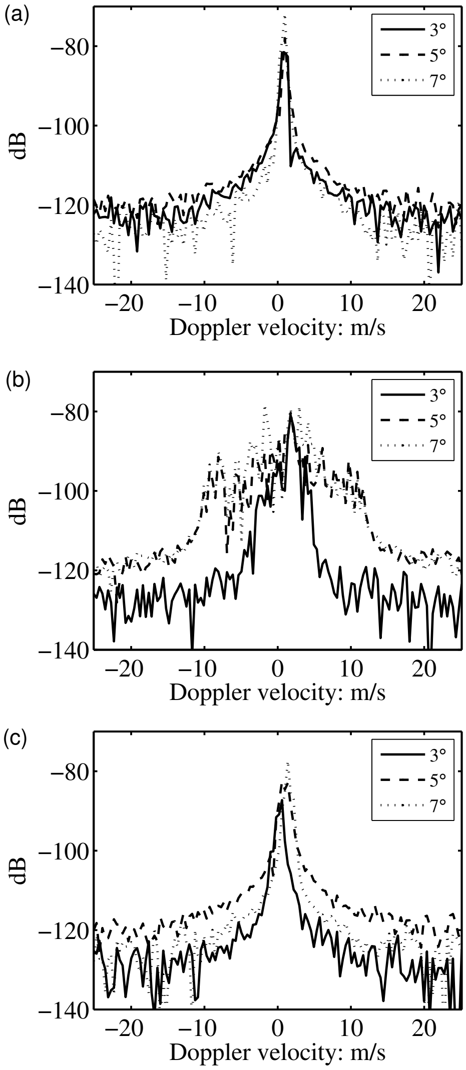

Figure 4.14: X band Radar Doppler velocity spectrum of raindrops while vortex cores in the same radar cell with 100 m range resolution: (a) cell 01, (b) cell 02, (c) cell 03

= 1, 10 and 20 s. At t = 1 s, the raindrops around the vortex core are disturbed by the wake vortex flow and two symmetric holes around the wake vortices appears. The raindrops'number concentration in these two holes is 0 and the concentration around the boundaries of these two holes is evidently enhanced. As time evolves, the raindrops tend to be concentrated along the boundaries between the two holes, the volume of these two holes is increasing and they are moving downward due to

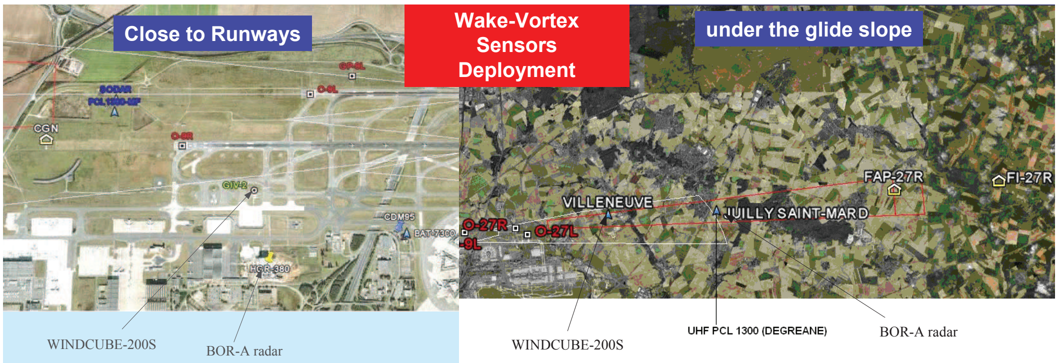

Figure 4.15: Illustration of sensors deployment for wake vortex monitoring (SESAR P12.2.2 XP0 Trials at Paris CDG Airport [26]

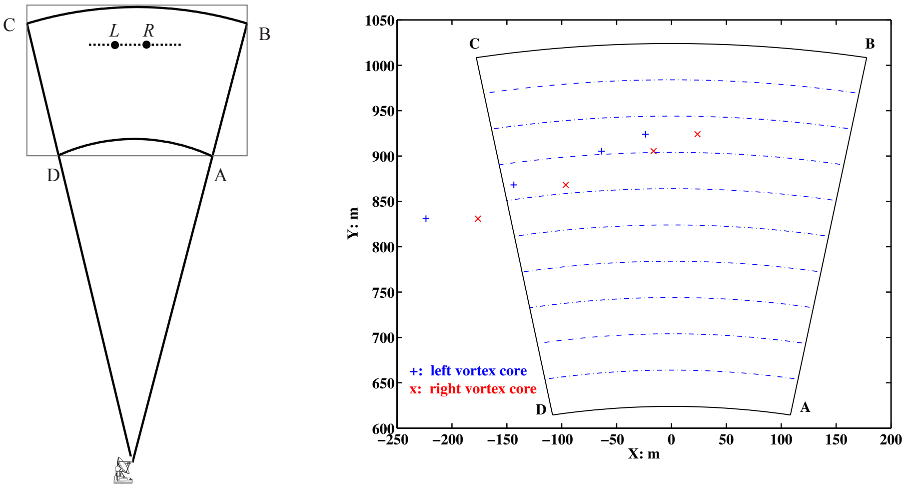

Figure 4.16: X band Radar-Wake vortex geometry configuration in scanning mode: under flight path. The four pairs of '+' and 'x' from up to down denote the locations of wake vortices at time t = 0 s, 10 s, 30 s and 50 s respectively.

the descent velocity induced by other vortex and advected by the horizontal cross wind. The velocity distribution of raindrops around the wake vortices are similar to the one observed in still air, even though under the effect of horizontal cross wind of -4 m/s. The horizontal velocity distribution is nearly axis-symmetrically distributed and the vertical velocity of raindrops between the two vortices is enhanced up to 16 m/s.

Considering a rain rate of 10 mm/h, the raindrop size distribution (DSD) model in still air is computed by Equation (2.13) and the raindrops' radar cross section (RCS) are computed by Rayleigh approximation in Equation (2.14). Combining the

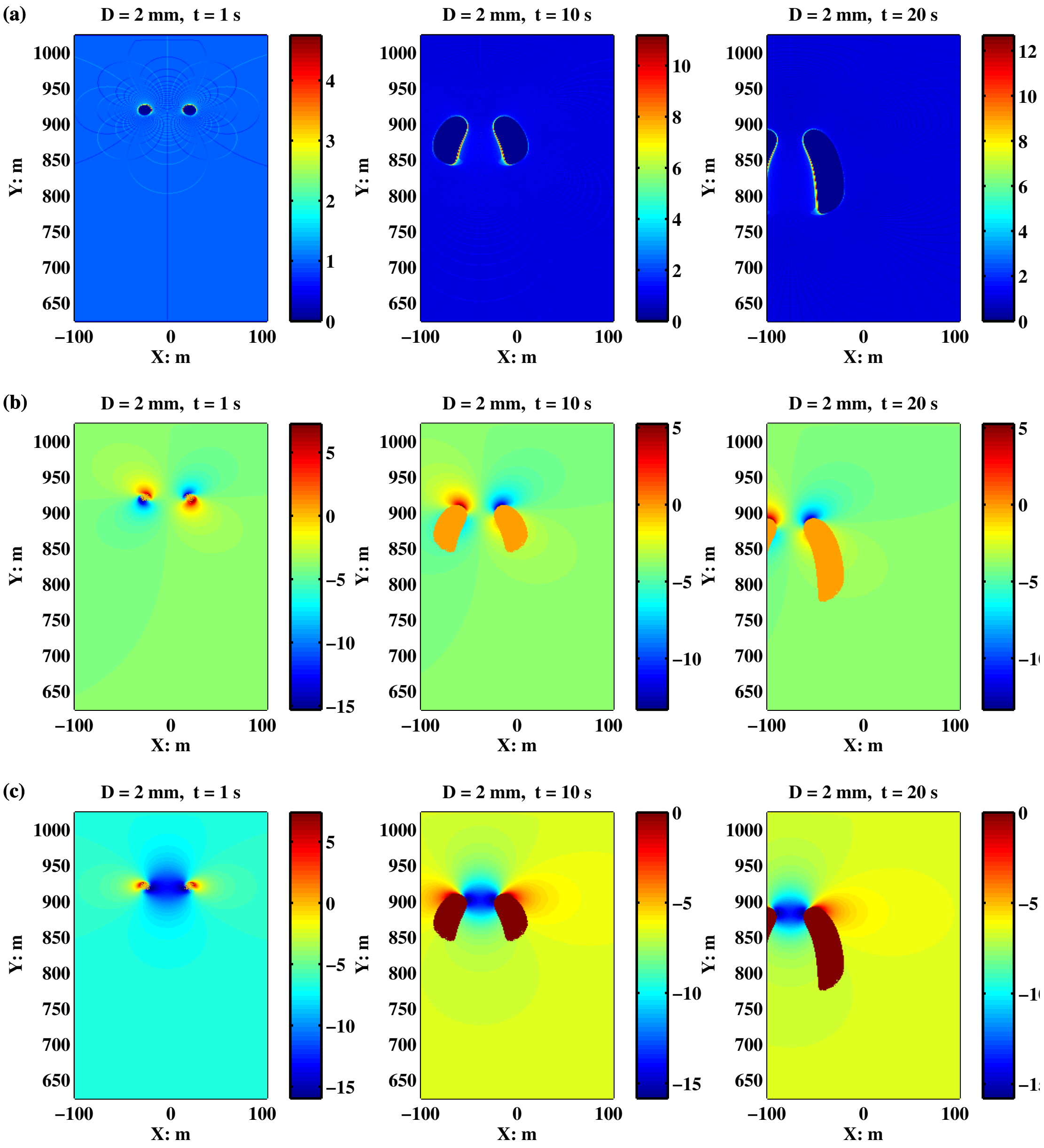

Figure 4.17: Distribution of raindrops of diameter 2 mm in the simulation region under horizontal cross wind of -4 m/s: (a) Number concentration, (b) Average horizontal velocity, (c) Average vertical velocity

raindrops' distribution in wake vortices for each diameter class, the radar reflectivity and Doppler velocity spectrum are then computed by the methodology described in Section 4.2.2 at each time step. The noise power at each Doppler velocity bin is also simulated according to the input radar parameters. The simulation time is set to be 50 seconds.

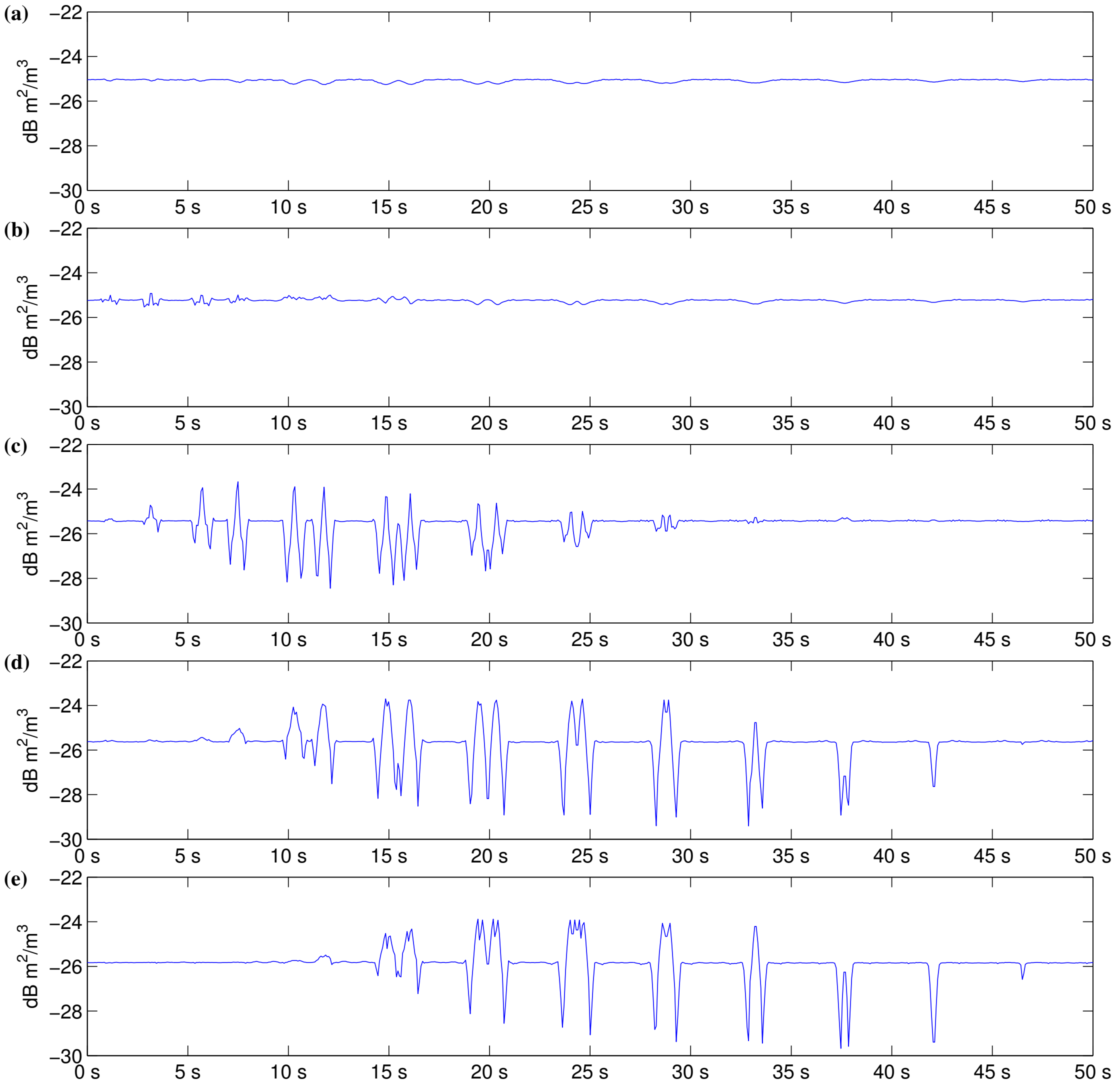

Figure 4.18: Radar reflectivity of raindrops in wake vortices for a rain rate of 10 mm/h: (a) r = 964 m, (b) r = 924 m, (c) r = 884 m, (d) r = 844 m, (e) r = 804 m

In Figure 4.18, the radar reflectivity of raindrops in 5 radar cells under rain rate of 10 mm/h is illustrated. At $r = 964$ m, the reflectivity of raindrops remains around -25 dB m^2/m^3 when the radar antenna scans over the simulation region for all the 50 seconds. At $r = 944$ m, the reflectivity of raindrops appears to slightly fluctuate at a bias of 0.5 dB when the radar antenna scans over the wake vortices. At $r =$ 884 m, 844 m and 804 m, the reflectivity of raindrops are fluctuating periodically at a bias of around 5 dB due to the enhanced and reduced concentration of raindrops around the wake vortices as shown in Figure 4.17(a). When the radar antenna beam covers most part of the region where the concentration of raindrop is enhanced, the peak values of radar reflectivity are therefore obtained; when the radar antenna beam covers most part of the region of the two holes, the minimum values of the radar reflectivity are therefore obtained. This kind of radar reflectivity fluctuations is caused by the geometrical relationships between the radar antenna beam and the two holes where the number concentration of raindrops are changed by vortex flow. In addition, it is evident that the reflectivity fluctuations in these three radar cells appear sequently in time, indicating the motion of the two holes due to the cross wind and descent velocity of wake vortex pair. However, as the volume of these two holes enlarge as time evolves, the radar reflectivity fluctuations are not sufficient to account for the location the core of the vortices.

In Figure 4.19, the radar Doppler velocity spectrum of raindrops in 5 radar cells are illustrated. At $r = 964$ m, from $t = 0$ to $t = 20$ s, the Doppler velocity spectrum is varying with time, but the variations are very small. At $r = 924$ m, 884 m and 844 m, the Doppler spectrum widths of the raindrops are extended periodically. In one period when the antenna scans over the simulation region, that is, the radar elevation angle varies from 80° to 100° and from 100° to 80°, the shape of the Doppler spectrum of raindrops is providing very valuable information on the raindrops' motion and distribution in each radar cell where the wake vortex exists. In order to better illustrate the influence of wake vortices on the raindrops' Doppler velocity spectrum, the Doppler velocity spectrums of raindrops in still air and in wake vortices are presented for comparison in Figure 4.21, and the time-Doppler velocity spectrums of raindrops at the range gates of 924 m and 884 m in one scanning period are illustrated in Figure 4.20 (a), (b).

Combining the simulation results in the above three figures, it can be noticed that:

(1) In each scanning period, the time-Doppler spectrum of raindrops has two peaks, which may indicate the existence of wake vortices in the radar cell.

(2) The Doppler spectrums widths of raindrops around the left vortex and right vortex are obviously extended, which can be explained by the raindrops' velocity distribution as shown in Figure 4.17 (b) and (c). Around the two vortices, the velocity variations of raindrops yields the extension of Doppler velocity spectrum.

(3) The Doppler spectrum of raindrops between the two vortices are shifted and the spectrum widths are also extended. This can be explained by the raindrops' vertical velocity distribution as shown in Figure 4.17 (c). Between the

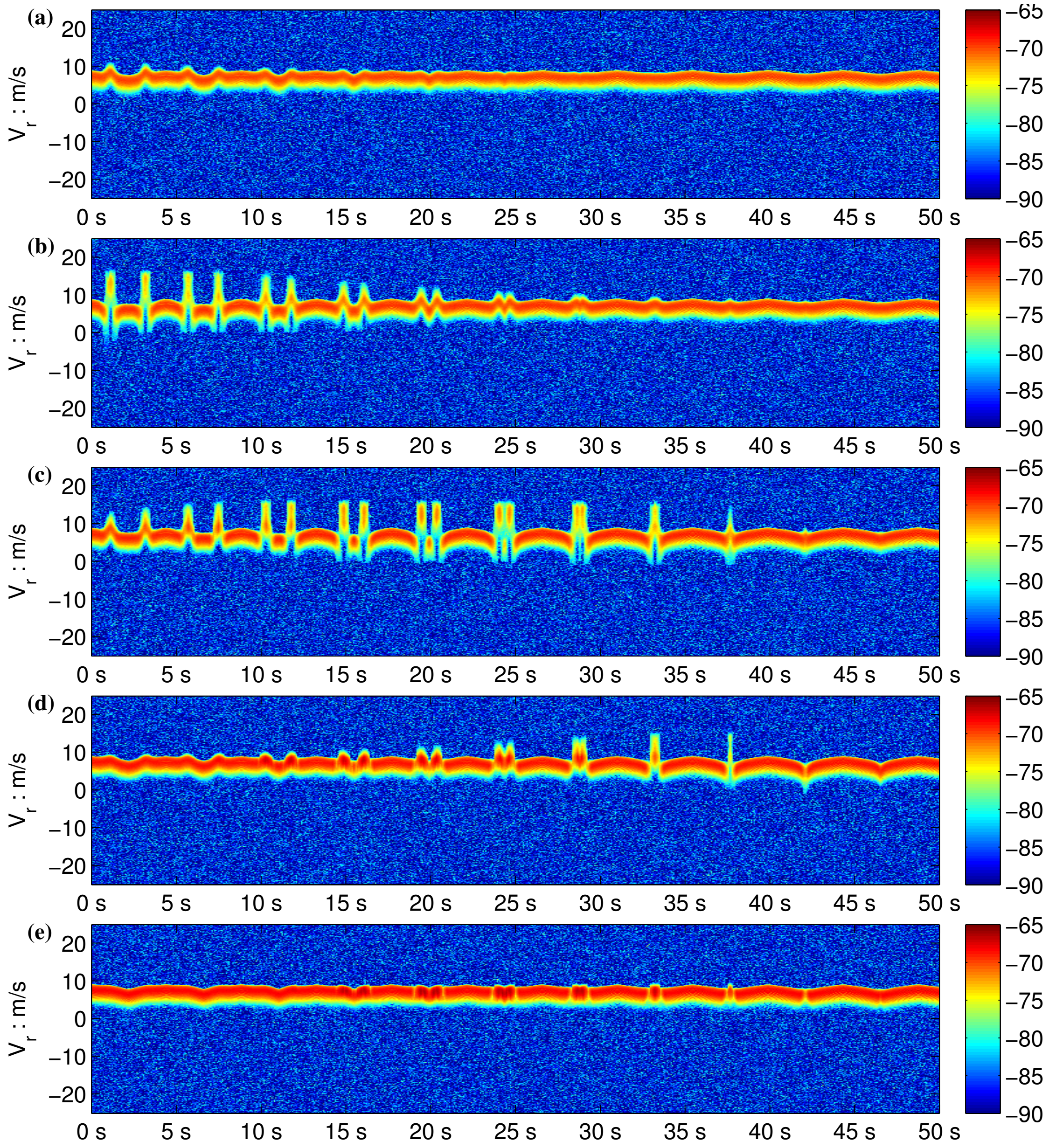

Figure 4.19: Time-Doppler velocity spectrum of raindrops in wake vortices for rain rate of 10 mm/h: (a) r = 964 m, (b) r = 924 m, (c) r = 884 m, (d) r = 844 m, (e) r = 804 m

two vortices, most of the raindrops have an increased vertical velocity with regards to their terminal velocity due to acceleration of the vortex flow, which are larger than their terminal falling velocities. When these raindrops are illuminated by the vertically pointing radar antenna beam, their radial velocities are therefore larger than the ones of raindrops in still air, thus yielding to the

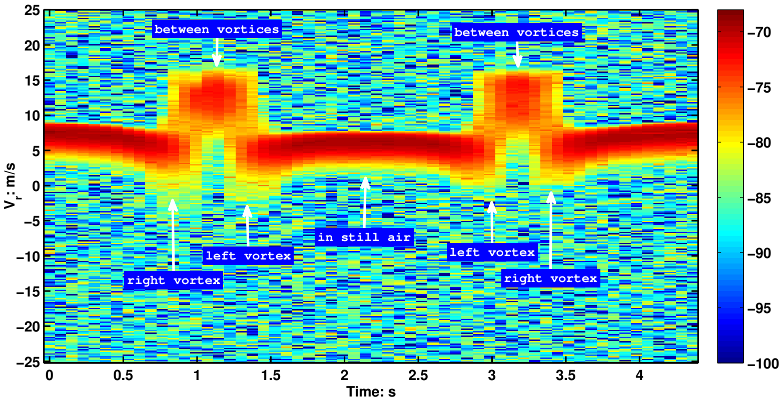

(a) Time-Doppler spectrum of raindrops at range of 924 m in one scanning period

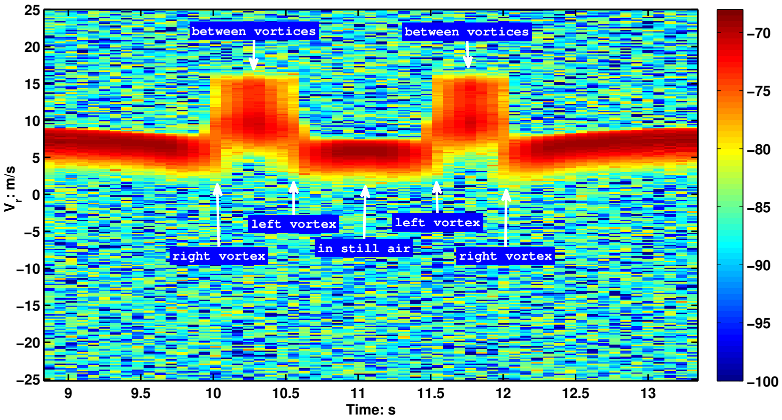

(b) Time-Doppler spectrum of raindrops at range of 884 m in one scanning period

Figure 4.20: Illustration of the details of the time-Doppler velocity spectrum of raindrops in wake vortices: the text arrows indicate when the radar antenna beam scans over the right vortex, the regions of between two vortices, left vortex and still air

shift of the Doppler spectrum and extension of the Doppler spectrum width.

(4) In each scanning period, the time interval between the two peaks in the time-Doppler spectrum is equal to the time taken by the radar to re-illuminate the raindrops between the two vortices. These time intervals are obviously decreasing as time evolves in Figure 4.18 (b), (c) and (e) respectively and these peaks appear in each radar sequently. As well, the time interval between the extended Doppler spectrums of raindrops around the right and left vortex is representative of the information about the vortex core separation. To

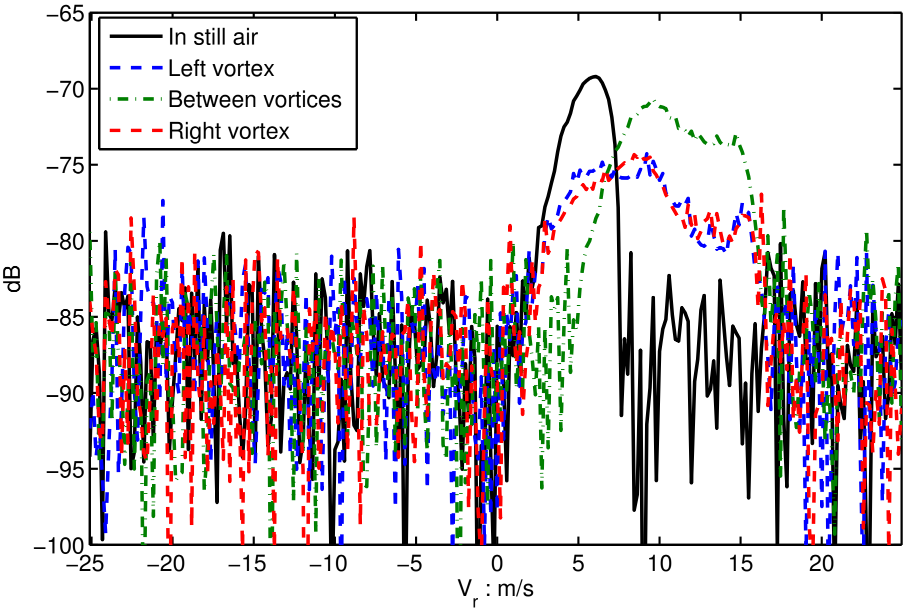

Figure 4.21: Comparison of the Doppler velocity spectrums of raindrops in still air and in wake vortices

conclude, these signatures provide clear indications of the location and motion of wake vortices when the two vortices approach the radar or one of them moves out of the simulation region under cross wind.

Simulation case: radar close to runways

Besides the deployment of radar under flight path, the radar can also be deployed on one side of the runway to monitor wake vortex. The advantage of this kind of deployment is the capability of monitoring the wake vortex behaviors near the ground, i.e., the ground effect. In the present work, the wake vortices ground effect is not considered. In Figure 4.22, the X band Radar-Wake vortex geometry configuration is illustrated. The X band radar is deployed at the origin of the XOY referential ordinates, 600 m away from the airport runways. The radar antenna is vertically scanning over the wake vortex region at a rate of $8^\circ/s$, that is to say, radar keeps the azimuth angle constant and the elevation angle varies from 0° to 30° and from 30° to 0° repeatedly, covering the fan-shaped region ABCD. The 3 dB beam width of antenna are $2^\circ \times 2^\circ$. The radar transmitting peak power is 600 W and the antenna gain is 39 dB. The radar range resolution is 40 m and 6 range cells from 520 m to 720 m are illuminated at each elevation angle. The radar system loss is assumed to be of 6 dB and the noise figure of 4 dB. The time interval for computing the radar signatures is set to be every 256 pulses, equal to 0.0765 s while the PRF is 3348 Hz. Considering the computation load, the Simulator B is adopted here.

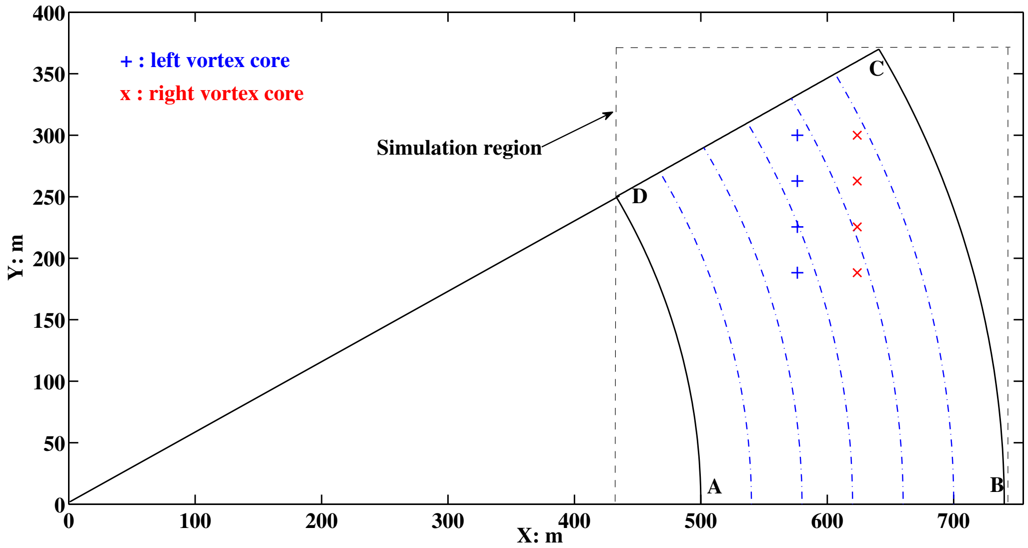

Figure 4.22: X band Radar-Wake vortex geometry configuration in scanning mode: Close to runways. The radar is located at the origin (0,0). The wake vortex pair is descending at a constant descent velocity. The four pairs of '+' and 'x' from up to down denote the locations of wake vortices at time t = 0 s, 20 s, 40 s and 60 s respectively.

The parameters of wake vortex and raindrops are assumed to be the same as the ones in the previous simulation for radar under flight path. In our analysis, the simulation region is defined as the rectangular box covering ABCD. In Figure 3.15, 3.16, 3.17, 3.18, 3.19 and 3.20, the raindrops' distribution in wake vortices at different time steps have been illustrated for $D = 0.5$ mm and $D = 2.0$ mm respectively.

In Figure 4.23, the radar reflectivity of raindrops in 5 radar cells under rain rate of 10 mm/h are illustrated. In Figure 4.24, the radar Doppler velocity spectrum of raindrops in 5 radar cells are illustrated. It can be noticed that:

(1) The simulation results for radar close to runways are similar to the ones of Figure 4.18 and 4.19 while the radar is deployed under the flight path. The radar reflectivity fluctuations indicate the enhanced and reduced number concentration of raindrops in the simulation region due to the existence of wake

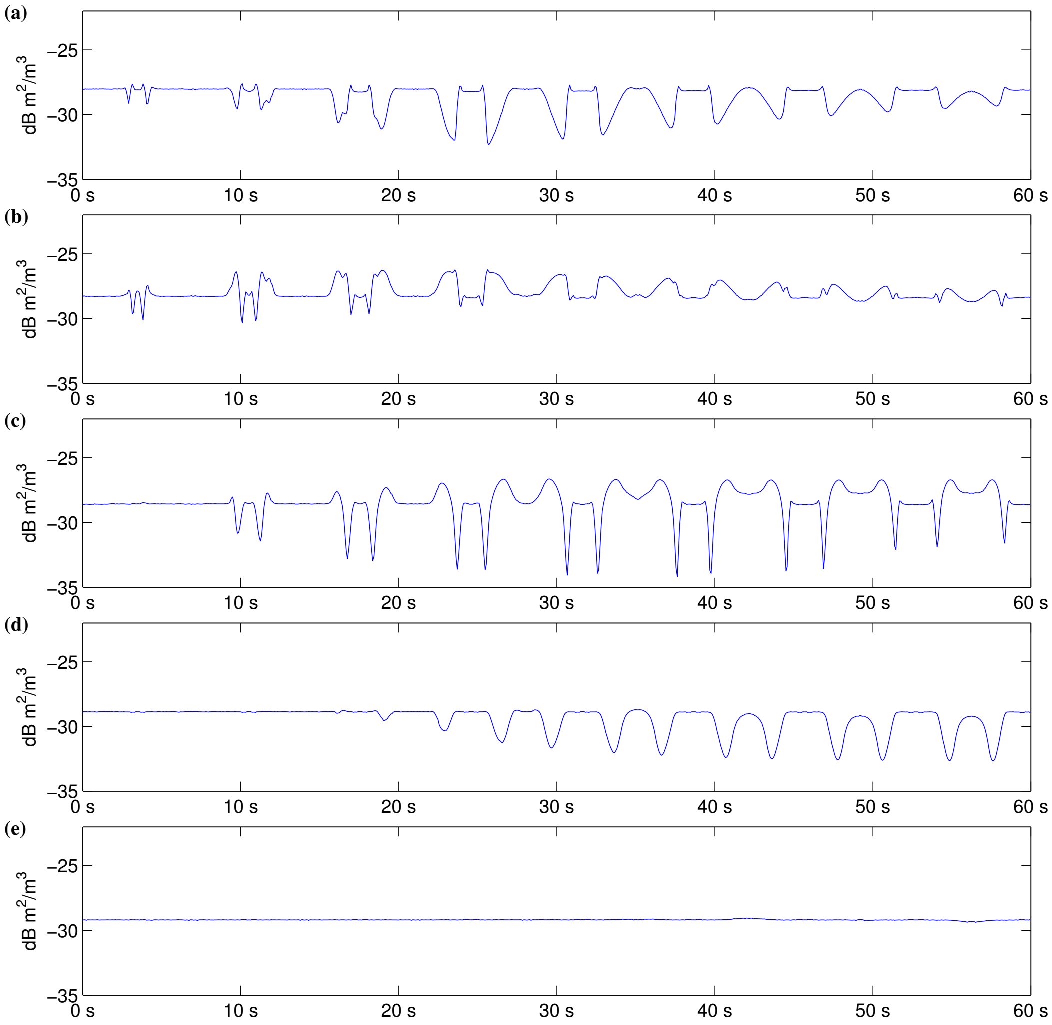

Figure 4.23: Radar reflectivity of raindrops in wake vortices for a rain rate of 10 mm/h: (a) r = 720 m, (b) r = 680 m, (c) r = 640 m, (d) r = 600 m, (e) r =560 m

vortices. The periodically extended Doppler velocity spectrums indicate the velocity distribution of raindrops in the simulation region and the geometrical relationship between the radar antenna beam and wake vortices.

(2) From Figure 4.22, the right vortex core is located in the radar cell at 680 m from the radar between $t = 0$ and $t = 40$ s, correspondingly in Figure 4.24 (b), in each scanning period, when the antenna encounters the right vortex core, the shape of Doppler spectrum of raindrops is changed and the dominant Doppler velocities are positive.

(3) From Figure 4.22, the left vortex core is located in the radar cell at 600 m from the radar between $t = 40$ s and $t = 60$ s, correspondingly in Figure 4.24 (d),

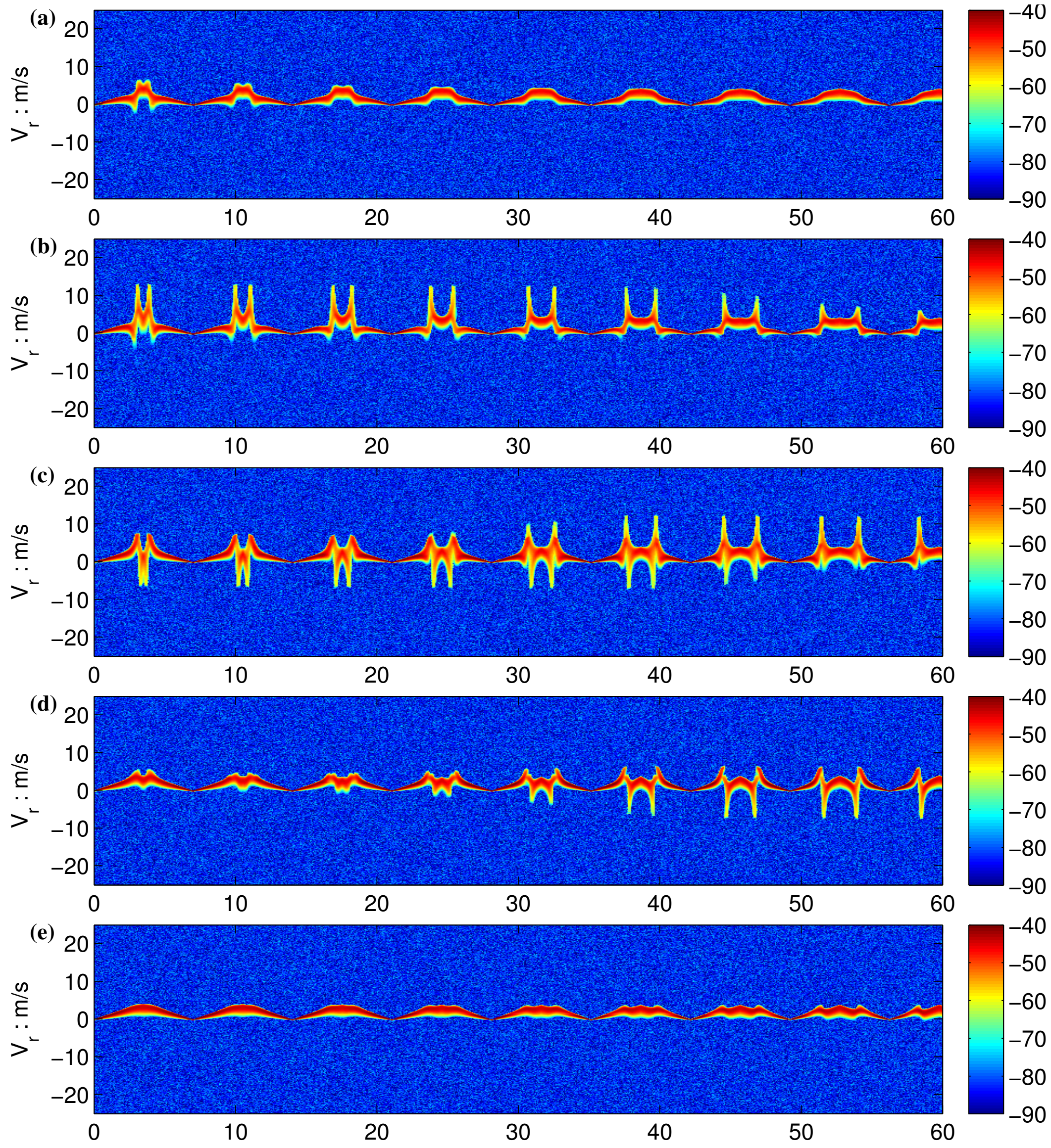

Figure 4.24: Time-Doppler velocity spectrum of raindrops in wake vortices for a rain rate of 10 mm/h: (a) r = 720 m, (b) r = 680 m, (c) r = 640 m, (d) r = 600 m, (e) r = 560 m

in each scanning period, when the antenna encounters the left vortex core, the shape of Doppler spectrum of raindrops is changed and the dominant Doppler velocities are negative.

(4) From Figure 4.22, the two vortex cores co-exist in the radar cell located at 640 m from the radar at around t = 40 s, correspondingly in Figure 4.24 (c) at around t = 40 s, the shape of Doppler spectrum of raindrops is changed and the dominant Doppler velocities are positive and negative alternatively.

(5) As shown in Figure 4.22, the right and left vortex cores are located in the radar cell located 680 m and 640 m from the radar respectively between t = 0 and t = 20 s, correspondingly, the Doppler spectrums in Figure 4.24 (b) and (c) seem to be symmetric along the axis of Doppler velocity. These phenomenon can be explained by the position of raindrops illuminated by radar antenna beam. At low elevation angle, when the antenna beam encounters the raindrops in the down part of the left vortex, the dominant Doppler velocities are positive, when the antenna beam encounters the raindrops in the up part of the left vortex, the dominant Doppler velocities are negative. These phenomenon is opposite for the raindrops around the right vortex.

4.4.4 Comparison with real data from THALES radar trials

In [26] and [45], the X-band Radar has successfully detected wake vortices generated by aircraft of categories heavy and medium (Table 2.1) in rainy conditions, via analysis of the Doppler signatures of raindrops. The results observed by Thales are compared in this section with the results obtained from Simulator B. In Thales radar trials, the radar is deployed close to runways and the geometry configuration is illustrated in Figure 4.25. In the plane XOY, the scanning area is noted as the fan-shaped region $ABCD$, corresponding to elevation angle of 50° and 80°. The location of the right vortex core is 700 m away from the radar with an elevation angle of 60° at the beginning of the simulations. The radar transmitted peak power is 70 W, and the scanning rate of radar antenna is $8°/s$. The radar range resolution is 40 m, yielding to 8 radar cells at each elevation in the region $ABCD$. Other radar parameters are the same as the one given in Table 4.1.

In scanning mode, the number of coherent integration pulses is 256. So in the simulation, the radar signature of raindrops in the radar scattering volume is simulated for a duration corresponding to 256 coherent pulses. The total observation time is 80 s. During this time, the raindrop's number concentration and velocity distribution around the wake vortex core are assumed to be constant. The parameters of wake vortex and raindrops are assumed to be the same as the ones in the previous simulation for radar under flight path. In Figure 4.26, the number concentration and velocity distribution for raindrops of diameters 0.5 mm and 2 mm are illustrated.

The rain rate is set to be 2 mm/h, and the raindrop DSD model in still air is the

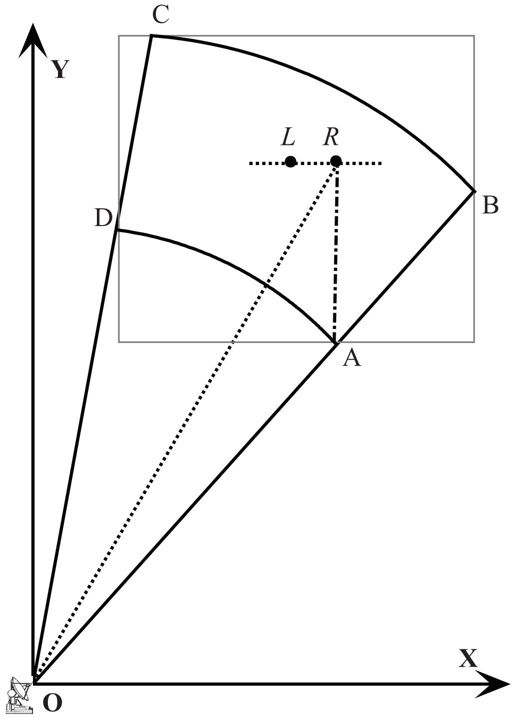

Figure 4.25: X band Radar-Wake vortex geometry configuration in scanning mode: Comparison with real data from THALES radar trials

one described in Chapter 2. According to the procedures of Simulator B, the radar reflectivity and Doppler spectrum of raindrops in each radar cell are simulated by integrating the contribution of radar average received power and Doppler signatures from each diameter class of raindrops. In Figure 4.27, the simulated time-Doppler radar spectrum of raindrops in the radar cells located 720 m, 680 m and 640 m away from the radar are shown to be basically consistent with the ones of Thales radar trials. It is easy to find from the simulation results that:

(1) When the radar antenna scans, the Doppler spectra of raindrops in these three radar cells are broadened repeatedly;

(2) In each repetition period, the Doppler spectrum of raindrops is broadened twice when the radar cell is illuminated by radar waves;

(3) As time evolves, the wake vortices are descending from one radar cell to the other;

(4) In scanning mode, the periodic extension of Doppler spectrum of raindrops provides good indication of the existence of wake vortex. The simulated results show good agreement with Thales radar trials results.

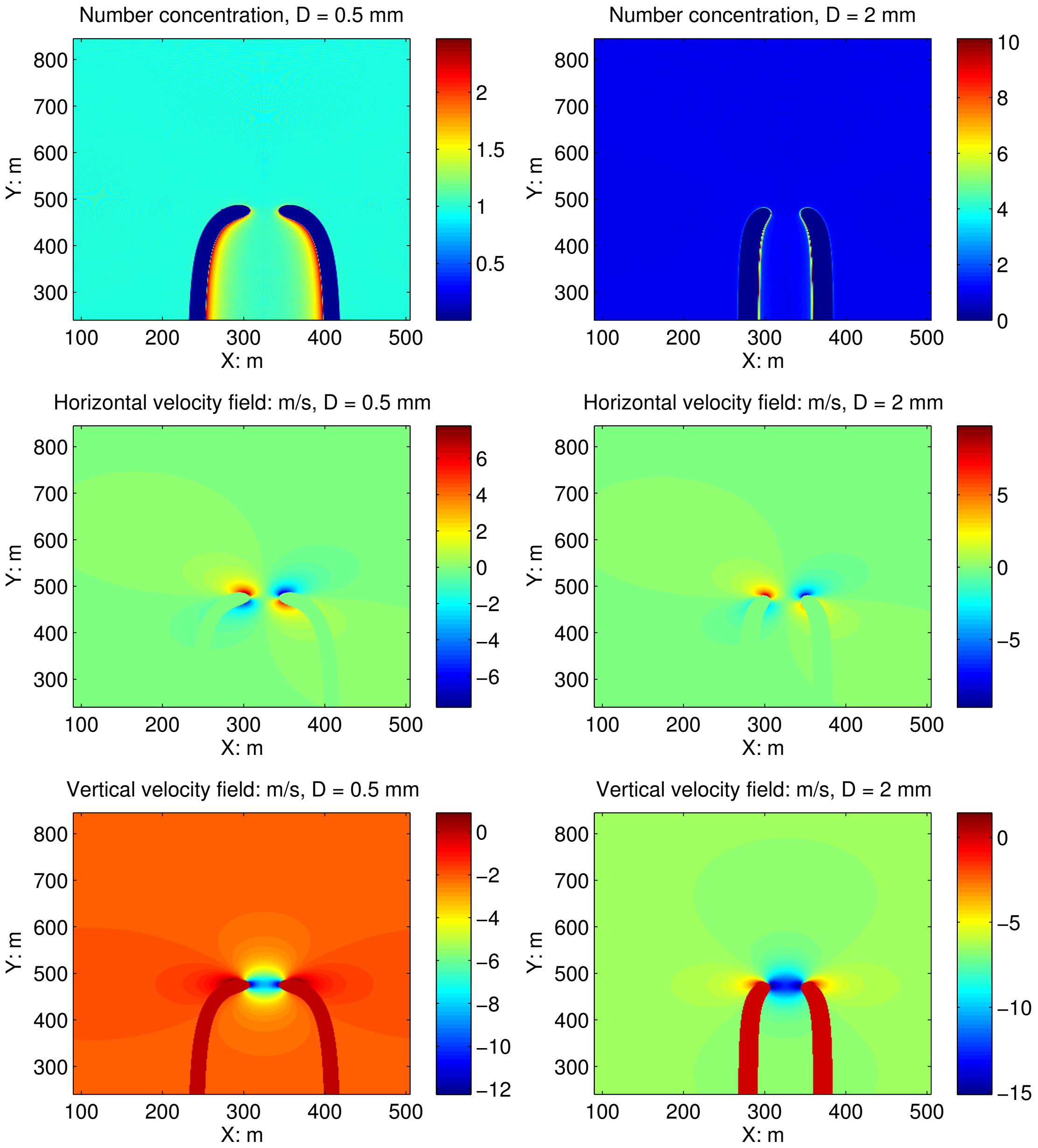

Figure 4.26: Raindrop's number concentration and velocity distribution in the rectangular box

(5) The location, descent velocity and vortex separation of the wake vortices can be possibly estimated from the time-Doppler spectrum of raindrops in successive radar cells.

(6) Considering different configurations of radar measurements or rain rates, the Simulators could be lately exploited for further study on the development of

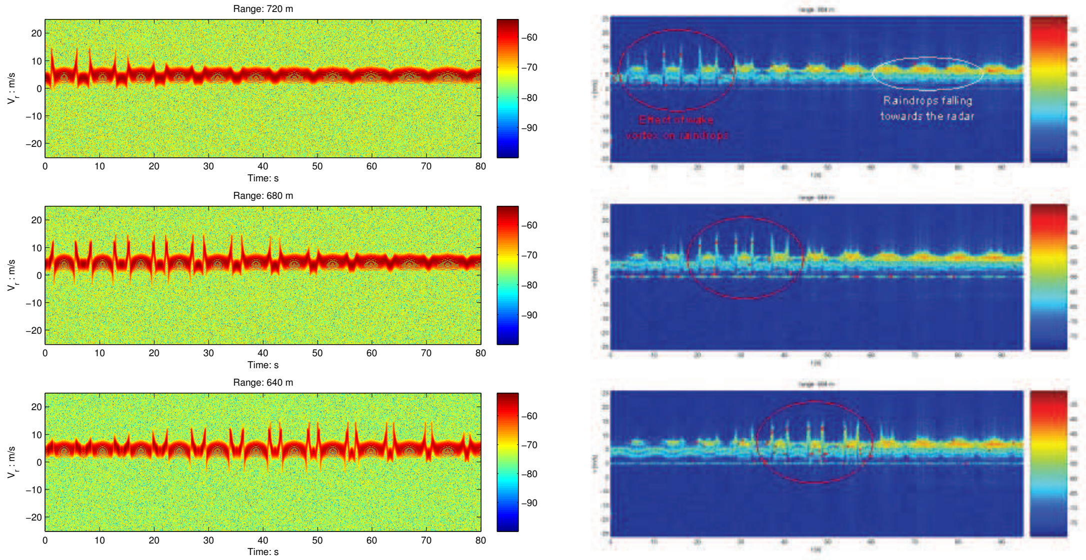

(a) Simulated time-Doppler spectrum of raindrops in wake vortices

(b) Time-Doppler spectrum observed by Thales radar trials in 2011 [26]

Figure 4.27: Comparison of the simulated results with X band radar trials

applicable wake vortex radar sensors in rain.

4.5 W band radar signatures

The W band radar is widely used for the analysis of microphysics of cloud and precipitation [191, 192]. Those radar could also been seen as efficient sensors for the monitoring of Wake vortices in rainy or foggy conditions. Recent W band radar trials to detect wake vortex in rainy weather have been reported by T. A. Seliga in 2009. The detection of aircraft wake vortices in light rain has been demonstrated using a low power (100 mW), solid-state W-Band (94 GHz) radar system, the observed radar reflectivity RHI (Range Height Indicator) plots showed clear evidence of enhanced droplet concentration between the vortices, with a dramatic reduction in droplet concentration in columns directly below and towards the outside of each vortex [27].

Actually, for the raindrops in one radar cell illuminated by the W band radar, the analysis of radar average received power and the peak Doppler velocity is of great interest. In the following sections, the radar average received power and the peak Doppler velocity profiles at each radar range cell as a function of antenna elevation angles will be simulated and analyzed by the two simulation schemes, and compared with the results obtained from W band radar trials reported in [27].

4.5.1 W band radar signatures: Simulator A

The simulation of the W band radar signature of raindrops in wake vortices using Simulator A is described in this section. In the wake vortex region, the raindrops are generated according to a given rain rate and DSD. When the radar antenna scans over the wake vortex region, for a given elevation angle, the radar signal from each individual raindrop in the radar cell is summed as I and Q radar signal. The radar signatures are then evaluated by executing traditional spectral analysis methods on the radar signal time series.

The radar parameters and geometry configurations described in [27] are taken as a reference to simulate the radar signature of the raindrops in wake vortices. The radar is deployed 1000 m away from the airport runways and it scans vertically in a plane perpendicular to the runway. The radar range resolution is 2 m. The radar antenna scanning rate is $5^\circ/s$ and the elevation angle varies between 7° and 14°. The antenna beam width is $0.18^\circ \times 0.18^\circ$. Other parameters can be found in Table 4.2.

Table 4.2: Input parameters for W band radar signature simulation

Parameters	Values
Radar frequency	94 GHz
Transmitted peak power	100 mW
Noise figure	12 dB
Antenna gain	58 dB
Antenna scanning rate	$5^\circ/s$
Pulse Repetition Frequency	20 kHz

Actually, in presence of raindrops, the attractive advantage of W band radar is its high resolution due to the achievable narrow beam width at this wavelength, enabling the possible retrieval of wake vortex local velocity field. The wake vortices of an A340 in stable stage are still considered in this example and assumed to be 200m above the airport runway. The rain rate is set to be 2 mm/h. In the region above the wake vortex, the initial raindrops are generated according to the size distribution given by Equation (2.13). In the wake vortex region, the initial raindrops are generated by computing the equation of motion of raindrops.

As soon as all the initial raindrops in wake vortex region are generated, the

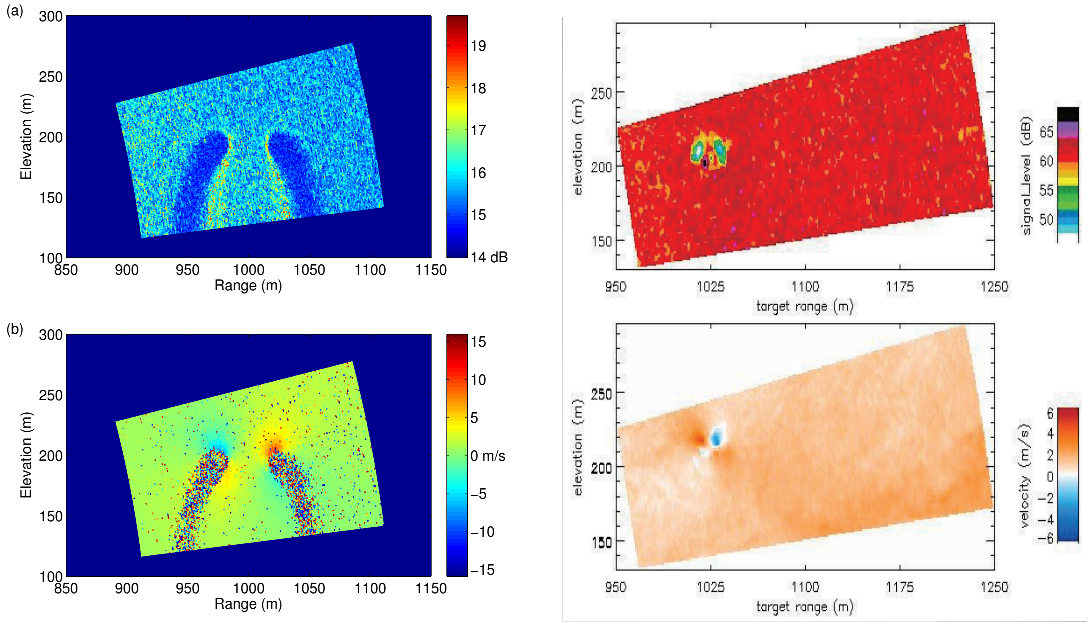

(a) Simulated W band radar signature of raindrops in wake vortices

(b) W band radar signature of raindrops by T. A. Seliga in 2009 [27]

Figure 4.28: Comparison of the simulated results with W band radar trials

radar signal time series are computed. For W band radar, the raindrop's radar cross section have to be approximated by Mie formula as illustrated in Figure 2.14 in Chapter 2. Based on the radar equation, at each elevation angle, the radar signal backscattered from each individual raindrop in the radar cell are superimposed. The Doppler processing is achieved by computing FFT on the radar signal time series with a coherent integration length of 256 samples. Considering a radar pulse repetition frequency of 20 kHz, the unambiguous Doppler velocity is 16 m/s and the Doppler velocity resolution is 0.12 m/s. For the Doppler velocity spectra of the raindrops at each radar cell, the peak Doppler velocity value is extracted to be representative of the local averaged radial velocity of raindrops, which can possibly depict the characteristics of the wake vortex field, because for the W band radar observation, the volume of each radar cell is small enough due to its high range and angular resolution.

In Figure 4.28, the average received power and the corresponding peak Doppler velocity at each radar cell as a function of the elevation angle are illustrated separately. The simulated results are very similar to the W-Band Radar observation in [27]. Various conclusions can be drawn:

(1) In the scanned radar reflectivity map, there are two columns with reduced reflectivity from raindrops due to the presence of a pair of wake vortices;

(2) Between these two columns, there are several radar cells with enhanced radar reflectivity due to the enhanced concentration of raindrops within wake vortices;

(3) The difference in the radar reflectivity level is about 6 dB (the absolute value is not comparable as the number of simulated raindrops is far lower than the actual one to get reasonable computing times);

(4) For the retrieved peak Doppler velocity map, both the negative and positive peak Doppler velocities are obtained in radar cells around the vortex cores asymmetrically;

(5) This kind of information on the radial velocity of raindrops within wake vortices is critical to estimate the vortex circulation for air traffic control application, as related to the danger associated with a wake vortex encountering;

(6) It has to be noticed that due to the low dimensions of the radar cells and the low number of simulated drops the simulated doppler information is not relevant in the radar cells with an extremely low reflectivity (i.e under the vortex cores).

4.5.2 W band radar time-evolving signatures: Simulator B

In [27], the temporal evolution of the wake vortex pair was observed by W band radar according to the recorded data at different times. In the experiment of March 26, 2009, the vortices were shown to move upwards and out of the RHI scanning region in 60 seconds, in contrast to normal behavior, which exhibits downward transport due to the mutual interaction of the two vortices. In the experiment of May 5, 2009, the vortices were generated in a complex atmosphere exhibiting both horizontal and vertical shear and the results illustrated the wake vortices drifted downwards from the height of around 32 m, and within around 20 seconds, were under the influence of ground effects.

In the above section, the W band radar signatures have been simulated, assuming that the raindrop's distribution in wake vortices is stationary. In order to better illustrate the W band radar signatures and interpret the physical phenomena observed by [27], the raindrop's time-evolving number concentration and velocity distribution in wake vortices as shown from Figure 3.15 to 3.20 in Section 3.3 are considered here for radar signatures simulations. Meanwhile, the Simulator $\mathbb{B}$ is adopted to simulate the time-evolving radar signatures of raindrops because it requires too much computation load to simulate the time-evolving raindrops.

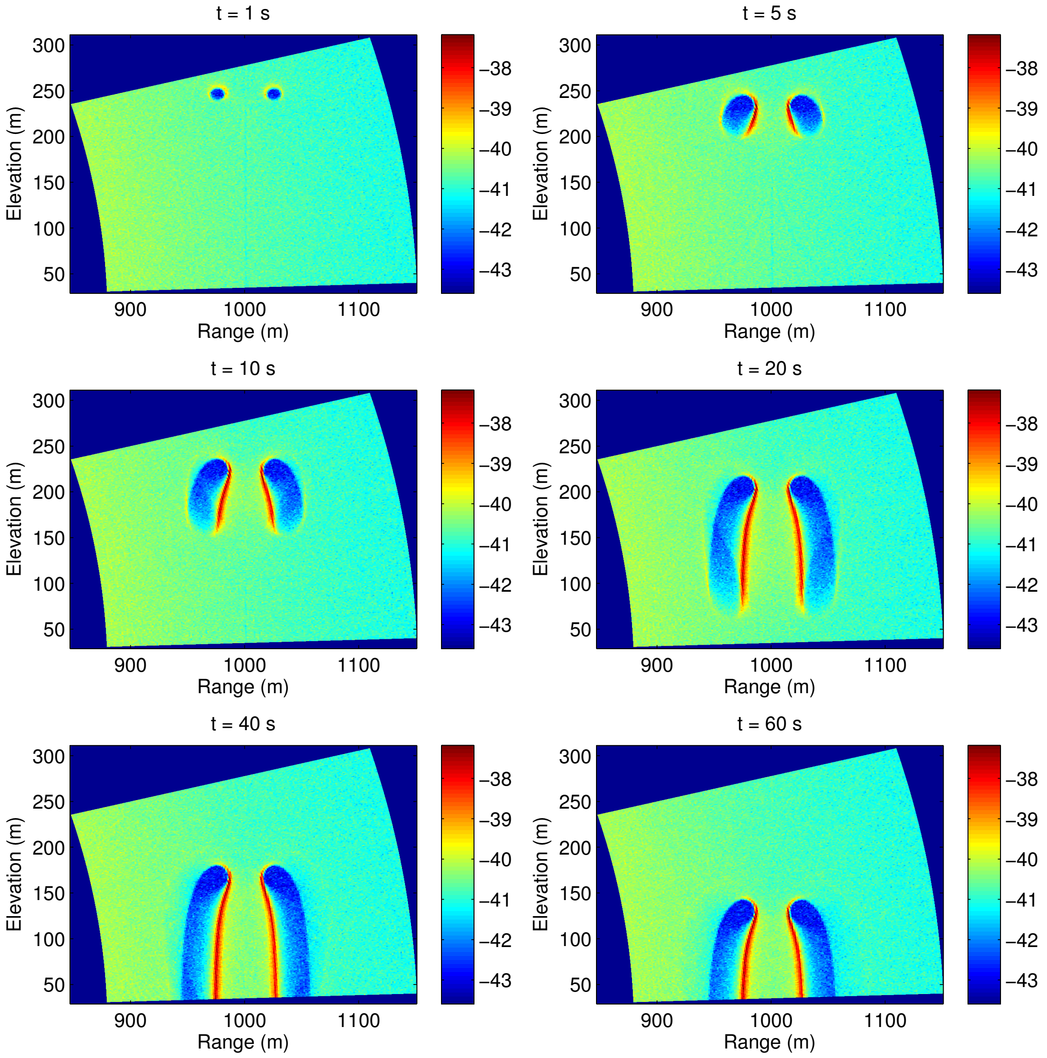

Figure 4.29: W band radar signatures of raindrops at different times for a rain rate of 2 mm/h: average received power

In this simulation, the parameters of W band radar, wake vortex and raindrops are the same as those used in Section 4.5.1. At $t = 0$, the raindrops are falling at their terminal falling velocity and their distributions in the simulation region are assumed to be the same as in still air. For raindrops of each diameter class, their number concentration and velocity distribution at each time step are updated by the methodology in Section 3.3.3. The rain rate is set to be 2 mm/h, the raindrop size distribution (DSD) model in still air is computed by Equation (2.13) and the raindrops' radar cross section (RCS) are computed by Mie formulas in Equation (2.15). Combining the raindrops' distribution in wake vortices for each diameter class, the radar average received power and Doppler velocity spectrum in each radar cell are then computed. For the Doppler velocity spectrum of the raindrops in each radar cell, the peak Doppler velocity value is extracted to be representative of the local averaged radial velocity of raindrops, which can possibly depict the characteristics of the wake vortex field.

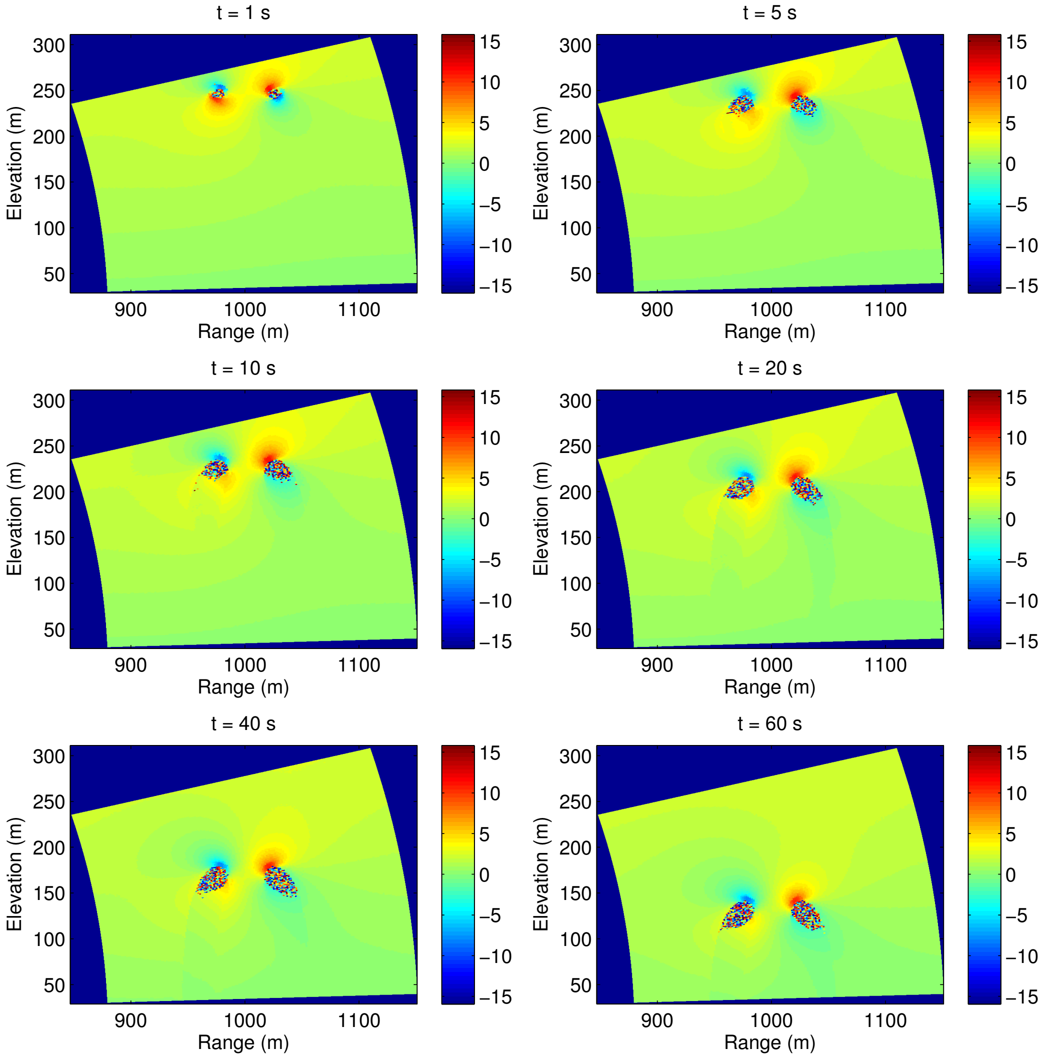

Figure 4.30: W band radar signatures of raindrops at different times under rain rate of 2 mm/h: peak Doppler velocity profile

In Figure 4.29, the radar average received power of raindrops in each radar cell are illustrated for different times (t = 1 s, 5 s, 10 s, 20 s, 40 s and 60 s). In

Figure 4.30, the peak Doppler velocity profiles of raindrops in each radar cell are illustrated for different times ($t = 1$ s, 5 s, 10 s, 20 s, 40 s and 60 s). The simulation results show preliminary agreement with the phenomena observed in [27]. From the simulated results, it is easy to find that in the radar cells below the wake vortices, the average received power exhibits both enhanced and reduced power levels. There are two columns which have a reduced average power and between these two columns there are two strip-shaped regions where the average received power is reduced. As time evolves, the length of the two columns and the two strip-shaped regions is increasing and their locations are moving downwards as expected, due to descent velocity induced by mutual interaction between two vortices.

4.6 Conclusions

In this chapter, the X band and W band radar signatures of raindrops in wake vortices have been modeled and simulated by two methodologies.

One methodology (Simulator A) is based on the simulation of radar signal time series, by superimposing the radar backscattered signal from each individual raindrop in each radar cell in the wake vortex region. The main interest of this methodology is that the outputs can be directly given to test radar signal Doppler processing chains. For practical application and exploitation, it demands too large memory usage and long computation time as the population of raindrops in the radar scattering volume increases.

Another methodology (Simulator B) is based on the raindrops' number concentration and velocity distribution in wake vortices, by integrating the contribution of radar average received power and Doppler signatures from each diameter class of raindrops in the radar cell. The radar signatures of raindrops in wake vortices under different rain rates or DSD models can be simulated very easily as the database of the raindrop's distribution is computed for raindrops of each diameter class, independent of the rain rate and DSD model.

Regarding the advantages of these two simulation methodologies, typical X band and W band radar parameters have been used to compute the radar signatures of raindrops in wake vortices.

For X band radar simulations, two radar configurations have been considered: staring mode and scanning mode. In staring mode, the Simulator A is adopted. It has been shown that the simulated particular shape of the Doppler spectrum of the raindrops within wake vortices can provide potential information for identifying wake vortex hazard in air traffic control. In scanning mode, the Simulator B is adopted and two kinds of radar deployment are analyzed respectively: under flight path and close to runways. The simulated fluctuations of radar reflectivity indicates an enhancement and a reduction of the concentration of raindrops at different positions of the wake vortices region. The simulated periodically extended Doppler velocity spectra implies the velocity distribution of raindrops in wake vortices, the geometrical relationships between the radar antenna beam and vortex cores and the motion of wake vortices due to descent velocity or cross wind. The simulated radar signatures are also compared with the results from Thales radar data in [26, 45] and the effectiveness of the simulator is preliminarily validated

For W band radar simulations, the two simulators are both tested and exploited. The radar is working in vertical scanning mode. From the results by Simulator A, the enhanced or reduced concentration of raindrops between the two vortex cores due to the influence of vortex flow is clearly observed by analyzing the average received power of raindrops in each radar range cell, to some extent, this phenomenon is consistent with the experimental results in [27]. From the results by Simulator B, the radar signatures of raindrops in wake vortices are obtained at different times, exhibiting the temporal evolution of distribution of raindrops in wake vortices and the motion of wake vortex pair under the effect of descent velocity.

Chapter 5

Interpretation of wake vortex radar signatures

In the previous chapter, radar parameters pertaining to different configurations used in recent experiments have been used to simulate the radar signatures of raindrops in wake vortices. The radar reflectivity and Doppler spectrum have been shown to be representative of the number concentration and velocity distribution of raindrops in each radar cell. Considering the analysis made in chapter 3, on the Stokes number of the flow, the issue is now to relate the local flow velocity field to the radar Doppler spectrum of the raindrops. In particular, the Doppler spectrum are broadened if the raindrops are disturbed by wake vortices. There are different factors that may affect the broadening of radar Doppler spectrum, including environmental parameters such as rain rate (DSD model), wake vortex characteristics (circulation), and radar parameters (radial range resolution, antenna beam width, radar elevation angle, etc.). In this chapter, the dependence of radar signatures on those parameters is studied by adopting the methodologies proposed in Chapter 4. Furthermore, wake vortex detection method and the retrieval of wake vortex parameters from the Doppler velocity spectrum in scanning mode for radar deployed under flight path are studied, preliminary results show effectiveness of the proposed methodology.

5.1 Introduction

For radar observation of raindrops in wake vortices, the estimation of the three moments of Doppler spectrum is of prime importance. As shown in Figure 4.21, the raindrops' motion in the region between the two vortices may add a bias to the mean Doppler velocity as the Doppler velocity spectrum is shifted, and the raindrop's motion in left vortex or right vortex may increase the value of spectrum width as the Doppler velocity spectrum is broadened. The radar Doppler spectrum contains convoluted information about the motion of raindrops and the wake vortex characteristics.

Compared to the zeroth (radar average power) and first moment (mean Doppler velocity) of the Doppler spectrum obtained from Doppler weather radar, the Doppler spectrum width has limited operational applications [175, 193]. The difficulties in interpreting the radar Doppler spectrum widths mainly lie in the various sources of estimation errors and how to relate σ_v to various meteorological phenomena [175]. The estimation errors depends on a wide range of factors, especially the overlaid weather signals and low signal-to-noise ratios. In the following analysis, the efforts are concentrated in revealing the relationships between the moments of Doppler spectrum and various parameters of rain, radar and wake vortex, thus, the signal-to-noise ratio is assumed to be sufficiently high.

5.2 Dependence of radar signatures on rain rate

In this section, the impact of rain rate on radar signatures of raindrops in wake vortices is analyzed. Rain rate is a measure of the rainfall intensity. For a given DSD model as illustrated in Chapter 2, the raindrops size distributions vary under different values of rain rate. For radar measurements of precipitation in still air, the rain rate can be obtained either by retrieving the DSD from the Doppler spectrum or using empirical relations [194], thus the Doppler spectrum exhibit a dependence on the rain rate whose magnitude depends on the radar configurations. For radar observations of raindrops in wake vortices, the situation is more complicated. It has been shown in Chapter 3 that the raindrops' distribution in wake vortices is not homogeneous, thus, the raindrops' distribution in each radar cell is different, depending on the relative position between the radar cell and the wake vortex. Therefore, it is much more difficult to retrieve the raindrops' distribution in wake vortices from the Doppler spectrum as usual retrieving methodologies are no longer effective.

In order to analyze the dependence of radar signatures on the rain rate, the X band radar signatures of raindrops in A320, A340 and A380 aircraft wake vortices

Table 5.1: Input parameters for Radar signatures interpretation

Parameters	Values
Radar frequency	10 GHz
Transmitted peak power	5000 W
Noise figure	4 dB
System Loss	6 dB
Antenna gain	39 dB
Beam width	$2^\circ \times 2^\circ$
Distance of wake vortex	1000 m
Pulse Repetition Frequency	3348 Hz
Number of pulses	256

are simulated respectively. The parameters corresponding to an A320, A340 and A380 are the same as shown in Table 2.1. The descent velocity of wake vortex pair and the vortex circulation decay are both taken into account in the simulation of wake vortex velocity field. The radar parameters are given in Table 5.1. In order to better illustrate the impacts of wake vortices on the raindrops' motion and distribution, the range resolution which can cover most of the raindrops near the two vortices should be of great interest. Thus, the radar range resolution and radar beam width are chosen to meet this requirement. The distance from radar to the wake vortex is set to be 1000 m and the radar antenna beam width is of $2^\circ \times 2^\circ$. For monitoring the wake vortices of A320, A340 and A380, the radar range resolution is set to be 60 m, 100 m and 120 m respectively. It is chosen so that the range resolution is around two times the vortex core separation. For comparison of the radar geometry configurations, the radar is assumed to be close to runway with an elevation angle of 2°, as well as under flight path with an elevation angle of 90°.

For raindrops, the minimum and maximum diameters are 0.5 mm and 4.0 mm respectively, and the diameter interval is 0.0625 mm. Five values of rain rate are considered here: 2 mm/h, 5 mm/h, 10 mm/h, 20 mm/h and 50 mm/h. After computing the raindrop size distribution (DSD) model in still air as given by equation (2.13), the raindrops' radar cross section (RCS) as given by equation (2.14) and the raindrops' distribution in wake vortices for each diameter class, the radar Doppler velocity spectrums of raindrops in the radar cell are then computed by the methodology in Section 4.2.2. The noise powers at each Doppler velocity bin are also simulated according to the input radar parameters. In Figure 5.1, the radar average received power for wake vortices of A320, A340 and A380 for different rain rates

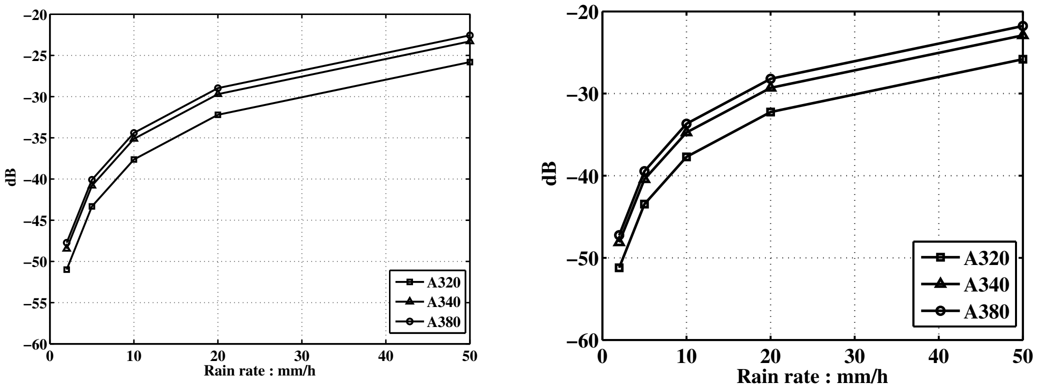

(a) Elevation angle: 2°

(b) Elevation angle: 90°

Figure 5.1: Radar average received power of raindrops in wake vortices of A320, A340 and A380 for different rain rates

are illustrated. The radar received power is increasing with the rain rate and with the radar resolution volume. The power level dependence on the aircraft type has only to be related to the increase of the resolution volume and does not constitute a good indicator for detection.

In Figure 5.2, the radar Doppler velocity spectra of raindrops in wake vortices of A320, A340 and A380 at time 30s are illustrated for different rain rates. It is easy to find that for raindrops in wake vortices, the rain rate has an impact on the spectrum power level, however, the shape of their Doppler spectrum is not too much depending on rain rate, and is not the same as for the raindrops in still air. This phenomenon can be explained by the contribution of raindrops' radial velocities due to the transport by wake vortex flow. For radar monitoring at an elevation angle of 2°, the Doppler spectrum of raindrops in still air is usually very narrow due to the very small radial velocity component, but for raindrops in wake vortices, the radial velocity components are affected by the wake vortex flow. For radar monitoring at an elevation angle of 90°, the Doppler spectrum of raindrops in still air is usually determined by the raindrops' size distribution which is depending on the rain rate, however for raindrops in wake vortices, their vertical velocity distribution is also affected by the wake vortex flow. Therefore, the Doppler spectrum of raindrops in wake vortices generated by A380 is always more broadened than those by A320 and A340.

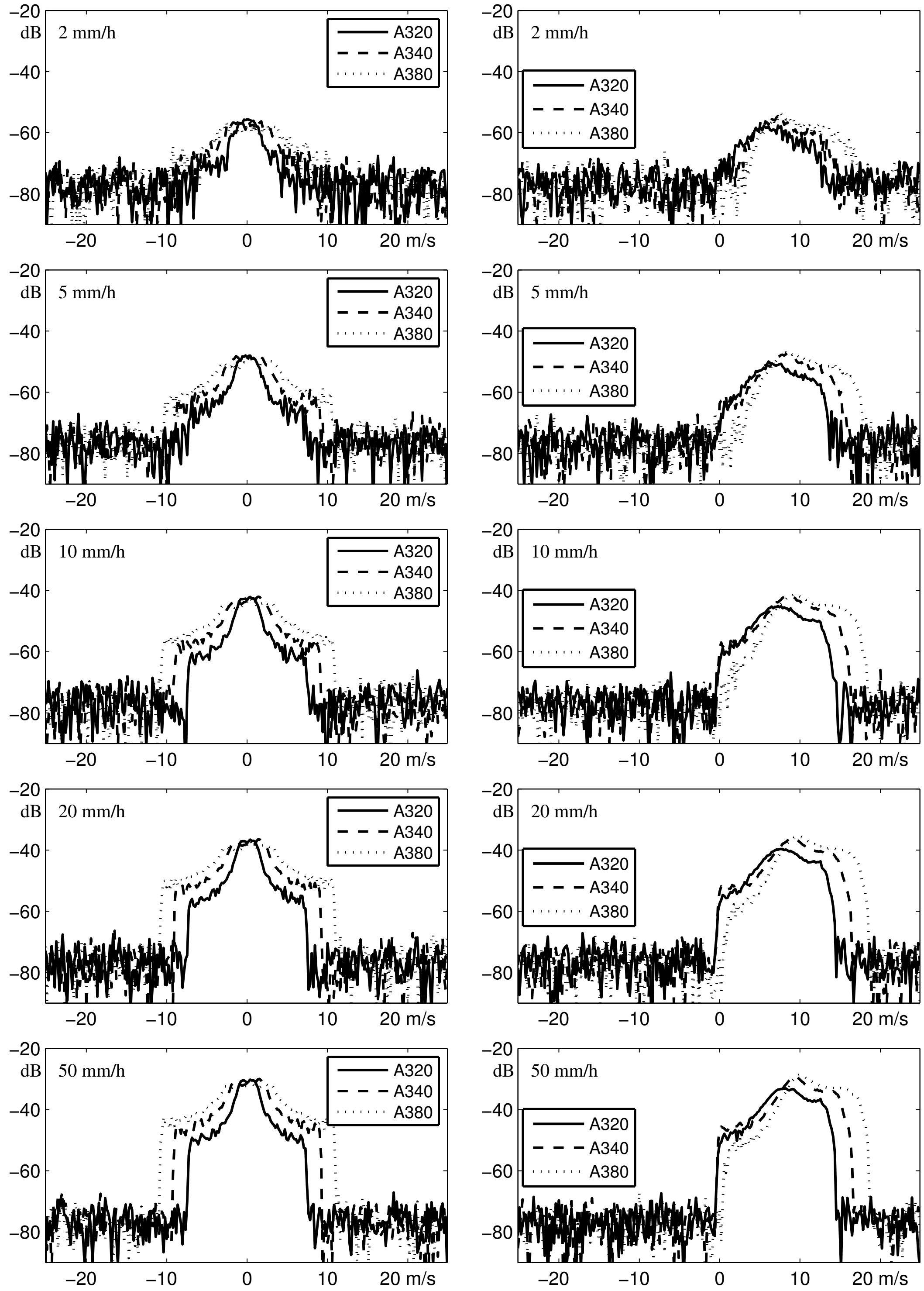

(a) Elevation angle: 2°

(b) Elevation angle: 90°

Figure 5.2: Radar Doppler velocity spectrums of raindrops in wake vortices of A320, A340 and A380 for different rain rates after 30s of simulations

Table 5.2: Some typical circulation values of A320, A340 and A380 wake vortex

Wake vortex volution time(s)	5	30	60	90	120
Circulation(A320: m^2/s)	276.5	232.2	178.9	125.7	72.47
Circulation(A340: m^2/s)	525.9	475.9	415.9	345.8	295.8
Circulation(A380: m^2/s)	874.5	795.6	700.9	606.2	511.5

5.3 Dependence of radar signatures on wake vortex circulation

In Section 3.2.4, the dependence of raindrops' trajectory on wake vortex circulation has been illustrated, showing that the motion characteristics of raindrops in wake vortices is representative of the vortex strength. In fact, wake vortex circulation has a determinative effect on the wake vortex velocity field, thus determining the raindrops' motion and distribution in wake vortices. Therefore, it is very interesting to infer the underlying wake vortex circulation information from the radar signatures. In this section, the dependence of radar signatures on wake vortex circulation is analyzed.

The radar simulation parameters are the same as in the previous section. The wake vortex circulation decay model given by Equation (2.8) is adopted here. The wake vortex circulation as a function of time has been illustrated in Figure 2.9 of Section 2.1.2 for an A320, A340 and an A380. Some typical circulation values of A320, A340 and A380 wake vortex are listed in Table 5.2. The total time for radar simulation is 120 s. In order to concentrate only on the analysis of the effect of vortex circulation, the distance from radar to the wake vortex is assumed to be constant, that is, the descent velocity of wake vortex pair is not taken into account.

The radar signatures of raindrops in wake vortices of an A320, A340 and A380 are computed for the time steps t = 5 s, 10 s, 15 s, 20 s, 25 s, 30 s, 40 s, 50 s, 60 s, 70 s, 80 s, 90 s, 100 s, 110 s and 120 s and for elevation angles of 2° and 90°. At each time step, the wake vortex circulation is updated according to the evolution model. In Figure 5.3, radar Doppler velocity spectra of raindrops in wake vortices at different evolution times are illustrated, the rain rate is 10 mm/h. From the results it can be noticed that, the shape of Doppler spectrum of raindrops in wake vortices is varying with time. For raindrops in A320 and A340 wake vortices, the broadening of Doppler spectrum is degraded as time increases, at time t = 120 s, the shape of Doppler spectrum tends to be the same as the one in still air due to the vortex circulation decay. For raindrops in A380 wake vortices, the broadening of Doppler

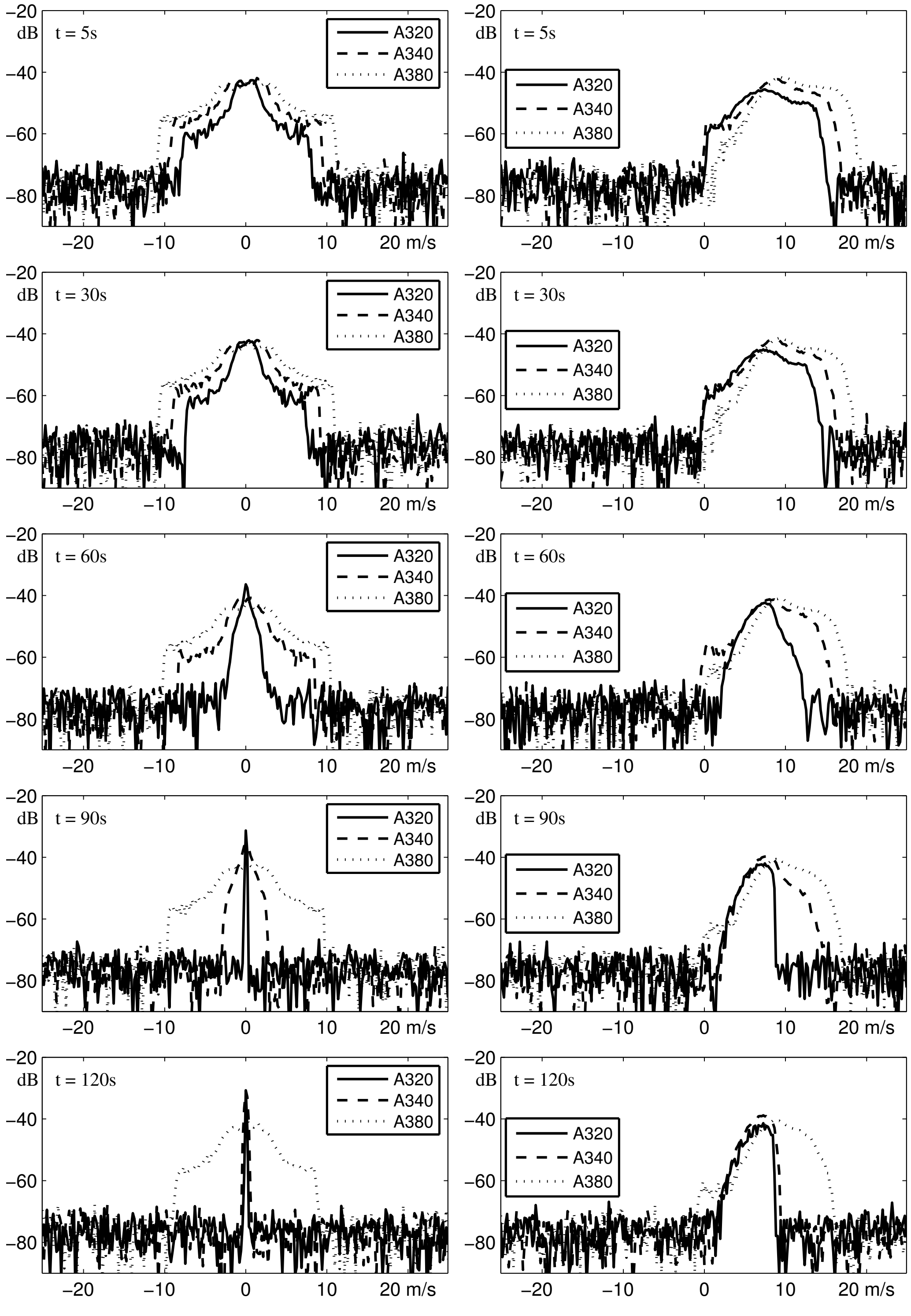

(a) Elevation: 2°

(b) Elevation: 90°

Figure 5.3: Radar Doppler velocity spectrum at different evolution times

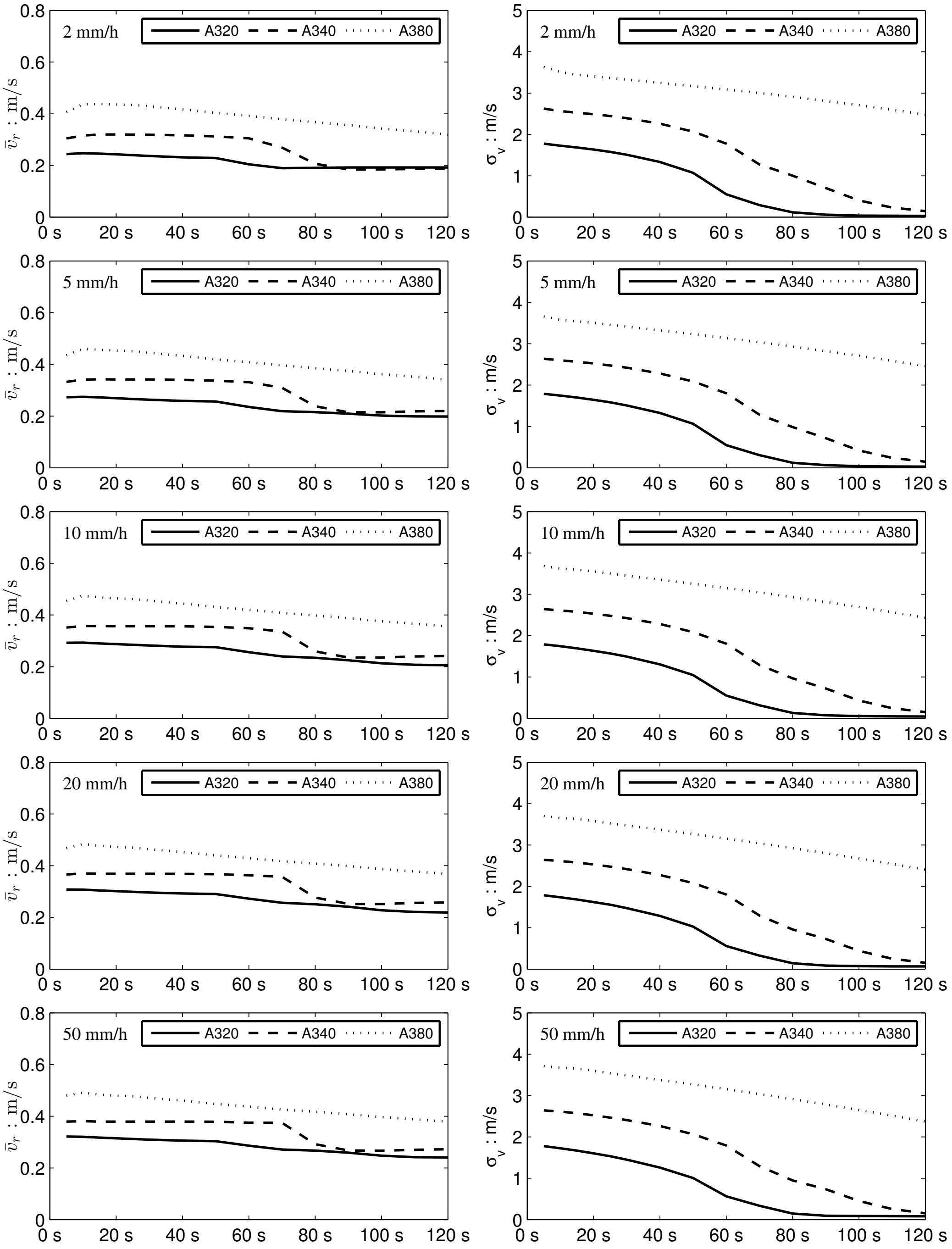

(a) Mean Doppler velocity (b) Doppler spectrum widths

Figure 5.4: Mean Doppler velocity and spectrum widths of raindrops in wake vortices as a function of the evolution time for different rain rates (Elevation angle: 2°)

spectrum is only lightly degraded, because at time t = 120 s, the A380 wake vortex circulation is still large enough to affect the raindrops' motion and distribution.

In order to better illustrated the effect of wake vortex circulation on raindrops' Doppler spectrum, the mean Doppler velocity and spectrum widths of raindrops as a function of evolution time for different rain rates are illustrated in Figure 5.4 and 5.5. From those results the following conclusions can be drawn:

(1) Both the mean Doppler velocity and spectrum width of raindrops decrease with time, and the decay rates depend on the aircraft type and time. For raindrops in wake vortices of an A380, the mean Doppler velocity and spectrum width is decreasing slower than the ones of an A320 and an A340, as the wake vortex circulation of A380 is much larger.

(2) When the radar is monitoring at an elevation angle of 2°, the raindrops' horizontal velocity distribution in the radar cell is approximately symmetric. Thus the mean Doppler velocity is approximately 0.

(3) When the radar is monitoring at an elevation angle of 90°, most of the illuminated raindrops have an enhanced vertical velocity that is much larger than the terminal falling velocity in still air due to the effects of vortex flow. As the vortex circulation decays, these raindrops' vertical velocity tends to be the same as the terminal falling velocity in still air again. Thus the mean Doppler velocity of raindrops is decreasing with time.

(4) The Doppler spectrum width is representative of irregularities of raindrops' motions due to wake vortex flow. For raindrops in an A320 wake vortices, the Doppler spectrum width tends to be constant (or the same as in still air) after t = 80 s for monitoring at 2° and after t = 60 s for monitoring at 90° respectively. This phenomenon implies a minimum circulation value Γ_{min} to broaden the Doppler spectrum of raindrops, that is to say, if the wake vortex circulation decays to a value smaller than Γ_{min}, the effect of wake vortex on raindrops' motion is no longer significant and the Doppler spectrum of raindrops in wake vortices is the same as the one in still air, thus incapable of providing critical information on the existence of wake vortex.

5.4 Dependence of radar signatures on radar parameters

Besides the rain rate and wake vortex circulation, the radar parameters such as antenna beam width, elevation angle and radial range resolution, are also very

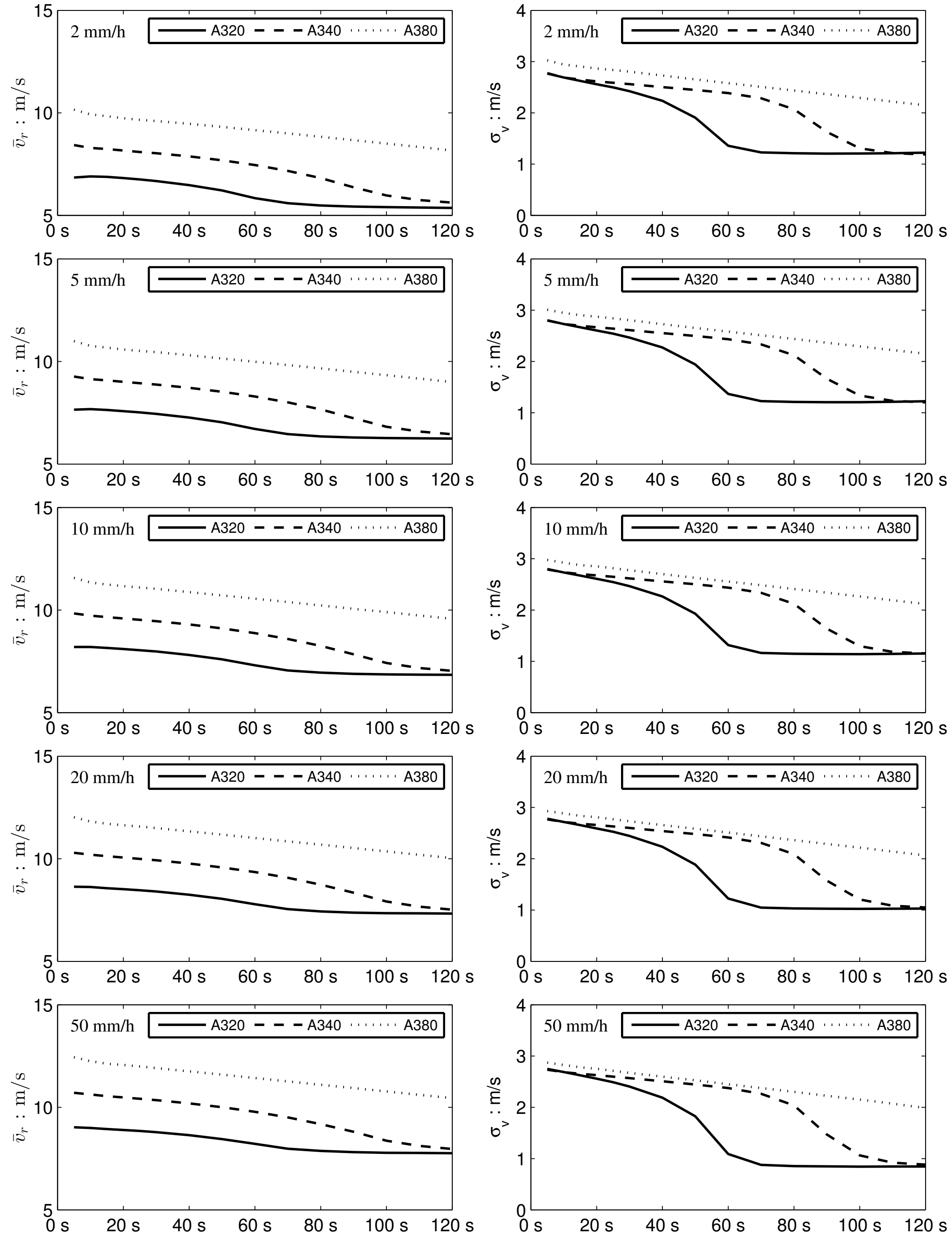

(a) Mean Doppler velocity (b) Doppler spectrum widths

Figure 5.5: Mean Doppler velocity and spectrum widths as a function of evolution time for different rain rates (Elevation angle: 90°)

critical factors affecting the Doppler spectrum shape. Here only the effects of the antenna elevation angle and radial range resolution of X band radar is considered and analyzed.

5.4.1 Effects of radar antenna elevation angle

For raindrops in still air, the Doppler spectrum is largely depending on the radar antenna elevation angle, as the radial velocity of raindrops in the radar cell varies with the antenna elevation angle. For raindrops in wake vortices, their Doppler spectrum should vary as the radar antenna scans. In the simulation, the distance between radar and wake vortex is set to be constant and the radar antenna elevation angles of $2°, 10°, 30°, 60°$ and $90°$ are considered. In Figure 5.6, the Doppler velocity spectrum of raindrops in wake vortices at different elevation angles are illustrated for times $t = 30$ s and 90 s. At time $t = 30$ s, the strength of A320, A340 and A380 wake vortices is still large enough to broaden the Doppler spectrum of raindrops in them. As the antenna elevation angle varies from $2°$ to $90°$, the Doppler spectrum of raindrops in wake vortices is changing in shape and shifting along the Doppler bin axis. At time $t = 90$ s, the strength of A320 wake vortices is small and the Doppler spectrum of raindrops is almost the same as that in still air, as the antenna scans from from $2°$ to $90°$, the mean Doppler velocity is shifting and the Doppler spectrum width is increasing with the elevation angle. The strength of A380 wake vortices is still large enough, thus the Doppler spectrum is also changing its shape and shifting along the Doppler bin axis when the antenna elevation angle varies. This phenomenon on the Doppler spectrum of raindrops in wake vortices under different antenna elevation angles is very helpful for designing new radar antenna scanning strategies over the wake vortex region.

5.4.2 Effects of radar radial range resolution

Radar radial range resolution is one of the key element determining the size of scattering volume and thus the number and distribution of raindrops in the radar cell. In Section 4.3.2, the radar Doppler spectrum of raindrops in wake vortices have been presented for range resolutions of 40m and 100m while the radar is working in staring mode, revealing the dependence of radar signatures on range resolution. Here the effects of range resolution on the radar signatures are studied for radar operating in scanning mode.

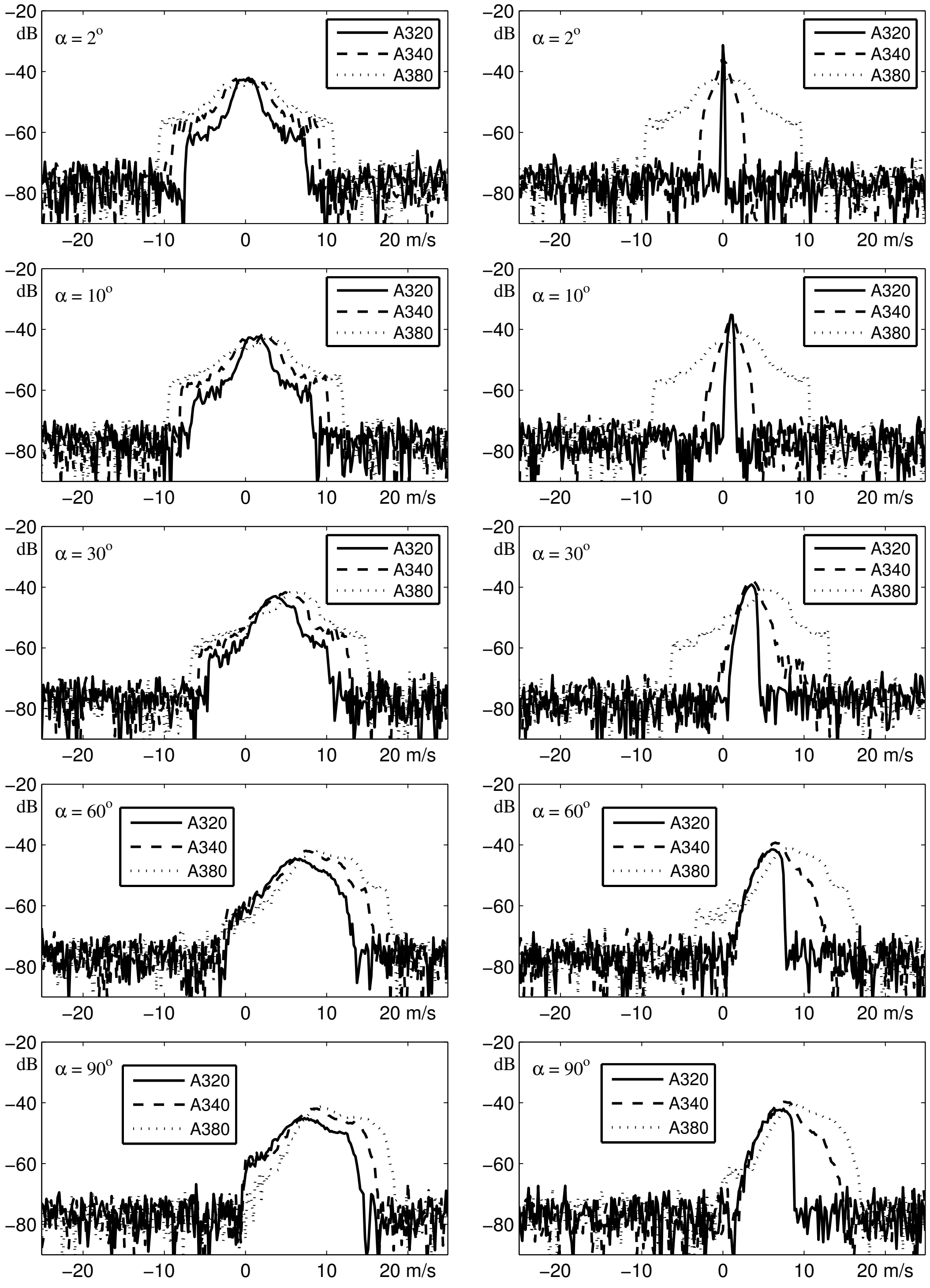

(a) t = 30s

(b) t = 90s

Figure 5.6: Doppler velocity spectrum of raindrops in wake vortices at different elevation angles

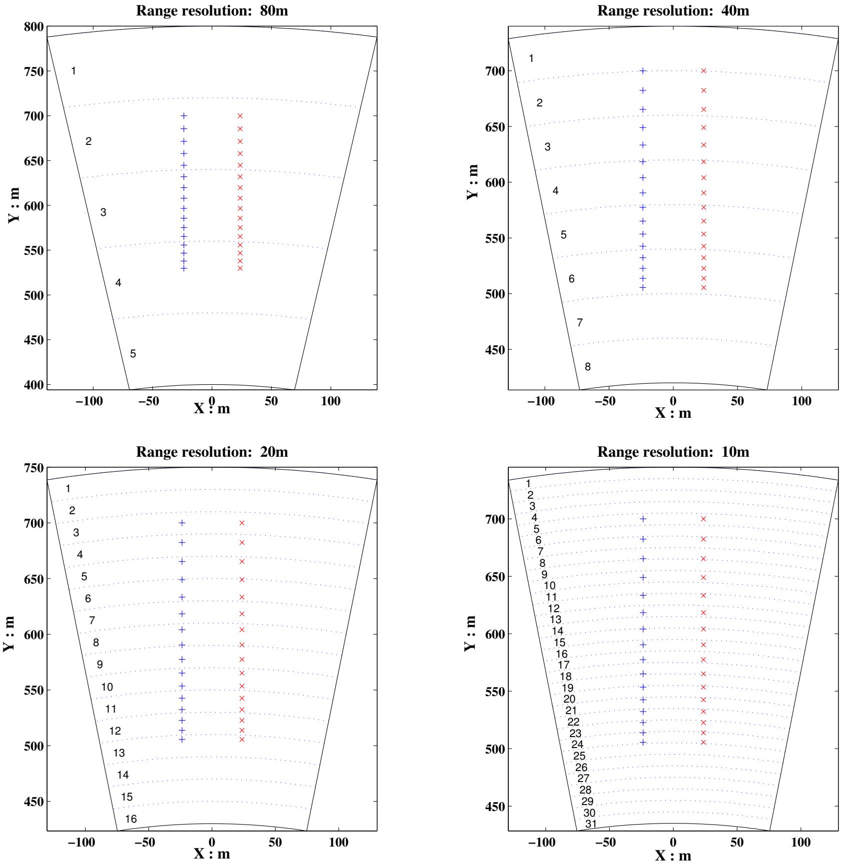

Figure 5.7: Radar geometry configurations for different radar range resolutions: 10 m, 20 m, 40 m and 80 m. +' and 'x' indicate the location of the left and right vortex respectively.

As shown in Figure 5.7, the radar geometry configurations are presented and four radar range resolutions, namely 80 m, 40 m, 20 m and 10 m, are considered. In each configuration, the radar is supposed to be deployed under the flight path and the 16 pairs of '+' and 'x' indicate the locations of wake vortex at various time steps ranging from $t = 0$ to $t = 150$ s with an interval of 10 s. The radar parameters are the same as those used in Section 5.2. The radar antenna is scanning from the elevation angle of 81° to 99° and then from 99° to 81° periodically, with a scanning rate of $8°/s$. The range weighting functions and antenna directivity are both taken into consideration. The total scanning time for the simulation is set to be 150 s, yielding to 65 scans if the range of elevation angle for one scan is 18° . During these 150 seconds, the wake vortex circulation is decaying and the wake vortex pair is descending as time increases. The circulation decay model given by

Equation (2.8) is utilized here and the descent velocity of vortex pair is assumed to be proportional to the vortex circulation. The raindrops' number concentration and velocity distribution also computed by the methodology proposed in Section 3.3. The rain rate is set to be 10 mm/h. After obtaining the radar reflectivity and Doppler spectrum of raindrops in each radar cell by the methodology in Section 4.2.2, the mean Doppler velocity and Doppler spectrum width are also computed.

In Figure 5.8, Figure 5.9, Figure5.10 and Figure 5.11, the radar reflectivity, mean Doppler velocity and Doppler spectrum width of raindrops are illustrated for range resolutions of 80 m, 40 m, 20 m and 10 m respectively. Comparing these simulation results, it is easy to come to the following conclusions:

(1) The effects of range resolution on radar signatures are significant according to the obtained radar reflectivity, mean Doppler velocity and Doppler spectrum width in each radar cell. For the highest resolutions of 10m or 20m, the radar signatures are reflecting a more detailed information about the local wake vortex flow which affects the raindrops' motion and distribution, and thus much more convincible for further wake vortex detection and parameter estimation.

(2) The radar reflectivity is representative of the total number and size distribution of raindrops in the radar cell. From the presented results, the enhanced and reduced radar reflectivity of raindrops in some radar cells may indicate the existence of wake vortex. The radar cells with enhanced reflectivity are located between the two columns of radar cells with reduced reflectivity. From the 5th scan to the 60th scan, the position of these two kinds of radar cells is descending, the number of this kind of radar cells is changing and the difference (in dBm^2/m^3) between the enhanced reflectivity and reduced reflectivity is also changing. This phenomena underlies the preferential concentration of raindrops in wake vortex flow and the evolution of raindrops' distribution in time, but it is still not enough for determining the exact location and strength of wake vortices.

(3) The mean Doppler velocity relates to the power weighted mean radial motion of raindrops. From the illustrated results, the mean Doppler velocity of raindrops is increased in some radar cells, and on each side of these radar cells, the mean Doppler velocity of raindrops is decreased in some other radar cells. As the radar is vertically pointing to the wake vortex with an elevation angle of around $90°/s$, the increased mean Doppler velocity implies that in these radar cells,

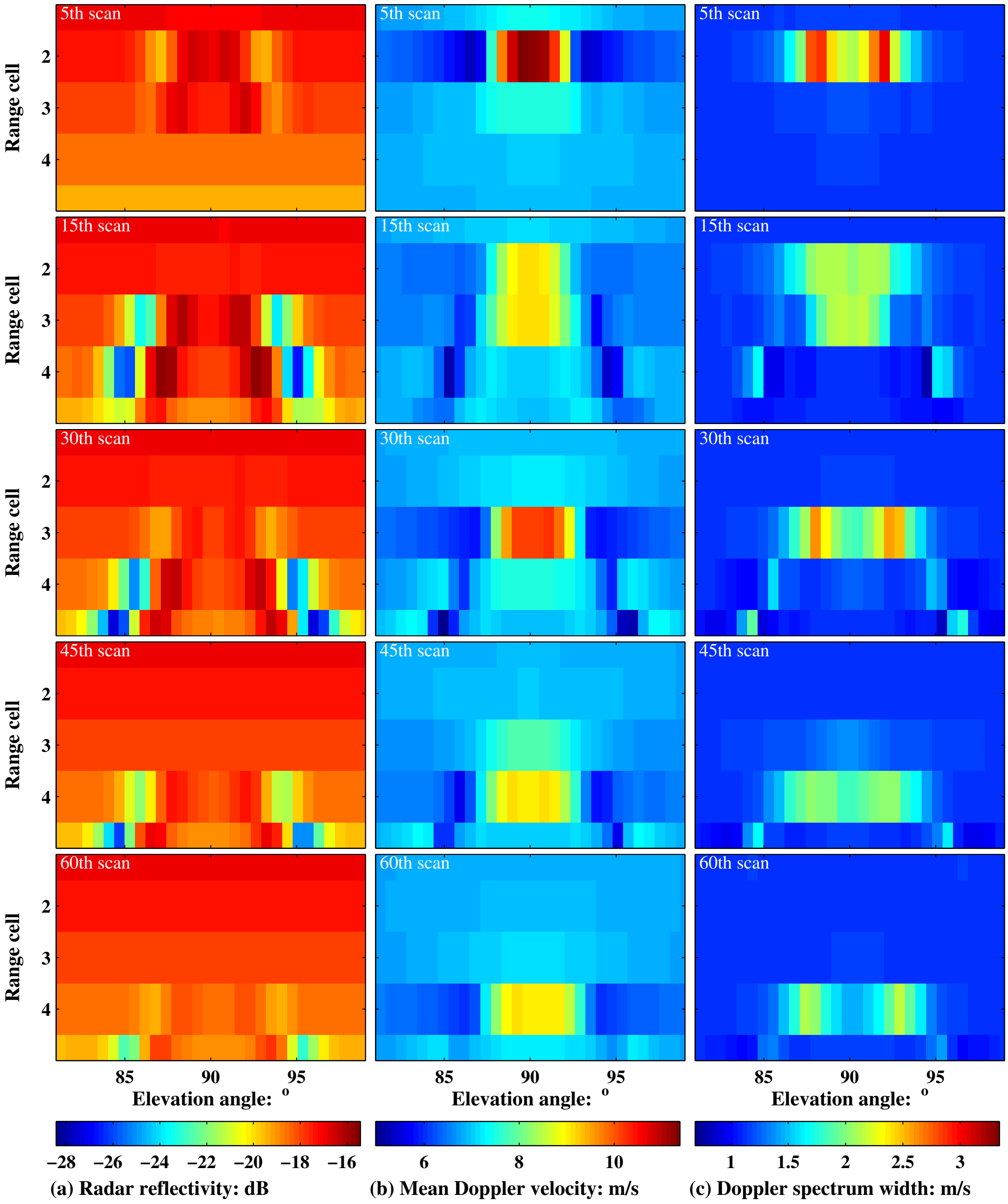

(a) Radar reflectivity: dB (b) Mean Doppler velocity: m/s (c) Doppler spectrum width: m/s

Figure 5.8: Radar signature of raindrops in wake vortices, range resolution: 80 m, observation under flight path

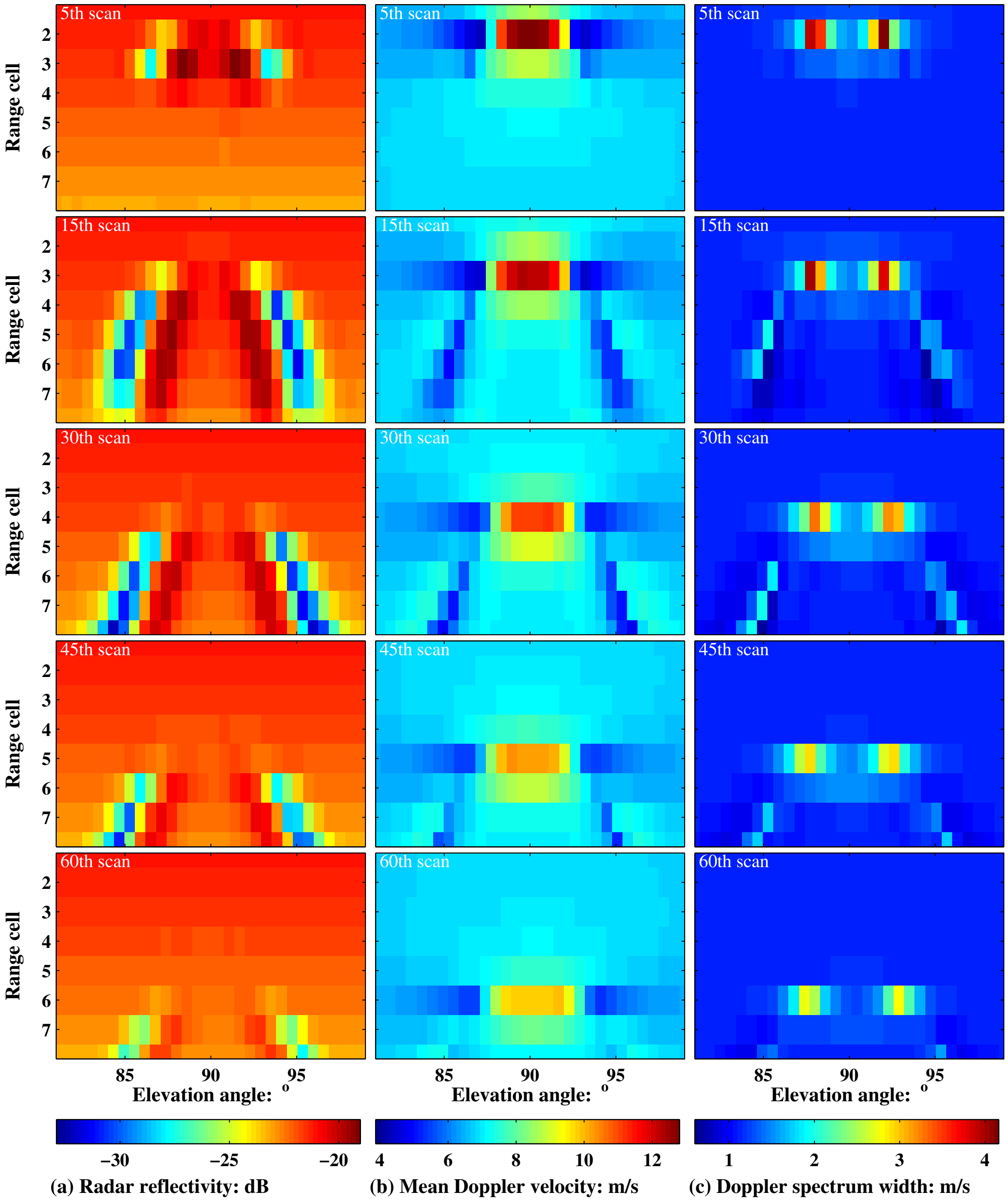

(a) Radar reflectivity: dB (b) Mean Doppler velocity: m/s (c) Doppler spectrum width: m/s

Figure 5.9: Radar signature of raindrops in wake vortices, range resolution: 40 m, observation under flight path

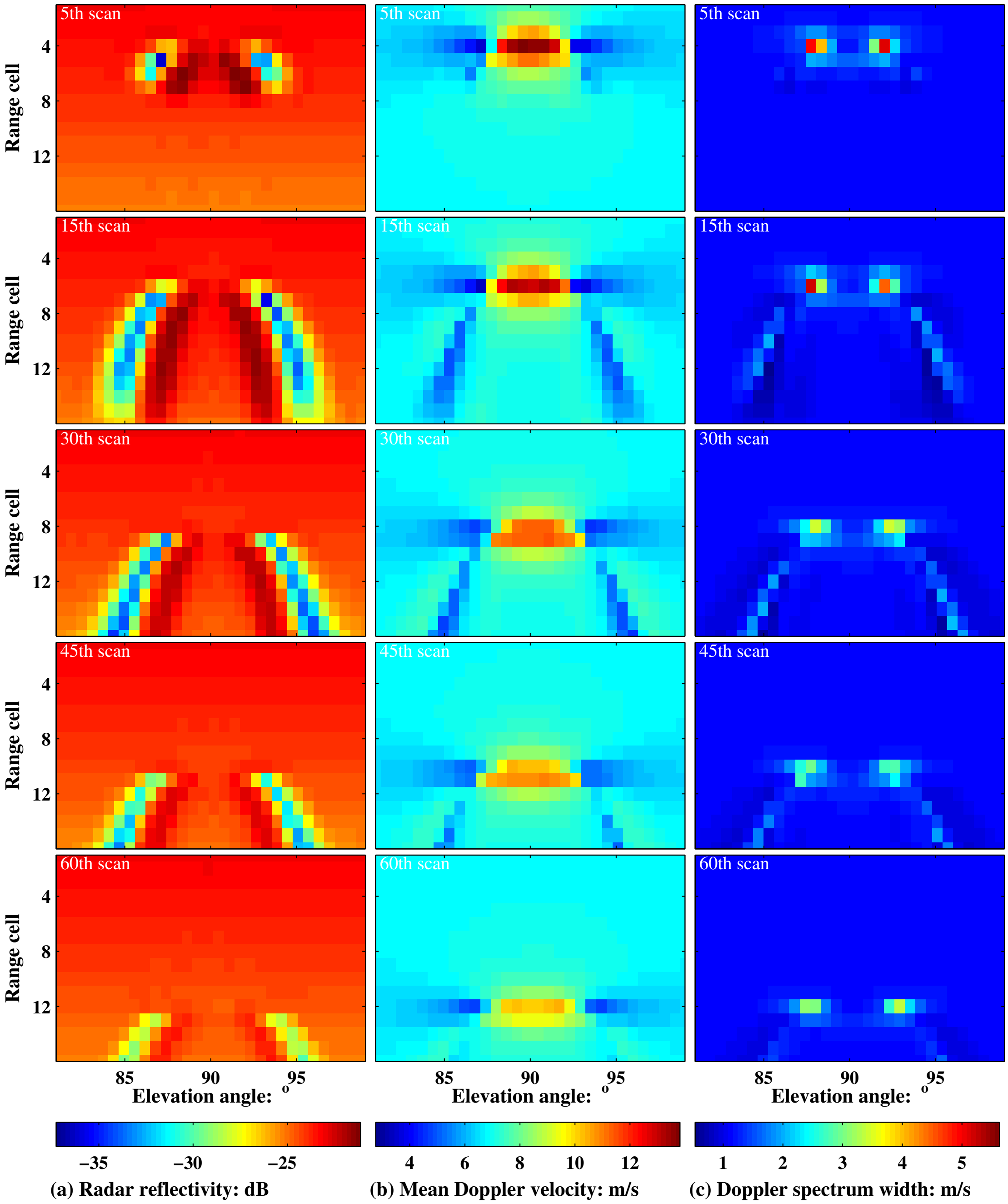

(a) Radar reflectivity: dB (b) Mean Doppler velocity: m/s (c) Doppler spectrum width: m/s

Figure 5.10: Radar signature of raindrops in wake vortices, range resolution: 20 m, observation under flight path

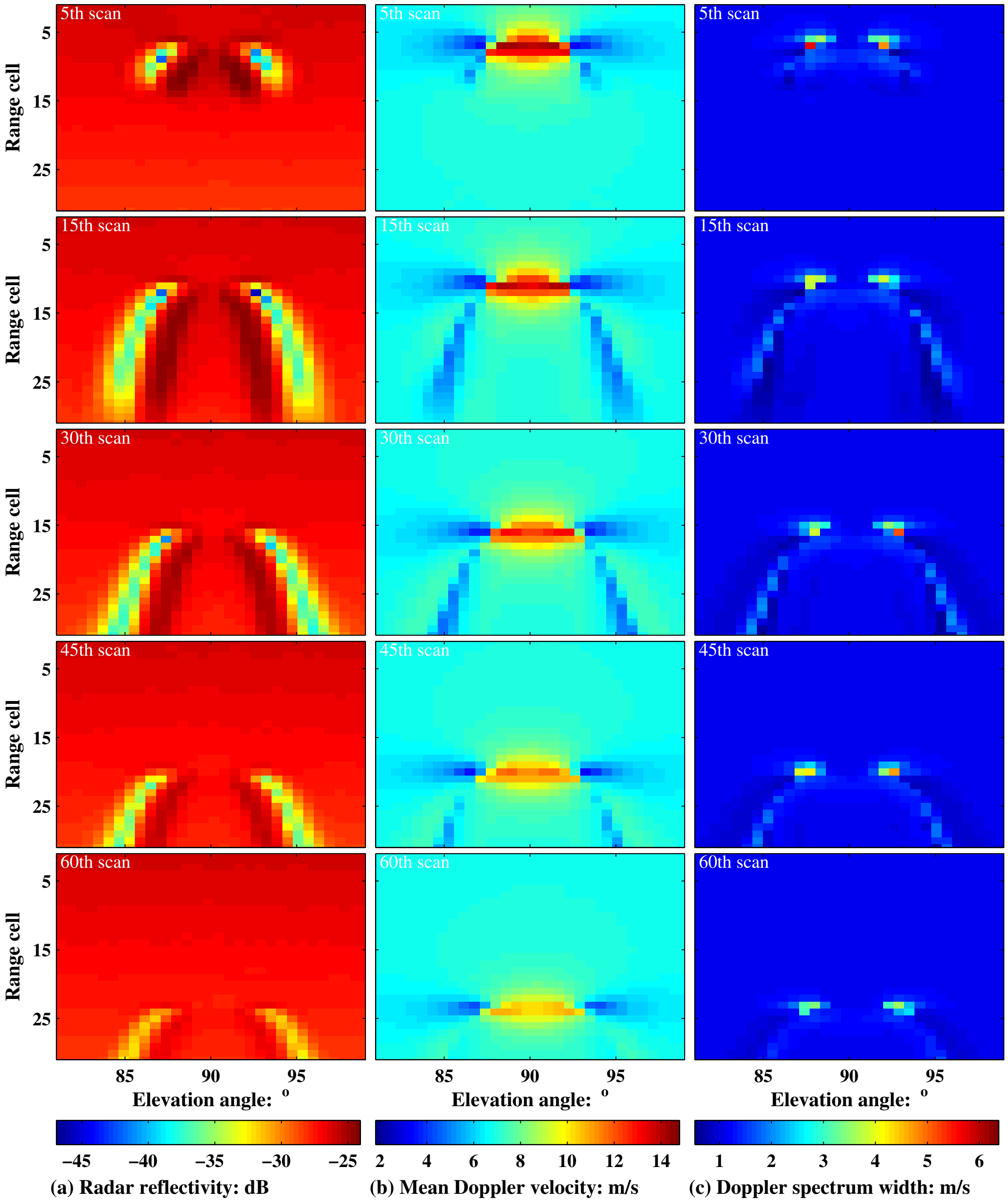

(a) Radar reflectivity: dB (b) Mean Doppler velocity: m/s (c) Doppler spectrum width: m/s

Figure 5.11: Radar signature of raindrops in wake vortices, range resolution: 10 m, observation under flight path

the vertical motion of raindrops is speeded up by the vortex flow, and the decreased mean Doppler velocity implies that in these radar cells, the vertical motion of raindrops is slowed down by the vortex flow. Thus, the obtained mean Doppler velocity of raindrops in each radar cell is a combination of the terminal falling velocity of raindrops in still air and the local flow velocity of wake vortex. Provided that the relationship between the velocity of raindrops in wake vortices, the terminal falling velocity of raindrops in still air and the local flow velocity of wake vortex could be established theoretically or empirically, it is possible to retrieve the wake vortex velocity field from the obtained radar reflectivity and mean Doppler velocity of raindrops in wake vortices.

(4) The Doppler spectrum width relates to the relative raindrop motions. From the illustrated results, there are two radar cells with obvious peaks in the Doppler spectrum width of raindrops for each scan, indicating the existence of two symmetric vortex cores at those locations. Actually, this phenomenon can be easily explained by the raindrops' trajectory in wake vortices as shown in Figure 3.2. Raindrops surrounding the wake vortex core move at various velocities and along various trajectories, thus their Doppler spectrum widths should be relatively large. Meanwhile, from the 5th scan to the 60th scan, the Doppler spectrum width tends to become smaller and smaller and the location of the peak values is descending. This phenomenon underlines the wake vortex circulation decay and the descent of the wake vortex pair, enabling the possibility of wake vortex detection and parameters estimation.

5.5 Wake vortex detection and parameters estimation

Based on the interpretation of raindrops' radar signatures in the above sections, it is possible to make some preliminary work on wake vortex detection and parameters estimation at this stage. The radar signatures of raindrops in wake vortices considering a range resolution of 10 m in Section 5.4.2 are utilized here for further study.

5.5.1 Wake vortex detection

Compared with other regular targets, wake vortex is a spatio-temporally evolving target. What distinguishes the wake vortex from the background atmosphere is

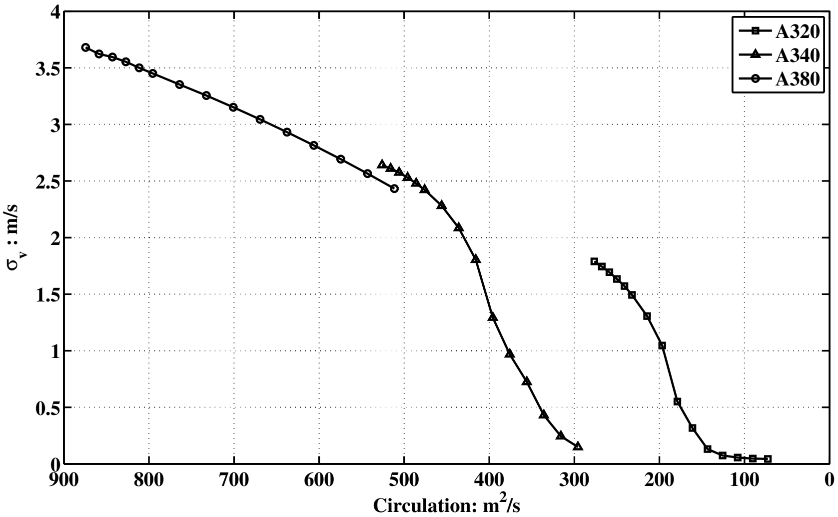

Figure 5.12: The Doppler spectrum width of raindrops is representative of wake vortex circulation

its Doppler signature due to the variability of velocity distribution inside or outside the wake vortices. In [195–198], the methods of information geometry have been introduced for wake vortex detection based on Doppler entropy. In [199], the detection algorithms are reviewed and executed by GPU parallel computation for real time wake vortex monitoring. However, in clear air, wake turbulence is always very difficult to be detected by Radar due to its low reflectivity.

As shown in Figure 5.12, the Doppler spectrum width of raindrops is representative of wake vortex circulation, as vortex circulation decays, the Doppler spectrum width of raindrops is decreasing. Here, the detection of wake vortex is achieved by the analysis of raindrops' Doppler spectrum width. Given the I & Q radar signal time series from a sequence of radar scans, the procedures for wake vortex detection can be summarized as the following:

(1) Computation of the Doppler velocity spectrum for raindrops in each radar cell and at each elevation angle;

(2) Estimation of the Doppler spectrum width by Equation 2.35;

(3) For the Range-Elevation map of Doppler spectrum width of raindrops at each scan, determination of the two radar cells with peak values of Doppler spectrum width by local peak detection algorithms.

In Figure 5.13, the wake vortex detection for the 11th scan is illustrated while

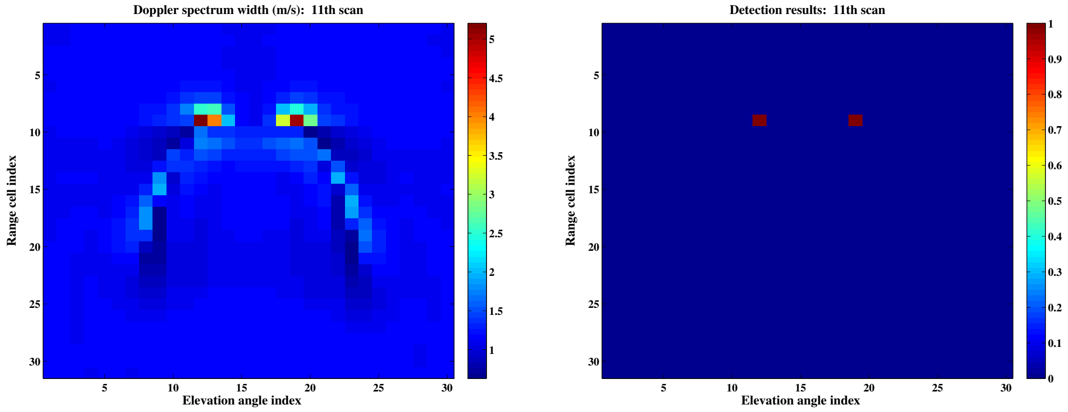

Figure 5.13: Wake vortex detection for the 11th scan (range resolution: 10m, under flight path observation)

the radar range resolution is 10 m, two peaks are detected at the 9th range cell, 12th elevation angle and the 9th range cell, 19th elevation angle respectively. The corresponding peak values of Doppler spectrum width are also obtained as 5.203 m^2/s and 5.045 m^2/s.

5.5.2 Wake vortex parameters estimation

The wake vortex parameters especially the vortex circulation are of great interest for air traffic control. The difficulty to retrieve the wake vortex parameters directly from the radar signatures of raindrops, is mainly due to the differences between the the motion of raindrops within wake vortex that is measured by the radar and the actual airflow [179]. However, considering some reasonable assumptions of the wake vortex decay model and descent velocity, it is possible to estimate the wake vortex parameters based on the wake vortex detection results from a sequence of radar scans.

Wake vortex position

For the Range-Elevation map of Doppler spectrum width at the kth ($k = 1, 2, \cdots, N_s$) scan, if the two local peaks are detected at ranges $r_1(k)$ and $r_2(k)$ and at elevation angles $\alpha_1(k)$ and $\alpha_2(k)$ respectively, the horizontal and vertical positions of the wake vortices can be obtained by:

$$\begin{cases} x_1(k) = r_1(k) * \cos(\alpha_1(k)); y_1(k) = r_1(k) * \sin(\alpha_1(k)); \\ x_2(k) = r_2(k) * \cos(\alpha_2(k)); y_2(k) = r_2(k) * \sin(\alpha_2(k)); \end{cases} \tag{5.1}$$

where $x_1(k),\ y_1(k)$ are the estimated horizontal and vertical locations of the left vortex and $x_2(k),\ y_2(k)$ are the estimated horizontal and vertical locations of the right vortex. In Figure 5.14, the estimated locations of the left vortex and right vortex from 65 scans of Doppler spectrum widths are illustrated. The estimated results show good agreement with the true locations of the wake vortices.

Vortex separation

In the previous simulation, no wind shear or atmospheric turbulence is taken into account. Thus, the separation between the two vortices can be considered as constant. Assuming that at the kth ($k = 1, 2, \cdots, N_s$) scan, the two vortices are detected by radar at the range of $r_1(k)$ and $r_2(k)$ and at the elevation angle of $\alpha_1(k)$ and $\alpha_2(k)$ respectively, thus according to the geometry configuration relationship, the vortex separation is given by:

$$b_0(k) = \sqrt{r_1(k)^2 + r_2(k)^2 - 2r_1(k)r_2(k)cos[\alpha_1(k) - \alpha_2(k)]} \tag{5.2}$$

and the estimation of vortex separation can be obtained from the average value of vortex separation at each scan, that is:

$$\widehat{b_0} = \frac{1}{N_s}\sum_{k=1}^{N_s} b_0(k) \tag{5.3}$$

In Figure 5.15, the vortex separation $b_0(k)$ computed from 65 scans is illustrated. The estimation of vortex separation is thus obtained as $\widehat{b_0} = 48.53$ m , while the separation between the two vortices generated by an A340 is $b_0 = 47.36$ m. As the vortex pair descends at a downwash velocity induced by the mutual interaction between two vortices, during the time for radar scanning from α_1 to α_2 at the kth scan, the distance the vortex pair descends is given by:

$$\Delta h(k) = \frac{|\alpha_1(k) - \alpha_2(k)|}{\omega_s} v_d(k) \tag{5.4}$$

where ω_s is the radar antenna scanning rate and $v_d(k)$ is the instantaneous descent velocity at the kth scan. It is easy to see that the distance $\Delta h(k)$ is inversely

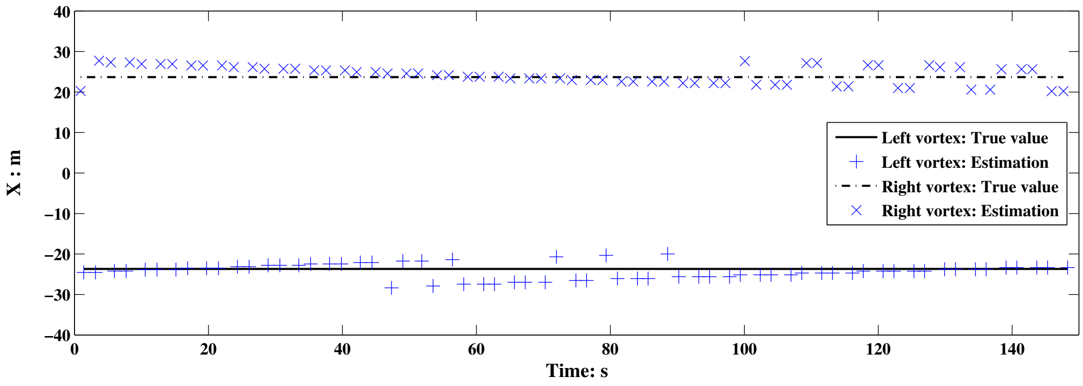

(a) Horizontal location

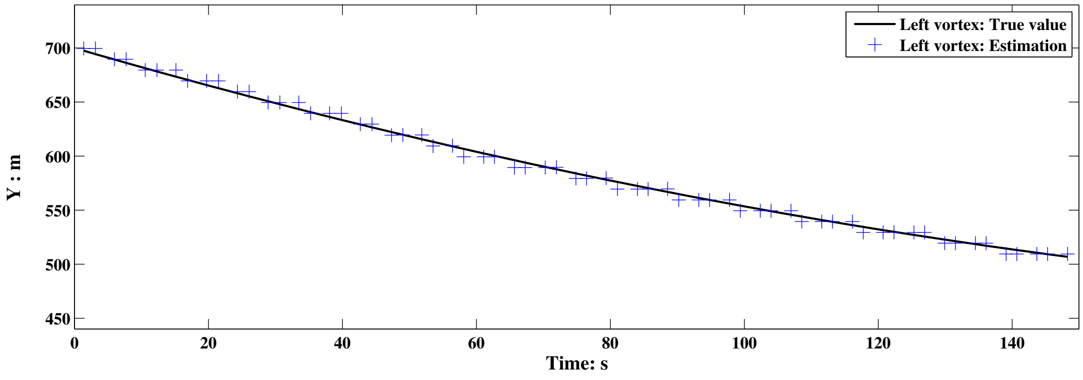

(b) Vertical location of left vortex

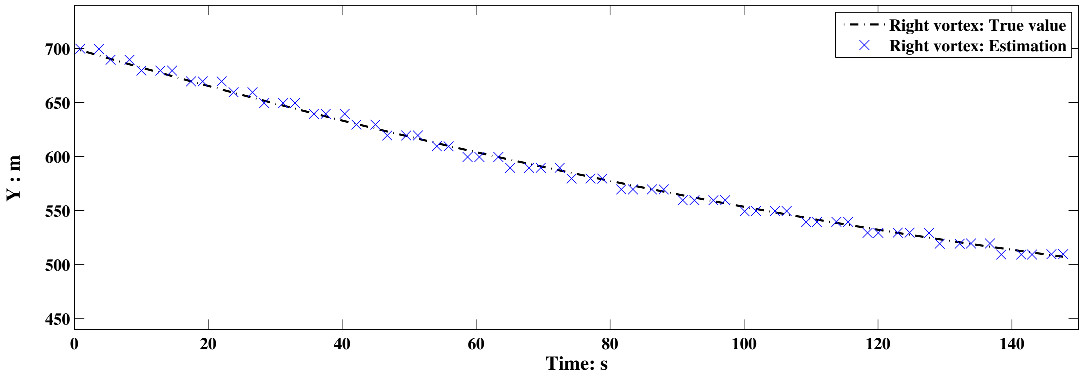

(c) Vertical location of right vortex

Figure 5.14: Estimated position of the wake vortex pair

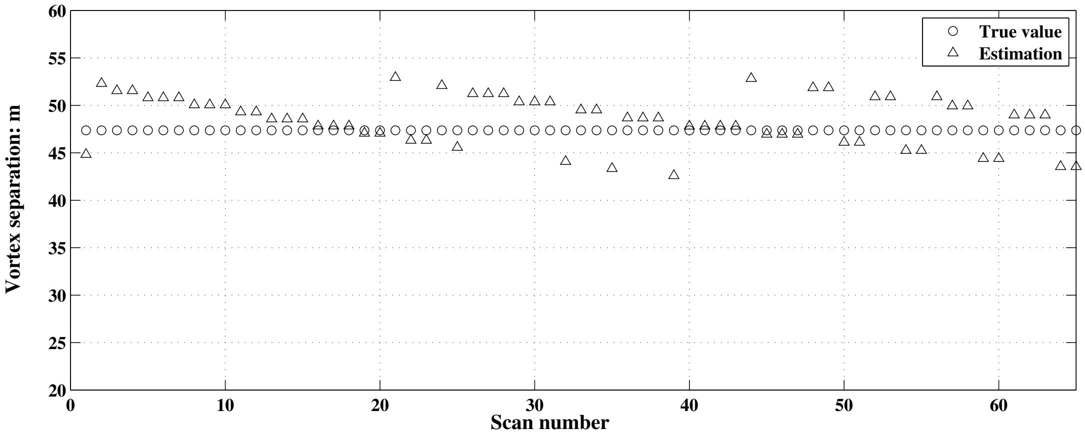

Figure 5.15: Vortex separation $\widehat{b}_0(k)$ computed from a sequence of scans

proportional to the antenna scanning rate and it is always much smaller than the radar range resolution, therefore, the vortex pair separation estimation error due to the descent of vortex pair can be neglected. The accuracy of the estimation is thus mainly determined by the radar range resolution, azimuthal resolution and reliability of vortex detection.

Vortex circulation and descent velocity

As described in Section 2.1.2, the descent velocity of a wake vortex pair is proportional to the circulation. Their relationship can be expressed by

$$\Gamma(t) = 2\pi v_d(t) b_0 \tag{5.5}$$

where $\Gamma(t)$ and $v_d(t)$ are the vortex circulation and descent velocity of wake vortex pair at time t respectively, and b_0 is vortex separation. Therefore, once one of them is estimated, the estimation of the other one is also accomplished. As discussed above, the height (vertical location) of the two vortices at each scan has been obtained from the wake vortex detection, so it should be easy to further estimate the descent velocity of the two vortices.

Assuming that the wake vortex circulation is decaying at a constant rate as given by Equation (2.8), the descent velocity $v_d(t)$ can be assumed to be linearly varying with time according to

$$v_d(t) = v_{d0} + a_d t \tag{5.6}$$

where v_{d0} is the initial descent velocity at time $t = 0$ and a_d is constant. If the initial height of wake vortex pair is y_0, the instantaneous height of the wake vortex pair is given by

$$y(t) = y_0 + v_{d0}t + \frac{1}{2}a_d t^2 \tag{5.7}$$

where v_{d0}, a_d and y_0 are the three parameters needed to be determined. Considering the two groups of detected values of $y(t)$ from a sequence of N_s scans, that is

$$\begin{cases} \mathbf{y}_1 = [y_1(1), y_1(2) \cdots y_1(N_s)]; \\ \mathbf{y}_2 = [y_2(1), y_2(2) \cdots y_2(N_s)]; \end{cases} \tag{5.8}$$

both of them can be taken as a series of sample values in Equation (5.7) at time:

$$\begin{cases} \mathbf{t}_1 = [t_1(1), t_1(2) \cdots t_1(N_s)]; \\ \mathbf{t}_2 = [t_2(1), t_2(2) \cdots t_2(N_s)]; \end{cases} \tag{5.9}$$

where $t_1(k)$ and $t_2(k)$ are the the times at which the wake vortices are detected at the elevation angles of $\alpha_1(k)$ and $\alpha_2(k)$. Thus, $(\mathbf{t}_1, \mathbf{y}_1)$ and $(\mathbf{t}_2, \mathbf{y}_2)$ are taken as two sets of observed data. In order to determine the optimal estimation of $[v_{d0}\ a_d\ y_0\ ]$ from the observed data, the difference between the model and the data should be minimized, that is:

$$\min Q_1(v_{d0}, a_d, y_0) = [y(\mathbf{t}_1) - \mathbf{y}_1]^T [y(\mathbf{t}_1) - \mathbf{y}_1] \tag{5.10}$$

for the estimation from the left vortex, and

$$\min Q_2(v_{d0}, a_d, y_0) = [y(\mathbf{t}_2) - \mathbf{y}_2]^T [y(\mathbf{t}_2) - \mathbf{y}_2] \tag{5.11}$$

for the estimation from the right vortex.

After estimating the parameters in Equation (5.7) , the vortex descent velocity and circulation can then be estimated from the computation of Equation (5.6) and Equation (5.5). In Figure 5.16, the estimated values of descent velocity of wake vortex pair at each scan are illustrated by comparison with the actual value used for simulations. In Figure 5.17, the estimated values of wake vortex circulation at each scan are illustrated by comparison with the actual value. The estimation results show a good agreement with the actual value. What is worth pointing out is that the above analysis has been made neglecting the crosswind. Nevertheless, those procedures of detection and parameter estimation can be easily extended to include this factor.

Finally, the relationship between the estimated wake vortex circulation and the Doppler spectrum widths of raindrop is illustrated in Figure 5.18, as the vortex

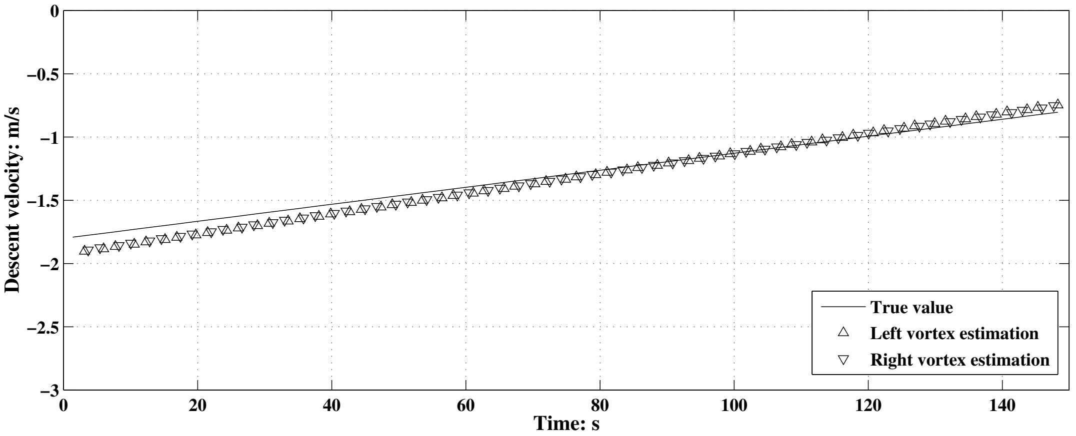

Figure 5.16: Estimated descent velocity of wake vortex pair (Radar under flight path observation)

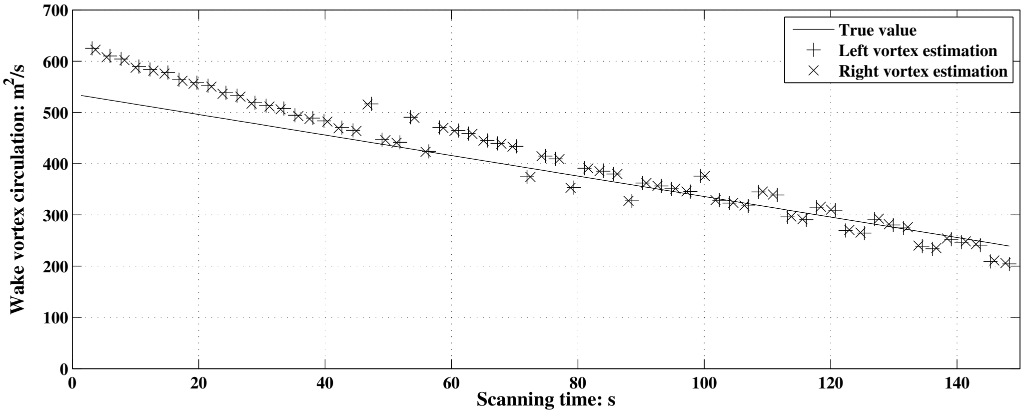

Figure 5.17: Wake vortex circulation estimation

circulation decays, the Doppler spectrum width of raindrops tends to decrease as well. Thus, the Doppler spectrum width of raindrops can be interpreted in terms of wake vortex strength.

5.6 Conclusions

In this chapter, an interpretation of the radar signatures of raindrops in wake vortices has been presented. It relies on the computation of the mean Doppler velocity and Doppler spectrum width. A preliminary study on wake vortex detection and parameter estimation has been accomplished.

The dependence of radar signatures on rain rate, wake vortex circulation, radar

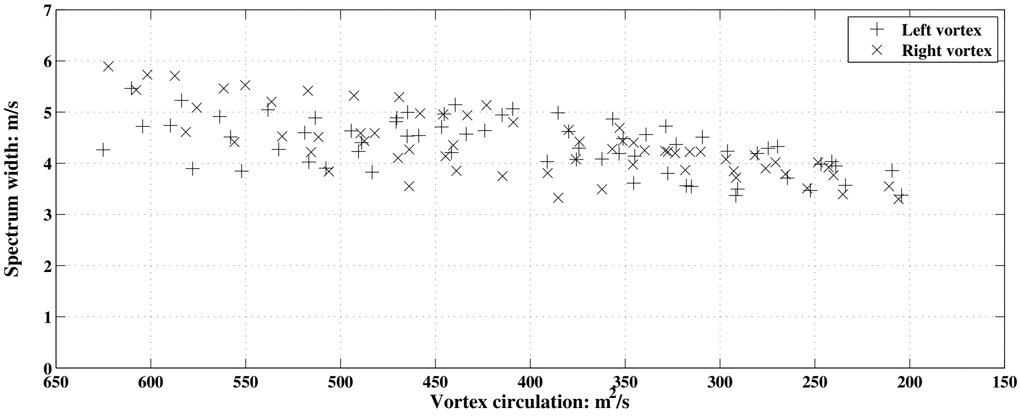

Figure 5.18: Relationship between the wake vortex circulation and the Doppler spectrum width of raindrops

antenna elevation angle and range resolution has been analyzed for three typical aircrafts, namely an A320, an A340 and an A380. One of the most attractive conclusion is that the Doppler spectrum width of raindrops is representative of the wake vortex circulation, as vortex circulation decays, the Doppler spectrum width of raindrops is decreasing.

A wake vortex detection method based on the analysis of Doppler spectrum width of raindrops is proposed. The simulated Doppler signatures of raindrops at 10 range resolution have been adopted to test the effectiveness of the detection method. Finally, the wake vortex parameters including the position, vortex separation, descent velocity and vortex circulation have been estimated from a sequence of scans. The preliminary results have shown effectiveness of the proposed estimation methodology.

Chapter 6

Conclusions and perspectives

Radar monitoring of wake vortices in rainy weather is a new challenging research topic for air traffic control applications. This thesis aims at modeling and simulating the radar signatures of wake vortices in rainy weather. This chapter summarizes the research work, highlights the main contributions and provides perspectives for future research.

6.1 Summary of the conducted research work

In rainy weather, the radar signatures of wake vortices are mainly caused by raindrops dragged by wake vortices. In the present study, the radar signatures of wake vortices in rainy weather have been modeled and analyzed in three successive steps.

Step 1: Simulation and modeling of the motion of raindrops in wake vortices

The motion and distribution of raindrops in wake vortices have been systematically studied in Chapter 3. Based on the computation of equation of motion, the raindrops' trajectory in wake vortices has been presented. Based on the analysis of the impacts of descent velocity, uniform crosswind and initial release position on raindrops' motion, the time evolving distribution of raindrops in wake vortices has also been presented. The phenomenon of enhanced and reduced concentration of raindrops in wake vortices has been illustrated and explained by numerical simulation. The raindrops' velocity distribution has been shown to be representative of the wake vortex velocity characteristics.

Step 2: Simulation of the radar signatures of raindrops

The X band and W band radar signatures of raindrops in wake vortices have been modeled and simulated by two methodologies in Chapter 4. The first simulation methodology is based on the computation of radar signal time series, the outputs can be directly given to test radar Doppler processing chains. The second methodology is based on the raindrops' number concentration and velocity distribution in wake vortices, by integrating the contribution of radar average received power and Doppler signatures from each diameter class of raindrops in the radar cell. The simulated X band radar signatures of raindrops in wake vortices have been compared with the results from Thales radar data in [26, 45] and the effectiveness of the simulation methodologies has been preliminarily validated. The simulated W band radar signatures of raindrops in wake vortices have also shown preliminary consistence with the experimental results reported in [27].

Step 3: Interpretation of the simulated radar signatures

The radar signatures of raindrops in wake vortices have been interpreted by the computation of three spectral moments in Chapter 5. The dependence of radar signatures on rain rate, vortex circulation and radar parameters has been studied for wake vortices generated by different aircraft types. The Doppler spectrum width of raindrops has been interpreted in terms of wake vortex circulation strength: as vortex circulation decays, the Doppler spectrum width of raindrops is decreasing. The simulated Doppler signatures of raindrops have been utilized to test the effectiveness of the wake vortex detection method proposed in this thesis. Based on the wake vortex detection results, the estimation of wake vortex position, core separation, descent velocity and vortex circulation has been achieved and the preliminary results have shown the effectiveness of the wake vortex parameter estimation methodology.

6.2 Main achievements

In the present study, the capability of X band and W band radar to detect wake vortex in rainy weather have been demonstrated by theoretical modeling and numerical simulations. In clear air, wake vortex is visible by eyes, due to colorful smoke particles involved in it and by Lidar, due to the motion of aerosol particles in it. In rainy weather, wake vortex is visible by radar, due to the motion of raindrops in it. Besides, a series of valuable models and methodologies, which can be further exploited for designing new wake vortex radar systems, have been developed in this thesis:

(1) A methodology to compute the raindrops' trajectory in wake vortices has been proposed.

(2) A methodology to compute the raindrops' distribution in wake vortices, in terms of relative number concentration, horizontal velocity distribution and vertical velocity distribution, has been presented.

(3) A wake vortex radar simulator based on radar signal time series has been developed, enabling the computation of raw radar signal backscattered by all the raindrops within the radar resolution volume.

(4) A wake vortex radar simulator based on the raindrops' number concentration and velocity distribution in wake vortices has been developed, enabling the computation of radar signatures much more efficiently.

(5) A methodology based on the computation of three spectral moments has been proposed to interpret the radar signatures of raindrops in wake vortices.

(6) A wake vortex detection method based on the analysis of Doppler spectrum width of raindrops has been proposed.

(7) A methodology to estimate the wake vortex characteristics, including the position, vortex separation, descent velocity and vortex circulation, has been proposed.

6.3 Future research perspectives

Radar monitoring of wake vortex in rainy weather is an interesting but challenging topic. Even though some contributions have been made in the present study, this is just a preliminary start on investigations into this topic, there are still some limitations because of the assumptions made to simplify the analysis. The current work could be improved by addressing various aspects that are listed below:

(1) Use of non-idealized atmospheric characteristics

The interaction between raindrops and wake vortices is a very complicated problem. The wake vortex always evolves through four phases: the wake formation phase, the stable phase, the unstable phase and the breakdown phase. In the present study, the wake vortex is assumed to be only in stable phase. Meanwhile, stratification of the atmosphere characterized by Bruns-Vaisala frequency is not taken into account, as well as, cross-wind, wind-shear and atmospheric turbulence caracterized by EDR (Eddy Dissipation Rate). The future work can be improved by integrating these atmosphere characteristics in the analysis of raindrops' motion. This challenging topic is of great practical significance. Firstly, the proper models of atmosphere, cross-wind, wind-shear and ambient atmosphere turbulence should be clarified. Secondly, the equations of motion of raindrops under the above atmospheric conditions before entering into wake vortex region should be analyzed. Thirdly, the background atmosphere is not in still air, the velocity field model of wake vortex will be different from the one we are using. The impacts of the cross-wind, wind-shear and ambient atmosphere turbulence on wake vortex velocity field should be analyzed. Lastly, the equations of motion of raindrops within wake vortex region under the above atmospheric conditions should be analyzed and computed again. To conclude, the atmospheric model, the wake vortex velocity field model and the equation of the motion of raindrops are the three key elements in the further research towards integrating these atmosphere characteristics.

(2) Interaction between raindrops and the effects of raindrops on wake vortex evolution

As described in Chapter 3, one-way coupling assumptions is considered for the motion of raindrops in wake vortices. However, the interaction between raindrops such as collision or coalescence and the effects of raindrops on wake vortex evolution, are both of great academic interest. In our previous simulations, in some regions of the wake vortices, the number concentration of raindrops is enhanced up to 10 times the one that can be found in still air, thus, the collision or coalescence between raindrops becomes probable. In this case, the raindrops' shape and size distribution will be changed. If collision or coalescence is producing larger raindrops, the radar reflectivity of raindrops will be underestimated in our simulations. On the other hand, the produced larger raindrops may have a positive effect to accelerate the decay rate of wake vortex circulation, thus, the potential effects of raindrops on wake vortex evolution should be further studied.

(3) Extension of the radar simulators to other hydrometeors

The radar simulators developed in this thesis can be extended to the study of radar signatures of other hydrometeors like fog, cloud or snow by analyzing a) the drop size distribution of the hydrometeors in still air; b) the motion and distribution of the hydrometeors in the wake vortices under the realistic assumptions; c) the RCS of the hydrometeors. The backscattering mechanism of the hydrometeor depends on its radio-electric size. The reflectivity of snow is small in the case of dry snow but can by extremely high when melting (size of a snowflakes but EM properties of liquid water). The kinematic of the snowflakes will tend to be closer to the one of small drops as the impact of the weight on them is small.

(4) Exploitation and upgrade of the radar simulators

The current radar simulators have the capability to simulate the radar signatures of raindrops in wake vortices with a flexibility on a large number of parameters. The exploitation of the radar simulators is of great significance for developing new radar systems dedicated to wake vortex monitoring. For example, more radar geometry configurations can be simulated and the optimal radar scanning strategy for wake vortex monitoring in rainy weather may be derived from those simulations, applying them candidate parameter estimation algorithms. The on-board wake vortex detection in rainy weather could also be simulated.

In the analysis made in Chapter 3, the raindrops are assumed to be spherical. Actually, the microstructure of raindrops may be much more complicated, especially for the raindrops moving in wake vortices. The microstructure of a raindrop usually refers to its nature, shape and orientation [155]. For raindrops advected by the wake vortices, the shape and orientation may be changed by the vortex flow and quite different the ones of the raindrops outside the vortex flow. Polarimetric Radar is very sensitive to this kind of change and the polarization of raindrops depends on physical parameters such as the shape and orientation. The polarization information of raindrops in wake vortices may be another important indicator for wake vortex detection. Thus, it will be very interesting to upgrade the current radar simulators by integrating the capability of polarimetric measurements. Of course, this upgrade is not very easy because it relies on the fundamental study of raindrops' shape and orientation under a fluctuating aerodynamic force.

The challenging technical problem of the current radar simulators is the huge demands of computation time and of hard memory. Thus, upgrading the radar simulators by GPU parallel Computation is of practical significance. In recent years, GPU computation has become increasingly applied in several scientific areas including the signal processing and radar simulations [199–204]. Parallel algorithms based on GPU hardware may have the same computation capability as tens of traditional CPUs [205]. Some years ago, the optimization of GPU programming largely depended on the knowledge of GPU architecture, however, in recent years, Nvidia launched CUDA which includes C/C++ software-development tools, function libraries, and a hardware-abstraction mechanism [205,206]. In the framework of CUDA, the kernel function is introduced to be executed in parallel by several threads, the threads are grouped into blocks, and the blocks are aggregated into a grid. For the first simulator based on radar signal time series, the simulation of radar signal of each independent raindrops can be paralleled as one thread. For the simulator based on the raindrops' distribution in wake vortices, the simulation of radar signatures of raindrops of each diameter class can be paralleled as one thread. Thus, considerable reduction in computation load can be envisaged.

(5) Wake vortex detection and characterization

Compared to the measurements made using Lidar, the wake vortex detection and characterization by radar still demands more efforts. In Chapter 5, preliminary research towards wake vortex detection and parameters estimation has been conducted. The wake vortex circulation estimation is based on the relationship between vortex circulation and the descent velocity of wake vortex pair and the estimation accuracy relies on the assumed vortex circulation model. However, the vortex circulation decay is always difficult to be predicted due to the effects of atmospheric conditions. In order to develop effective methods for wake vortex circulation estimation, an X band radar with high range and angular resolution could be used for more simulations. Based on the interpretation of simulated radar signatures, the relationship between the radar observed mean radial velocity of raindrops, the raindrops' terminal falling velocity in still air and the wake vortex velocity field could be established. Thus, the wake vortex circulation estimation could be achieved by the retrieval of wake vortex velocity field from the radar signatures of raindrops in wake vortices.

Bibliography

[1] P. Choroba. *Comprehensive study of the wake vortex phenomena to the assessment of its incorporation to ATM for safety and capacity improvements.* PhD thesis, University of Zilina, 2006.

[2] P. Bowen. Air to air: Gallery of vortices. `http://www.airtoair.net/gallery/gallery-vortices.htm`, 2004.

[3] Wikipedia. Contrail — wikipedia, the free encyclopedia, 2013. [Online; accessed 5-March-2013].

[4] Wikipedia. Wake turbulence — wikipedia, the free encyclopedia, 2013. [Online; accessed 5-March-2013].

[5] W. H. Gilson. Radar measurements of aircraft wakes. Technical report, Lincoln Lab., F19628-90-C-0002, U.S. Air Force, 1992.

[6] F. Barbaresco, A. Jeantet, and U. Meier. Wake vortex detection & monitoring by X-band Doppler radar : Paris Orly radar campaign results. In *Proceedings of IET International Radar Systems Conference*, pages 1–5, 2007.

[7] D. Vanhoenacker-Janvier, D. Kahina, and F. Barbaresco. Model for the calculation of the radar cross section of wake vortices of take-off and landing airplanes. In *EuRAD 2012, European Radar Conference*, 2012.

[8] F. Holzapfel, T. Gerz, F. Kopp, E. Stumpf, M. Harris, R. I. Young, and A. Dolfi-Bouteyre. Strategies for circulation evaluation of aircraft wake vortices measured by lidar. *Journal of Atmospheric and Oceanic Technology*, 20(8):1183–1195, August 2003.

[9] F. Kopp, S. Rahm, I. Smalikho, A. Dolfi, J. Cariou, M. Harris, and R. I. Young. Comparison of wake-vortex parameters measured by pulsed and continuous-wave lidars. *Journal of aircraft*, 42(4):916–923, 2005.

[10] R. Frehlich and R. Sharman. Maximum likelihood estimates of vortex parameters from simulated coherent Doppler Lidar data. *Journal of Atmospheric and Oceanic Technology*, 22(2):117–130, 2005.

[11] R. J. Rodenhiser. An ultrasonic method for aircraft wake vortex detection. Master's thesis, Worcester polytechnic institute, August 2005.

[12] Y. Zhang, F. Y. Wang, and J. C. Hardin. Spectral characteristics of wake vortex sound during roll-up. Technical report, NASA, 2003.

[13] S. Bradley, E. Mursch-Radlgruber, and S. von Hunerbein. Sodar measurements of wing vortex strength and position. *Journal of Atmospheric and Oceanic Technology*, 24(2):141–155, February 2007.

[14] A. S. Ginevsky and A. I. Zhelannikov. *Foundations of Engineering Mechanics: Vortex Wakes of Aircrafts.* Springer-Verlag Berlin Heidelberg, 2009.

[15] T. J. Myers. *Determination of Bragg Scatter in an Aircraft Generated Wake Vortex System for Radar Detection.* Phd thesis, Virginia Polytechnic Institute and State University, 1997.

[16] D. A. Hinton and C. R. Tatnall. A candidate wake vortex strength definition for application to the NASA Aircraft Vortex Spacing System (AVOSS). Technical Report 110343, NASA Langley Research Center, Hampton, VA, 1997.

[17] T. Gerz, F. Holzï¿½pfel, and D. Darracq. Commercial aircraft wake vortices. *Progress in Aerospace Sciences*, 38(3):181 – 208, 2002.

[18] G. Winckelmans, T. Duquesne, V. Treve, O. Desenfans, and L. Bricteux. Summary description of the models used in the Vortex Forecast System (VFS). Technical report, VFS version with added improvements done after completion of the Transport Canada funded project, 2005.

[19] F. Barbaresco and U. Meier. Radar monitoring of a wake vortex: Electromagnetic reflection of wake turbulence in clear air. *Comptes Rendus Physique*, 11(1):54 – 67, 2010.

[20] J. S. Marshall and W. M. Palmer. The distribution of raindrops with size. *Journal of Meteorology*, 5:165–166, 1948.

[21] F. Fang. Raindrop size distribution retrieval and evaluation using an s-band radar profiler. Master's thesis, University of Central Florida, 2003.

[22] C. Ulbrich. Natural variations in the analytical form of the raindrop size distribution. *Journal of Climate and Applied Meteorology*, 22:1764–1775, 1983.

[23] P. A. Owolawi. *Characteristics of Rain at Microwave and Millimetric Bands for Terrestrial and Satellite Links Attenuation in South Africa and Surrounding Islands*. PhD thesis, University of KwaZulu-Natal, 2010.

[24] D. Atlas, R. C. Srivastava, and R. S. Sekhon. Doppler radar characteristics of precipitation at vertical incidence. *Reviews of Geophysics*, 11(1):1–35, 1973.

[25] V. N. Bringi and V. Chandrasekar. *Polarimetric Doppler Weather Radar: Principles and Applications*. Cambridge University Press, 2004.

[26] F. Barbaresco. Radar/Lidar Sensors for Wind & Wake-Vortex Monitoring on Airport: First results of SESAR P12.2.2 XP0 trials campaign at Paris CDG Airport. In *WakeNet3-Europe 4th Major Workshop "Wake Turbulence in Current Operations and Beyond"*, 2012.

[27] T. A. Seliga and J. B. Mead. Meter-scale observations of aircraft wake vortices in precipitation using a high resolution solid-state W-band radar. In *The 34th conference on Radar Meteorology*, 2009.

[28] C. Breitsamter. Wake vortex characteristics of transport aircraft. *Progress in Aerospace Sciences*, 47(2):89 – 134, 2011.

[29] Wikipedia. Wingtip vortices — wikipedia, the free encyclopedia, 2013. [Online; accessed 5-March-2013].

[30] V. J. Rossow and A. P. Brown. Effect of jet-exhaust streams on structure of vortex wakes. *Journal of aircraft*, 47(3):1076–1082, May-June 2010.

[31] P. Minnis, J. K. Ayers, R. Palikonda, and D. Phan. Contrails, cirrus trends, and climate. *Journal of Climate*, 17(8):1671–1685, April 2004.

[32] O. Boucher. Atmospheric science: Seeing through contrails. *Nature Clim. Change*, 1(1):24–25, April 2011.

[33] A. J. Heymsfield, G. Thompson, H. Morrison, A. Bansemer, R. M. Rasmussen, P. Minnis, Z. Wang, and D. Zhang. Formation and spread of aircraft-induced holes in clouds. *Science*, 333(6038):77–81, 2011.

[34] V. J. Rossow. Lift-generated vortex wakes of subsonic transport aircraft. *Progress in Aerospace Sciences*, 35(6):507 – 660, 1999.

[35] R. C. Nelson. The trailing vortex wake hazard: Beyond the takeoff and landing corridors. In *AIAA Atmospheric Flight Mechanics Conference and Exhibit, Providence, Rhode Island*, 2004.

[36] R. C. Nelson. Trailing vortex wake encounters at altitude - a potential flight safety issue. In *AIAA Paper 2006-6268*, 2006.

[37] G. C. Hay and R. H. Passman. Wake turbulence training aid. Technical report, U. S. Departement of Transportation, 1995.

[38] F. H. Proctor, D. W. Hamilton, D. K. Rutishauser, and G. F. Switzer. Meteorology and Wake Vortex Influence on American Airlines FL-587 Accident. Technical Report 213018, NASA Langley Research Center, 2004.

[39] P. R. Veillette. Data show that U.S. wake-turbulence accidents are most frequent at low altitude and during approach and landing. *Flight Safety Digest*, 21(3-4):1–47, 2002.

[40] Eurocontrol. Airport operations: Wake vortex. `http://www.eurocontrol.int/articles/wake-vortex`, May 2012.

[41] A. V. Bobylev, V. V. Vyshinsky, G. G. Soudakov, and V. A. Yaroshevsky. Aircraft vortex wake and flight safety problems. *Journal of Aircraft*, 47:663–674, 2010.

[42] Wikipedia. Single european sky atm research — wikipedia, the free encyclopedia, 2012. [Online; accessed 7-March-2013].

[43] A. R. Jameson and A. B. Kostinski. Partially coherent backscatter in radar observations of precipitation. *Journal of the Atmospheric Sciences*, 67(6):1928–1946, 2010.

[44] Z. Liu, N. Jeannin, F. Vincent, and X. Wang. Development of a radar simulator for monitoring wake vortices in rainy weather. In *IEEE CIE International Conference on Radar*, volume 1, pages 284–287, 2011.

[45] F. Barbaresco, P. Brovelli, P. Currier, O. Garrouste, M. Klein, P. Juge, Y. Ricci, and J. Schneider. Radar sensors for wind & wake-vortex monitoring on airport : First results of sesar p12.2.2 xp0 trials campaign at paris cdg airport. In *The 7th European Conference on Radar in Meteorology and Hydrology*, Toulouse, 2012.

[46] Z. Liu, N. Jeannin, F. Vincent, and X. Wang. Modeling the radar signature of raindrops in aircraft wake vortices. *Journal of Atmospheric and Oceanic Technology*, 30(3):470–484, 2013.

[47] J. Li. *Study on the radar signatures of aircraft wake vortices*. PhD thesis, National university of defense technology, 2010.

[48] J. N. Hallock. Aircraft wake vortices: an assessment of the current situation. Technical report, U.S. Department of Transportation, Cambridge, MA 02142, 1991.

[49] F. Lanchester. *Aerodynamics*. Constable, London, 1907.

[50] S. Andrew and J. Carten. Aircraft wake turbulence: An interesting phenomenon turned killer. *Air University Review*, May July-August 1971.

[51] C. to Conduct an Independent Assessment of the Nation's Wake Turbulence Research and N. R. C. Development Program. *Wake Turbulence: An Obstacle to Increased Air Traffic Capacity*. The National Academies Press, 2008.

[52] F. Holz apfel and T. Gerz. Aircraft wake vortices: From fundamental research to operational application. In U. Schumann, editor, *Atmospheric Physics*, Research Topics in Aerospace, pages 219–237. Springer Berlin Heidelberg, 2012.

[53] Z. O. Bleviss. Theoretical analysis of light plane landing and take-off accidents due to encountering the wakes of large airplanes. Technical report, Douglas Aircraft Co., 1954.

[54] L. J. Garodz. Measurements of boeing 747, lockheed c5a and other aircraft vortex wake characteristics by tower fly-by technique. In J. Olsen, A. Goldburg, and M. Rogers, editors, *Aircraft Wake Turbulence and Its Detection*, pages 265–285. Springer US, 1971.

[55] J. E. Hackett and J. G. Theisen. Vortex wake development and aircraft dynamics. In J. Olsen, A. Goldburg, and M. Rogers, editors, *Aircraft Wake Turbulence and Its Detection*, pages 243–263. Springer US, 1971.

[56] V. J. Rossow and B. E. Tinling. Research on aircraft /vortex-wake interactions to determine acceptable level of wake intensity. *Journal of Aircraft*, 25(6), 1988.

[57] J. C. Houbolt. Aircraft response to turbulence including wakes. In J. Olsen, A. Goldburg, and M. Rogers, editors, *Aircraft Wake Turbulence and Its Detection*, pages 509–522. Springer US, 1971.

[58] J. Menkes and F. H. Abernathy. An estimate of the power required to eliminate trailing vortices by suction. *Proceedings of the IEEE*, 58(3):326–327, 1970.

[59] R. M. Huffaker, A. Jelalian, and J. A. L. Thomson. Laser-doppler system for detection of aircraft trailing vortices. *Proceedings of the IEEE*, 58(3):322–326, 1970.

[60] R. M. Huffaker, A. V. Jelalian, W. H. Keene, and C. M. Sonnenschein. Application of laser doppler systems to vortex measurement and detection. In J. Olsen, A. Goldburg, and M. Rogers, editors, *Aircraft Wake Turbulence and Its Detection*, pages 113–124. Springer US, 1971.

[61] C. C. Easterbrook and W. W. Joss. The utility of doppler radar in the study of aircraft wing-tip vortices. In J. Olsen, A. Goldburg, and M. Rogers, editors, *Aircraft Wake Turbulence and Its Detection*, pages 97–112. Springer US, 1971.

[62] V. W. Ramsey. *Acoustic-Scattering from Aircraft Trailing Vortex*. PhD thesis, Stanford university, 1973.

[63] R. B. Chadwick, J. Jordan, and T. Detman. Radar detection of wingtip vortices. In *9th Conference on Aerospace and Aeronautical Meteorology*. AMS, 1983.

[64] J. H. Olsen, A. Goldburg, and M. Rogers, editors. *Aircraft Wake Turbulence and Its Detection*. Springer US, 1971.

[65] D. C. Burnham, M. Gorstein, J. N. Hallock, R. D. Kodis, and T. Sullivan. Aircraft wake vortex sensing systems. Technical Report DOT-TSC-FAA-72-13, Transportation systems center, Cambridge, MA., June 1971.

[66] A. J. Bilanin, M. E. Teske, and J. Curtiss, Howard C. Feasibility of an onboard wake vortex avoidance system. Technical Report 19910009761, NASA (Unspecified Center), 1987.

[67] M. R. Brashears and J. N. Hallock. Aircraft wake vortex transport model. *Journal of aircraft*, 11(5):265–272, May 1974.

[68] T. H. Moulden and W. Frost. Effects of fog droplets on wake vortex decay rate. Technical report, The University of Tennessee Space Institute, 1976.

[69] S. J. Barker and S. C. Crow. The motion of two-dimensional vortex pairs in a ground effect. *Journal of Fluid Mechanics*, 82:659–671, 9 1977.

[70] D. C. Burnham and J. N. Hallock. Chicago Monostatic Acoustic Vortex Sensing System : Volume I. Data Collection and Reduction. Technical report, U.S. Department of Transportation, 1979.

[71] D. C. Burnham and J. N. Hallock. Chicago Monostatic Acoustic Vortex Sensing System : Vol. II. Decay of B-707 and DC-8 Vortices. Technical report, U.S. Department of Transportation, 1981.

[72] D. C. Burnham and J. N. Hallock. Chicago Monostatic Acoustic Vortex Sensing System : Vol. III. Decay of B-707 and DC-8 Vortices. Executive Summary. Technical report, U.S. Department of Transportation, 1982.

[73] D. C. Burnham and J. N. Hallock. Chicago Monostatic Acoustic Vortex Sensing System : Vol. IV. Wake Vortex Decay. Technical report, U.S. Department of Transportation, 1982.

[74] G. T. Holbrook, D. M. Dunham, and G. C. Greene. Vortex wake alleviation studies with a variable twist wing. Technical report, NASA: Langley Research Center, Nov 1, 1985.

[75] H. D. Fuhrmann and E. C. Stewart. An evaluation of the measurement requirements for an in-situ wake vortex detection system. Technical report, NASA Langley Research Center, Hampton, Virginia, May 1996.

[76] F. Proctor, D. Hinton, J. Han, D. Schowalter, and Y. Lin. Two dimensional wake vortex simulations in the atmosphere: Preliminary sensitivity studies. In *35th AIAA Aerospace Sciences Meeting and Exhibit, Reno, Nevada, AIAA*, 1997.

[77] A. I. Mackenzie. Measured changes in c-band radar reflectivity of clear air caused by. Technical report, NASA Langley Research Center, Hampton, Virginia, 1997.

[78] R. E. Marshall, A. Mudukutore, and V. L. H. Wissel. Radar reflectivity in wingtip-generated wake vortices. Technical report, National Aeronautics and Space Administration, Langley Research Center, 1997.

[79] R. E. Marshall, A. Mudukutore, V. L. H. Wissel, and T. Myers. Three-centimeter doppler radar observations of wingtip-generated wake vortices in clear air. Technical Report NASA/CR-97-206260, NASA Langley Research Center, 1997.

[80] K. Shariff and A. Wray. Analysis of the radar reflectivity of aircraft vortex wakes. *Journal of Fluid Mechanics*, 463:121ï¿$\frac{1}{2}$C161, 2002.

[81] J. M. Hanson and F. J. Marcotte. Aircraft wake vortex detection using continuous-wave radar. *Johns Hopkins APL Technical Digest*, 18:348–357, 1997.

[82] R. J. Iannuzzelli and C. E. Schemm. Aircraft wake detection using bistatic radar: Analysis of experimental results. *Johns Hopkins APL Technical Digest*, 19:299–314, 1998.

[83] S. D. Campbell, T. J. Dasey, R. E. Freehart, R. M. Heinrichs, M. P. Matthews, G. H. Perras, and G. S. Rowe. Wake vortex field measurement program at memphis. Technical report, MIT Lincoln Laboratory, Lexington, MA, 1997.

[84] W. Tank. Airplane wake detection with a vhf cw bistatic radar. In *Aerospace Sciences Meeting and Exhibit, 35th*, Reno, Jan 1997.

[85] W. L. Rubin. Radar-acoustic detection of aircraft wake vortices. *Journal of Atmospheric and Oceanic Technology*, 17(8):1058–1065, August 2000.

[86] W. L. Rubin. The generation and detection of sound emitted by aircraft wake vortices in ground effect. *Journal of Atmospheric and Oceanic Technology*, 22(5):543–554, May 2005.

[87] J. C. Hardin and F. Y. Wang. Sound generation by aircraft wake vortices. Technical report, Titan Corporation, Billerica, Massachusetts and Volpe National Transportation Systems Center, Cambridge, Massachusetts, December 2003.

[88] F. Y. Wang, H. S. Wassaf, and A. Gulsrud. Acoustic imaging of aircraft wake vortex dynamics. In *23rd AIAA Applied Aerodynamics Conference*, Toronto, Ontario Canada, June 2005.

[89] Z. C. Zheng and R. L. Ash. Study of aircraft wake vortex behavior near the ground. *AIAA Journal*, 34(3):580–589, 1996.

[90] R. M. Heil. Characterizing the wake vortex signature for an active line of sight remote sensor. Technical report, Radar systems laboratory, Clemson University, 1994.

[91] R. E. Marshall and T. Myers. Wingtip generated wake vortices as radar target. *IEEE Aerospace and Electronic Systems Magazine*, 11(12):27–30, 1996.

[92] V. V. Vyshinsky. Flight safety, aircraft vortex wake and airport operation capacity. *Air & Space Europe*, 3(3–4):206 – 208, 2001.

[93] G. Rat and F. Bertin. Etude théorique de la détection des vortex générés dans le sillage des avions à l'aide d'un radar. Technical report, CNRS/CRPE, 1992.

[94] D. J. Shephard, A. P. Kyte, and P. D. F. Tait. Radar measurement of the Wake Vortex of a H.S. 748 and a B.A.C. One-Eleven, Preliminary trials Report. Technical report, GEC-Marconi Research Center, MTR-92/55A, 1992.

[95] D. Shephard, A. Kyte, and C. Segura. Radar wake vortex measurements at F and I band. In *Radar and Microwave Imaging, IEE Colloquium on*, pages 7/1 –7/5, nov. 1994.

[96] R. T. Neecea, C. L. Britt, J. H. White, A. Mudukutore, C. Nguyen, and B. Hooper. Wake Vortex Tracking Using a 35 GHz Pulsed Doppler Radar, 2005.

[97] F. Köpp. Doppler lidar investigation of wake vortex transport between closely spaced parallel runways. *AIAA Journal*, 32(4):805–810, 1994.

[98] F. Köpp, I. Smalikho, S. RAHM, A. DOLFI, J.-P. CARIOU, M. HARRIS, R. I. Young, K. Weekes, and N. GORDON. Characterization of aircraft wake vortices by multiple-lidar triangulation. *AIAA Journal*, 41(6):1081–1088, 2003.

[99] M. Harris, R. I. Young, F. Köpp, A. Dolfi, and J.-P. Cariou. Wake vortex detection and monitoring. *Aerospace Science and Technology*, 6(5):325–331, 2002.

[100] F. Köpp, S. Rahm, and I. Smalikho. Characterization of aircraft wake vortices by 2-μ m pulsed doppler lidar. *Journal of Atmospheric and Oceanic Technology*, 21(2):194–206, 2004.

[101] S. M. Hannon and J. A. Thomson. Aircraft wake vortex detection and measurement with pulsed solid-state coherent laser radar. *Journal of Modern Optics*, 41(11):2175–2196, 1994.

[102] S. M. Hannon, J. A. L. Thomson, S. W. Henderson, and R. M. Huffaker. Windshear, turbulence, and wake vortex characterization using pulsed solid state coherent lidar. In *SPIE's 1995 Symposium on OE/Aerospace Sensing and Dual Use Photonics*, pages 94–102. International Society for Optics and Photonics, 1995.

[103] R. Sussmann and K. M. Gierens. Lidar and numerical studies on the different evolution of vortex pair and secondary wake in young contrails. *Journal of Geophysical Research*, 104:2131–2142, 1999.

[104] F. Köpp. Wake-vortex characteristics of military-type aircraft measured at airport oberpfaffenhofen using the dlr laser doppler anemometer. *Aerospace Science and Technology*, 3(4):191–199, 1999.

[105] D. Darracq, A. Corjon, F. Ducros, M. Keane, D. Buckton, and M. Redfern. Simulation of wake vortex detection with airborne dopple lidar. *Journal of Aircraft*, 37(6):984–993, 2000.

[106] M. Keane, D. Buckton, M. Redfern, C. Bollig, C. Wedekind, F. Kopp, and F. Berni. Axial detection of aircraft wake vortices using doppler lidar. *Journal of Aircraft*, 39(5):850–861, 2002.

[107] E. Coustols, L. Jacquin, F. Moens, and P. Molton. Status of onera research on wake vortex in the framework of national activities and european collaboration. In *European Congress on Computational Methods in Applied Sciences and Engineering*, 2004.

[108] R. P. Dougherty, F. Y. Wang, E. R. Booth, M. E. Watts, N. Fenichel, and R. E. D'Errico. Aircraft wake vortex measurements at denver international airport. *AIAA Paper*, 2880(10), 2004.

[109] N. E. Fine and D. C. Kring. Opto-acoustic tracking of aircraft wake vortices. In *11 th AIAA/CEAS Aeroacoustics Conference(26 th Aeroacoustics Conference)*, pages 1–26, 2005.

[110] D. Pruzan. Evaluation of an ultrasonic vortex detection system. In *43rd AIAA Aerospace Sciences Meeting and Exhibit*, 2005.

[111] W. L. Rubin, D. C. Burnham, E. A. Spitzer, and R. P. Rudis. Robust low cost airport wake vortex sensor. *Journal of Aircraft*, 37(3):377–382, 2000.

[112] S. Boluriaan and P. J. Morris. Two-dimensional simulations of wake vortex detection using radio acoustic sounding systems. *AIAA journal*, 40(11):2247–2256, 2002.

[113] M. Frech. A simple method to estimate the eddy dissipation rate from SODAR/RASS measurements. In *16th Symposium on Boundary Layers and Turbulence*, 2004.

[114] P. J. Morris, D. K. McLaughlin, T. B. Gabrielson, and S. Boluriaan. The Development of a Plan for the Assessment, Improvement and Deployment of a Radar Acoustic Sounding System (RASS) for Wake vortex detection. Technical report, The Pennsylvania State University, 2004.

[115] D. A. Hinton. An aircraft vortex spacing system (avoss) for dynamical wake vortex spacing criteria. In *The AGARD 78th Fluid Dynamics Panel Meeting and Symposium, Trondheim, Norway*, 1996.

[116] J. Konopka and H. Fischer. The wake vortex warning system at Frankfurt Airport. In *The 24th Digital Avionics Systems Conference*, volume 1, 2005.

[117] T. Gerz, F. Holzäpfel, W. Bryant, F. Köpp, M. Frech, A. Tafferner, and G. Winckelmans. Research towards a wake-vortex advisory system for optimal aircraft spacing. *Comptes Rendus Physique*, 6:501 – 523, 2005.

[118] J. C. Smith and S. M. Dollyhigh. Wake Vortex Advisory System (WakeVAS) Evaluation of Impacts on the National Airspace System. Technical report, Swales Aerospace, Hampton, Virginia, 2005.

[119] R. B. Perry, D. A. Hinton, and R. A. Stuever. NASA wake vortex research for aircraft spacing. In *35th Aerospace Sciences Meeting & Exhibit, Reno, NV, AIAA*, 1997.

[120] T. Astheimer, D. Hilton, C. Baldoni, G. Ho, J.-M. Bara, G. O'Connel, R. Brown, M. Standar, R. Cato, J. Stenson, O. Dlugi, A. Sohn, M. Erb, and G. Tauss. SESAR Master Plan. Technical Report DLM-0710-001-02-00, EuroControl, 2008.

[121] H. Swenson, R. Barhydt, and M. Landis. Next Generation Air Transportation System (NGATS) Air Traffic Management (ATM)-Airspace Project. Technical report, NASA Ames Research Center and NASA Langley Research Center, 2006.

[122] J. G. Kong. Safety Evaluation of A380 Wake Turbulence Separation. *Applied Mechanics and Materials*, 278:31–34, 2013.

[123] K. Feigh, L. N. Sankar, D. P. Schrage, B. Huff, A. Flick, and V. Manivannan. APA Suite Sensitivity Study & Model Scoring Methodologies. Technical Report DTFAWA-09-A-8000, Georgia Institute of Technology, 2010.

[124] V. I. Tatarski. *Wave Propagation in a Turbulent Medium.* McGraw-Hill, New York, 1961.

[125] F. H. Proctor. The Terminal Area Simulation System. Technical Report DOTIFAAIPM-86/50, NASA Contractor Report 4046, 1987.

[126] D. C. Lewellen and W. S. Lewellen. Large-eddy simulations of the vortex-pair breakup in aircraft wakes. *AIAA Journal*, 34(11):2337–2345, 1996.

[127] O. Zeman. The persistence of trailing vortices: A modeling study. *Physics of Fluids*, 7(1):135–143, 1995.

[128] T. J. Myers and W. A. Scales. Determination of aircraft wake vortex radar cross section due to coherent bragg scatter from mixed atmospheric water vapor. *Radio Science*, 34(1):103–111, 1999.

[129] J. Li, X. Wang, T. Wang, and Z. Liu. Study on the scattering characteristics of stable-stage wake vortices. In *IEEE International Radar Conference*, Paris, September 2009.

[130] J. Li, X. Wang, and T. Wang. Scattering mechanism of aircraft wake vortex generated in clear air. In *IEEE International Radar Conference*, Washington, 2010.

[131] J. Li, X. Wang, T. Wang, J. Li, S. Xiao, and Z. Liu. High range resolution profile of simulated aircraft wake vortices. *IEEE Transactions on Aerospace and Electronic Systems*, 48(1):116–129, 2012.

[132] D. Vanhoenacker-Janvier, K. Djafri, R. della Faille de Leverghem, B. van Swieten, and F. Barbaresco. Simulation of the radar cross-section of wake vortices in clear air. In *The 7th European Conference on Radar in Meteorology and Hydrology (ERAD)*, 2012.

[133] V. R. Noonkester and J. H. Richter. FM-CW radar sensing of the lower atmosphere. *Radio Science*, 15(2):337–353, 1980.

[134] J. D. Nespor, B. Hudson, R. L. Stegall, and J. E. Freedman. Doppler radar detection of vortex hazard indicators. Technical report, NASA Langley Research Center, 1994.

[135] F. Barbaresco, J. P. Wasselin, A. Jeantet, and U. Meier. Wake Vortex Profiling by Doppler X-band radar : Orly trials at Initial Take-Off & ILS interception critical areas. In *Proceedings of IEEE Radar Conference, RADAR '08*, 2008.

[136] W. Gautier, A. Stehle, B. Schonlinner, V. Ziegler, U. Prechtel, and W. Menzel. Antenna Arrays for RF-MEMS based 77 GHz On-Board Wake Vortex Detection Sensor. In *2nd International ITG Conference on Antennas, INICA '07*, pages 217–221, March 2007.

[137] T. A. Seliga and J. B. Mead. High Resolution W-Band Radar Detection and Characterization of Aircraft Wake Vortices in Precipitation. In *WakeNet3-Europe/Greenwake dedicated workshop on "Wake vortex & wind monitoring sensors in all weather conditions"*, March 2010.

[138] P. Drake and M. Sarcione. X-band wake vortex radar. In *WakeNet3-Europe/Greenwake dedicated workshop on "Wake vortex & wind monitoring sensors in all weather conditions"*, March 2010.

[139] F. Barbaresco, J. C. Deltour, K. Pham, and M. Hagen. Horizontal Wind Field Estimation from Radar Reflectivity Data & Calibration with Doppler and Bistatic Radar Data. Its use for Wake Turbulence Forecasting on Airport within the framework of the European IST Project ATC-WAKE. In *RADAR 2004 - International Conference on Radar Systems*, 2004.

[140] D.-I. Lee. Advanced uses of weather radar. Technical report, Pukyong National University, 2006.

[141] J. Li, X. Wang, and T. Wang. Modeling the dielectric constant distribution of wake vortices. *IEEE Transactions on Aerospace and Electronic Systems*, 47(2):820 –831, april 2011.

[142] D. Saban. *Wake Vortex Modelling and Simulation for Air Vehicles in Close Formation Flight*. PhD thesis, Cranfield University, 2010.

[143] T. Hofbauer and T. Gerz. Shear-layer effects on the dynamics of a counter-rotating vortex pair. In *Proceedings of 38th Aerospace Sciences Meeting and Exhibit*, 2000.

[144] M. P. Matthews, J. T. Dasey, G. H. Perras, and C. S. D. Planetary boundary layer measurements for the understanding of aircraft wake vortex behavior. In *7th Conf. on Aviation Weather Systems, Long Beach, CA, Amer. Meteor. Soc.*, 1997.

[145] D. C. Burnham. Effect of ground wind shear on aircraft trailing vortices. *AIAA Journal*, 10(8):1114– 1115, 1972.

[146] C. H. Liu and L. Ting. Interaction of decaying trailing vortices in spanwise shear flow. *Computers and Fluids*, 15(1):77–92, 1987.

[147] Z. C. Zheng and K. Baek. Inviscid interactions between wake vortices and shear layers. *AIAA Journal*, 36(2):477–480, 1999.

[148] D. J. Hill and P. G. Saffman. Counter-rotating vortex patches in shear: a model of the effect of wind shear on aircraft trailing vortices. *Proceedings of the Royal Society of London. Series A: Mathematical, Physical and Engineering Sciences*, 458(2023):1527–1553, 2002.

[149] F. H. Proctor and N. N. Ahmad. Crosswind shear gradient affect on wake vortices. In *3rd AIAA Atmospheric Space Environments Conference*, 2011.

[150] D. Hamilton and F. Proctor. Wake vortex transport in proximity to the ground. In *Proceedings of The 19th Digital Avionics Systems Conference*, 2000.

[151] F. Holz apfel. Probabilistic two-phase wake vortex decay and transport model. *Journal of Aircraft*, 40(2):323–331, 2003.

[152] F. Holzapfel, T. Hofbauer, D. Darracq, H. Moet, F. Garnier, and C. F. Gago. Analysis of wake vortex decay mechanisms in the atmosphere. *Aerospace Science and Technology*, 7:263–275, 2003.

[153] F. Holz apfel and R. E.Robins. Probabilistic two-phase aircraft wake-vortex model: Application and assessment. *Journal of Aircraft*, 41(5):1117–1126, 2004.

[154] F. H. Proctor, N. N. Ahmad, G. F. Switzer, and F. M. Limon Duparcmeur. Three-phased wake vortex decay. In *AIAA Paper*, 2010.

[155] H. Sauvageot. *Radar Meteorology.* Artech House Publishers, 1992.

[156] B. Lim. Derivation of the shape of raindrops. Technical report, School of Applied and Engineering Physics, Cornell University, 2006.

[157] K. V. Beard and C. Chuang. A new model for the equilibrium shape of raindrops. *Journal of the Atmospheric Sciences*, 44, 1987.

[158] W. Bentley. Studies of raindrops and raindrop phenomena. *Monthly Weather Review*, 10:450–456, 1904.

[159] E. Villermaux and B. Bossa. Single-drop fragmentation determines size distribution of raindrops. *Nature Physics*, 5:697–702, 2009.

[160] D. Atlas and C. W. Ulbrich. The physical basis for attenuation-rainfall relationships and the measurement of rainfall parameters by combined attenuation and rader methods. *J. Rech. Atomos.*, 8, 1974.

[161] H. Jiang, M. Sano, and M. Sekine. Weibull raindrop-size distribution and its application to rain attenuation. *IEE Proceedings on Microwaves, Antennas and Propagation*, 144(3):197 –200, 1997.

[162] R. L. S. Gunn and T. W. R. East. The microwave properties of precipitation particles. *Quarterly Journal of the Royal Meteorological Society*, 80:522–545, 1954.

[163] D. N. Moisseev, V. Chandrasekar, C. M. H. Unal, and H. W. J. Russchenberg. Dual-Polarization Spectral Analysis for Retrieval of Effective Raindrop Shapes. *Journal of Atmospheric and Oceanic Technology*, 23(12):1682–1695, 2006.

[164] T. Kobayashi and A. Adachi. Retrieval of arbitrarily shaped raindrop size distributions from wind profiler measurements. *Journal of Atmospheric and Oceanic Technology*, 22(4):433–442, 2005.

[165] P. Kollias, J. Rémillard, E. Luke, and W. Szyrmer. Cloud radar doppler spectra in drizzling stratiform clouds: 1. forward modeling and remote sensing applications. *Journal of Geophysical Research: Atmospheres*, 116(D13):D13201, 2011.

[166] P. Kollias, W. Szyrmer, J. Rémillard, and E. Luke. Cloud radar doppler spectra in drizzling stratiform clouds: 2. observations and microphysical modeling of drizzle evolution. *Journal of Geophysical Research: Atmospheres*, 116(D13):D13203, 2011.

[167] A. R. Bohne. Radar detection of turbulence in precipitation environments. *Journal of the Atmospheric Sciences*, 39(8):1819–1837, 1982.

[168] F. J. Yanovsky, H. W. J. Russchenberg, and C. M. H. Unal. Retrieval of information about turbulence in rain by using doppler-polarimetric radar. *IEEE Transactions on Microwave Theory and Techniques*, 53(2):444 –450, 2005.

[169] V. V. Marchuk, Y. P. Ostrovsky, I. V. Mazura, and F. J. Yanovsky. Methods of turbulence detection by analyzing precipitation behaviour. In *2006 International Radar Symposium*, May 2006.

[170] Y. S. Khraisat and F. J. Yanovsky. Reflections from raindrops in case of turbulence: phenomenological analysis and signal processing. In *Proceedings of SPIE, the International Society for Optical Engineering*, 2007.

[171] Y. S. H. Khraisat and F. J. Yanovsky. Joint influence of rain rate and turbulence on radar signal spectrum width. In *2007 European Microwave Conference*, pages 1708 –1711, October 2007.

[172] G. D. Nastrom. Doppler radar spectral width broadening due to beamwidth and wind shear. *Annales de Geophysique*, 15:786–796, 1997.

[173] T.-Y. Yu, Y. Wang, A. Shapiro, M. B. Yeary, D. S. Zrnic, and R. J. Doviak. Characterization of tornado spectral signatures using higher-order spectra. *Journal of Atmospheric and Oceanic Technology*, 24(12):1997–2013, 2007.

[174] T.-Y. Yu, R. R. Rondinel, and R. D. Palmer. Investigation of non-gaussian doppler spectra observed by weather radar in a tornadic supercell. *Journal of Atmospheric and Oceanic Technology*, 26(3):444–461, 2009.

[175] M. Fang, R. J. Doviak, and V. Melnikov. Spectrum Width Measured by WSR-88D: Error Sources and Statistics of Various Weather Phenomena. *Journal of Atmospheric and Oceanic Technology*, 21(6):888–904, June 2004.

[176] R. J. Doviak, D. S. Zrnic, and D. S. Sirmans. Doppler weather radar. *Proceedings of the IEEE*, 67(11):1522 – 1553, November 1979.

[177] E. Loth. Particles, drops, and bubbles: Fluid dynamics and numerical methods. Book Draft for Cambridge University Press, May 2010.

[178] A. B. Kostinski and R. A. Shaw. Droplet dynamics: Raindrops large and small. *Nat Phys*, 5(9):624–625, September 2009.

[179] D. C. Dowell, C. R. Alexander, J. M. Wurman, and L. J. Wicker. Centrifuging of hydrometeors and debris in tornadoes: Radar-reflectivity patterns and wind-measurement errors. *Monthly Weather Review*, 133(6):1501–1524, June 2005.

[180] S. Lovejoy and D. Schertzer. Turbulence, raindrops and the l1/2 number density law. *New Journal of Physics*, 10:075017 (32pp), 2008.

[181] R. Monchaux, M. Bourgoin, and A. Cartellier. Analyzing preferential concentration and clustering of inertial particles in turbulence. *International Journal of Multiphase Flow*, 40:1–18, 2012.

[182] F. Barbaresco, P. Juge, M. Klein, Y. Ricci, J. Schneider, and J. Moneuse. Optimising runway throughput through wake vortex detection, prediction and decision support tools. In *2011 Tyrrhenian International Workshop on Digital Communications - Enhanced Surveillance of Aircraft and Vehicles (TIWDC/ESAV)*, pages 27 –32, September 2011.

[183] M. Brooker. *The Design and Implementation of a Simulator for Multistatic Radar Systems*. PhD thesis, University of Cape Town, 2008.

[184] ARM. Measurement: Radar reflectivity. `http://www.arm.gov/measurements/radarreflect`, 2012.

[185] B. L. Cheong, R. D. Palmer, and M. Xue. A time series weather radar simulator based on high-resolution atmospheric models. *Journal of Atmospheric and Oceanic Technology*, 25(2):230–243, 2008.

[186] C. Capsoni and M. D'Amico. A physically based radar simulator. *Journal of Atmospheric and Oceanic Technology*, 15:593–598, 1998.

[187] C. Capsoni, M. D'Amico, and R. Nebuloni. A multiparameter polarimetric radar simulator. *Journal of Atmospheric and Oceanic Technology*, 18:1799–1809, 2001.

[188] M. A. Richards, j. A. Scheer, and W. A. Holm. *Principles of modern radar: Basic principles*. SciTech Publishing, Inc., 2010.

[189] L. Sauvage, E. Isambert, G. Winckelmans, J. Cariou, and A. Dolfi. WV SEPARATIONS TECHNOLOGY CASE-Preparation of Wake Vortex Detection Technology Case. Technical Report TRSC52/2004, Eurocontrol EEC, 2004.

[190] D. S. Zrnic. Simulation of weatherlike doppler spectra and signals. *Journal of Applied Meteorology*, 14(4):619–620, 1975.

[191] R. Lhermitte. A 94GHz Doppler radar for cloud observations. *Journal of Atmospheric and Oceanic Technology*, 4:36–48, 1987.

[192] R. M. Lhermitte. Cloud and precipitation remote sensing at 94 GHz. *IEEE Transactions on Geoscience and Remote Sensing*, 26(3):207 –216, may 1988.

[193] M. Fang and R. J. Doviak. Coupled Contributions in the Doppler Radar Spectrum Width Equation. *Journal of Atmospheric and Oceanic Technology*, 25(12):2245–2258, December 2008.

[194] G. Zhang, J. Vivekanandan, and E. Brandes. A method for estimating rain rate and drop size distribution from polarimetric radar measurements. *IEEE Transactions on Geoscience and Remote Sensing*, 39(4):830 –841, April 2001.

[195] F. Barbaresco. Innovative tools for radar signal processing Based on Cartan's geometry of SPD matrices & Information Geometry. In *Proceedings of IEEE Radar Conference, RADAR '08*, 2008.

[196] F. Barbaresco, A. Jeantet, and U. Meier. Wake vortex X-band radar monitoring: Paris-CDG Airport 2008 campaign results & prospectives. In *Proceedings of IEEE Radar Conference - Surveillance for a Safer World*, pages 1–6, 2009.

[197] L. Yang, M. Arnaudon, and F. Barbaresco. Riemannian median, geometry of covariance matrices and radar target detection. In *2010 European Radar Conference (EuRAD)*, pages 415 –418, 2010.

[198] L. Yang, M. Arnaudon, and F. Barbaresco. Geometry of covariance matrices and computation of median. In *Proceedings of the 30th International Workshop on Bayesian Inference and Maximum Entropy Methods in Science and Engineering*, 2010.

[199] Z. Liu and F. Barbaresco. Doppler information geometry for wake turbulence monitoring. In F. Nielsen and R. Bhatia, editors, *Matrix Information Geometry*, pages 277–290, 2012.

[200] S. Bash, D. Carpman, and D. Holl. Radar Pulse Compression Using the Nvidia CUDA Framework. In *IEEE High Performance Extreme Computing Conference*, volume 1, page 1, 2008.

[201] Y. Lu, K. Wang, X. Liu, and W. Yu. A GPU based real-time SAR simulation for complex scenes. In *Proceedings of IEEE International Radar Conference*, Bordeaux, France, 2009.

[202] J. Pettersson. Radar Signal Processing with Graphics Processors (GPUs). Master's thesis, Uppsala Universitet, 2010.

[203] R. Weber, A. Gothandaraman, R. J. Hinde, and G. D. Peterson. Comparing hardware accelerators in scientific applications: A case study. *IEEE Transactions on Parallel and Distributed Systems*, 22(1):58 –68, 2011.

[204] B. Zhang, G.-b. Liu, D. Liu, and Z.-l. Fan. Real-time software gnss signal simulator accelerated by cuda. In *2010 2nd International Conference on Future Computer and Communication [Volume 1]*, 2010.

[205] D. De Donno, A. Esposito, L. Tarricone, and L. Catarinucci. Introduction to GPU Computing and CUDA Programming: A Case Study on FDTD [EM Programmer's Notebook]. *IEEE Antennas and Propagation Magazine*, 52(3):116 –122, 2010.

[206] NVIDIA. *NVIDIA CUDA Programming Guide Version 1.0*. NVIDIA, 2007.

Publications

Journal paper:

Z. Liu, N. Jeannin, F. Vincent, and X. Wang. *Modeling the Radar Signature of Raindrops in Aircraft Wake Vortices*[J]. Journal of Atmospheric and Oceanic Technology, 30(3): 470-484, 2013.

Book chapter:

Zhongxun Liu and Frdric Barbaresco. *Doppler information geometry for wake turbulence monitoring*. In Frank Nielsen and Rajendra Bhatia, editors, Matrix Information Geometry, pages 277–290. Springer Berlin Heidelberg, 2013.

Conference & workshop:

Zhongxun Liu, Nicolas Jeannin, Francois Vincent, Florent Christophe, Xuesong Wang. *A new Simulation Scheme for Radar Signatures of Raindrops in Wake Vortices*[C]. 93rd American Meteorological Society Annual Meeting, Austin, 2013

Zhongxun Liu, Nicolas Jeannin, Francois Vincent, Xuesong Wang.*Simulations of a Doppler Radar for monitoring wake vortices in rainy weather* [C]. 7th European Conference on Radar in Meteorology and Hydrology, Toulouse, 2012

Z. Liu, N. Jeannin, F. Vincent, X. Wang. *Radar Monitoring of Wake Turbulence in Rainy Weather: Modelling and Simulation*. WakeNet3-Europe 4th Major Workshop, Langen, February, 2012

Zhongxun Liu, Nicolas Jeannin, Francois Vincent, Xuesong Wang. *Development of a Radar Simulator for Monitoring Wake Vortices in Rainy Weather*[C]. IEEE International Radar Conference, Chengdu, 2011

Zhongxun LIU. *A Radar Simulator for Monitoring Wake Turbulence in Rainy Weather*. WakeNet3-Europe 3rd Major Workshop, Southampton, May, 2011